TECHNISCHE UNIVERSITÄT MÜNCHEN

Lehrstuhl für Physikalische Chemie

Mechanistic Studies on Thermal and Photocatalytic Alcohol Reforming on Semiconductors and Metal Cluster-Semiconductor Hybrid Materials

Constantin Alexander Walenta

Vollständiger Abdruck der von der Fakultät für Chemie der Technischen Universität München zur Erlangung des akademischen Grades eines

Doktors der Naturwissenschaften

genehmigten Dissertation.

Vorsitzender: Prof. Dr. Hubert A. Gasteiger
Prüfer der Dissertation:

1. Prof. Dr. Ulrich K. Heiz
2. Prof. Dr. Martin Stutzmann
3. Prof. Dr. Bettina V. Lotsch (Max-Planck-Institut für Festkörperforschung)

Die Dissertation wurde am 26.02.2018 bei der Technischen Universität München eingereicht und durch die Fakultät für Chemie am 04.04.2018 angenommen.

Abstract

Despite of intense research efforts, photocatalytic processes for the generation of renewable fuels are still lacking the requirements for successful application on industrial scale. Research strategies have so far been focused on material screening due to the complexity of the underlying processes. To gain a deeper fundamental understanding of the underlying mechanisms, defined semiconductor and metal cluster-semiconductor model systems are studied under UHV conditions.
By the clear assignment of key properties for both, thermal and photochemical reactions, mechanisms on a molecular scale can be elucidated for photochemical, photo-thermal and thermal reactions. By combining the knowledge from single crystal studies with observations under catalytic conditions, complex molecular mechanisms of alcohol reforming on metal cluster-semiconductor hybrid materials are unraveled. A hole mediated disproportionation reaction is revealed to be a new photocatalytic reaction mechanism for hydrogen evolution from methanol and other alcohols. The role of the metal co-catalyst in this reaction is the dehydroxylation of the semiconductor surface. Furthermore, it is demonstrated how the selectivity of photocatalytic reactions is influenced by temperature, which is often neglected in many studies.

Zusammenfassung

Trotz der intensiver Forschung mangelt es photokatalytischen Prozessen zur Gewinnung erneuerbarer Brennstoffe immer noch an den Anforderungen für eine erfolgreiche industrielle Anwendung. Forschungsansätze fokussieren sich aufgrund der Komplexität der zu Grunde liegenden Prozesse zumeist auf die Suche neuer Materialien. Um ein tiefgehendes Verständnis der vorliegenden Mechanismen zu erhalten, werden wohldefinierte Halbleiter und Metalcluster-Halbleiter Modellsysteme im Ultrahochvakuum studiert.
Dank einer klaren Zuordnungen von Schlüsseleigenschaften für thermische und photochemische Reaktionen können Mechanismen auf einer molekularen Ebene für photochemische, photothermische und thermische Reaktionen erforscht werden. Die Kombination aus Erkenntnissen von Einkristallstudien mit Beobachtungen unter katalytischen Bedingungen ermöglichte es, komplexe molekulare Mechanismen auf Metallcluster-Halbleiter Hybridmaterialien aufzuklären. Eine Loch-vermittelte Disproportionierungsreaktion wurde als neuer Mechanismus für photokatalytische Reaktionen zur Wasserstoffentwicklung aus Methanol und anderen Alkoholen gefunden. Die Rolle des Metall Ko-Katalysators in dieser Reaktion liegt in der Dehydroxylierung der Halbleiteroberfläche. Darüberhinaus wird gezeigt, in wie weit die Selektivität photokatalytischer Reaktionen von der Temperatur beeinflusst wird, welche oft in vielen Studien vernachlässigt wird.

Contents

1. Introduction and Motivation **1**

2. Concepts in Photocatalysis **5**
2.1. Consequences from Band Bending for Photochemistry 5
2.2. Fate of the charges 7
2.3. Photocatalytic Activity 8
2.4. Enhancing Photocatalysis with Bias 9
2.5. Reaction Mechanisms in Alcohol Reforming 11

3. Experimental **12**
3.1. UHV Apparatus 12
3.1.1. Analysis Chamber 12
3.1.2. Cluster Source 15
3.2. Laser Systems 15
3.3. Sample Preparation and Characterization 16
3.3.1. TiO_2(110) 16
3.3.1.1. Redcued TiO_2(110) 16
3.3.1.2. Oxidized TiO_2(110) 18
3.3.1.3. Hydroxylated TiO_2(110) 19
3.3.2. $Ga_2O_3(\bar{2}01)$ 19
3.3.3. GaN(0001) 20
3.3.4. Pt_x/TiO_2(110) 22
3.4. Typical Reactivity Measurements 22
3.4.1. Temperature Programmed Desorption 22
3.4.2. Photon-Stimulated Desorption 23
3.4.3. Photocatalytic Measurements 24

4. Doping-Dependent Adsorption and Photon-Stimulated Desorption of CO on MBE-grown GaN(0001) **26**

5. Ethanol Chemistry on GaN(0001) **28**
5.1. Ethanol Surface Chemistry on MOCVD-grown GaN(0001) 28
5.1.1. Ethanol Thermal chemistry on MOCVD-grown GaN(0001) 28
5.1.2. Ethanol Photochemistry on MOCVD-grown GaN(0001) 35
5.2. Ethanol Surface Chemistry on MBE-grown GaN(0001), GaO_x/GaN(0001) and $Ga_2O_3(\bar{2}01)$ 37

6. Alcohol chemistry on α-Fe_2O_3(0001) **39**
6.1. Experimental Methods 40
6.2. Characterization of the α-Fe_2O_3(0001) surface 40
6.3. Thermal Chemistry of Methanol and Ethanol 43

6.4. Photochemistry of Ethanol on α-Fe_2O_3(0001) 46
6.5. Summary 47

7. Ethanol Chemistry on TiO_2(110) 49
7.1. Quantified Thermal Ethanol Chemistry on r-TiO_2(110) 49
7.2. The Mechanism of Ethanol Photo-Oxidation on TiO_2(110) 55

8. Photocatalytic Selectivity Switch to C-C Scission: α-Methyl Ejection of tert-Butanol on TiO_2(110) 62

9. The Mechanism of H_2 Evolution from Methanol on Pt_x/TiO_2(110) 75

10. Tuning the Selectivity of Photoreactions: Temperature Control in Water-Free Alcohol Reforming TiO_2(110)-Supported Pt Clusters 90
10.1. Results 90
10.1.1. Methanol 90
10.1.2. Ethanol, Benzaldehyde and Cyclohexanol 95
10.1.3. tert-Butanol 97
10.2. Discussion 98
10.2.1. Photoactive Intermediates and Reaction Sites 98
10.2.2. A Detailed Mechanistic Picture for Alcohol Reforming 101
10.2.3. Mechanistic Consequences for Applied Systems 104

11. Single-Atom Photocatalysis of Methanol on Pt_1/TiO_2(110) - Co-Catalysts at the Lowest Size-Limit 106

12. O_2-PSD from differently prepared TiO_2(110) 109
12.1. Effect of surface preparation 110
12.2. Effect of Pt-loading 112

13. Conclusion and Outlook 115

Bibliography 118

List of Abbreviations 144

List of Figures 145

Acknowledgements 148

List of Publications 150

Appendices 152

A. Further Experimental Details 153
A.1. The Cluster Source 153

A.2. Chemicals 159

B. TPD and TOF Quantification 160

C. Doping-Dependent Adsorption and Photon-Stimulated Desorption of CO on GaN(0001) 163

D. Ethanol Surface Chemistry on MBE-grown GaN(0001), GaO_x/GaN(0001) and $Ga_2O_3(\bar{2}01)$ 175

"Whatever it is you're seeking won't come in the form you're expecting."

Kafka on the shore - Haruki Murakami

1 Introduction and Motivation

Since the discovery of photoelectrochemical water-splitting on TiO_2 by Fujishima and Honda[1], many research efforts have been carried out to drive chemical reactions catalytically with light.[2–10] One major driving force behind all of those studies is the hope, that water-splitting will one day solve all global energy and environmental problems and make future society independent of fossil fuels and feedstocks. The main idea behind photocatalytic water-splitting remains very intriguing: The amount of energy by sunlight-irradiation on earth in one hour equals the global energy demand of mankind for one year.[11] Since hydrogen is a common feedstock in the chemical industry[12,13] and also a possible fuel for future transportation[14–16] and energy conversion[17–21], that sparked the concept of the "hydrogen economy".[13,22] Further estimations show that even at an efficiency of only 5%, an area of 1/10 of the Sahara desert full of photoreactors would match the energy demand by mankind in H_2.[11] Apart from water-splitting, which is considered one of the holy grails in chemistry[2,17], major directions of research include photocatalytic methane activation[23,24], photocatalytic CO_2 fixation[25–28] and photocatalytic steam reforming of alcohols[29–33] or biomass.[34,35] Despite those many efforts, the only application for artificial photocatalysts that is already in wide-spread use, is the decomposition of organic pollutants in waste-water treatment.[36,37] A "gold-rush" to the highest efficiencies for photocatalytic water-splitting[17,38], similar to the one for photovoltaic devices[39,40], was observed over the last 30 years. In contrast to the standard testing for photovoltaic devices, such a system has not yet been established for photocatalytic studies, which is heavily criticized by leading researcher's in the field.[41–43] Figure 1.1 shows a selection of record quantum efficiencies for full water-splitting devices for the last 20 years. The reported efficiencies range over six orders of magnitude over the last 20 years. While some very efficient catalysts are already known like the one reported by Kudo[44] in 2003 with 56%, this efficiency was obtained at at irradiation wavelength of 270 nm, which is virtually not present in the solar spectrum.

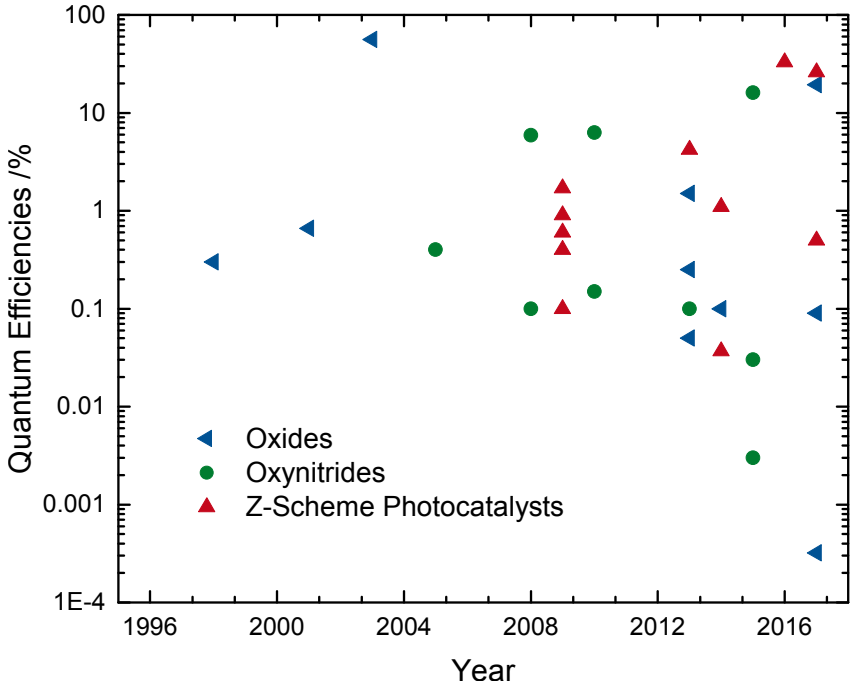

Figure 1.1. Selection of reported quantum yields on a semi-logarithmic scale for previous demonstrations of light-driven full water-splitting. The representation is based on an idea by Fabian *et al.*[17] The values were obtained from previous literature reports.[38,44–64] Although in this representation, the photocatalysts are only classified by the semiconductor properties and the exact experimental conditions are quite different for the measurements, no clear trend towards more efficient photocatalysts can be seen.

While the efficiency of the catalyst might not be as crucial as discussed above, a scale-up to macroscopic amounts certainly is. In Figure 1.2, the actual amounts of produced molecular hydrogen and oxygen are shown and no study exceeds one mol per h. To stress this point even more, that means that the total amount of formed hydrogen for those very efficient catalysts is actually less than 2 g hydrogen per hour. Although envisioned for some time[17], only this year the group of Domen presented an extended photocatalyst reactor panel of 1 m^2.[65]

A major drawback that most photocatalysts have in common with electrochemical systems, are sluggish oxygen evolution kinetics.[66,67] Hence, recent developments focussed on understanding and enhancing the oxygen evolution reaction to increase the overall performance.[68–72]

As the reader may already grasp from this small extract, the complexity of the photocatalytic systems is immense. In the photocatalysts, whose performances are presented in Figures 1.1 and 1.2, 29 different chemical elements from the periodic table are used in the light harvester and further 8 additional ones in the co-catalysts. Most approaches focus on an improvement of the performance by further increasing the complexity i.e. by band-engineering[73], taking a second co-catalyst[74], which might be modified even more by core-shell formation[57,75,76] or meta-stable degrees of oxidation[69,77] The overwhelming complexity becomes most evident, when taking a closer look at Degussa P25 TiO_2 pow-

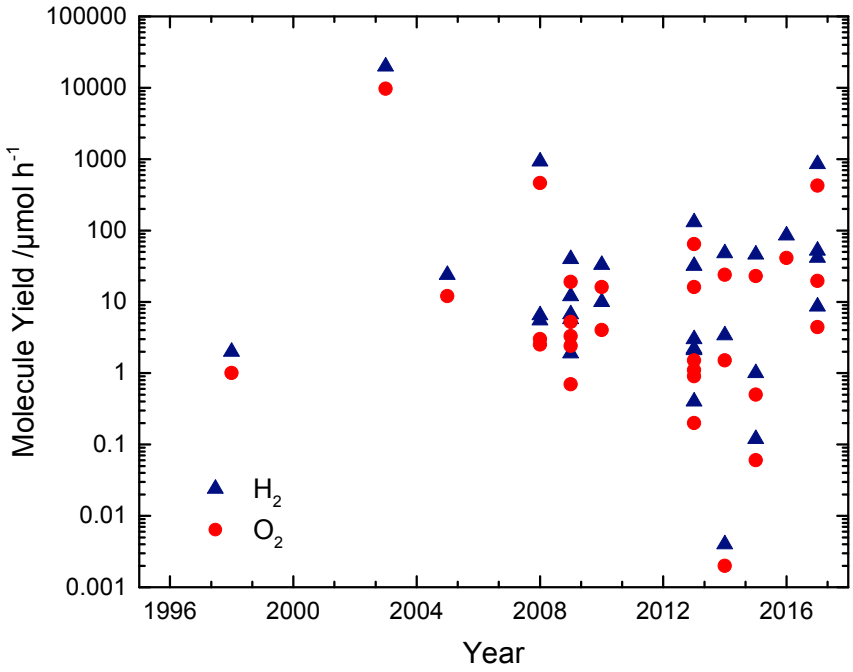

Figure 1.2. Selection of reported amounts of H_2 and O_2 from photocatalytic water-splitting systems an a semilogarithmic scale. Note that yields from the studies are considered stoichiometric for the shown studies.[38,44–64] The figure illustrates, how the actual amounts of H_2 in total never exceed one mol per hour of H_2. The yields vary over eight orders of magnitude for the shown systems.

ders, the most often used semiconductor in photocatalysis.[78,79] Although P25 is very active for photocatalysis, the actual composition of the material is rather a rough estimate of a 70:30 or an 80:20 composition of anatase and rutile.[78] In a quantitative study, Ohtani *et al.* showed that their material composition was 78:14:8 of anatase, rutile and an amorphous phase, respectively. The high photocatalytic activity is often attributed to a possible core-shell phase or a synergistic effects of anatase and rutile phases[80,81], which, however, could not be confirmed by the previously mentioned study.[78] Ohtani describes these effects further as "[...] myths, speculations without any scientific proof".[78] Extensive recent work shows that a quantitative determination of electron trap states of TiO_2[82,83] and other metal oxide powders[83,84] by photoacoustic spectroscopy is a better indicator for photocatalytic performance of a certain powder and their mixtures.

The approach to study photocatalysis in this thesis is explicitly not from an application perspective, but with a surface science approach. This approach in general aims to reveal the reaction mechanisms on a molecular level and, as it was shown in the past, was successfully carried out for many industrially important catalytic reactions.[85–93] Therefore, the presented work focusses on a molecular understanding of phenomena arising on the semiconductor's surface upon photon-excitation with a photon energy over the band gap of the semiconductor material. In this regard, the work of Yates' group on rutile TiO_2(110) can be considered pioneering in the field[94–98] and made TiO_2 one of the most investigated semiconductor for thermal and photochemical processes.[79,99–104]

While a previous attempt to investigate full water splitting on Cu_2O[45] under UHV conditions[105] did not find any catalytic activity, single crystal studies on TiO_2 and other semiconductors prevailed for the determination of photochemical mechanistic elementary steps.[79,94,106–111] In the scope of this work, an ultra-high vacuum setup has been expanded with a size-selected cluster source in order to study metal cluster-semiconductor hybrid materials in very well defined conditions. As a prerequisite, the knowledge of the thermal and photochemistry of the bare semiconductors is studied to understand the underlying mechanisms of the partial reactions. In further experiments, metal clusters are landed on the semiconductor and the resulting co-catalyst loaded hybrid materials are investigated under photocatalytic conditions. In this regard, alcohol reforming is chosen as a model reaction, since the alcohols are regularly used in more applied studies under ambient conditions[30,32,112] and are further considered as a possible renewable feedstock for energy provision.[30,113]. The main goal of this thesis comprises identifying thermal and photochemical reaction intermediates and pathways both on bare semiconductors and co-catalyst loaded ones to investigate the mechanisms of photocatalytic hydrogen production under very well defined conditions.
In Chapter 2 some general concepts from photocatalysis are presented to give the reader some conceptual background. The experimental setup and catalyst preparations are described in Chapter 3. In Chapters 4 and 5, the results of a cooperation with the chair of experimental semiconductor physics at the Walter Schottky Institute at the Technical University of Munich are presented. Here, gallium nitride is investigated, since the electronic properties such as the doping, the band gap and the surface morphology of this semiconductor can be tailored by the growth method and the conditions. The effect of these parameters on the surface chemistry and photochemistry was explored for carbon monoxide and ethanol. In Chapter 6, the results of a further collaborative project with the group of Prof. Cynthia Friend at Harvard University on the thermal- and photochemistry of methanol and ethanol on a haematite $Fe_2O_3(0001)$ model surface are presented. Further, the quantified mechanistic pathways of thermal ethanol chemistry on $TiO_2(110)$ are determined and two mechanisms for the photochemistry of ethanol on this surface are found in Chapter 7. In another mechanistic study (Chapter 8) of alcohol photochemistry it was found that the photochemistry of tert-butanol constitutes two photochemical pathways for tert-butanol, namely the photo-oxidation to acetone and the photothermal dehydration to isobutene. In Chapter 9, a new mechanism for photocatalytic methanol reforming on a platinum cluster loaded $TiO_2(110)$ surface is presented. It has been described, that a photocatalytic disproportionation reaction takes place, while formaldehyde is formed on the semiconductor and molecular hydrogen desorbs form the Pt clusters. In Chapter 10, the transferability of this mechanism is shown by changing the reactant to other alcohols. Further, different selectivities for the photoreactions have been observed in the cases of methanol and tert-butanol, which changed by the reaction temperature. In addition, in Chapter 11 $TiO_2(110)$ decorated with Pt_1 is also shown to be an active catalyst for hydrogen evolution form methanol. After a summary and conclusion, additional information is given in the appendix.

2

Concepts in Photocatalysis

2.1. Consequences from Band Bending for Photochemistry

The first concept introduced in the chapter is the one of band bending in extended semiconductors. Zhang and Yates published a very dense and comprehensive review of band bending and discussed the consequences for semiconductor surface chemistry and surface physics.[98] A very small area of this review will be presented here, to establish a picture of the photochemical driving forces on extended semiconductors.

In a semiconductor, band bending may exist due to surface states, adsorbates, metal contacts or field effects. Surface states may exist due to dangling bonds and defects or the intrinsic polarity of the material like in the case of ZnO and GaN. On an n-type semiconductor, the surface states are intrinsically negatively charged and the charge balance is kept by positive donors in the space charge region (SCR). The result is an upward band-bending in the dark (see Figure 2.1). When the semiconductor is illuminated with photon energies above the band gap, an electron in the conduction band and a hole in the valence band can be formed. Due to the band bending, the holes preferentially migrate from the bulk to the surface, where they can neutralize the negatively charged surface states. The photoelectrons in the SCR move preferentially towards the bulk, since they are still repelled by the negative charges at the surface. Consequently, under illumination a flattening of the bands occurs and the driving force for the charge migration is reduced. On a p-type semiconductor the same applies with opposite charges and a downward band bending. In the p-type semiconductor, the electrons are the minority charge carriers instead of the holes in the n-type semiconductor.

The electronic structure of the surface and therefore the band bending in dark and illuminated conditions can obviously be altered by the adsorption of a molecule, the deposition of metal particles and, of course, other reactants as well as even by a bulk solution phase. All of these altering cases, however, are commonly needed in photocatalytic reactions, which makes a disentangling of the effects a tedious task. Therefore, O_2 photochemistry is commonly used as chemical probe for influences on the surface electronic structure.[98,114,115]

Following the line of thought for n-type semiconductors, in the TiO_2 single crystal studies, photoholes are found to be the driving force for photo-oxidation processes on the n-type semiconductors.[106,114–121] This consensus is established from many studies of photo-oxidation of alcohols, aldehydes and ketones in the last years with mainly one exception: the photo-induced dissociation of oxygen on TiO_2(110).[122,123] Chemical in-

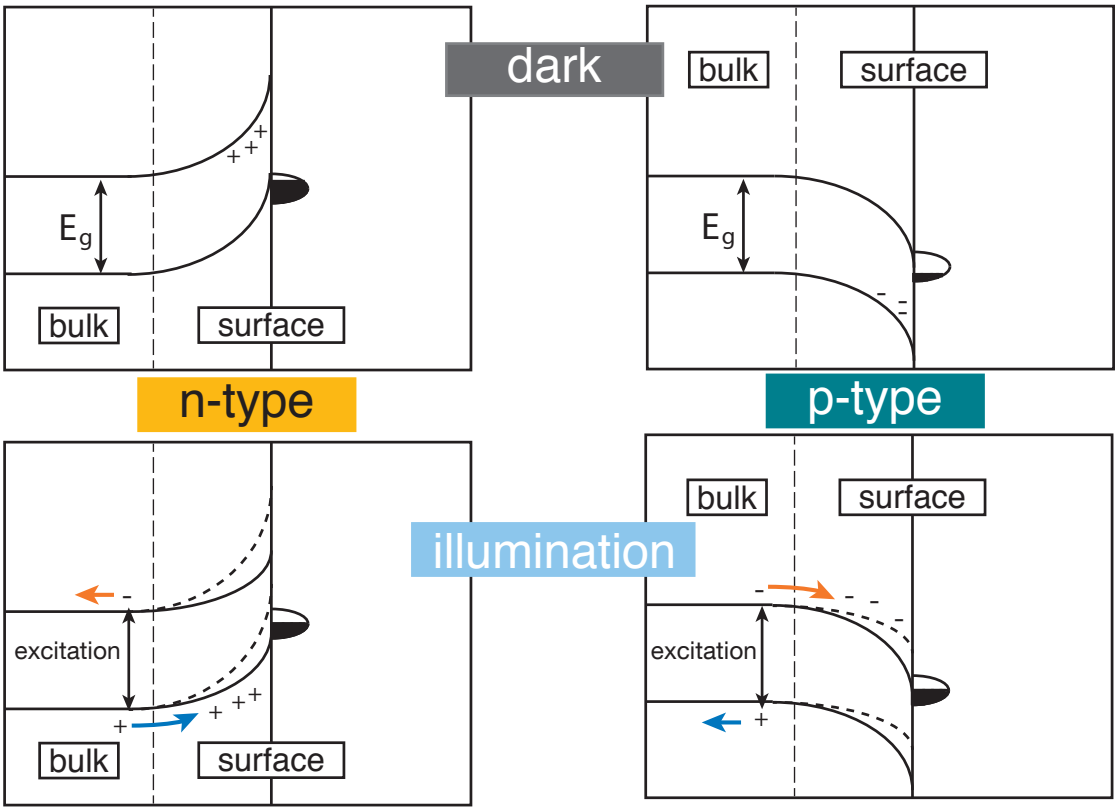

Figure 2.1. Band Bending models for an n-type and p-type semiconductor in the dark and the illumination case. In the upper left panel, an n-type semiconductor is shown in the dark. In such a case, a space charge region (SCR) is formed, in which positive donor states reside, while the surface is negatively charged. This is indicated by the filling of the surface states, in this case the black states on the surface. Under illumination (lower left panel), an electron-hole pair is created with the electron in the conduction band and the hole in the valence band. Due to the band bending, the holes are subject to a driving force towards the surface. There, they neutralize the negatively charged surface states. Electrons in the SCR instead preferentially travel to the bulk. By the neutralization of the surface states, the band bending is reduced and the surface states are less negatively charged, consequently also reducing the driving force for the holes to travel to the surface.
The dark case for a p-type semiconductor shows a downward band bending and negative donor states in the SCR, while the surface states are charged positively. Under illumination, the band bending in this case results in a driving force for the electrons toward the surface and charge it more negatively, indicated by a filling of the surface states. Consequently, holes preferentially travel to the bulk due to the band bending, until the driving force is reduced by a flattening of the bands.

tuition in these studies leads to a picture, where the oxygen dissociation is facilitated by a not further specified electron upon UV irradiation.[122–126] Oxygen dissociation is also of paramount importance for the CO photo-oxidation on TiO_2(110).[127–130] While for the photo-oxidation of organics on the n-type TiO_2 the hole is the consensual driving force for the photo-oxidation processes, for the oxygen chemistry on the TiO_2(110) surface the picture is less clear. While the photoholes are thought to be responsible for a neutralization

and desorption of surface bound O_2^--species[97,131,132], molecular oxygen dissociation is found as a competing process attributed to electrons.[121–123,126]
In summary, for some chemical reactions like the oxidation of organics on the surface, hole-mediated photo-oxidation mechanisms are well accepted on n-type semiconductors and the macroscopic band bending picture corroborates the observed photochemical mechanism on a molecular scale. However, this agreement of the band bending with the observed molecular mechanism is not established for other observed photochemical phenomenons like the dissociation of oxygen by electrons[122] or the photodesorption of weakly bound butenes.[133,134]

2.2. Fate of the charges

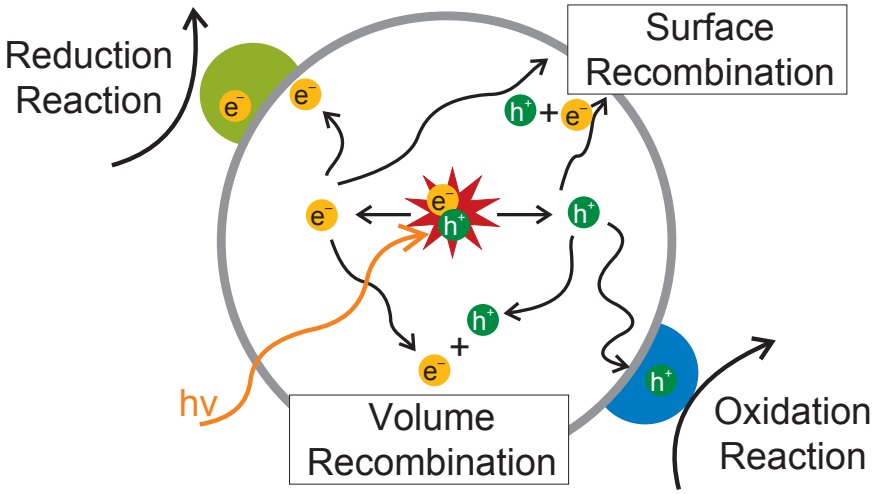

Figure 2.2. Scheme of the photoexcitation in a solid nanoparticulate semiconductor. Upon the formation of an exciton by illumination, the photon-generated charges need to be spatially separated. Two major deexcitation events may occur, namely the recombination of the charges in the bulk or on the surface, which are both undesired for photocatalysis. The desired reaction pathway is the chemical reaction with molecules on the surface, either a reduction reaction facilitated by electrons or an oxidation reaction mediated by the holes. Possible co-catalysts are displayed as green and blue particles on the semiconductor's surface.

While band bending is a phenomenon on extended materials and corroborates most photochemical observations on single crystals, most photocatalysts are nano-sized semiconductor particles to achieve high active surface areas.[135,136] However, for very small particles with sizes of about 10 nm, band bending from the bulk to the surface is generally[1] thought to be negligible.[98] Upon illumination with photon energies above the band gap, an electron-hole pair is formed and, as a general prerequisite, the photon-

[1] Exceptions may i.e. result from special dopant concentrations and are described in more details elsewhere.[98]

generated charges (electron in the conduction band and hole in the valence band) need to be spatially separated.
As illustrated in Figure 2.2, the two undesired reaction pathways for the charge carriers are surface recombination and volume recombination.[43,98] The desired pathway for the charge carriers is a reaction on the surface (in a co-catalyst), where the electrons reduces a molecule, while the hole oxidizes one on the surface. In this picture of the nanoparticulate semiconductors, both photon-generated charge carriers travel to the surface, where they facilitate photochemical reactions in molecules. The efficiency of such a system is determined by a wealth of parameters, such as the charge carrier recombination length, trap states, charge transfer at the interface between semiconductor and molecule or semiconductor to co-catalyst, diffusion of the species, the rate of the chemical reactions, back-reactions of intermediates and many others.[43,135,137] In summary, this scheme illustrates how complex a photo-reaction on a nano-sized photocatalyst can be and how unknown some basic parameters and pathways are, which are usually also strongly dependent on each other.[10]

2.3. Photocatalytic Activity

The term photocatalytic activity is often used as an equivalent to photocatalytic reaction rate, however it is misleading from the original meaning in thermal catalysis[41], where it describes a property of a catalyst that is directly related to an active site. In most photocatalytic systems, the active site is actually unknown and even if so, the concept of the active site does not include the strong dependence on photon-generated charge carriers in the semiconductor.[41,42] Therefore, a number of conventions have been established by different research groups in the field. The first one mentioned here, will be the turnover frequency (TOF), as described in in the following:

$$\mathrm{TOF} = \frac{\text{Number of reacted molecules}}{\text{active sites} \times \text{time}} \tag{2.1}$$

Since the term active site may be inappropriate for most photocatalytic systems[41], alternative definitions normalized to the number of atoms in the photocatalyst or the number of surface atoms are used.[43] Ohtani proposed a comparison of relative rate constants as measure for the photocatalytic reaction rate.[41] By assuming that the electron and the hole induce a redox reaction, a rate constant k_{redox} can be estimated. As illustrated before in Fig. 2.2, the charge carriers can also recombine mutually and therefore $k_{recombination}$ affects the photocatalytic reaction rate. In the most simple kinetic assumption, he proposes the following for the intrinsic photocatalytic activity:

$$\text{intrinsic photocatalytic activity} = \frac{k_{redox}}{k_{recombination}} \tag{2.2}$$

However, $k_{recombination}$ cannot be estimated easily, since it does not produce any chemical species. Addressing the problem of charge recombination at interfaces and understand-

ing the nature of governing factors is thought to be a prerequisite for improving photocatalysts in general.[72,138] The most common measure for photocatalytic activity is the quantum yield.[43,135] Since for particle suspensions in solution, scattering and reflection are not straight forward to be determined, usually an apparent quantum yield (AQY) is used:

$$\mathrm{AQY} = \frac{\text{number of reacted electrons}}{\text{number of incident photons}} \tag{2.3}$$

It should be noted here, that the number of photons can be determined by a calibrated photodiode or chemical actinometry[135], while the number of the reacted electrons in general is based on three mechanistic assumptions: a stoichiometric reaction of both charge carriers[43], electrochemical mechanisms with two electrons per H_2 and four holes per O_2 (in the case of water splitting) and no side-reactions. Especially for the comparison to solar cells, the term solar-to-hydrogen (STH) was coined, describing the performance of a given photocatalyst under simulated sunlight[135,137]:

$$\mathrm{STH} = \frac{\text{Output energy}}{\text{Energy of incidence solar light}} = \frac{r_{H_2} \times \Delta G}{\rho_{Sun} \times A_{Reactor}} \tag{2.4}$$

By measuring the rate of hydrogen evolution (r_{H_2}), knowing the Gibbs enthalpy for water-splitting ($\Delta G = 237$ kJ mol^{-1}) and the solar energy spectrum constant ($\rho_{Sun} = 1003$ W m^{-2})[137] and the geometric area of the reactor ($A_{Reactor}$), the STH yield can be calculated. A theoretical maximum of the STH yield of 48% is estimated for a reactor assuming 100% quantum efficiency for the photocatalyst. In summary, each of the definitions has its drawbacks, either because it is difficult to determine certain parameters (e.g. the rate constants for all processes) or because the definition of the catalyst and its active site may be inappropriate.

2.4. Enhancing Photocatalysis with Bias

Fabian *et al.* generalized the concept of enhancing hydrogen evolution with certain experimental parameters by the introduction of five different categories: electrical, optical, thermal, pressure and chemical bias.[17] Those biases are applied to reduce slow charge recombination, increase the yield of charge separation and collection as well as increase the rates of electrocatalysis. The concept behind each bias is described very detailed in the review[17], while the following section will focus on the chemical bias. For photoelectrochemical water-splitting, the excitation (Eq. 2.5) takes place in the semiconductor and the charge carrier recombination is not taken into account. The photocatalytic water-splitting is then usually divided into two half cell reactions (Eq. 2.6 and 2.7), amounting to the net Equation 2.8.

$$h\nu \xrightarrow{\text{Semiconductor}} h^+ + e^- \tag{2.5}$$

$$4H^+ + 4e^- \longrightarrow 2H_2 \tag{2.6}$$

$$2O^{2-} + 4h^+ \longrightarrow O_2 \tag{2.7}$$

$$2H_2O + 4\,h\nu \xrightarrow{\text{Semiconductor}} 2H_2 + O_2 \tag{2.8}$$

This rather general mechanism with separated half cell reactions is the basis of most interpretations of photocatalytic reactions, although some of the actual reaction intermediates are still unclear.[135,139–141]

A common approach in the literature, when studying new photocatalysts, is focussing on one of the half reactions.[69,74,142–148] Since it is the desired product from a fuel standpoint, many of the previous studies chose the photocatalytic formation of molecular hydrogen. This half cell reaction (see Eq. 2.6) is not necessarily studied by water-splitting, but the chemical bias can be exploited (see Fig. 2.3). Usually this means that a hole-scavenger or a water-hole scavenger mixture is used to study the H_2 evolution.[33,144,149] One of the most common hole scavengers are small alcohols such as methanol and ethanol, which get photo-oxidized readily on the photocatalyst, so that the nature of the charge-transfer reaction of electron for the hydrogen evolution can be studied.[33,144]

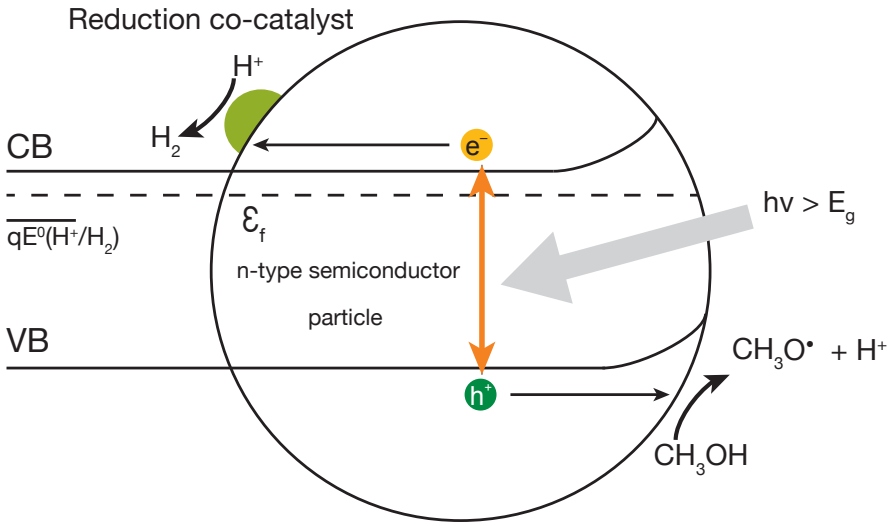

Figure 2.3. The conventional model for chemical bias as proposed by Domen and coworkers.[17] Hydrogen evolution from methanol is observed by a reduction of protons with photoelectrons at the co-catalyst, while the photohole oxidizes the alcohol. Note that the content of the scheme is exactly adapted from reference[17], only with changes in the design.

2.5. Reaction Mechanisms in Alcohol Reforming

While, at first, commonly used as a hole-scavenger, photocatalytic reforming of methanol and ethanol has attracted some attention for a renewable H_2 production[4,30–32,35,81,150–153], since both alcohols can be obtained as a sustainable feedstock.[113,154,155] Also the by-products formaldehyde[156] and acetaldehyde[157] are important industrial chemical building blocks, especially when they are obtained in water-free conditions. The focus of previous studies on alcohol reforming lies essentially on the H_2 production from a variety of alcohols[152,158] and sugars[158–161], but also a variety of products and intermediates are obtained in the photo-oxidation. For small alcohols, the consensual first reaction steps can be described by the following expression:[30,32,81,150,162]

$$RCH_2OH \xrightarrow[\text{Noble Metal}/TiO_2]{h\nu} RHC{=}O + H_2\uparrow \tag{2.9}$$

While the corresponding aldehyde or ketone is usually identified as the major by-product, other found reaction products include CH_4, CO_2, CO, C_2H_4, C_2H_6, H_2O, carboxylic acids, 1,1-diethoxyethane and more complex products in various ratios.[30,150,163–168]
Some products are assigned to direct photo-oxidation mechanisms on the semiconductors surface, others are believed to originate from indirect hole transfer via hydroxy-radicals in solution[30,31,166,169,170] or could be assigned to thermal reactions.[171,172] Furthermore, the role of the co-catalyst remains in general elusive, especially for the oxidation side of the photoreaction. In agreement with many studies[30,81], the co-catalyst is a prerequisite for photocatalytic hydrogen formation, but its exact role in the mechanism of the co-catalyst is debated: Some think, in analogy to electrochemical mechanisms, that protons are reduced to molecular hydrogen by photoelectrons[143,144,173–177], while others think of the co-catalyst rather as a charge sink and assign the active site for the reduction reaction also to the semiconductor.[164,170,178–180]
In summary, the mechanistic picture of photocatalytic water-splitting is mainly dominated by electrochemical half cell reactions and the development of higher efficiencies has reached an impasse over the last years. While widely recognized as a very complex and inherently interdisciplinary problem[41,82,138], even the mechanistic details of model reactions like the hydrogen evolution from alcohols are not completely understood. In this regard, photocatalytic studies in very well defined conditions via the surface science approach and the possibility of single parameter studies offer the potential of investigating the underlying governing factors for photocatalytic reactions.

3
Experimental

This chapter gives an overview of the experimental techniques that are all combined in one apparatus.

3.1. UHV Apparatus

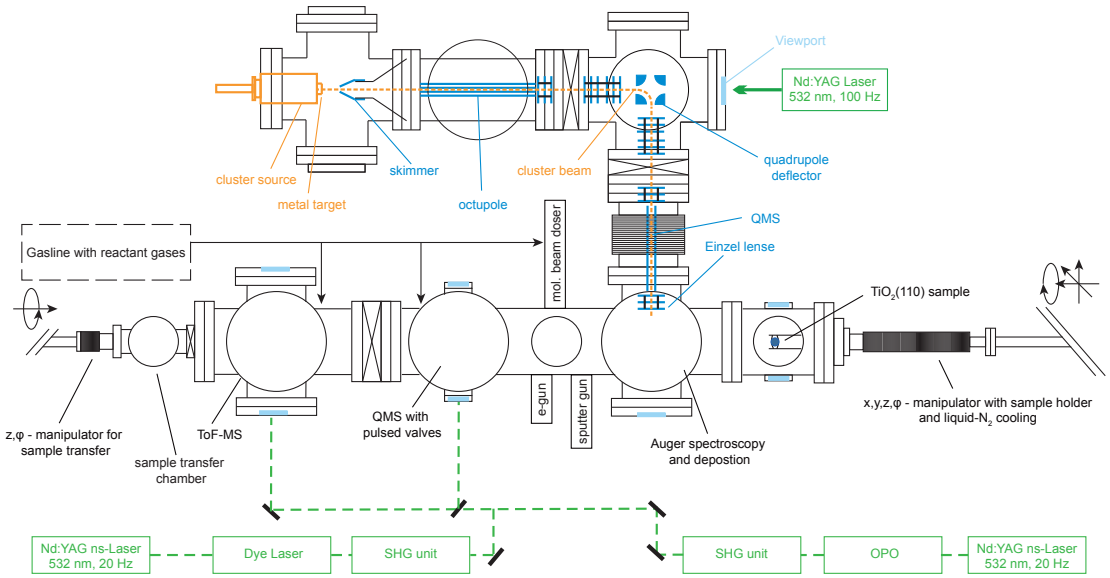

Figure 3.1. An overview of the experimental apparatus used in this work. It consists of several surface preparation and analysis techniques, a laser vaporization cluster source, a transfer chamber and two laser systems for photocatalytic experiments.

3.1.1. Analysis Chamber

The analysis chamber, built in 2014, is described in more detail elsewhere.[181–184] Briefly, it is an UHV apparatus with a base pressure of $8 \cdot 10^{-11}$ mbar and a liquid-N_2 cooled x, y, z, ϕ-manipulator (VAB Vakuum GmbH). Further, an Auger Electron Spectrometer (CMA 100m Omicron Nanotechnology GmbH) is used for surface analysis, a sputter gun (IQE 11/35, SPECS GmbH) for surface preparation and a QMS (QMA 430, Pfeiffer Vacuum GmbH) with electron ionization for the analysis of desorbing molecules. Technical descriptions as well as theoretical background information of the used techniques can be found elsewhere.[12,183–190] Over the course of the thesis, a molecular beam doser

in the design from Yates' group was implemented for a directional dosing on the surface. The properties of the beam doser have been characterized thoroughly in earlier works.[183,190–192]. While there is an empirical relation to estimate the flux on the surface[193,194], it should be noted that the behavior for alcohols and water differs greatly from the use of gases, which makes a calibration and quantification by TPD necessary. The gasline for the dosage of the reactant gases allows for the use of five different samples and can be heated separately from the main chamber. A base pressure of $2.0 \cdot 10^{-9}$ mbar can typically be obtained in the gas line. A list of all used reactants and gases is given in Appendix A.2. All liquids are further degassed and purified by pump-freeze cycles and the purity of all reactants is checked by applying a background pressure of molecules in the chamber and performing a QMS mass scan. Further, a transfer chamber for sample exchange with the UHV manipulator was constructed and implemented. It consists of a small chamber with a z,ϕ-manipulator (Ferrovac MDG40) with a sample transfer tool (SPECS, SH2/12 ISR) and is pumped by a turbo pump (Pfeiffer Vacuum, HiPace 80) to achieve a base pressure of $2.0 \cdot 10^{-10}$ mbar.
The TiO_2 single crystal holder is of a similar design as from the Yates group[97,190] and has been described in great detail in a previous thesis.[183] The TiO_2(110) single crystals (Surface-net GmbH) used in this work are of cylindrical shape with a diameter of 1.0 cm. The crystal is clamped with a Ta sheet (0.125 mm) to a Ta heating plate (1.0 cm in diameter, 1 mm in height) as demonstrated in Figure 3.2(a). Between the crystal and the heating plate, a thin gold foil (0.025 mm) is placed for a better thermal conductivity. The resistive heating is performed via the heating wires (W with 26% Re, Omega Engineering) that are able to heat the crystal over 1000 K.[184] The temperature is monitored via the calibrated

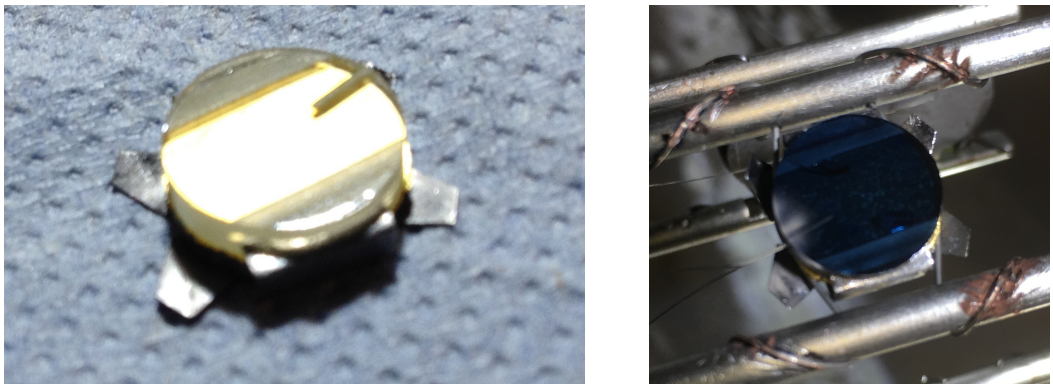

(a) TiO_2**(110) on Ta mount** **(b)** TiO_2**(110) on the manipulator**

Figure 3.2. (a) A picture of the rutile TiO_2(110) single crystal mounted on the Ta heating plate with a gold foil in between. The mechanical stability is given by home-built Ta clamps made from thin sheets.
(b) An image of the TiO_2(110) fixed on the manipulator via the resistive heating wires. The crystal has a blue color, since it has already been bulk-reduced to some extent. The thermocouple is inserted into the hole in the semiconductor on the side, which is also visible in (a). The heating wires are strained into the grooves of the heating plate, that is clamped to the crystal.

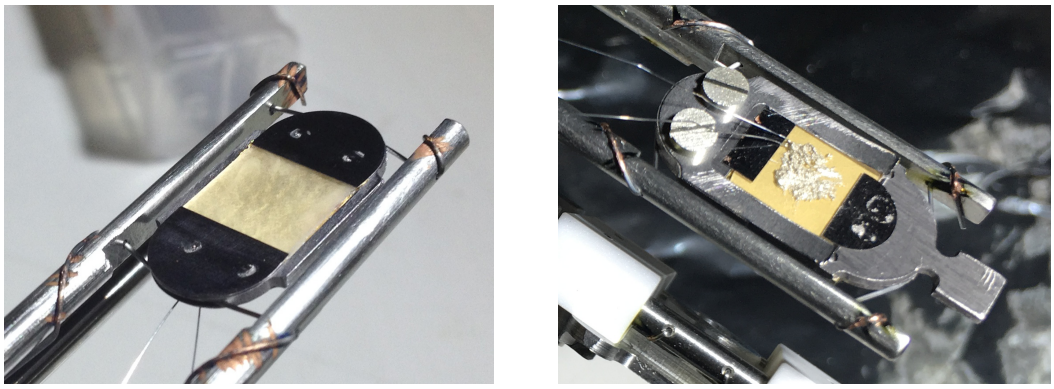

(a) 1st Generation GaN sample holder **(b)** 2nd Generation GaN sample holder

Figure 3.3. (a) A picture of an MOCVD-GaN(0001) sample mounted in the newly created sample holder. The molybdenum rods are adjusted to the size of the sample holder, while the Ta sample holder itself has a cut-out, where the GaN(0001) on sapphire sample is placed. To ensure a good thermal conductivity, gold foil is positioned between the sapphire and the tantalum cut-out. The electric conductivity and mechanic stability is facilitated by thin Ta sheets (0.1 mm), that are spot-welded on top of the sample holder. (b) A picture of the second generation GaN(0001) sample holder, which is now of a three layer design. While the base layer is fixed to the manipulator via the heating wires, in the middle part a section of the sample holder can be removed via the transfer tool. Note, that in the photo a dummy crystal is mounted in the holder for temperature calibration measurements.[196] The topmost layer is a thin tantalum sheet, which acts as a spring to ensure thermal conductivity and mechanic stability with the removable part of the sample holder.

readout[195] of a twisted type-C thermocouple (Omega Engineering). The thermocouple is inserted into a hole drilled in the side of the rutile single crystal without any adhesive (see Fig. 3.2(a) and (b)).

For the measurements with the GaN(0001), a new sample holder was designed. It was based on the idea of the heating plate, since the MOCVD- and MBE-grown GaN(0001) films used in this work are grown on a sapphire support. They are fixed in the cut-out of the tantalum sample holder with spot-welded Ta sheets, to ensure a good electric conductivity. In the first generation sample holder, the whole assembly was then fixed to the Mo rods of the sample holder by the heating wires. The sample holder was able to cool the sample down to liquid N_2-temperatures and heat it to temperatures over 1300 K, where gallium nitride decomposes.[196,197]

The second generation sample holder consists basically of 3 layers and the two on the bottom are based on the first generation sample holder. Similar to the TiO_2 sample holder, the base plate is used for heating. In the middle layer, the GaN samples can be fixed by spot-welded tantalum sheets and moved onto the second generation assembly. The thin Ta sheet on top acts as a spring for mechanic stability. The second generation sample holder can be used for any sample with dimensions of less then 10×10 mm^2 and the study on Ga_2O_3 single crystal surface was also performed with the second generation sample holder.

3.1.2. Cluster Source

The co-catalysts in this work are clusters generated using a newly built, modified laser vaporization cluster source similar to the one designed by Heiz *et al.*.[198] A general scheme including all parts of interest is also depicted in Figure 3.1. A platinum metal target[1] (⩾99.95% purity, ESG Edelmetalle) is mounted on an electric motor and rotated in a hypocycloidal manner to ensure a uniform ablation of the target.[2] Metal ablation is facilitated with a frequency doubled Nd:YAG laser (6 W, 9 ns pulse width, 100 Hz, SpitLight DPSS, InnoLas GmbH), that is focussed on the metal target and a small plasma is generated. This plasma is instantly cooled by a helium (He 6.0, Westfalen Gas) pulse from a home-built piezo valve and extracted into the vacuum chamber. The metal atoms are thermalized via collisions with He carrier gas and upon the supersonic expansion, resulting in metal cluster formation. An unknown fraction of the clusters is positively charged and guided with electrostatic lenses and an octupole ion guide (Kenwood HT Transceiver, TS-5700) to a quadrupole bender. The bender allows for a separation of the cationic clusters from the neutral ones and steers them into a quadrupole mass filter (Extrel 150 QC, USA) to facilitate a mass selection with atomic precision. This quadrupole mass filter can also be used in ion guide mode for measurements with a size-distribution of clusters.[3] Further electrostatic lenses guide the cluster beam to the analysis chamber, where the clusters are soft-landed on the samples. A description of the characterization of the clusters' kinetic energy and the mass selection accuracy can be found elsewhere.[200] The cluster coverage is monitored with a picoammeter (Keithley 6487) by measuring the neutralization current of the soft-landed cationic clusters with a home-made LabView application.[201] The software not only offers online current-measurements, but also an input for the relevant crystallographic data, which enables the calculation of the cluster coverage in %ML.[201] The experimental implementation of the cluster source and some control experiments are described in more detail in other reports.[200,202,203] The optimization of the cluster current is a multiple parameter optimization problem, consisting of about 50 parameters in the given setup and geometry. The voltage of the home-built ion optics is controlled digitally between +500 V and -500 V. A list of the all the experimental parameters can be found in Table A.1 in Appendix A.1 and the resulting cluster mass distribution is shown in Figure 9.6.

3.2. Laser Systems

Two laser systems have been used for the irradiation of the single crystals in this work. First, a Nd:YAG pumped dye laser (Spectra Physics, Quanta Ray GCR 3, 10 ns pulse

[1] For all the experiments presented here, a platinum metal target is used.

[2] The rotation speed is varied over one cycle to compensate for sections with a low angular velocity. A detailed description can be found in a previous work.[199]

[3] These are further named "unselected clusters". The size-distribution nonetheless is governed by the production conditions and ion guide settings.

length) is frequency tripled by a third harmonic generation unit. While the fundamental and green components are dumped, the 355 nm pump pulses are directed into a dye laser (Scanmate 2E, Lambda Physik GmbH). The resulting laser light is frequency doubled in a second harmonic generation (SHG) unit and separated with 4 Pellin-Broca prisms from the pump light beam. The resulting laser pulses in this work had a wavelength of 266.5 nm and the intensity was usually set to 600 μJ with a gradual grey filter to avoid any heating effects. The laser beam illuminates the entire single crystal surface in the UHV.
After the movement of the laboratory, an additional laser system was put into operation. It consists of a Nd:YAG laser (Innolas Spitlight High Power 1200, 222 mJ/pulse at 355 nm and 20 Hz, 7 ns pulse width) which pumps an optic parametric oscillator (OPO) unit (GWU, premiScan ULD/400 with modifications from Innolas) with two crystals (β-bariumborate) with different cutting angles for wavelengths between 420 nm and 500 nm and 520 nm to 700 nm respectively. The output of the OPO is then frequency doubled in a SHG unit and the fundamental beam is separated by a rotatable prism. The resulting pulses have an energy of 900 μJ at 241.8 nm. The whole OPO as well as the SHG unit are controlled by a home-made LabView application.[201]

3.3. Sample Preparation and Characterization

3.3.1. TiO_2(110)

3.3.1.1. Redcued TiO_2(110)

The reduced TiO_2(110) surface [r-TiO_2(110)] (Surface-net GmbH) is generally obtained by Ar^+-sputtering (1.0 keV, $5 \cdot 10^{-6}$ mbar, 10 μA ion current) at 100 K and a consecutive annealing in vacuum to 820 K (10 min). A newly purchased, transparent TiO_2(110) single crystal is mounted. Annealing at 900 K for 1 h is performed, to generate enough bulk defects to ensure a good conductivity for AES measurements and sputtering.[189] The material is then of light blue color. Initial contaminations such as calcium and potassium as well as some sulfur are cleaned by the aforementioned sputter-annealing cycles. A typical Auger electron spectrum is shown in Fig. 3.4, only comprising the characteristic titanium and oxygen features.
The bulk reduction of the TiO_2 single crystal is accompanied by a formation of surface defects such as bridge-bonding oxygen vacancies.[208] However, to the authors knowledge, there is not yet a quantitative description how the bulk reduction degree influences the BBO vacancy density on the surface, although a further bulk reduction to darker blue crystals coincides with an increase of the BBO vacancy density on the surface.[118,208] In titration experiment, the BBO-vacancies can be quantified with respect to the Ti-lattice sites on the TiO_2(110)-surface by H_2O-TPD. Water adsorbs dissociatively in the defect sites forming two hydroxyl groups that eventually recombine at 450 K.[205] Integrating the signal vs. the full Ti-lattice site peak leads to the value for the BBO-vacancy density.

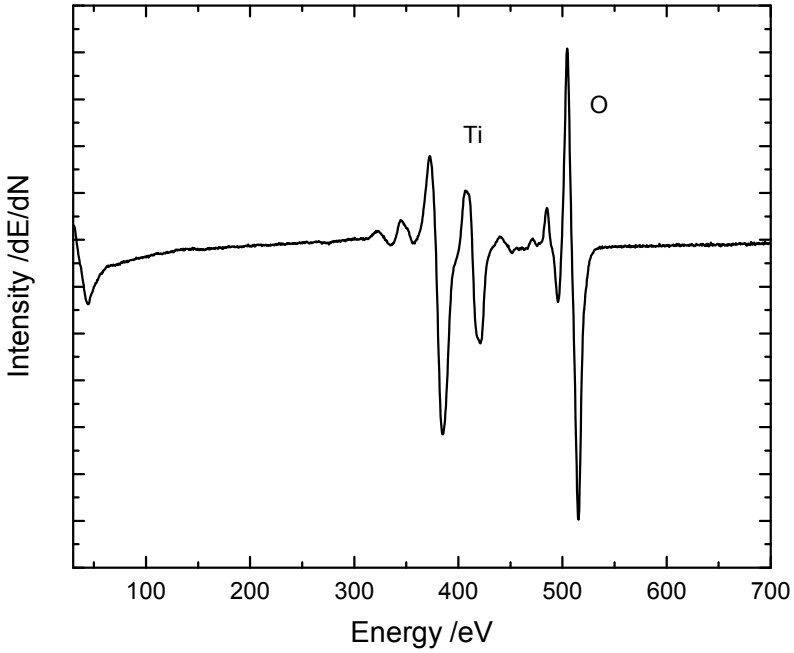

Figure 3.4. Typical Auger electron spectrum of a clean r-TiO_2(110) surface.[185,204]

In this case (Fig. 3.5) and for the crystal used in Chapters 8, 9, 10 and 11), the defect density is 6% $\pm$ 1%.
As a further reference measurement, the O_2-PSD (Fig. 3.6) is only observed on the slightly reduced and blue TiO_2(110) crystals, indicating a certain level of bulk reduction, which is accompanied by a certain degree of BBO vacancies. The latter ones are needed for

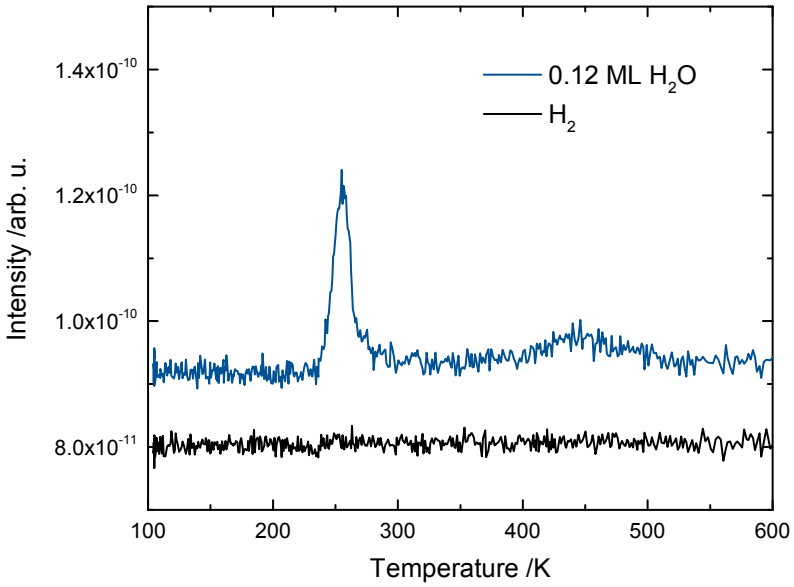

Figure 3.5. TPD of 0.12 ML H_2O from TiO_2(110). While the feature around 270 K is clear attributed to water desorbing from Ti-lattice sites, the broad feature around 450 K originiates from water desorbing from BBO-vacancies.[205] No molecular hydrogen is evolved for the r-TiO_2(110).[206] The traces are offset for clarity.

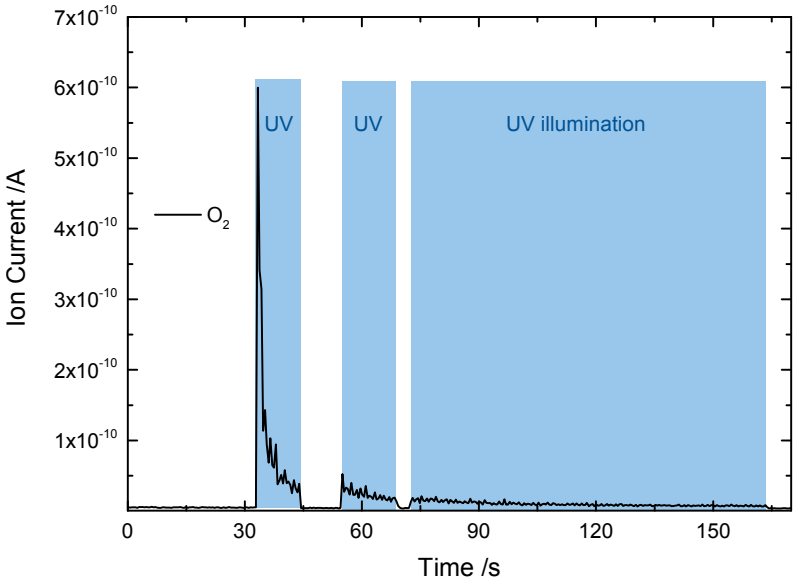

Figure 3.6. Exemplary O_2-PSD on r-TiO_2(110) of 1 L O_2 at 110 K. UV illumination by the dye-laser setup is indicated by the blue areas. Upon illumination, an immediate desorption of oxygen is observed that drops also directly when blocking the illumination. The signal does not rise to the initial intensity, when illuminating the surface again, but rather picks up at the intensity that was observed immediately before blocking.[207]

the photochemical desorption to happen. The O_2-PSD was first observed on powdered TiO_2 by Yanagisawa and Ota[209] and has since been a continuously studied reaction to probe the photo-activity of TiO_2(110) surfaces.[79,95,114,115,120,207,210,211] It has been shown that desorbing oxygen species have an internal energy equivalent to temperatures above 1600 K. Therefore, thermal contributions are ruled out since the measurements usually take place at cryogenic conditions.[183,212]
However, the exact mechanism of the photodesorption, the active site and the influence of co-adsorbates are still not clear.[122,124,125,132,207,213]

3.3.1.2. Oxidized TiO_2(110)

The oxidized TiO_2(110) [o-TiO_2(110)] is obtained by exposing the r-TiO_2(110) surface to 1 to 20 L of O_2 at 100 K, followed by short annealing to 293 K to heal the BBO-vacancies.[101,214] The atomic structure of the oxidized surface is still controversial.[215] STM measurements showed that annealing the r-TiO_2(110) in an oxygen background ($2 \cdot 10^{-6}$ mbar) at 1000 K and cooling to room temperature in the same oxygen atmosphere leads to an undefined surface, containing islands, oxidized Ti-interstitials and a variety of step edges.[216] Furthermore in the employed cleaning procedure not all BBO-vacancies are filled[217], but even the dissociation of molecular oxygen on Ti-lattice atoms is observed by STM.[101,218] Recent work from Wendt and co-workers suggests that glass capillary dosing of O_2 directly onto the surface will achieve an o-TiO_2(110) surface without BBO vacancies.[219] The AES spectrum of o-TiO_2(110) in Fig. 3.7 shows no appreciable difference to the one for r-TiO_2(110) (Fig. 3.4).

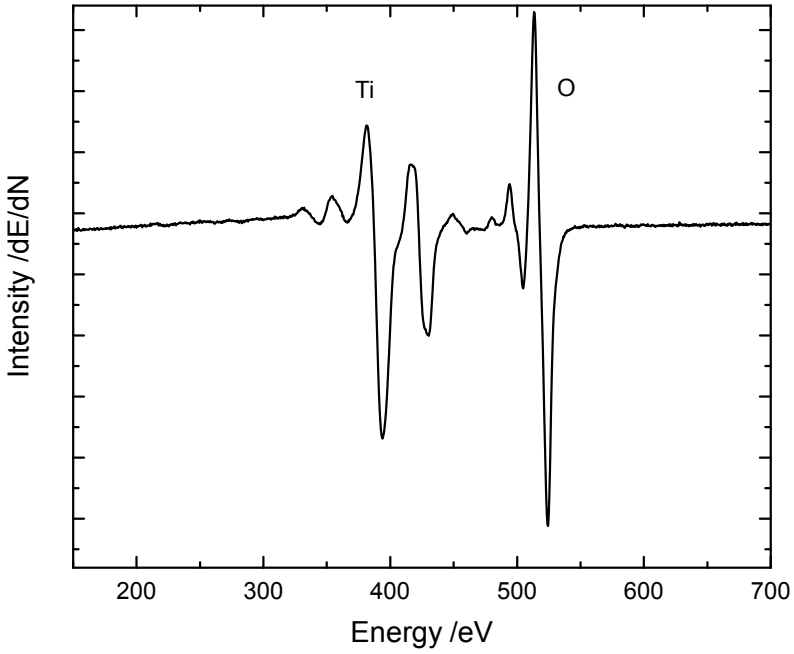

Figure 3.7. Typical Auger electron spectrum of a clean o-TiO_2(110) surface. No appreciable difference was observed to the one of r-TiO_2(110) (Fig. 3.4).

3.3.1.3. Hydroxylated TiO_2(110)

The hydroxylated TiO_2(110) [h-TiO_2(110)] is prepared by dosing 2 ML of water on the r-TiO_2(110) at 100 K and a subsequent short annealing step to 350 K in a procedure adapted from Dohnálek and co-workers.[101,121,220]

3.3.2. $Ga_2O_3(\bar{2}01)$

The $Ga_2O_3(\bar{2}01)$ single crystal (Tamura Cooperation, Tokyo, Japan) is chosen, since the surface represents the natural growth direction of gallium oxide on GaN(0001).[221] The bang gap is about 4.8 eV[222–224] and the crystal is transparent. The initial carbon and sulfur contaminations are removed by a cleaning procedure of Ar^+-sputtering (100 K, 1.0 keV, $5 \cdot 10^{-6}$ mbar, 10 μA ion current), annealing with O_2 (800 K, $2 \cdot 10^{-6}$ mbar) and vacuum annealing at 800 K for 30 min each. The resulting AES spectra (Fig. 3.8) did not show contaminations apart from trace amounts of argon.

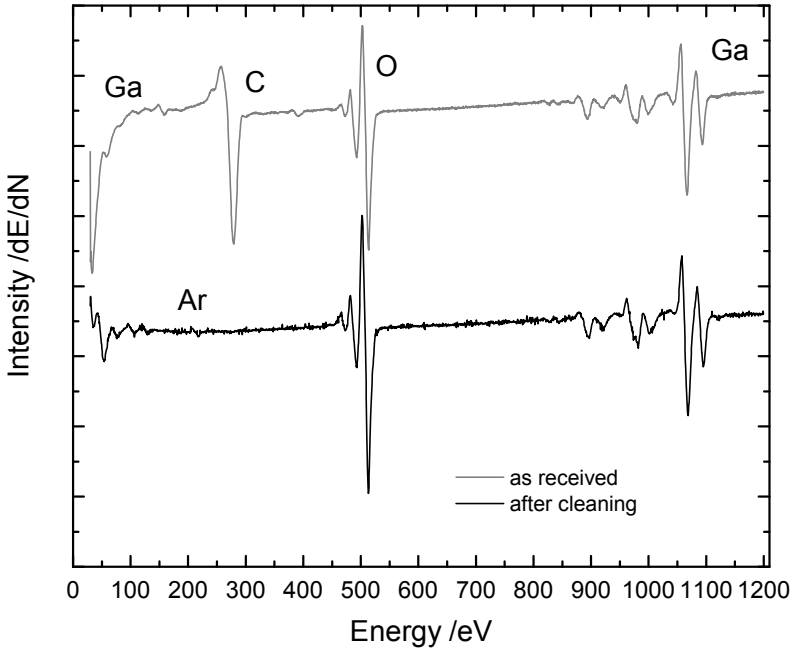

Figure 3.8. Typical Auger electron spectrum of a $Ga_2O_3(\bar{2}01)$ surface (black). The grey line represents the AES spectrum directly after mounting the crystal. It exhibits mainly contaminations by carbon and a small amount of sulfur. The AES spectra of the cleaned surface shows the characteristic Ga peaks around 100 eV and between 800 eV to 1150 eV as well as the oxygen one at 509 eV. Trace amounts of argon at 215 eV are residues from the sputtering conditions.

3.3.3. GaN(0001)

Although GaN(0001) is commonly used in surface science studies as shown by these reviews[225,226], no consensual cleaning recipe for samples from air has so far been established.[226] Simple evaporation of GaN(0001) at 1300 K resulted in an appreciable AES spectrum with very low carbon and oxygen content,[196] but the surface morphology was not kept intact and a rough surface was obtained as probed by ex-situ AFM. Annealing in NH_3 at various temperatures in this work did neither significantly change the carbon contamination nor the oxygen content as determined by AES. Generally, a review of the employed cleaning techniques is given by Bermudez[225] and Nemanich and co-workers.[226] For the GaN samples in this work[4], carbon impurities were usually removed by Ar^+-sputtering (0.5 keV, $1 \cdot 10^{-6}$ mbar, 2 μA ion current, 80 K) for 10 min with a subsequent vacuum annealing to 800 K for 5 min. If necessary, further cleaning cycles with shorter bombardment times were performed until no carbon was left on the surface as determined by AES. As an additional probe, ex-situ AFM was used to confirm the surface morphology after the reactivity measurements in the UHV. It is believed that Ar^+sputtering of GaN(0001) samples likely creates nitrogen vacancies and gallium dangling bonds that can easily be oxidized. On all samples, some "native" oxide ex-

[4] The MOCVD-, HVPE- and MBE-grown samples were obtained from the cooperating group of Prof. Martin Stutzmann from the Walter Schottky Institute at TUM

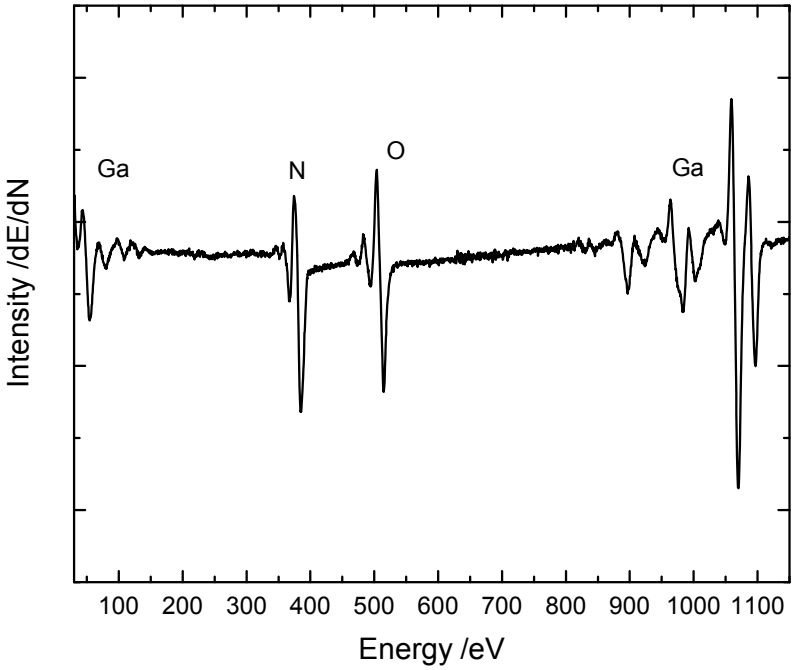

Figure 3.9. Typical Auger electron spectrum of a MBE-grown GaN(0001) surface. The oxygen peak shows that a "native" oxide is present on the surface.

ists, that cannot be removed form the surface (Figures 3.9 and 3.10). Its presenece is a well-known phenomenon in literature.[227–232] However, in this work the degree of surface oxidation is varied to identify the contribution of the "native" oxide.[231,232] Further and more detailed descriptions of the cleaning procedures for the used GaN(0001) sam-

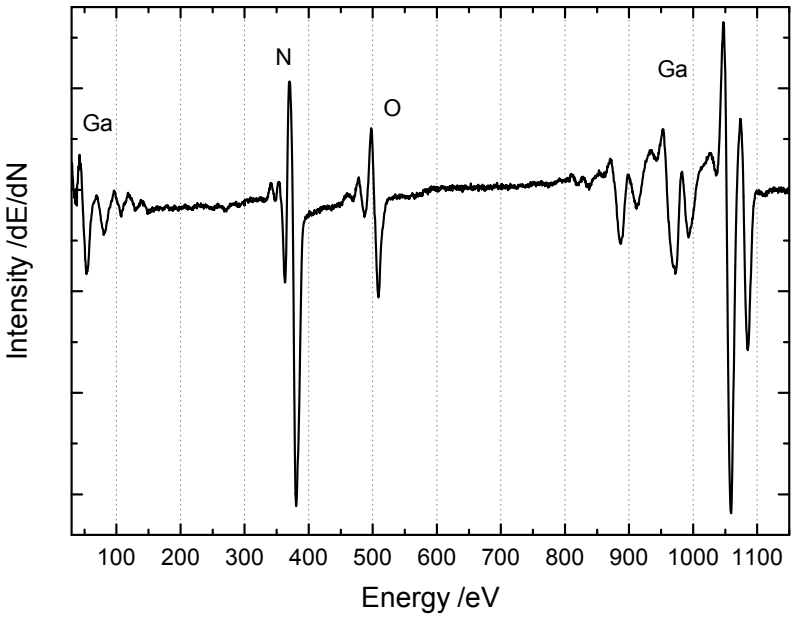

Figure 3.10. Typical Auger electron spectrum of a MOCVD-grown GaN(0001) surface. The oxygen peak shows that the occurrence of the native oxide is independent of the preparation method of GaN.

ples are given in the publications for MBE-grown GaN(0001)[231,232] and MOCVD-grown GaN(0001).[233]

3.3.4. $Pt_x/TiO_2(110)$

The metal cluster-semiconductor hybrid materials are obtained by first preparing a clean crystal surface with one of the above described cleaning cycles. While the crystal is cooled to liquid nitrogen temperatures, the cluster source is already in operation and the cluster current is checked behind the QMF with a picoammeter (Keithley 6487) by measuring the neutralization current of the cationic clusters. For doing so, a bias voltage of -200 V is applied at the picoammeter, while the ion optic right behind the electrode selected for the measurement of the cluster current is set to +500 V in order to repell the clusters from this lense. Usually, the cluster source is operated for 15 min, until a stable cluster current is observed.[5] Furthermore, the mass spectra of the cluster beam then does not show the formation of oxide or carbide clusters within the experimental sensitivity. When the sample temperature is less than 120 K, the gate is opened and the cluster neutralization current is monitored online with the LabView application.[200,201] The application offers the possibility to select a value in ML with respect to the theoretical surface atom density of TiO_2 in this case.[6] Once the deposition is finished, the gate to the cluster source is immediately closed to avoid contaminations. During the deposition, the pressure in the main chamber (mainly consisting of He) is about $1{\cdot}10^{-7}$ mbar, while upon closing the gate the pressure drops back to $\leqslant 1 \cdot 10^{-10}$ mbar. Previous work of the Heiz group[198,234–237] and others in the cluster community[238–248] established the neutralization current as the most precise control over the cluster coverage.

3.4. Typical Reactivity Measurements

In this part, the working principles of the three mainly used reactivity measurements are presented and some details of the experimental parameter space are discussed.

3.4.1. Temperature Programmed Desorption

Temperature Programmed Desorption (TPD) is a well established technique in surface science, not only to gain insights for coverage determinations, but also for reaction pathways. The fundamentals of the techniques and the in-depth data analysis are very well described in the literature.[187,188] The measurement principle is shown in Figure 3.11. The adsorbate coverage in this work is typically performed at 100 K, either by background dosage or the molecular beam doser. Then, the sample is placed at a given distance from the QMS, usually about 2 mm below the skimmer of the QMS in a line of sight

[5] Typically, a cluster current of 5 nA of unselected platinum clusters is obtained on the sample. The highest current observed for unselected clusters was about 12 nA.

[6] For size-selected clusters, the observed current on the sample was in the range of 90 pA for Pt_{13} and 350 pA for Pt_1.

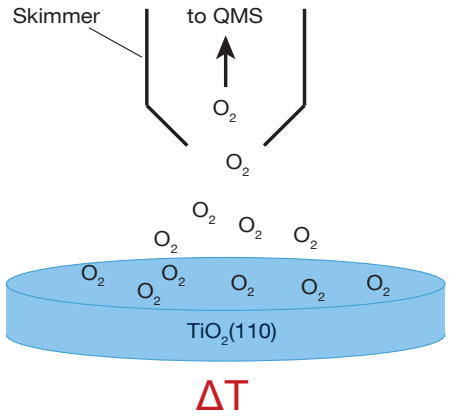

Figure 3.11. Measurement principle of a temperature programmed desorption experiments. The adsorbed species in this scheme is O_2, which desorbs upon heating the single crystal with a linear heating rate.

geometry. Then, a heating ramp is either performed by the PID controller (Eurotherm 2408) or manually with a typical heating rate of around 1.2 K/s up to 800 K or higher temperatures. During the heating rate, the desorbing species are monitored with the QMS to identify desorption and/or reaction products. Afterwards, if necessary, another cleaning cycle is performed and the next experiment can be started when the sample is cooled down. By varying the coverage, the saturation coverages of an adsorbate and products formed from the adsorbate on the surface can be determined. Furthermore, by the desorption temperatures the adsorption energies of the adsorbate can be estimated.[187] By integrating over all the reaction products, the coverage dependent reaction channels can be explored in a quantitative manner.[249,250]

3.4.2. Photon-Stimulated Desorption

Photon-Stimulated Desorption measurements are an established technique to monitor the desorption of molecule upon illumination.[207,210,211,251] The surface is covered with the adsorbate at 100 K and positioned with a distance of about 4 mm under the QMS in a line-of-sight geometry. The reaction is initiated by unblocking the laser, that then illuminates the semiconductor. A scheme is shown in Figure 3.12. If the photon energy is above the band gap, excitons are formed and in n-type and p-type semiconductors and the respective minority charge carrier travels to the surface. In the case of the O_2-PSD on TiO_2(110), photo-holes are believed to be responsible for the neutralization of an O_2^- species on the surface and a consecutive desorption of molecular oxygen.[131] The incident light energy is monitored before every experiment with a powermeter and can be adjusted by a gradual gray filter (Thorlabs GmbH) or by neutral UV filters (Thorlabs GmbH) with optical densities between 0.4 and 1.0. To further analyze the formed reaction products at cryogenic temperatures, a consecutive post irradiation-temperature programmed desorption (PI-TPD) can be carried out to investigate the conversion of the reactant with respect to the illumination time. To elucidate photochemical reaction path-

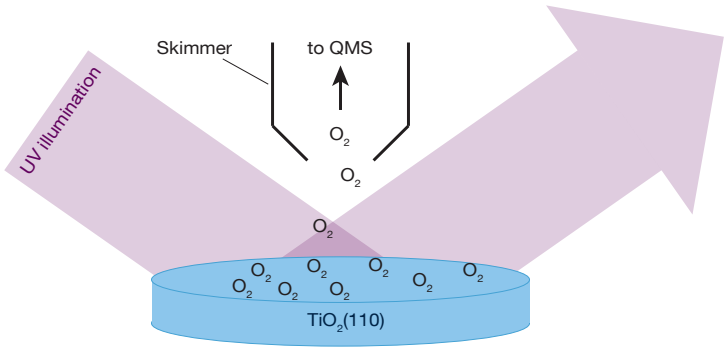

Figure 3.12. Measurement principle of a Photon Stimulated Desorption (PSD) experiments. The surface is covered with molecules (in this case O_2) and illuminated under isothermal conditions, while the molecule desorption is monitored with the QMS.

ways, the PSD experiment can be performed at different temperatures, for which the photochemical reaction product can thermally form and/or desorb.[252,253] Furthermore, the orientation of the crystal with respect to the QMS can be varied to investigated angular distributions of the photoreaction products, which gives further insights in the adsorption geometries of the photo-reactive species.[125,254–256] An in-depth analysis of the time of flight of the different products desorbed upon illumination can show different reaction/excitation pathways for the same photo-product.[213,253,257,258]

3.4.3. Photocatalytic Measurements

The photocatalytic measurements in this work are carried out similarly to the PSD experiments. For single-coverage photocatalytic measurements a certain amount of molecules is dosed onto the surface of the metal cluster decorated semiconductor. Then, the catalyst temperature is set to a value, for which both reaction products can desorb and, consecutively, illumination is started. For the continuous photocatalytic experiments, a certain

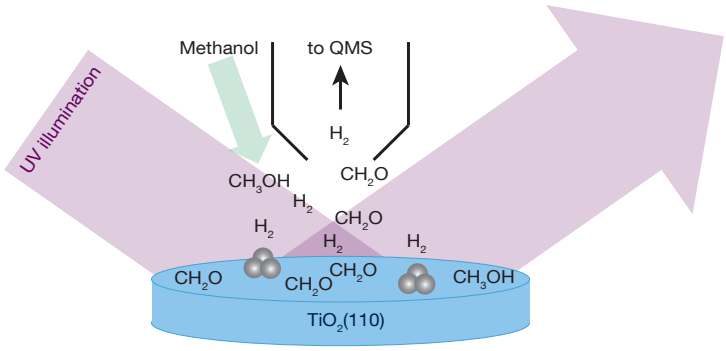

Figure 3.13. Principle of the photocatalytic measurements of the metal cluster decorated semiconductor. The reaction is always started by the UV illumination and the background pressure of the reactant (here methanol). The catalyst temperature can also be changed during one run.

background pressure of the reactant is established and the freshly prepared catalyst is set to the reaction temperature, to ensure a reactant saturation at the surface. The photocatalytic reaction is then started by the UV illumination.

4

Doping-Dependent Adsorption and Photon-Stimulated Desorption of CO on MBE-grown GaN(0001)

While GaN is already used technologically[259–261] and photocatalytically[262–264], the surface chemistry and especially the reactivity of the bare material have been largely unexplored. Previous studies focussed on functionalization of the the surface[265–267] or electronic properties[268–278] including their relations to surface defects. A comprehensive review of the surface science of GaN was published in 2017 by Bermudez.[225]
In this work, CO is used as a chemical probe to investigate the surface properties of MBE-grown GaN(0001) surfaces. Further details can be found in the respective publication[231] in Appendix C.
In brief, CO only physisorbs on the MBE-grown GaN(0001) surface and is inert towards oxidation, also in the presence of oxygen. However, the amount of CO adsorption is found to be a function of the bulk n-type dopant concentration (see Fig. 4.1(a)). In order to describe this effect, a model was developed (see Fig. 4.1(b)), relating the amount of CO

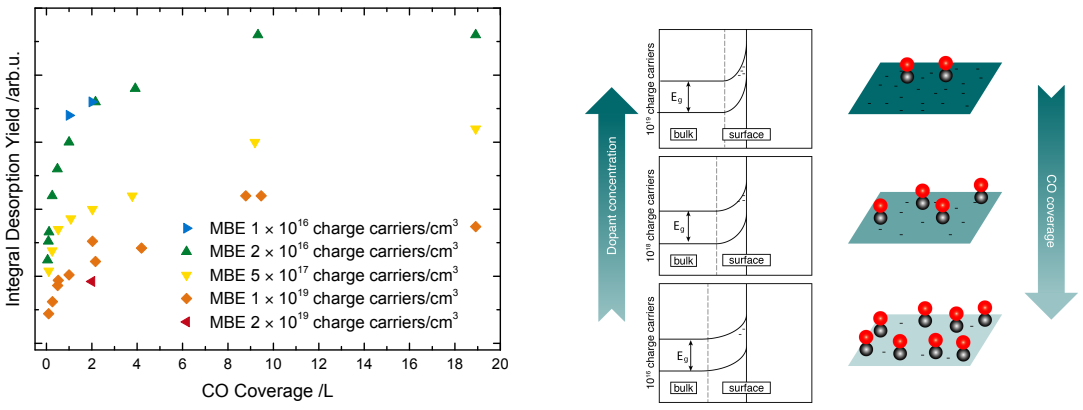

(a) CO Adsorption Yields **(b)** SCR Model for CO Adsorption

Figure 4.1. (a) Integrals of CO desorption from several MBE-grown GaN(0001) samples with different dopant concentrations. The dopant concentrations are given in charge carriers per cm^3.
(b) Model for the doping-dependent CO adsorption. The higher the n-doping, the more negatively charged surface states are present at the surface, when a constant band bending is considered. The most negatively charged surface can physisorb only the smallest amounts of CO, possibly due to repulsive interactions of the negative charge on the surface with the molecule.

adsorption to the negatively charged semiconductor surface states. Carbon monoxide seems to be repelled on the surface by the negative charges.[1] Therefore, for highest n-type dopant concentration, the smallest amount of CO can adsorb on the surface. Since a similar band-bending of about 1 eV is found for different Ga-face n-type GaN(0001) samples[279,280], the space-charge region does not extend as far into the semiconductor as for less n-doped samples. This results in a different amount of negatively charged surface states. Additionally, a photon-stimulated desorption of physisorbed CO was found upon illumination with photon energies above the band gap. Upon illumination, an exciton is created and the photoholes travel to the surface. There, they either extinguish negatively charged surface states causing a flattening of the bands or facilitate the CO-desorption by weakening the polarization of the physisorbed CO bond (Fig. 4.2).

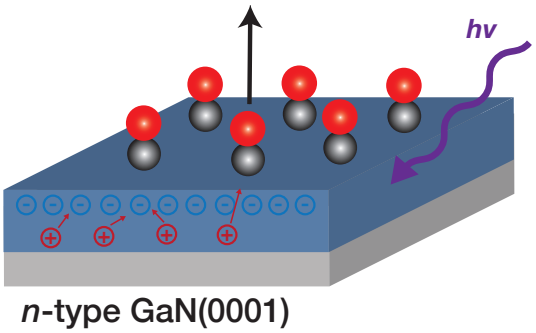

Figure 4.2. Illustration of the CO PSD on n-type MBE-grown GaN(0001) at cryogenic temperatures. Under illumination, holes travel to the surface and either extinguish the negatively charged surface states or are responsible for the photon-stimulated desorption of CO.

Although only a certain portion of the physisorbed CO can be photodesorbed, no distinct binding site was found in this study. While it was found that the adsorption of CO is independent of the surface oxidation state, it significantly affects the photoactive centers, which get passivated upon oxidation. However, since the PSD of CO can also be observed on p-type GaN(0001), it seems that the desorption of CO is rather assigned to a change in the electronic structure of the surface upon illumination, than a specific charge carrier neutralizing a bound species as believed for $O_2/TiO_2(110)$.[131] Over the course of this thesis, another example for the photoactivity of CO was found on $TiO_2(110)$, where CO is desorbed from Ti-interstitials upon illumination.[281]

[1] A similar behavior was found for NH_3 on $TiO_2(110)$, where the molecule is repelled by the BBO-vacancies.[220]

5
Ethanol Chemistry on GaN(0001)

In the following, ethanol is chosen as a probe molecule to investigate the surface chemistry of gallium nitrides, since ethanol on oxide supports (such as TiO_2, ZnO or Fe_2O_3) can undergo both reductive (to ethylene) and oxidative reaction (to acetaldehyde) pathways.[282–287] In addition to the aforementioned pathways, complete reduction to coke formation is observed on catalytically active metals such as Pt[288], Pd[289], Ru[290] and Ni[291], which is highly undesired. In the following, a mechanistic study of ethanol on GaN(0001) is presented, that shows a high activity and and preferential dehydrogenation to acetaldehyde, which makes it a possible future support material for such reactions.

5.1. Ethanol Surface Chemistry on MOCVD-grown GaN(0001)

These results are part of a publication, where the nitride surface chemistry is benchmarked against a well-known TiO_2(110) model catalyst.[233]

5.1.1. Ethanol Thermal chemistry on MOCVD-grown GaN(0001)

In Figure 5.1, the raw data of the relevant traces for 0.85 ML ethanol desorption from n-type GaN(0001) are shown. The charge carrier concentration of $1.4 \cdot 10^{17}$ cm^{-3} was determined by Hall measurements. Ethanol (mass 31) desorbs in a broad feature between 250 K and 450 K, peaking around 320 K. Fragments of 29 and 27 occur also in the cracking pattern of ethanol as observed below 300 K. However, at the temperatures above they deviate from the expected ethanol cracking pattern, indicating a reactivity towards acetaldehyde (mass 29) and ethylene (mass 27) as well. The trace for hydrogen (mass 2) is shown as well and in grey color. It is found that a feature around 450 K is superimposed with a rising background. This background is attributed to hydrogen desorbing from the bulk sapphire as it was observed in a blank TPD experiment (data not shown) to 800 K without any adsorbate.
For a quantitative analysis of the TPD data, a correction including cracking pattern contribution, experimentally determined QMS transmission coefficients and ionization cross sections is applied to identify the products in a quantitative way. The method is further explained in Appendix B.
A coverage series of TPDs of ethanol on MOCVD-grown GaN(0001) is shown in Figure 5.2. For the smallest coverage, no ethanol desorbs during the TPD run and all of the alcohol reacts. With rising coverages, first a feature around 350 K is saturated and then a

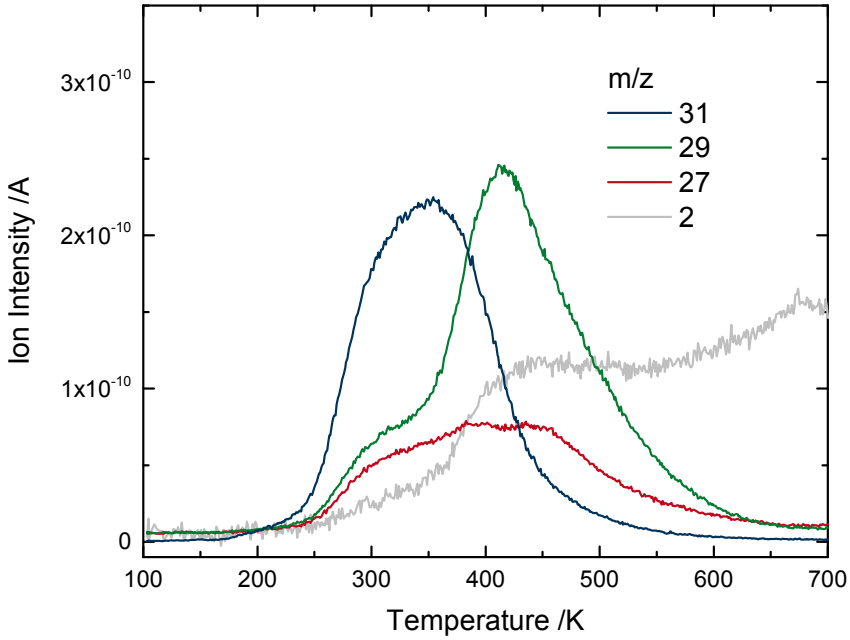

Figure 5.1. Uncorrected relevant mass fragments for a TPD of 0.85 ML ethanol on an MOCVD-grown GaN(0001). Ethanol is identified by mass trace 31, acetaldehyde by 29, ethylene by 27 and hydrogen by 2. Note that the significant hydrogen background is also obtained in blank experiments and is attributed to outgassing from the bulk sapphire wafer. The mass traces 29 and 27 also contribute to the cracking pattern of ethanol, but above 350 K a deviation is observed indicating an reaction.

second one appears around 210 K, which is shifting to lower temperatures. The overall recorded signal for an initial molecule coverage of 1.00 ML matches the expected concentration of Ga^{3+}-lattice sites of $6.0 \cdot 10^{14}$ cm^{-2} calculated from a atomically flat surface using the unit cell dimensions [292].

For the lowest ethanol coverage, no intact ethanol desorption is observed, but all the alcohol reacts either to acetaldehyde or ethylene as depicted in Fig. 5.3. With rising ethanol coverage, both, the acetaldehyde and ethylene features are growing respectively until no further molecule yield is observed by increasing the coverages higher than 1 ML. Both reaction products are observed at higher temperatures than the molecular ethanol desorption, indicating that a more strongly bound species is responsible for their formation. In analogy with many studies on oxides, this species is attributed to be ethoxys from dissociative ethanol adsorption, since they presumably facilitate both, dehydrogenation and dehydration, pathways. [284–286]

AES data after 8 TPD runs shows no formation of carbon deposits, indicating that all carbon-containing species desorb and that the carbon mass balance can be closed. Based on the stoichiometry, both acetaldehyde and ethylene should be accompanied by the by-products H_2 and H_2O, respectively. The corrected hydrogen trace is shown in Figure 5.4. Molecular hydrogen is evolved around 450 K and the yield also increases with the initial alcohol coverage and levels off once an initial coverage of a monolayer of ethanol is reached. The overall molecular hydrogen yield, however, matches the acetaldehyde for-

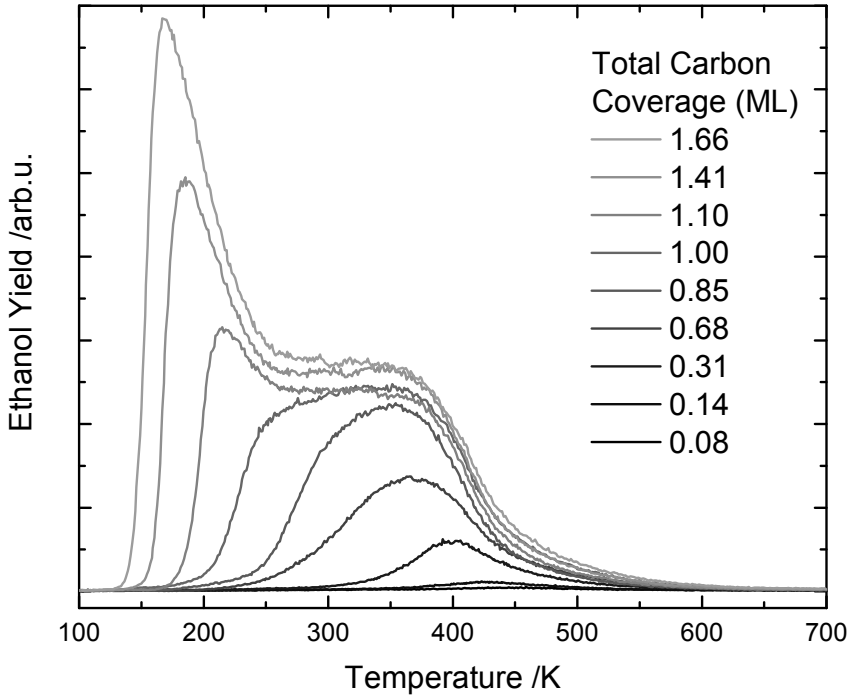

Figure 5.2. Coverage series of ethanol dosages on a MOCVD-grown GaN(0001). Note that a coverage of 1 ML is set to the trace with the saturated 350 K feature. For the calculations of the desorption yield, the reactive species are also added to the total carbon content. For the smallest initial dosage, no ethanol desorption is observed, indicating that all the alcohol reacts. Eventually, with rising dosages, at peak at around 350 K evolves. With higher coverages, this feature saturates and another peak around 200 K, shifting to even lower temperatures, is observed.

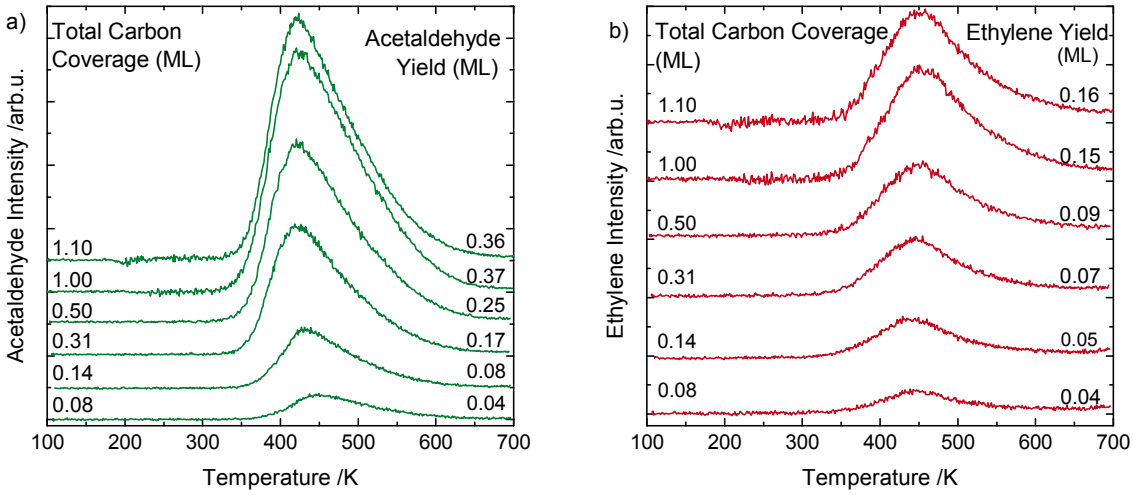

Figure 5.3. Acetaldehyde (a) and ethylene (b) yields from TPD experiments of ethanol on MOCVD-grown GaN(0001). Acetaldehyde as well as ethylene are evolved around 450 K. Once an initial coverage of 1 ML is reached, the product formation saturates, also shown in the respective integrated molecule yield displayed on the right. The traces are offset for clarity.

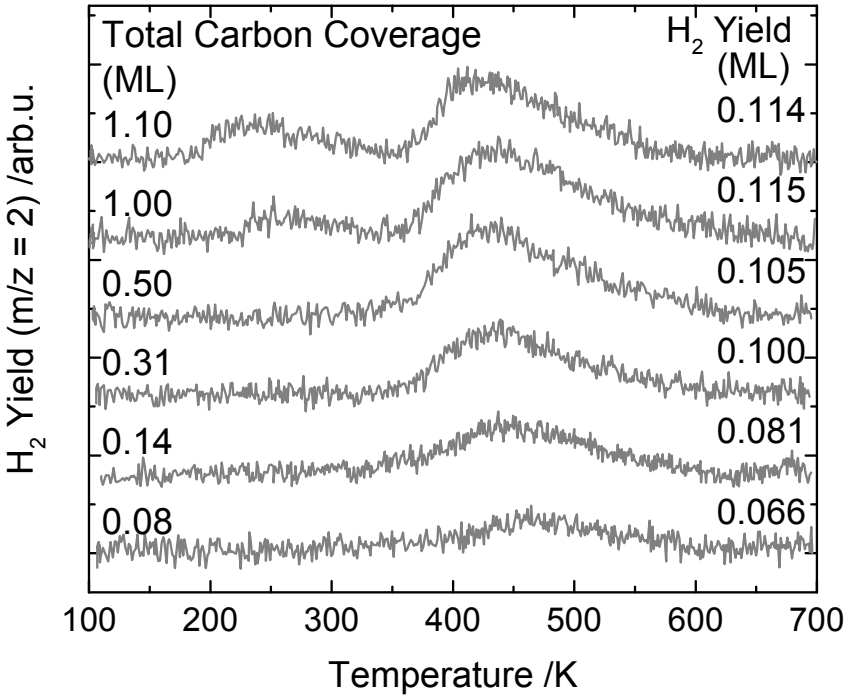

Figure 5.4. Hydrogen yields from the ethanol TPD experiments. The traces are corrected for the rising background observed in Fig. 5.1. For all coverages, a H_2 peak is observed around 450 K, matching the reaction temperature of acetaldehyde. The integrated molecular hydrogen desorption yields are displayed on the right over the respective traces. Approaching monolayer coverages of ethanol, the hydrogen desorption as well as the reactivity in Fig. 5.3 are saturated. For high coverages of ethanol, a small signal appears around 220 K, which is attributed to cracking of ethanol in the QMS.

mation only qualitatively, since it is not stoichiometric to the acetaldehyde yield and in general lower than expected from the acetaldehyde signal.[1] At ethanol coverages higher than a monolayer, an additional feature in the H_2 yield seems to appear. This is attributed to be an artifact, as there is a considerable error in the background subtraction and especially the cracking pattern at high signal intensities of ethanol in the QMS.

Since ethylene is also observed as the ethanol dehydration product, water formation is expected. In Figure 5.5, the water traces of several ethanol TPDs are displayed, but no water is observed. A first assumption, that the entire oxygen of H_2O remains on the surface as part the native oxide on MOCVD-grown GaN(0001)[227–232] (see also in Chapter 3.3.3), can be ruled out. Although ethylene formation is a minor reaction channel with about 0.1 ML, over the course of about 20 TPD runs, more than 2 ML of oxygen would be left on the surface to form an oxide film. However, the reactivity of the TPDs did not change in the experiments over several runs and no molecular oxygen desorption was observed (data not shown). Furthermore, no appreciable change in the AES spectra after all experiments was observed. The fate of the oxygen remains unclear, especially since a

[1] Note, for the smallest investigated ethanol coverage, more H_2 than acetaldehyde is evolved. However, especially because of the background subtraction of the H_2, the value is somehow within the experimental uncertainties.

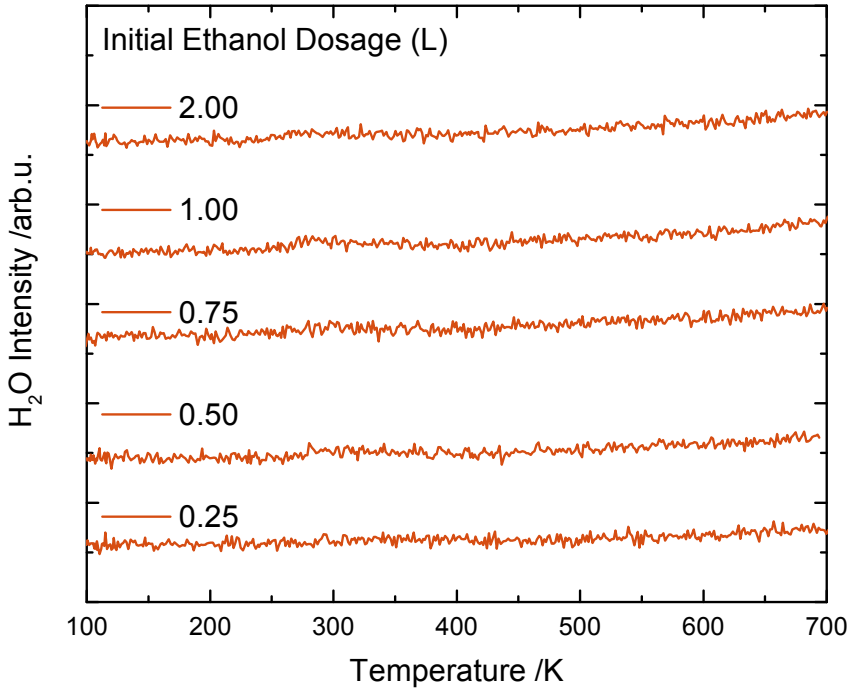

Figure 5.5. Water traces from ethanol TPDs on GaN. For all ethanol coverages (given in dosages here), no water desorption was observed.

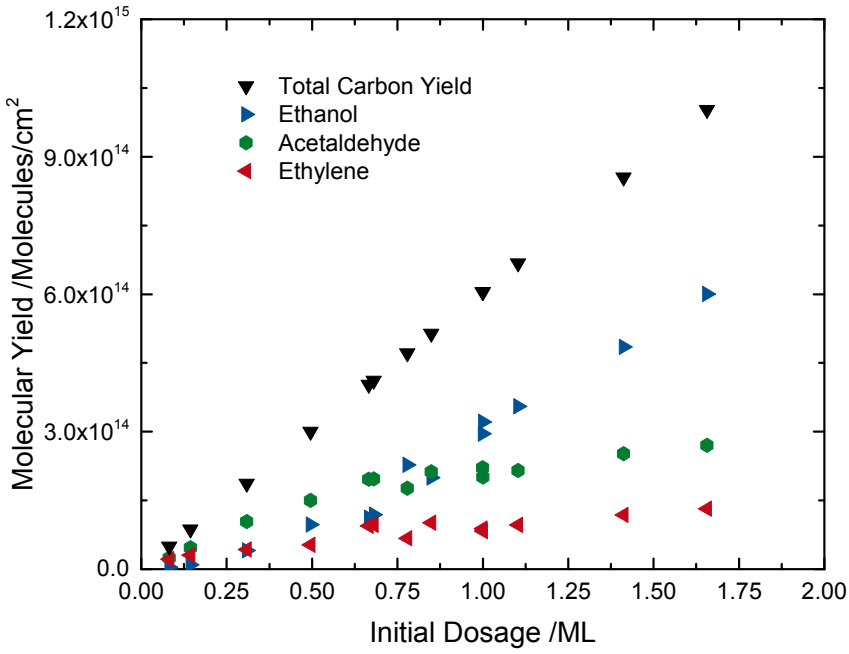

Figure 5.6. Integrated molecule yields from a TPD coverage series of ethanol on a MOCVD-grown GaN(0001) sample. The molecule yields up to 2 ML are shown. After a coverage of 0.6 ML of initial ethanol dosage, no further increase in acetaldehyde and ethylene yields are obtained, indicating that the reactive sites are saturated at this coverage.

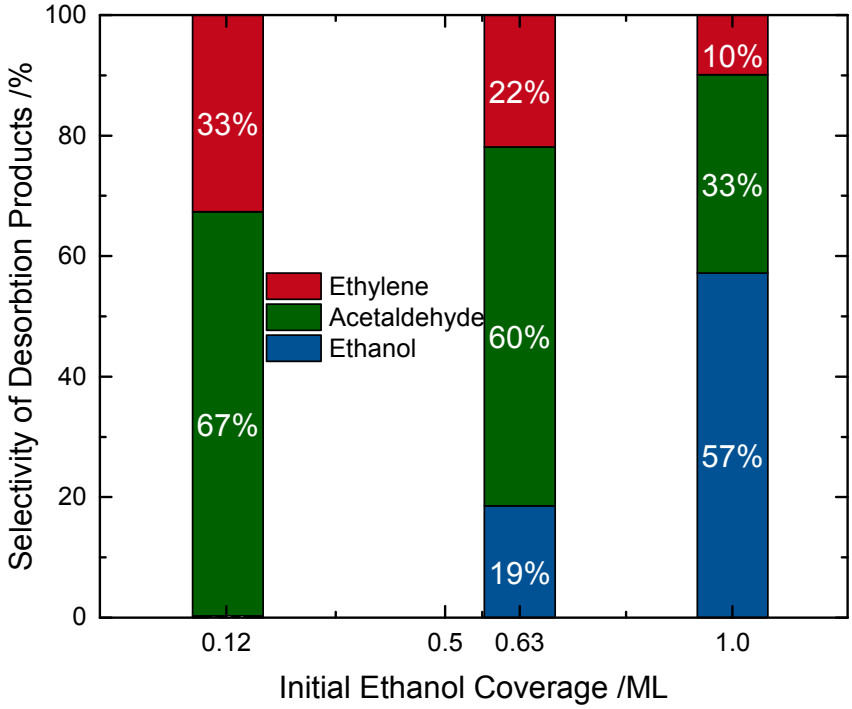

Figure 5.7. Coverage-dependent normalized selectivities for all desorbing carbon species for three exemplary ethanol TPD runs.

follow-up study on MBE-grown GaN(0001) showed, that with a rising degree of oxidation, the ethanol reactivity vanishes as presented in Chapter 5.2.[232]
The carbon mass balance however can be closed and the coverage-dependent desorption yields are displayed in Fig. 5.6. The saturation behavior of the reactivity can easily be seen in this representation, showing that the reactivity is saturated at about 0.6 ML of ethanol dosage. Higher ethanol coverages only result in more ethanol desorption. At the low-coverage limit, all of the ethanol reacts to acetaldehyde and ethylene. The selectivity of converted ethanol in the reactivity saturation regime limit is about 70% acetaldehyde and 30% ethylene. This behavior is displayed in normalized selectivities in Fig. 5.7, showing normalized amounts of all desorbing species.
The reactivity of the surface can be described by the following reaction equations. Ethanol, at least partly, adsorbs dissociatively on the Ga^{3+}-sites on the surface (Eq. 5.1), which is the origin of both reaction channels on the surface:

$$\underset{\text{ethanol}}{CH_3CH_2OH} + Ga_{surf} + N_{surf} \longrightarrow \underset{\text{ethoxy}}{CH_3CH_2O{-}Ga_{surf}} + N_{surf}H \tag{5.1}$$

The dehydrogenation of the ethoxy species is attributed to an αH-abstraction in analogy to reactivity studies on oxides (Eq. 5.2).[282,285] This picture is also consistent with the desorption temperatures, since ethoxy species are generally more strongly bound than

molecular ethanol and at the reaction temperature of about 450 K both formed products (acetaldehyde and hydrogen) are liberated upon formation (Eq. 5.3).

$$\underset{\text{ethoxy}}{CH_3CH_2O{-}Ga_{surf}} + N_{surf}H \xrightarrow{\alpha\text{H-abstraction}} \underset{\text{acetaldehyde}}{CH_3CHO{-}Ga_{surf}} + N_{surf}H_2 \tag{5.2}$$

$$\underset{\text{acetaldehyde}}{CH_3CHO{-}Ga_{surf}} + N_{surf}H_2 \longrightarrow \underset{\text{acetaldehyde}}{CH_3CHO}\uparrow + H_2\uparrow + Ga_{surf} + N_{surf} \tag{5.3}$$

The other reaction pathway is the formal dehydration of ethanol. Studies on TiO_2(110) showed, that the mechanism is likely to proceed via a βH-abstraction and is attributed to a concerted scission of the C-O bond in a cyclic transition state.[285,293] Ethylene is liberated upon formation and immediately desorbs (Eq. 5.4). Formally, a hydroxyl and the surface amine could recombine to form water (Eq. 5.5) and complete the catalytic cycle. However, no water is observed in the investigated temperature range.

$$\underset{\text{ethoxy}}{CH_3CH_2O{-}Ga_{surf}} + N_{surf}H \xrightarrow{\beta\text{H-abstraction}} \underset{\text{ethylene}}{C_2H_4}\uparrow + Ga_{surf}OH + N_{surf}H \tag{5.4}$$

$$Ga_{surf}OH + N_{surf}H \longrightarrow H_2O\uparrow + Ga_{surf} + N_{surf} \tag{5.5}$$

Although unlikely, some of the H_2 could stem from a recombination of the two hydrogen atoms in this reaction channel, leaving a formal oxide on the surface behind. Concluding the discussion above, the fate of the oxygen in this reaction channel still remains elusive. This lack of stoichiometry and water formation, however, is a known obstacle in surface science studies for ethanol dehydration.[283,294,295] From the amount of reaction products for 1 ML, it is deduced with the described mechanism, that at least 43% of ethanol are bound dissociatively on the surface. A shift in the leading edge of the ethanol desorption feature is also characteristic for a second-order desorption[220,296], indicating that ethanol is also formed by recombinative desorption of ethanol, inferring even a higher degree of dissociatively bound ethanol.

For a structure-function relation, the wurzite GaN(0001) surface is compared to the wurzite ZnO(0001) surface. On this surface, a dehydrogenation reaction of ethanol is predominantly observed, while dehydration is a minor reaction pathways.[294,295] In these studies, the reactivity was limited and attributed to only occur on step edges and defect sites. However, STM studies on ZnO(0001) have shown, that instead of atomic point-defects, triangular structures are found on the surface.[297–299] The edges and steps of those structures lead to dangling bonds and a stabilization of partial charges, that may faciliate ethoxy formation on the surface.[283,297] With an amount of 43% of conversion of a monolayer ethanol and a saturation of the reaction behavior at 0.6 ML initial coverage, it is ruled out that special defect sites may be the active sites for the reaction. Instead, the high amount of ethoxy intermediate is attributed to the oxophilicity of Ga and the binding properties of hydrogen to the surface. This may result on the formation of Ga-H species[300] or the expected surface amines. The binding of molecular and atomic hydrogen on GaN(0001) and its influence from and on the semiconductor's electronic structure

at the surface and vice versa are still not very well understood.[301–304] Molecular hydrogen formation from ethanol dehydrogenation was detected around 450 K, at a similar temperature as Vohs and co-workers reported trace amounts of H_2 for the ZnO(0001) surface.[283] Full stoichiometry was not achieved, which is a common phenomenon in such studies.[283,294,295] This may be due to residual surface amines or diffusion in the bulk. In contrast, most oxides form stable hydroxyls and thus prevent molecular hydrogen formation, which ultimatively leads to water formation at high temperatures.[305–309] The desorption of D_2 from a GaN film was observed at significantly lower temperatures[310] as that from hydroxyls on i.e. TiO_2-surfaces, which remain stable up to 1000 K.[311] From this perspective, surface amines seem less stable than surface hydroxyls and, therefore, facilitate the formation of molecular hydrogen. Wurzite-structured nitrides in general might therefore be superior support materials than oxides for thermal alcohol reforming for hydrogen production. They may represent a new material class for thermal[312,313] and photocatalytic[152,159,169,314,315] alcohol reforming materials, adding to oxide-supported metals and unsupported metal catalysts.[316–319]

5.1.2. Ethanol Photochemistry on MOCVD-grown GaN(0001)

Bare GaN particles show some photocatalytic activity with[75,262,263,320,321] and without any (noble) metal co-catalyst.[322,323] In order to study the photocatalytic activity 0.82 ML ethanol are dosed on the sample at 100 K and the desorbing masses are monitored before and during UV-illumination (Fig. 5.8 a), but no desorbing species are observed. A post-irradiation TPD after 20 min of irradiation at 100 K shows no significant difference to a TPD run without illumination (Fig. 5.8 b). Upon illumination, holes travel to the surface on this n-type GaN(0001) and either extinguish the negatively charged surface states and/or oxidize adsorbed species on the surface, if the molecule has a favorable

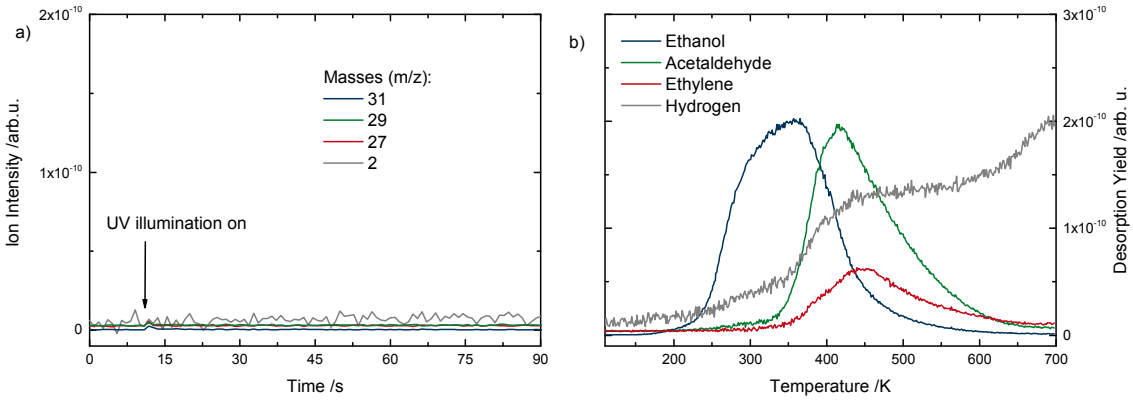

Figure 5.8. Isothermal illumination experiment of 0.82 ML ethanol on MOCVD-grown GaN(0001) at 100 K depicted in a). Laser irradiation with 266 nm UV light (600 µJ pulse energy) from the dye laser shows no immediate product desorption and a consecutive post-irradiation TPD (b) after 20 min irradiation neither results in additional peaks nor in a different product distribution than an ethanol TPD without irradiation. The exact illumination conditions for the photochemistry are the same as in Chapters 4 and 7.2.

energy level alignment with the valance band.[324] The lack of photo-reactivtiy of ethanol on GaN(0001) shows, that no energy states exist that enable photo-oxidation on this surface. In comparison with TiO_2, GaN generally shows a higher energetic position of the valence band with respect to vacuum[325], that might hinder a desirable adsorbate-band alignment for photo-oxidation.

5.2. Ethanol Surface Chemistry on MBE-grown GaN(0001), GaO_x/GaN(0001) and $Ga_2O_3(\bar{2}01)$

In this work, n-type doped MBE-grown GaN(0001) samples were used to monitor the effect of surface oxidation on the reactivity of ethanol. Further details are presented in Appendix D. Although the GaN(0001) MBE-surface exhibits a different morphology [326–328] than MOCVD-grown samples [229,327–330], the observed chemistry is similar. By monitoring the dehydrogenation channel of ethanol via an ethoxy intermediate it is shown, that the formation of an oxide layer inhibits the reactivity towards ethanol. A $Ga_2O_3(\bar{2}01)$ single crystal is used as a reference model system for gallia chemistry, since this crystal facet is the natural growth direction of epitaxial gallium oxide growth on GaN(0001). [221] Besides some native oxide[2], the dehydrogenation activity is similar to the previously described MOCVD-grown GaN(0001). When a native oxide film is closed, since it grows in a layer-by-layer manner, [331,332] the reactivity of the nitride vanishes. The oxide film still shows dissociative adsorption, which is indicated by the shift in the leading edge [220,296], but no reactivity. The single crystal model oxide confirms this lack of reactivity, and even, only exhibits molecular adsorption of ethanol in agreement with previous studies for methanol on gallium oxide powders. [333,334] The reactivity results are illustrated in Figure 5.9.

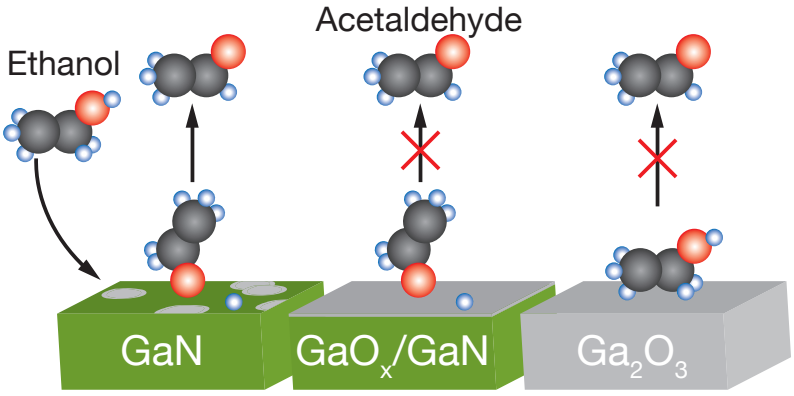

Figure 5.9. A scheme of the work presented for the described results. The reactivity of ethanol to acetaldehyde was used to probe the degree of surface oxidation. Upon full oxidation of the GaN(0001) surface, acetaldehyde is no longer observed as a dehydrogenation product, although the alcohol adsorption is still dissociatively. $Ga_2O_3(\bar{2}01)$ is investigated as a reference system and no reactivity is observed.

While the influence of the oxide film on the band bending is still under discussion [276,335], photoelectron spectrosopy [280,336] and electrochemical [277] studies reveal that the surface states are removed. The lack of reactivity can also be rationalized by a removal of these surface states, i.e. negative charges at the surfaces are removed, which depletes the reactivity of the n-type semiconductor. These results are an example of the fragile chemistry (and electronic properties as well) of oxynitride materials, which depend on the surface

[2] This is discussed earlier in Chapter 3.3.3.

composition.[337] Furthermore, this work illustrates how crucial the control of surface chemistry can be for the reactivity and it should strongly be considered when tailoring new oxynitride photocatalysts by bend-engineering only.[53,54,60,73]

6

Alcohol chemistry on α-Fe_2O_3(0001)

The results presented here were obtained in a collaboration with Dr. Andrew Crampton in the group of Prof. Dr. Cynthia Friend at Harvard University (MA, USA). Different alcohols were chosen to monitor the thermal and photochemical reactivity of an earth-abundant semiconductor, that offers in principle the possibility for hydrogen production with visible light.

The surface structure of the α-Fe_2O_3(0001)-surface has been a long standing controversy for the past decades.[338,339] Parkinson concludes, that "α-Fe_2O_3(0001) is certainly the most difficult and controversial of the iron oxide surfaces, partly because the preparation conditions required to create a stoichiometric surface are out of the comfort zone of surface science experiments".[338]

Haematite iron oxide is a semiconductor of earth abundant elements with a band gap of 2.2 eV.[340,341] The (0001)-surface has attracted a lot of attention in photocatalysis and photoelectrocatalysis both experimentally[67,342–347] and theoretically.[348–352] Water oxidation, although with sluggish kinetics, is facilitated without any co-catalyst on the surface.[343] Recently, Zandi *et al.* discovered spectroscopically the Ferryl-species (Fe=O) as an intermediate in the oxygen evolution reaction from water.[350,353] However, almost all other mechanistic intermediates and details of reaction sites remain unknown. Therefore, the goal of this project was to investigate adsorption sites, thermal reaction channels and ultimatively the photochemistry in UHV to gain further insights into photochemical mechanisms that are transferable to a benchmark of thin-film haematite photoelectrodes.

In the following, the denomination of Parkinson is followed for the three surface terminations of the α-Fe_2O_3(0001) crystal.[338] Structures created by sputtering and annealing up to 1000 K in oxygen atmosphere ($1 \cdot 10^{-6}$ mbar) are assigned to the reduced *Fe_3O_4(111)-like* termination. Annealing in the same oxygen background to 1173 K results in the so-called *"bi-phase"*-termination. This termination essentially refers to the LEED pattern consisting of hexagonal "florets" around the integer order spots.[354] The structure is predominantly described as $Fe_{1-x}O(111)/\alpha$-Fe_2O_3(0001) with ordered islands of FeO coinciding with the Fe_3O_4(111)-like termination.[355] Experimentally, the *stoichiometric* termination of the α-Fe_2O_3(0001)-surface has been reported once *in vacuo* by annealing the haematite film on Pt(111) to 1100 K at 1 mbar O_2[356] or by annealing a haematite single crystal in atomic oxygen.[357]

Previous surface science studies on stoichiometric haematite surfaces were performed on the α-Fe_2O_3(012) surface, where two different surface terminations can be prepared by annealing in molecular oxygen.[358–361] Very recent work from Parkinson's group sup-

plied an extensive characterization by AFM, STM, XPS and UPS of the α-Fe_2O_3(012) surface.[362] The only alcohol reactivity study on this surface found a methanol disproportionation reaction at high temperatures and showed that the redox-chemistry can be influenced by the oxidation state of the iron cations in the surface.[359] This disproportionation reaction was also observed for the magnetite Fe_3O_4(111)[363] and Fe_3O_4(001)[364] surfaces, making it the perfect model reaction for a quantitative evaluation of alcohol reactivity on the stoichiometric α-Fe_2O_3(0001)-surface.

6.1. Experimental Methods

The experiments with iron oxide single crystal surfaces were done at Professor Cynthia Friend's group at Harvard University. The ultra-high vacuum apparatus is equipped for thermal and photochemical measurements in the UHV and has also been described elsewhere.[365,366] Briefly, it is equipped with a QMS (Hiden Analytical) with a skimmer for thermal reactivity measurements and a Xenon Lamp (Sutter Instruments, Lamda 10-3) with several filters for photochemical measurements. The surface preparation is monitored with LEED (Princeton Research Instruments, 11-020) and Auger Electron Spectroscopy (Physical Electronics Industries, PHI 10-805). The chamber is also equipped with several molecular beam dosers of in-house design, one of them connected to an ozone source (LG-7 CD Laboratories) for surface cleaning procedures with high oxidation potentials. The α-Fe_2O_3(0001) single crystal (SurfaceNet GmbH, Germany) is mounted on a tantalum sheet with gold foil. Tungsten wires are cemented to the back of it (Aremco, Ceramabond 569) and are mounted on the liquid nitrogen-cooled manipulator. The temperature, which is measured with a type-K thermocouple, can be controlled up to 1000 K by resisitive heating with a PID controller (Eurotherm 2404). Surface cleaning is routinely achieved by Ar^+-sputtering ($1.5 \cdot 10^{-5}$ torr, 0.5 keV, 2 μA sputter current, 25 min) and subsequent annealing at 1000 K in an ozone atmosphere of $2.6 \cdot 10^{-6}$ Torr for 20 min. The ozone concentration is monitored online and regulated to 70 g/nm^3. The source for UV-illumination is a 300 W Xe lamp with a 400 nm short pass filter (3.1 eV, Asahi Spectra). From previous work, the flux at the surface is estimated to be 92 mW/cm^2, 14% of which are >400 nm.[365] TPD measurements were carried out in a line-of-sight geometry between 200 and 800 K. Methanol (Sigma-Aldrich, $\geqslant$99.98%) and ethanol were purified by pump-freeze cycles. The dosage was performed at 200 K and the data presented is corrected for ionization cross sections, transmission coefficients, cracking patterns and their respective detector efficiencies (see also Appendix B).

6.2. Characterization of the α-Fe_2O_3(0001) surface

The characterization of the α-Fe_2O_3(0001) surface after a cleaning cycle is performed by AES and LEED. For the above mentioned crystal preparation, an AES spectrum is shown

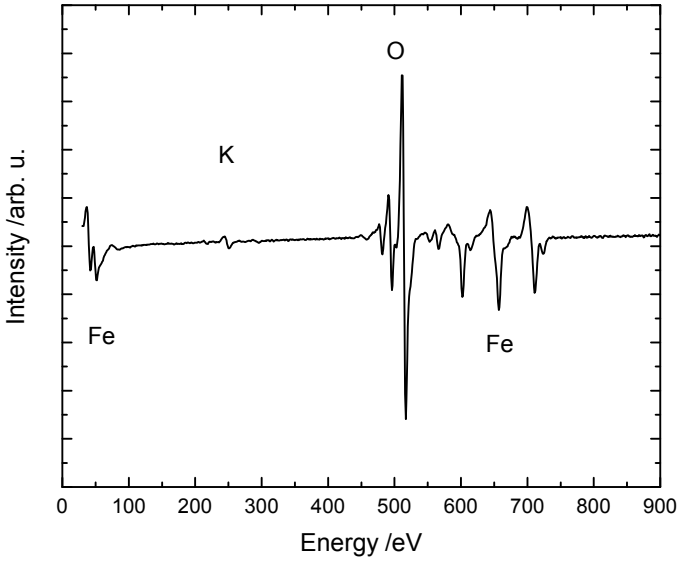

Figure 6.1. Auger Electron Spectrum of the Ozone-annealed α-Fe_2O_3(0001)-crystal. The single crystal shows the characteristic signals 490 eV and 510 eV for oxygen and the ones for iron at 47 eV, 598 eV, 651 eV and 703 eV.[185] The small feature around 250 eV is attributed to a K contamination of the natural crystal. Quantitative AES analysis yields a contamination of 1% within the 8 uppermost single crystal layers. Note, that the Fe-peak at 47 eV shows a peak splitting, characteristic of Fe^{3+}-cations in the surface region.[358]

in Figure 6.1. Apart from a small potassium contamination[1], only iron and oxygen peaks are observed within the expected stoichiometry. The peak splitting for the iron signal at 47 eV suggests that the full oxidation was achieved, since it is characteristic of Fe^{3+}-cations in the surface region.[358]

LEED measurements allow for a further characterization of the oxidized α-Fe_2O_3(0001) surface. In the above mentioned conditions, a $(\sqrt{3} \times \sqrt{3})$R30° LEED pattern is observed (upper part of Fig. 6.2), which is in very good accordance to previous work on haematite films on Pt(111).[356] The LEED measurements further show, how crucial the surface structure depends on the preparation conditions. Cycles of sputtering an oxygen annealing in a $1 \cdot 10^{-6}$ torr background result in a LEED pattern with hexagonal florets attributed to the *"bi-phase"*-reconstruction (Fig. 6.2).[354,355] When sputtered and annealed to 900 K in vacuum, the crystal termination exhibits the well-known $Fe_3O_4(111)(2 \times 2)$ reconstruction.[354,369,370] All of the LEED patterns and corresponding surface structures are given in Figure 6.2. A further discrimination of the Fe-termination is only possible by LEED I-V curves[339] or SPM techniques.

As a further observation, the oxygen signals from dosing oxygen and ozone are presented in Figure 6.3. While oxygen does not adsorb in the investigated temperature range,[2] molecular was oxygen desorption was observed when cooling the crystal down to 300 K

[1] The potassium is a known contamination in natural single crystals and amounts to 1% in the first eight layers. Therefore, it is deemed insignificant for the LEED and TPD results presented here.

[2] The lowest cooling temperature achieved was 180 K.

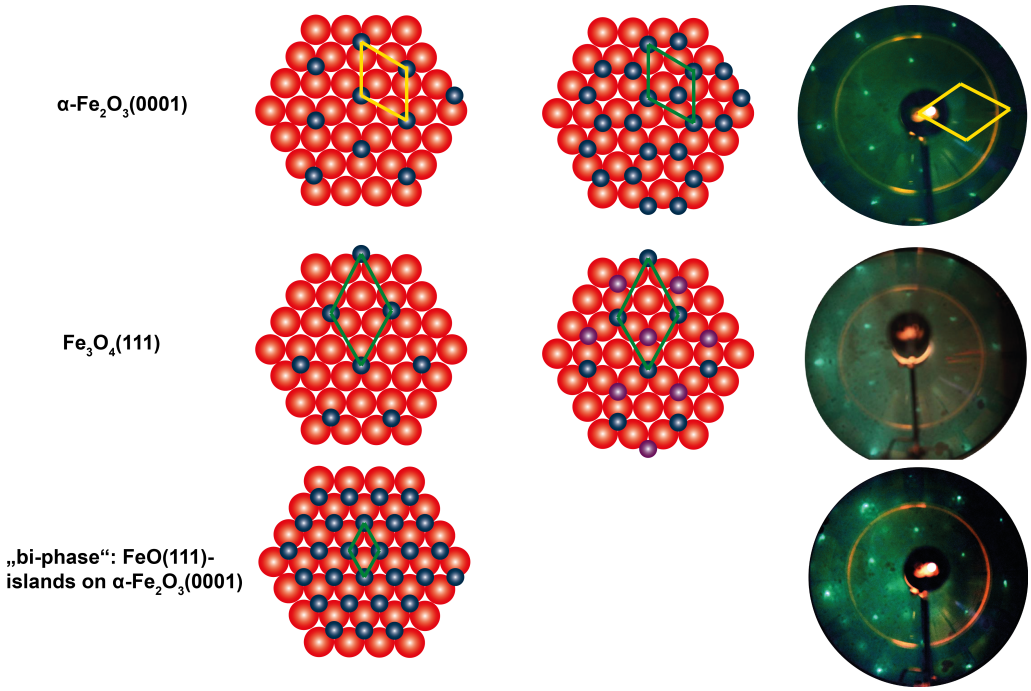

Figure 6.2. An overview of LEED patterns for different surface terminations of a α-Fe_2O_3(0001) single crystal and corresponding structural models proposed by Weiss and coworkers.[356,367,368] Three different surface terminations of α-Fe_2O_3(0001) have been reported so far, which were mostly determined by LEED and STM measurements.[368] The assignment of the LEED patterns stems from thin films on Pt(111).[356] The surface nomenclature on the left labels the termination surface. For haematite and magnetite reconstructions, two iron terminations are possible from the crystal structure. However, they are not distinguishable from each other without SPM techniques. Oxygen atoms are shown in red, while iron atoms are given in dark blue and purple. The parallelograms represent the unit cells in real and reciprocal space, respectively.

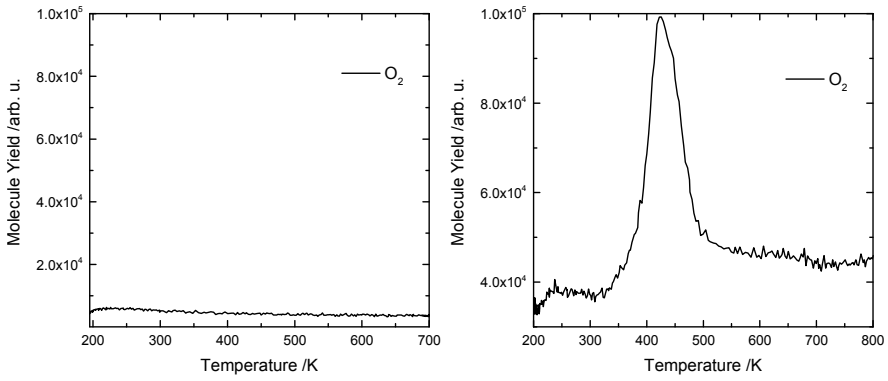

Figure 6.3. TPD results from dosing 1L of oxygen at 200 K on a clean α-Fe_2O_3(0001) surface and from cooling down the surface to 300 K in ozone atmosphere ($1 \cdot 10^{-6}$ mbar) after the cleaning cycle. While on the stoichiometric α-Fe_2O_3(0001) no molecular oxygen desorbs, the ozone covered surface shows some molecular oxygen in the TPD run around 450 K.

in an ozone atmosphere. Possibly, residual ozone is still adsorbed even above 300 K, which decomposes readily on the surface yielding molecular oxygen around 420 K. For the reactivity measurements, the ozone background pressure is turned off at the annealing temperature, just before cooling the sample.

6.3. Thermal Chemistry of Methanol and Ethanol

Adsorption of methanol and TPD from the stoichiometric α-Fe_2O_3(0001) surface leads to three distinct desorption features at 280 K, 370 K and 620 K (Fig. 6.4). The desorption of methanol accompanied by formaldehyde at 620 K is indicative for a disproportionation mechanism, similar to that observed on TiO_2 [365,371] and Fe_3O_4.[364] A similar behavior was reported earlier from Henderson for the α-Fe_2O_3(012) surface,[359] and attributed to the disproportionation of methoxy groups, although the yields did not follow the expected stoichiometry. The feature around 370 K might be from recombinative desorption of methanol, while the main feature around 280 K might be attributed to molecular methanol on the surface in analogy to the study of Henderson on the α-Fe_2O_3(012) surface.[359] The small formaldehyde signal around 300 K and the oxygen one in Fig. 6.3 might be indicators that the ozone preparation could lead to O-adatom formation.[372]

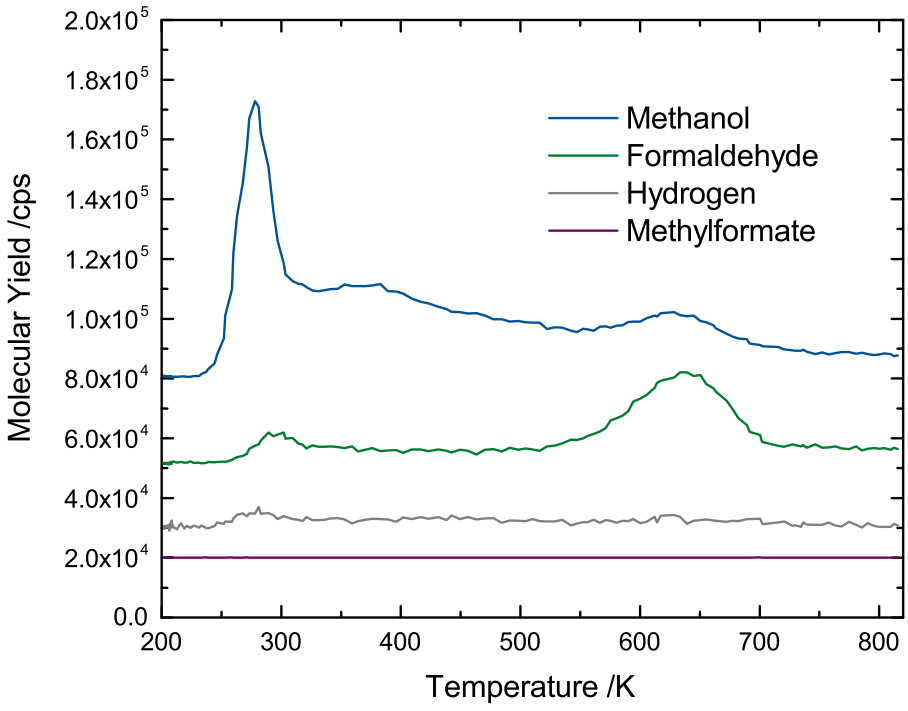

Figure 6.4. TPD of 0.42 ML of methanol adsorbed at 200 K on a α-Fe_2O_3(0001) surface. Around 650 K, a high temperature feature of equal amounts for both, methanol and formaldehyde, is obtained. It is attributed to a disproportionation reaction of methoxy species on the surface. Most methanol desorbs between 250 K and 400 K, which is assigned to molecular adsorption. No further side-products such as hydrogen and methylformate are observed. The traces are offset for clarity.

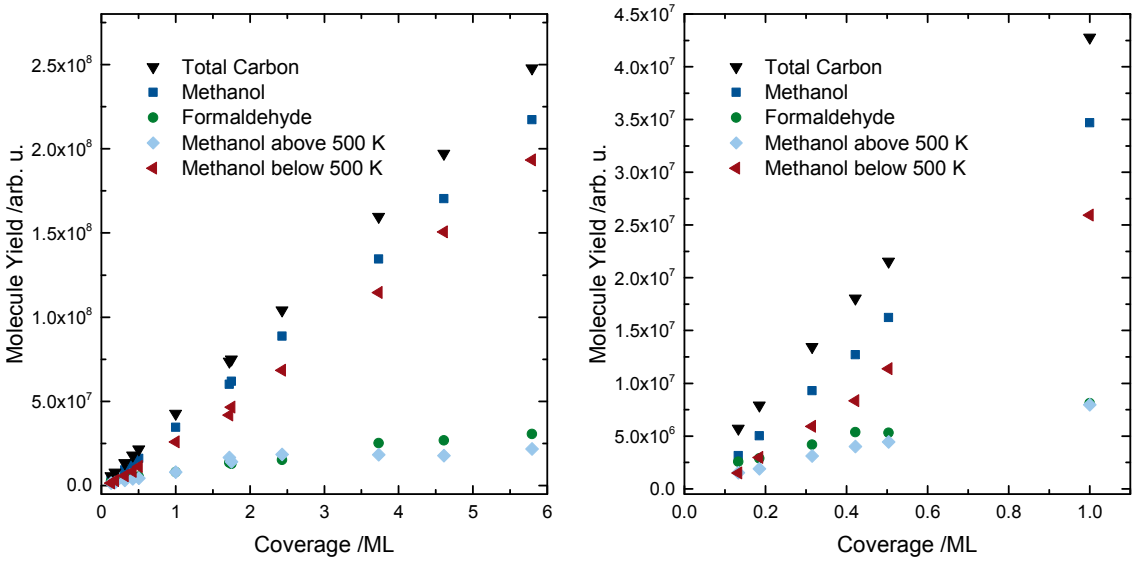

Figure 6.5. Integrated molecule yields from a TPD coverage series of methanol on α-Fe_2O_3(0001). In the left panel, the molecule yields up to 6 ML are shown, while in the right panel the reactivity below 1 ML is displayed in more detail. Analyzing the high temperature features in more details, above 500 K equal amounts of methanol and formaldehyde are obtained. Since no formation of carbon deposits is observed over 10 TPD experiments, the carbon mass balance can be closed.

From TiO_2(110), they are known to have a strong oxidation potential.[107,372,373] No molecular hydrogen formation was observed during all the experiments (see Fig. 6.4) and some water formation was observed, although super-imposed with background H_2O from the ceramic glue. The extremely broad water feature of the glue strongly depends on the duration of the cleaning procedure and the experiment's history. Higher oxidation products like methylformate are not obtained in this work. No coking is observed by AES after consecutive TPD runs for all alcohols. Therefore, the carbon mass balance can be closed and the coverage dependent desorption yields are shown in Fig. 6.5. When integrating only the high temperature signals of methanol and formaldehyde, stoichiometric desorption yields are obtained for the disproportionation reaction. The high temperature formaldehyde feature saturates with coverages high than 1 ML and further dosage mostly results in further alcohol desorption.

Ethanol adsorption on the Fe_2O_3(0001) surface demonstrated similar characteristics as for methanol (Fig. 6.6). High temperature evolution of acetaldehyde and ethanol are observed at 630 K and the slight shift to higher temperatures may be explained by a higher stability of the ethoxy species on the surface, originating from the longer chain length.[374] The molecular yield of the acetaldehyde also saturates at coverages around one monolayer and higher dosage only results in more molecular ethanol desorption from the peaks around 290 K and 385 K. The dehydrogenation pathway is observed for both alcohols, but dehydration to ethylene is not observed for ethanol (data not shown). This supplies further evidence, that a fully oxidized α-Fe_2O_3-(0001) surface is achieved, since the dehydration is usually attributed to oxygen vacancies in the surface[285,295], which

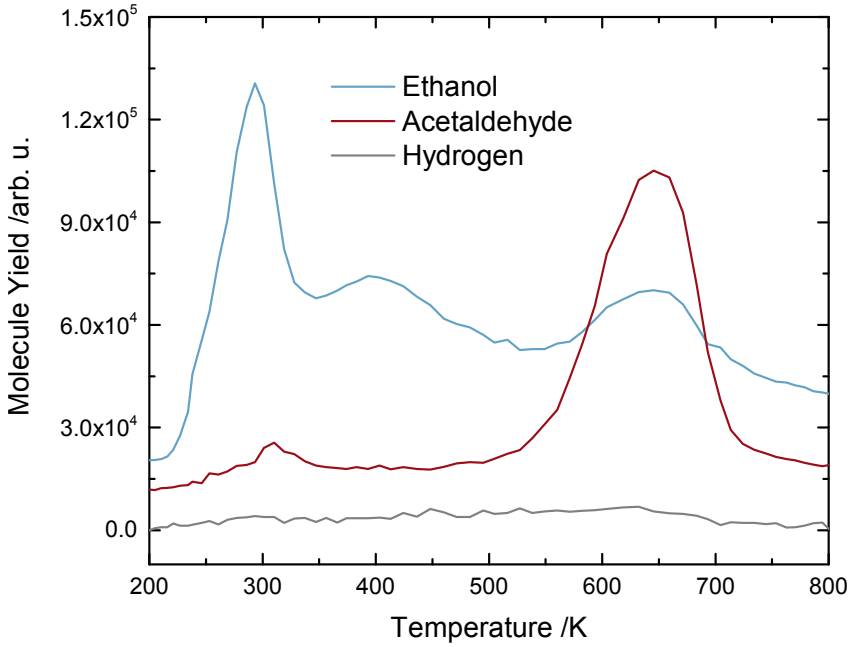

Figure 6.6. TPD of 0.91 ML of ethanol adsorbed at 200 K on a α-Fe_2O_3(0001) surface. At 650 K, both, ethanol and acetaldehyde, are evolved. The main ethanol feature is observed at 290 K with a shoulder at 400 K. Although acetaldehyde as a dehydrogenation product is obtained at the high temperature feature, no hydrogen is evolved. The traces are offset for clarity.

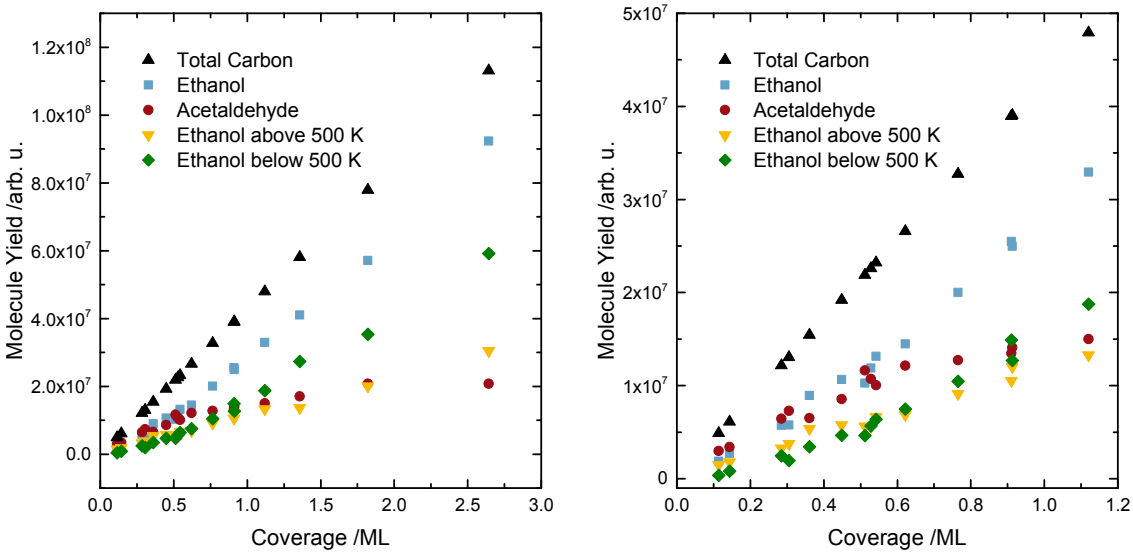

Figure 6.7. Integrated molecule yields from a TPD coverage series of ethanol on α-Fe_2O_3(0001). In the left panel, the molecule yields up to 3 ML are shown, while in the right panel the reactivity below 1.2 ML is displayed in more detail. The analysis of the high temperature features in more details gives no clear stoichiometric trend, since in the low coverage regime more acetaldehyde than total ethanol is evolved. As the formation of carbon deposits is not observed over 13 TPD experiments, the carbon mass balance can be closed. No ethylene desorption is obtained in any of these experiments.

"heal" the surface by alcohol deoxygenation. The coverage-dependent yields (Fig. 6.7) show, that only a crude stoichiometry is obtained for the high temperature features of ethanol and acetaldehyde.

In analogy to the behavior of GaN reported in Chapter 5.2, an interpretation based on the surface states of the n-type semiconductor can be given.[232] A change in reactivity of the surface states has been also demonstrated by photo-electrochemical experiments for water splitting,[375] since these could facilitate a lower energy pathway for the proton abstraction from the alcohol. These results also corroborate the methanol chemistry on iron oxide surfaces, where two different active intermediates for methanol oxidation where observed on a hematite photoelectrode.[376] The surface states are presumably a possible reason for dissociative alcohol adsorption on the semiconductor, since (somewhat) localized charges on the surface may facilitate dissociative adsorption of the alcohol as observed on previous polar surfaces.[294]

6.4. Photochemistry of Ethanol on α-Fe_2O_3(0001)

Photochemical experiments have been performed by dosing 0.91 ML at 200 K and illumination both with visible and UV light (see Fig. 6.8). No change in any trace is observed for both experiments, while a variety of possible products has been scanned including hydrogen, acetaldehyde, water, methyl radicals and further oxidation products such as CO and CO_2. Also the post irradiation-temperature programmed desorption (PI-TPD) experiments show no significant changes in the desorption features with respect to thermal desorption (compare Fig. 6.9 also with Fig. 6.6). The photo-oxidation reactions in haematite are always reported for photo-electrochemical systems, where an external bias

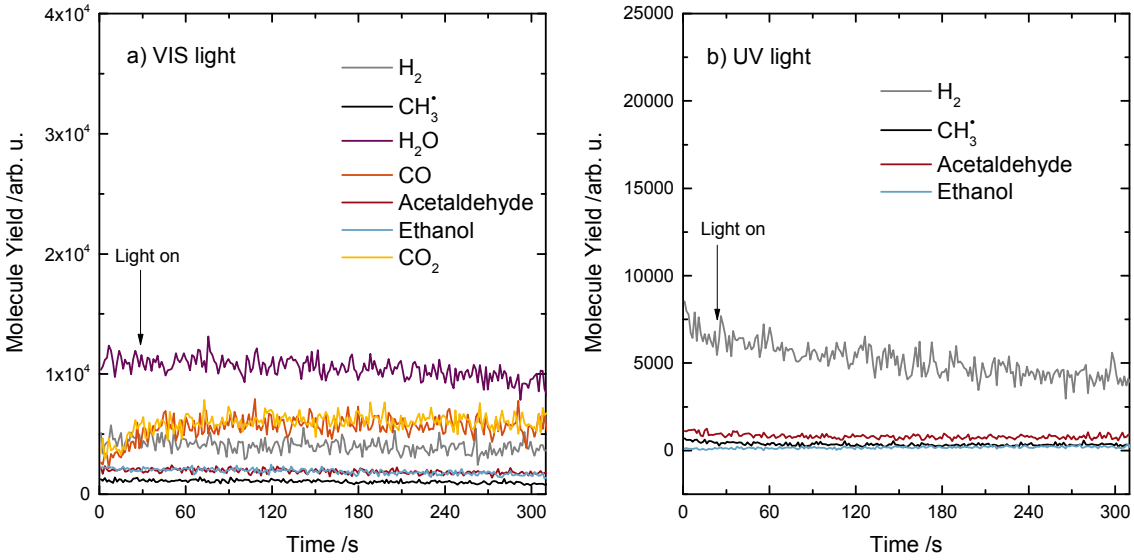

Figure 6.8. Isothermal illumination experiment of 0.91 ML ethanol on α-Fe_2O_3(0001) at 200 K. Neither visible nor UV light illumination results in a desorbing photoproduct. Illumination is started 30 seconds after the traces and ended after a further 300 s.

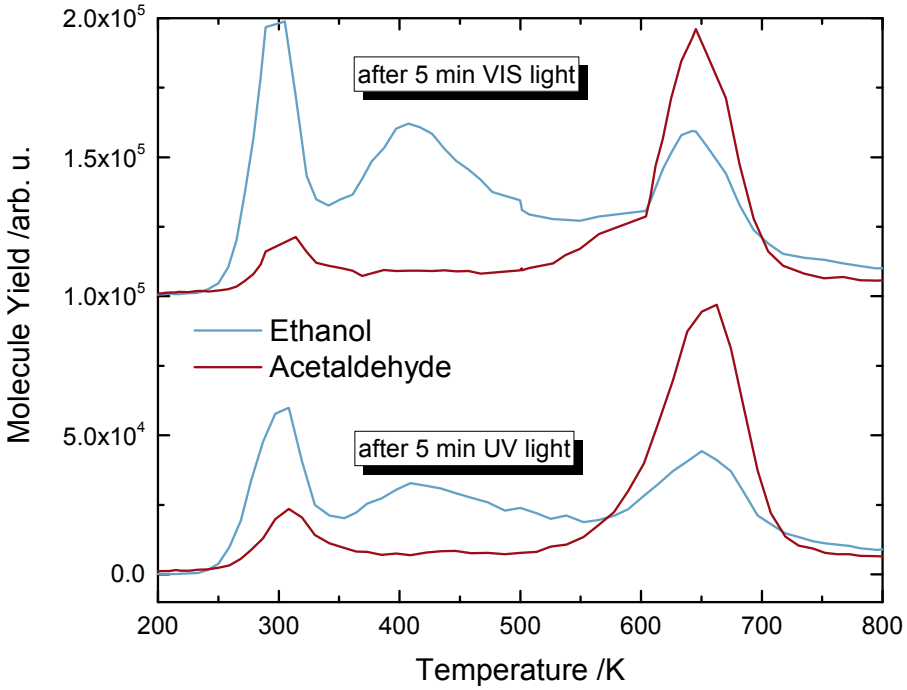

Figure 6.9. TPD experiments after the corresponding illumination experiments shown in Fig. 6.8. No further products were obtained, that are formed during the illumination and the reactivity remains unchanged with respect to the thermal chemistry (see Fig. 6.8).

voltage is applied.[67,344,353,377–380] Without an external bias, no photoreaction was observed on the haematite, which could be either due to an unsuitable valence band position[325] or due to the short charge carrier lifetimes (below 1 ps)[381–383] or hole diffusion length (2 to 4 nm).[341]

6.5. Summary

In summary, annealing in ozone after sputtering proves to be a viable approach to preserve a stoichiometric α-Fe_2O_3(0001) surface as shown by LEED and AES. The thermal chemistry on the stoichiometric surface reveals a high-temperature dehydrogenation pathway for methanol as well as ethanol, indicating a general absence of dehydration reaction channels for aliphatic alcohols. The reason for this reactivity could result from a surface redox-reaction or a disproportionation reaction. Also, a high temperature reconstruction as obtained on magnetite(100) surface could not be ruled out.[384]
For both alcohols, the reactivity is saturated with monolayer coverages. The two additional desorption features at intermediate (380 K) and low temperatures (285 K) appear for both alcohols, indicating two further adsorption sites that are unreactive, possibly due to dissociative and molecular adsorption on the oxide. These three adsorption states are in agreement with photo-electrochemical experiments, in which two differently bound alcohol species have been identified as intermediates.[376] This result stresses the significance of the chemical species of the molecule on semiconductor surfaces, both via the

influence of surface states in thermal catalysis as well as the reactive species in photocatalysis. Further, ozone cleaning is demonstrated a viable technique for single crystal semi-conductor preparation, while the conditions are less harsh than in oxygen plasma treatments.[372] The comparison between the nature of thermal intermediates and adsorbed species from surface science studies with their corresponding species under ambient conditions is of great importance for understanding and tailoring the chemical processes on the surfaces of promising photocatalytic materials.

7

Ethanol Chemistry on TiO_2(110)

In the following, the thermal chemistry of ethanol is studied on a TiO_2(110) model catalyst to investigate possible reaction pathways. This TiO_2 model catalyst has been investigated previously for thermal and photocatalytical reforming of biomass, alcohols and polyols.[81,159,160,249,250,385–389]

7.1. Quantified Thermal Ethanol Chemistry on r-TiO_2(110)

Parts of these results have been published previously[233] and all experimental details can found in this publication.
The thermal reaction pathways of ethanol on TiO_2 surface has been previously investigated and the dehydration product ethylene[284–286] and the dehydrogenation products

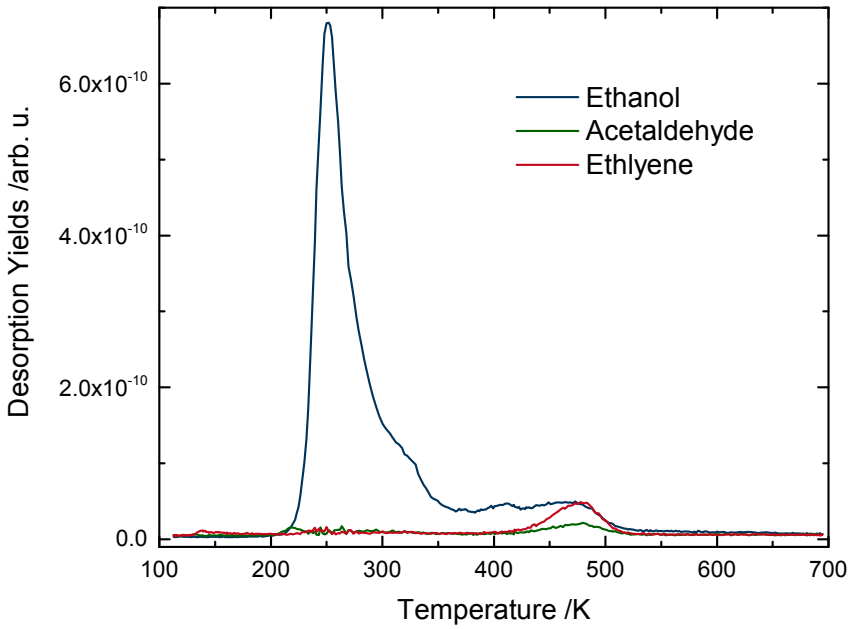

Figure 7.1. TPD for 0.66 ML (0.6 L) of ethanol on a r-TiO_2(110) surface. The majority of ethanol desorbs around 270 K, tailing to higher temperatures with a high temperature feature around 480 K. This behavior is in good agreement with previous studies.[286,374] Further, the high temperature feature is accompanied by the desorption of acetaldehyde, as the dehydrogenation product, and ethylene, as the dehydration product. The traces are set to the same baseline.

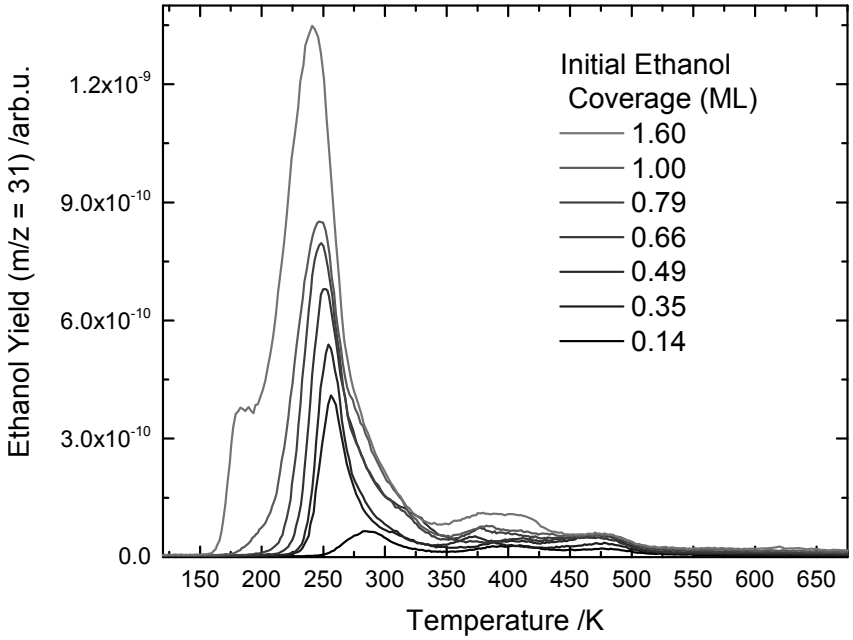

Figure 7.2. Series of TPDs of different ethanol coverages. The coverage of 1.0 L only shows a signal around 270 K and is set to 1 ML in this study. The TPDs as a function of coverage indicate, that at this coverage most Ti-lattice sites are filled. The next higher coverage investigated already shows an additional peak around 170 K. This additional peak can be attributed to ethanol desorbing from bridging oxygens on the surface.[374] While it is obvious, that this definition of 1 ML ($\equiv 5.2 \cdot 10^{14}$ cm^{-2} Ti-sites) includes a significant absolute error, the conventional coverage determination from literature also results in an uncertainty of 0.16 ML.[374] The traces are set to the same baseline.

acetaldehyde[284,285] have been identified as the two reaction channels. Those products both desorb at the same temperature around 480 K.

Ethanol also desorbs in a high-temperature feature in this region, which could be attributed to the recombination of ethoxy species with hydrogen atoms from the dehydration and dehydrogenation reaction channels to form molecular ethanol again. The main peak, however, occurs around 270 K, which is assigned to ethanol desorbing from Ti-lattice sites.[374] From stoichiometry, molecular hydrogen should be formed upon dehydrogenation. However, molecular hydrogen is not observed. The hydrogen atoms lead to hydroxylation and consecutively to water formation on the surface, that is also the side-product of the dehydration from ethanol to ethylene. Successively, this is known to lead to a formal reduction of the surface[285] (see also Eq. 7.3 in the following), but upon annealing to temperatures higher than 500 K a "bulk-assisted reoxidation"[390] takes place so that the BBO-vacancy concentration remains constant, as H_2O-TPD titration reveals.

All traces of the carbon containing products are also evaluated for all coverages, but only exemplary ones for acetaldehyde and ethylene can be seen in Fig. 7.3. For both products, the high temperature feature was integrated for the determination of the molecule yield. Note, that the heavy noise, both in a) and b), around 290 K results from the cracking pattern correction and a noise accumulation. Previously, a minor low temperature ethy-

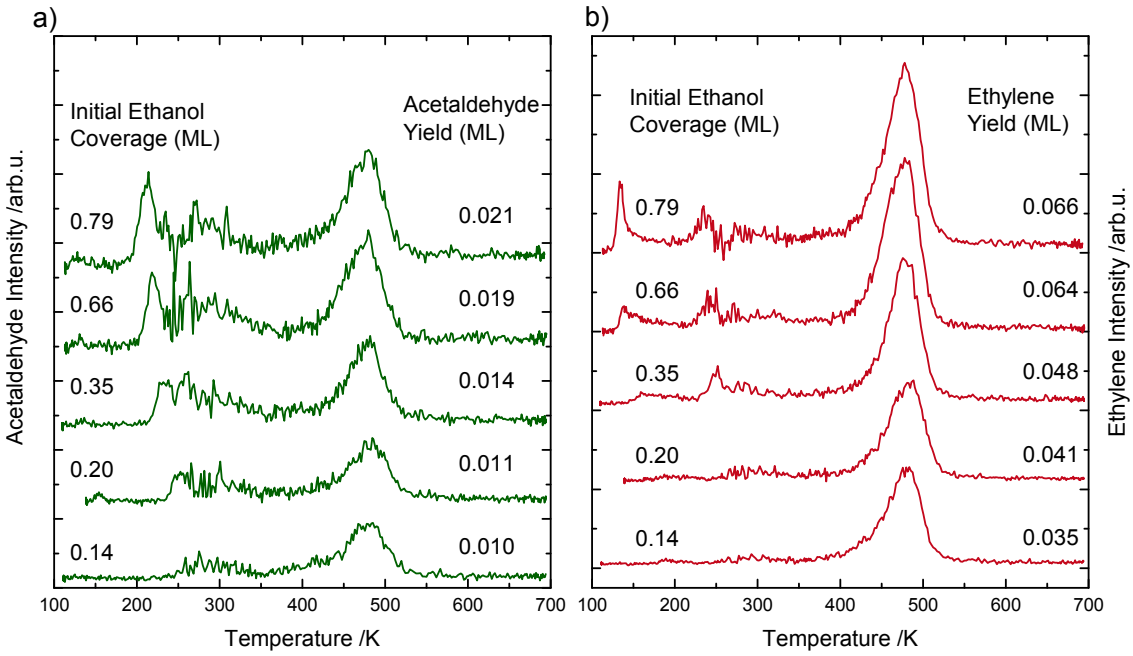

Figure 7.3. Acetaldehyde (a) and ethylene (b) yields from TPD experiments of ethanol on r-TiO_2(110). Both products are evolved around 450 K from ethoxy species strongly bound to the surface.[285] Both reaction channels saturate at an initial coverage of 0.66 ML, for acetaldehyde around 2% and for ethylene at about 6.5% of 1 ML, respectively.

lene peak has also been observed by Dohnalek and co-workers,[285] but at best only trace amounts are detected in this work. It may be speculated, that the reaction may occur on Ti-interstitial sites, which are highly dependent on the degree of bulk reduction of the

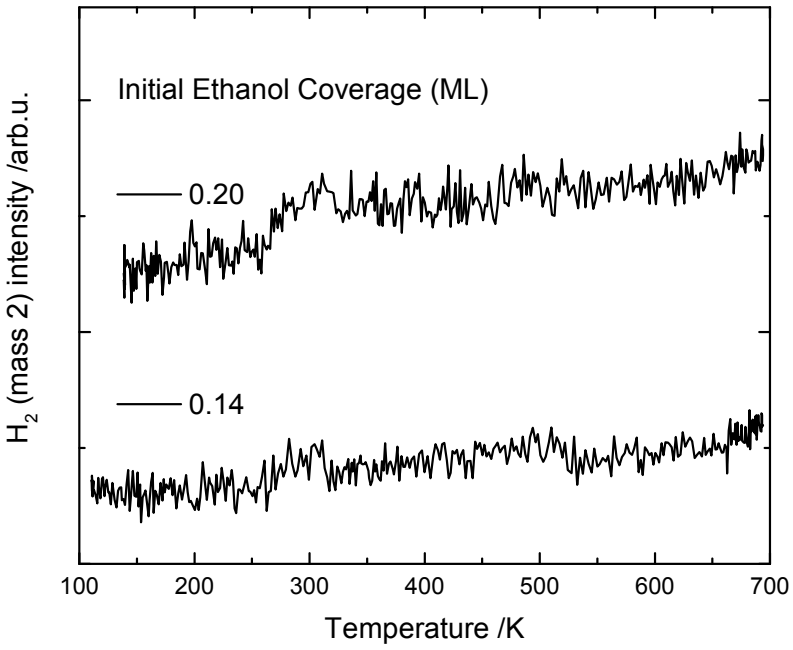

Figure 7.4. Hydrogen traces for two exemplary ethanol TPD experiments on the r-TiO_2(110) surface. No significant formation of molecular hydrogen is observed.

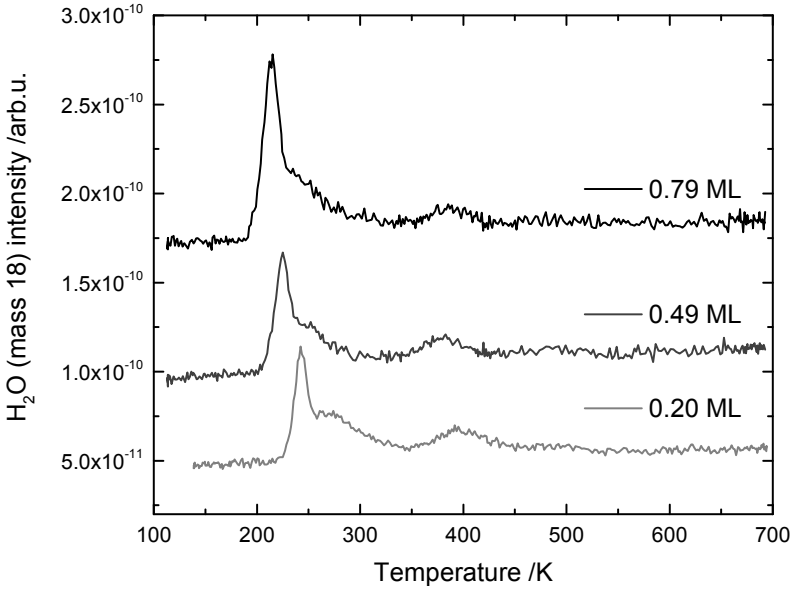

Figure 7.5. Water traces for three exemplary ethanol TPD experiments on the r-TiO_2(110) surface. The initial coverages of ethanol are given above the respective water trace. Two major signals are observed for all those ethanol TPDs, one saturated around 400 K and ohne around 240 K. In this setup, the thermocouple was mounted differently with regards to later studies, so the peaks appear around 40 K shifted with regard to the literature of the bare system.[374] Further, the co-existence of another alcohol is also known to shift the water desorption feature to lower temperature.[371]

single crystal and the preparation history.[391] However, for increasing initial coverages in Fig. 7.3(b) some small acetaldehyde signal can be detected around 240 K, but no meaningful assignment of the peak is possible, since the peak is strongly influenced by the cracking pattern analysis as well as an increase in the heating current in this temperature region. No hydrogen is evolved from both reaction channels, as shown in Fig. 7.4 which is in accordance with literature.[285,286] It is known for some oxides in general[282,392,393] and TiO_2(110) in particular[285], that if molecular hydrogen formation is not facile, the hydrogen atoms from reaction eventually form water.[1] The water signals (Fig. 7.5) show that in all the TPD experiments, water formation occurs and especially water desorbing from BBO-sites is obtained for all coverages. Since no "coking" is observed for aliphatic alcohols on TiO_2(110) in general and AES after 9 TPD runs indeed did not show carbon deposits (data not shown), the carbon mass balance can be closed. Therefore, the coverage dependent selectivity can be evaluated (Fig. 7.6) and shows that no further increase of reaction products after an initial coverage of 0.5 ML takes place. Adsorption of more ethanol only results in a higher ethanol desorption. The overall conversion with respect to 1 ML is 2% acetaldehyde and 7% of ethylene, which is in good agreement with the estimated defect concentration of 10%±2% by H_2O-TPD.

This study of ethanol reactivity on the r-TiO_2(110) shows that dehydration to ethylene is the major thermal reaction pathway for ethanol on r-TiO_2(110), while the dehydrogena-

[1] The exceptions (like ZnO(0001)[283]) prove the rule.

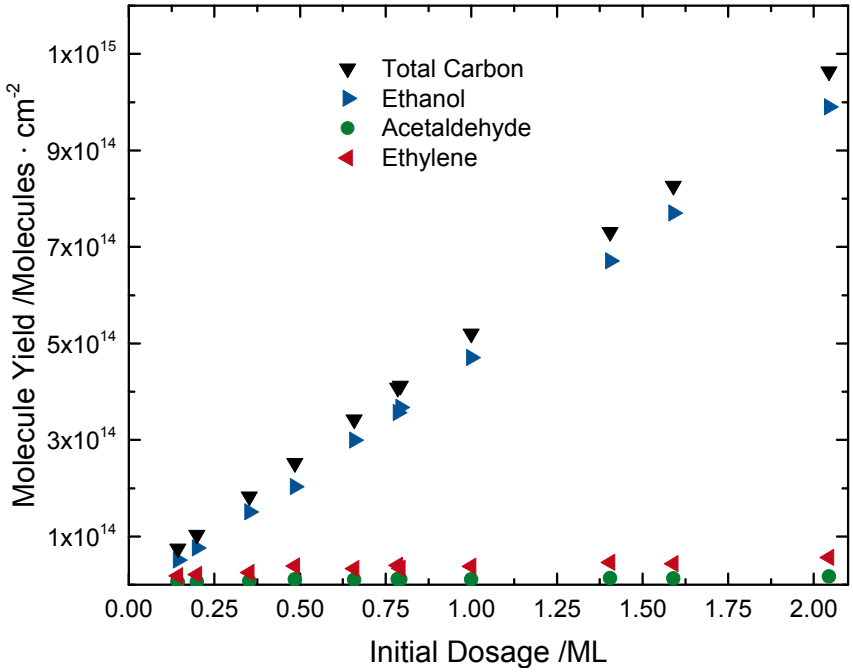

Figure 7.6. Integrated molecule yields from a TPD coverage series of ethanol on r-TiO_2(110). Molecule yields up to 2.1 ML are shown. After a coverage of 0.66 ML of initial ethanol dosage, no further increase in acetaldehyde and ethylene yields are obtained, indicating that the reactive sites are saturated at this coverage.

tion to acetaldehyde only contributes to 2% of the monolayer coverage. Both reaction channels are believed to occur in the same reaction site, the BBO-vacancy, which matches the overall conversion of 9% of 1 ML.

Ethanol adsorbs dissociatively on the BBO-vacancies[284,285] and to some extent also in regular Ti troughs.[308,394,395] However, based on the overall conversion in a TPD experiment, only the displayed reaction pathways are attributed to occur only in BBO-vacancies, while ethoxy from regular Ti-lattice sites desorbs recombinatively to form ethanol. The mechanism of the acetaldehyde formation is generally rationalized by the following reaction equations:

$$\underset{\text{ethanol}}{CH_3CH_2OH} + Ti_{vac} + O_{br} \longrightarrow \underset{\text{ethoxy}}{CH_3CH_2O{-}Ti_{vac}} + O_{br}H \tag{7.1}$$

$$\underset{\text{ethoxy}}{CH_3CH_2O{-}Ti_{vac}} + O_{surf}H \xrightarrow{\alpha\text{H-abstraction}} \underset{\text{acetaldehyde}}{CH_3CHO{-}Ti_{vac}} + O_{br}H_2 \tag{7.2}$$

$$\underset{\text{acetaldehyde}}{CH_3CHO{-}Ti_{vac}} + O_{br}H_2 \longrightarrow \underset{\text{acetaldehyde}}{CH_3CHO}\uparrow + H_2O\uparrow + Ti_{vac} \tag{7.3}$$

The major reaction pathway is the dehydration of ethanol, where previous studies showed, that the mechanism is likely to proceed via a βH-abstraction and a concerted scission of

the C-O bond in a cyclic transition state.[285,293] Both ethylene (Fig. 7.4) and water (Fig. 7.5) are formed and eventually desorb, restoring the initial surface configuration.

$$\underset{\text{ethoxy}}{CH_3CH_2O{-}Ti_{vac}} + O_{br}H \xrightarrow{\beta\text{H-abstraction}} \underset{\text{ethylene}}{C_2H_4}\uparrow + Ti_{vac}OH + O_{br}H \tag{7.4}$$

$$Ti_{vac}OH + O_{br}H \longrightarrow H_2O\uparrow + Ti_{vac} + O_{br} \tag{7.5}$$

In summary, the high temperature reaction channels have been studied quantitatively and a saturation of converted acetaldehyde and ethylene was obtained at the BBO-vacancy concentration. Both mechanisms are attributed to occur in the BBO-vacancy in agreement with previous studies[284,285], but the underlying effect that governs the selectivity remains still elusive.

7.2. The Mechanism of Ethanol Photo-Oxidation on TiO_2(110)

The results in this chapter have previously been published.[305] The detailed experimental conditions and illumination properties can be found in the respective paper.[305]
When a coverage of 1 L ethanol is irradiated with UV-light at 110 K, no desorption products are observed (data not shown). A PI-TPD is carried out and an additional peak around 220 K appears, that can be clearly assigned to acetaldehyde (Fig. 7.7(b)). A control experiment without UV-illumination is given in Fig. 7.7(a), which shows no significant acetaldehyde production after 5 min of waiting after the dosage and before the TPD experiment.

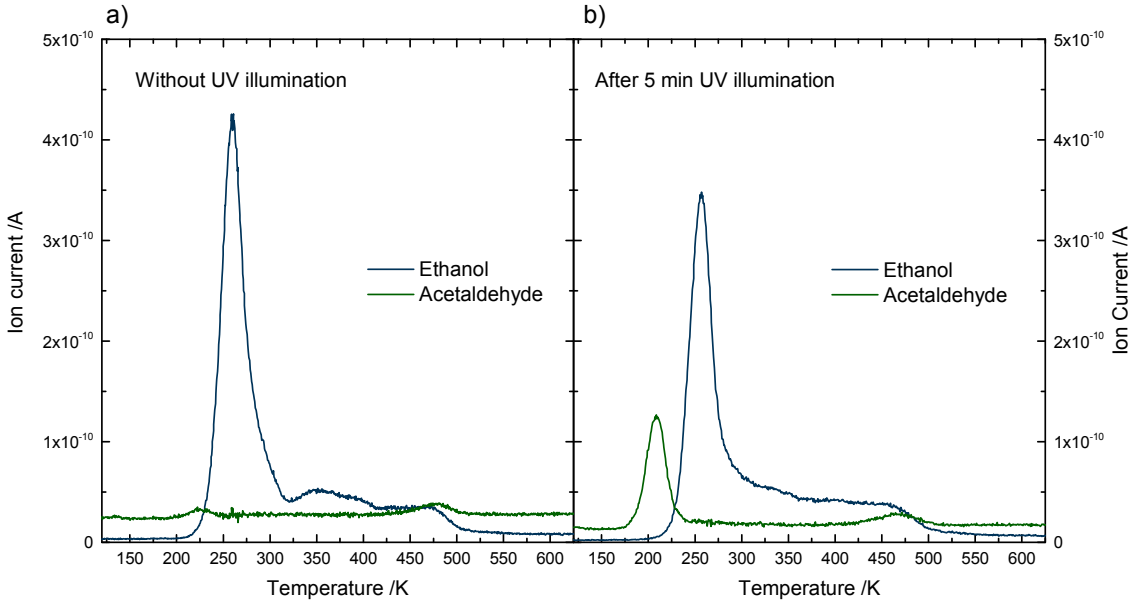

Figure 7.7. TPD experiments without UV illumination (a) and after 5 min of UV illumination (b) are displayed. The experiment in the left panel is carried out after a waiting time of 5 min, to exclude any background adsorption. It shows no significant difference to the immediate TPD result (Fig. 7.1). In (b), an additional peak around 220 K of acetaldehyde is observed, while the overall ethanol desorption yield is decreased.

When the adsorbed ethanol is illuminated at 110 K with UV light for 5 min, a new acetaldehyde feature appears around 210 K in a subsequent TPD run (Fig. 7.7b)). This desorption feature of the produced acetaldehyde is consistent with earlier photochemistry studies of ethanol[396,397] and with thermal desorption of acetaldehyde at high coverages.[398] However, molecular hydrogen formation is not observed during both TPD experiments. To elucidate, whether hydrogen can just simply not desorb at temperatures lower than the reaction temperature and therefore presumably leads to water formation, the illumination experiment is carried out at the acetaldehyde desorption temperature of around 220 K (Fig. 7.8). Upon illumination, an immediate rise in acetaldehyde is seen, followed by a multi-exponential decay. At the temperature of 222 K, neither ethanol desorption nor hydrogen evolution is observed. Only Idriss and co-workers observed very

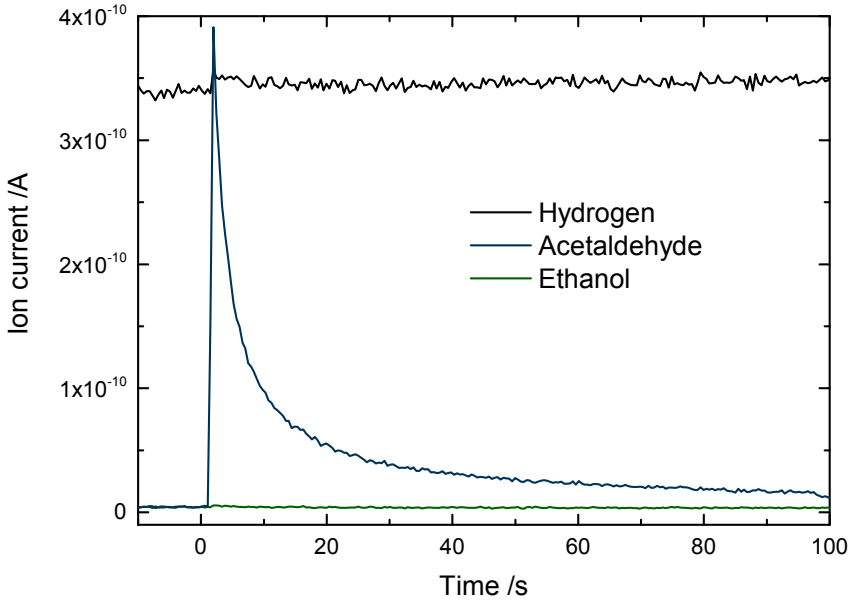

Figure 7.8. Isothermal UV illumination experiment carried out at 222 K. After the initial dosage of 1 L of ethanol is performed at 120 K, the crystal temperature is increased to 222 K. Upon illumination (start at 1 s) an immediate rise in acetaldehyde desorption is obtained, while significant changes in H_2 and ethanol desorption are not observed. Illumination is stopped after 98 s in this experiment.

small quantities of molecular hydrogen [395], but they carefully never assign the molecular H_2 signal to the photo-product acetaldehyde.

The conversion of acetaldehyde is investigated in the following by accumulating the photo-product at cryogenic temperatures and in PI-TPD experiments after different illumination times. The integral of the 220 K peak of acetaldehyde from Fig. 7.7 for various illumination times shows a saturation after 5 min of UV-illumination (Fig. 7.10(a)). Since hydrogen desorption is not observed, water is monitored as a by-product of the reaction (Fig. 7.9). While some water is also obtained in the blank experiment, a clear increase in the feature(s) above 300 K is obtained upon illumination. When this desorption above 300 K is integrated, a very similar trend to the saturation of acetaldehyde is found (Fig. 7.10(b)). The rise characteristics after only a few seconds, as well as the saturation value and behavior do match the acetaldehyde integrals perfectly, indicating a poisoning of the reaction by site-blocking. If illumination is stopped and started again in Fig. 7.8, the acetaldehyde intensity does only pick up at the level where the photo-reaction is terminated, similar to the behavior of the O_2-PSD shown earlier (Fig. 3.6). This indicates, that a poisoning of the photo-reactive site takes place although the photo-product can desorb. The poisoning is also observed, if ethanol is dosed again after the photoreaction (data not shown), indicating that site-blocking is not associated with the acetaldehyde only.

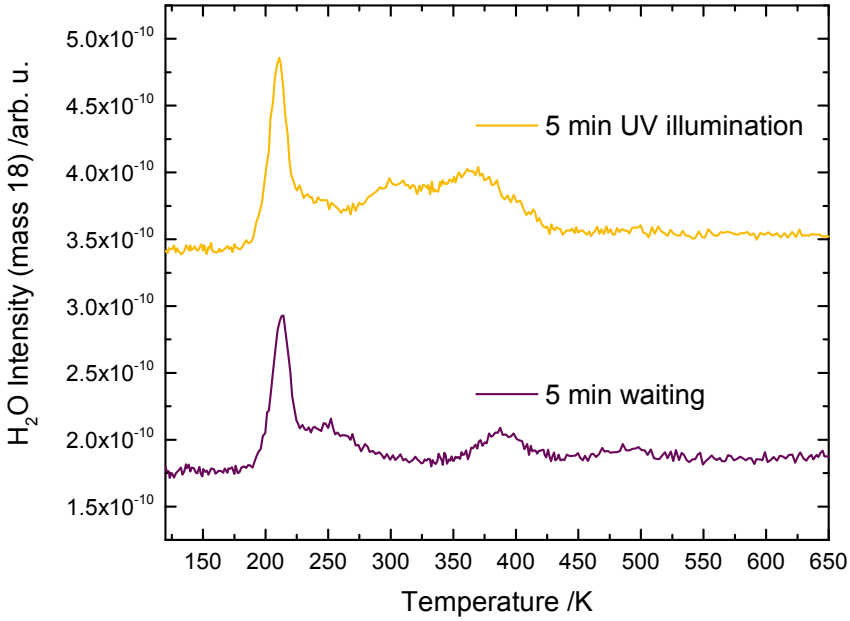

Figure 7.9. Water traces of the experiments (a) and (b) shown in Fig. 7.7. Water is observed both in the waiting and the PI-TPD experiment, presumably from background adsorption or co-dosage. While the peak around 220 K does not differ for both experiments, substantially more water is observed between 300 K and 450 K. The traces are offset for clarity.

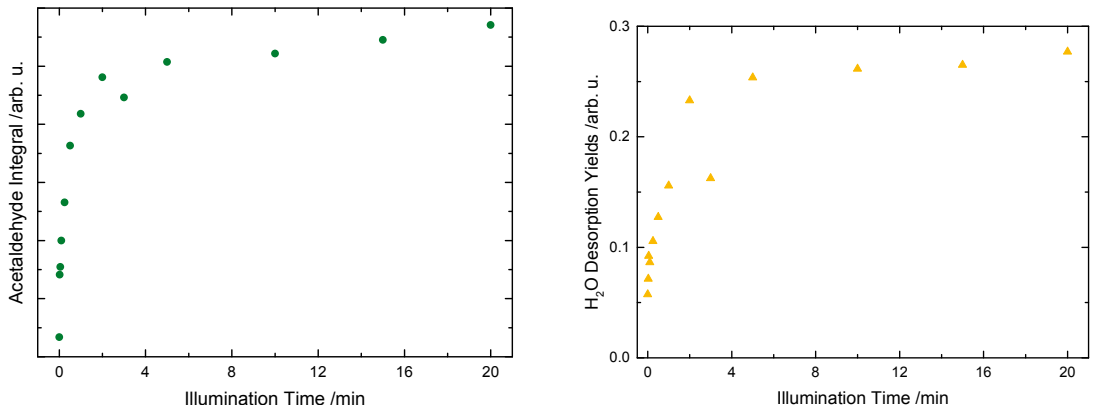

(a) Acetaldehyde integrals **(b)** Water integrals

Figure 7.10. (a) The integrals of the acetaldehyde signal around 220 K in PI-TPD experiment (Fig. 7.7(b)) after different illumination times at 110 K. Even after an illumination of 1 s, a substantial amount of acetaldehyde is produced and the signal saturates after an illumination time of approximately 5 min of UV-irradiation in cryogenic conditions.
(b) Integrals of the water signal between 300 K and 450 K from PI-TPD experiments (Fig. 7.7) after the different illumination times. Similar to the trend for acetaldehyde production on the r-TiO_2(110) (a), an immediate rise in the water desorption in that temperature windows is observed, which saturates after 5 min.

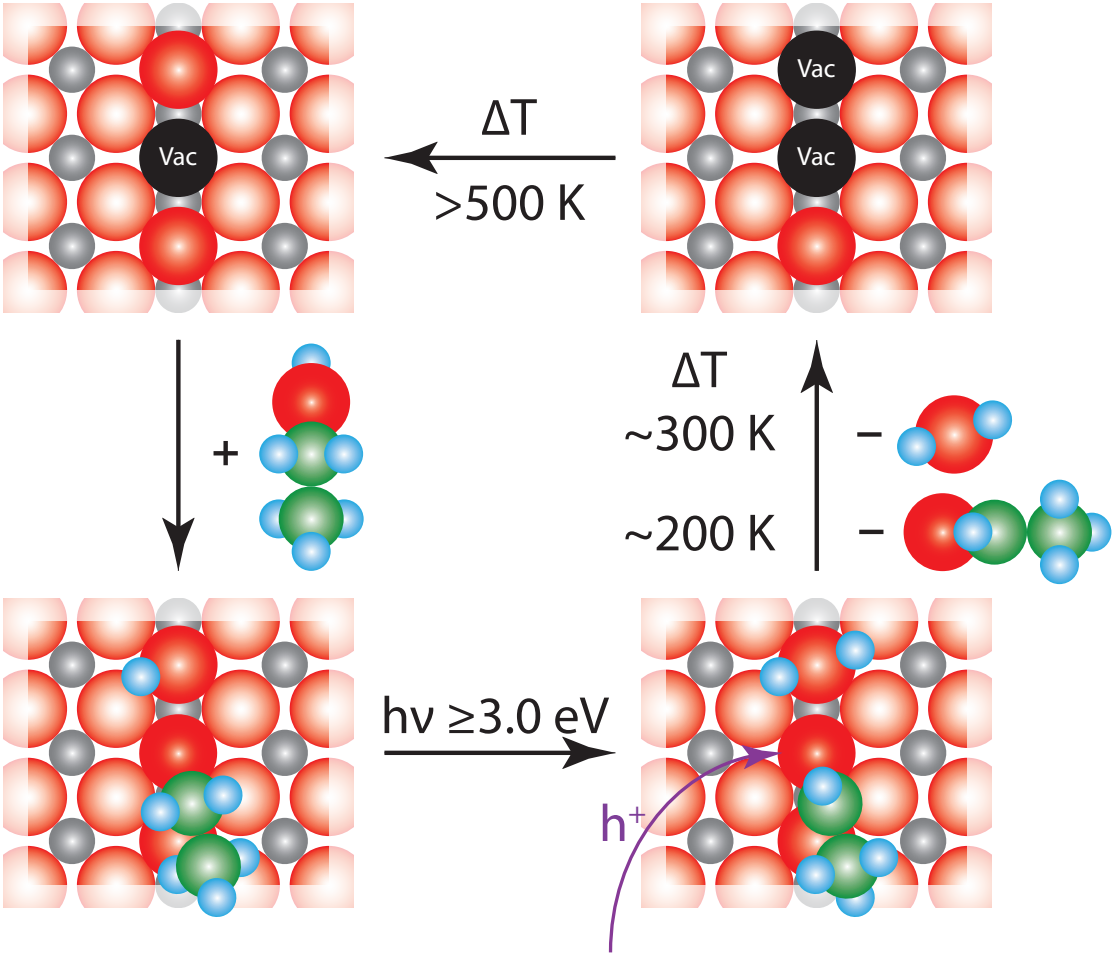

Figure 7.11. Scheme of the photochemical reaction mechanism of ethanol on the r-TiO_2(110) surface. The figure displays the relevant reaction steps starting from the top left. Ethanol adsorbs in a BBO-vacancy in a dissociative way, forming an ethoxy in the oxygen bridge and a hydroxyl. Under UV-illumination on the n-type semiconductor. photoholes travel to the surface and photo-oxidize the ethoxy species by α-H abstraction to form acetaldehyde bound to the defect. The abstracted H-atom forms another hydroxyl on the row, while the two hydroxyls are in an equilibrium with water formation.[205,306,399] When the temperature is high enough, the desorption barrier of acetaldehyde is overcome first and subsequently water also desorbs on a further increase in temperature, leaving formally two BBO-vacancies behind. Note, that these do not have to be neighboring, since hydroxyls easily can diffuse along the BBO row.[400,401] The doubling of the vacancy concentration after ethanol photo-oxidation was later confirmed by an STM study.[402] When heating the crystal to higher temperatures, the vacancy concentration equilibrates again by reducing the bulk of the single crystal.[390] The Ti-atoms are presented in grey, the oxygen ones in red, carbon in green and hydrogen in light blue. Note, that the BBO-vacancies are presented in black. Reproduced from[305] with permission from the PCCP Owner Societies.

From all these findings, a mechanistic picture (Fig. 7.11) can be drawn for the photo-oxidation of ethanol. Ethanol adsorbs dissociatively by forming an ethoxy and a bridging hydroxyl (Eq. 7.1). Upon UV irradiation in a n-type semiconductor, holes travel to the surface and electron move into the bulk due to the upward band bending.[98] The adsorbed ethoxy is photo-oxidized by the generated photohole by α-abstraction and another hydroxyl or a paired one respectively is created:

$$\underset{\text{ethoxy}}{CH_3CH_2O{-}Ti_{vac}} + OH_{br} \xrightarrow{h^+} \underset{\text{acetaldehyde}}{CH_3CHOTi_{vac}} + 2OH_{br} \tag{7.6}$$

The bound acetaldehyde desorbs from the BBO-vacancy leaving the initial adsorption site behind (Eq. 7.7). The two hydroxyls either exist separately or as a paired hydroxyl[101,306,401] and can thermally recombine above 300 K to form water (Eq. 7.8).[205]

$$\underset{\text{acetaldehyde}}{CH_3CHO{-}Ti_{vac}} \longrightarrow \underset{\text{acetaldehyde}}{CH_3CHO\uparrow} + Ti_{vac} \tag{7.7}$$

$$2OH_{br} \longrightarrow H_2O\uparrow + Ti_{vac} + O_{br} \tag{7.8}$$

The mechanism is not catalytic, since the water formation leads to a further reduction of the surface and the BBO-defect concentration is doubled, which was confirmed by the work from Wendt and co-workers later.[402] The vacancy concentration from TPD experiment to TPD experiment however remains quite constant, since the surface is reoxidized by the bulk.[390]

Most studies on the ethanol photo-oxidation on TiO_2(110) also investigate aerob conditions either by pre-oxidizing the crystal[402,403] or performing the illumination experiments in an oxygen atmosphere.[395,396,403] The pre-oxidation as well as the atmosphere complicates the assignment of sites on the surface significantly[2], as not all BBO-vacancies are filled by pre-oxidation[101,217,218,399] and O-adatom formation does not necessarily scale with the defect concentration, since it occurs also on regular Ti troughs.[101,218] A PI-TPD experiment after 1 min of UV-irradiation on an o-TiO_2(110) surface similar to Fig. 7.7b) is displayed in Fig. 7.12. Oxygen is generally thought to promote the photo-oxidation[395,396], so after 1 min of UV irradiation substantially more acetaldehyde is obtained than on the reduced surface, while the temperature of the desorption feature remains the same. A distinct difference is observed in the water desorption, since no peak above 300 K is obtained, but the intensity of the 220 K feature also includes water formed in the photoreaction and is, hence, increased. The high temperature features are similar to the thermal chemistry on the r-TiO_2(110) surface. The observation is in good agreement with all previous studies, since oxygen from the gas-phase or on the pre-oxidized surface generates O-adatoms. These are known to promote alkoxy-formation, as observed by Henderson and co-workers[371] and further studies revealed that alkoxy are the photoac-

[2] The effect of oxygen on the TiO_2(110) surface is discussed in Chapter 3.3.1.2

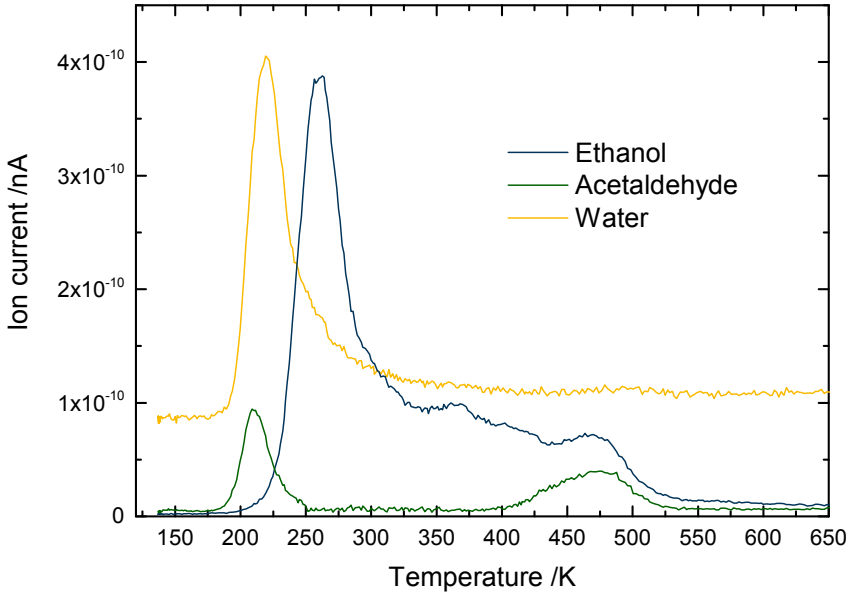

Figure 7.12. PI-TPD of ethanol on an o-TiO_2(110)-surface after 1 min of UV illumination at 120 K. Note, that the surface is prepared by cooling down the crystal after the annealing in an oxygen atmosphere to 300 K[404]. Similar to the reduced surface, an acetaldehyde peak is observed at 220 K. The water trace, however, is significantly different, since no feature is obtained at the temperature between 300 K and 450 K, indicating possibly a different reaction mechanism in comparison.

tive species.[116] By increasing the oxygen-background pressure, effectively the O-adatom concentration is increased, leading to an increased ethoxy formation.[32] Under the assumption, that all BBO vacancies are filled[3], the ethoxy photo-oxidation can also readily occur on Ti-lattice sites in agreement with previous reports.[397,402] The absence of the water peak above 300 K indicates, that the O adatoms are consumed by the water formation, since at this temperature water desorption from the Ti troughs is expected. Therefore, the photo-oxidation mechanism can be explained by the following set of reaction equations:

$$\underset{\text{ethanol}}{CH_3CH_2OH} + Ti_{lattice} + O_{ad} \longrightarrow \underset{\text{ethoxy}}{CH_3CH_2O{-}Ti_{lattice}} + O_{ad}H \tag{7.9}$$

$$\underset{\text{ethoxy}}{CH_3CH_2O{-}Ti_{lattice}} + O_{ad} + O_{ad}H \xrightarrow{h^+} \underset{\text{acetaldehyde}}{CH_3CHO{-}Ti_{lattice}} + 2O_{ad}H \tag{7.10}$$

$$\underset{\text{acetaldehyde}}{CH_3CHO{-}Ti_{lattice}} + 2O_{ad}H \longrightarrow \underset{\text{acetaldehyde}}{CH_3CHO}\uparrow + H_2O\uparrow + Ti_{lattice} + O_{ad} \tag{7.11}$$

This mechanism is also not catalytic on the o-TiO_2(110) surface, since an O adatom is consumed in the reaction scheme. In oxygen atmosphere, these are readily restored by dissociative oxygen adsorption.[218]

Interestingly, neither of the both presented mechanisms is catalytic on the surface. In both cases, this is attributed to the water formation from hydroxylation (Equations 7.8

[3] Although this assumption might be inaccurate, the enhancement of the acetaldehyde production in all studies suggest a parallel mechanism not involving the BBO vacancy as a binding site.[396,402]

and 7.11). However, the reaction can be driven catalytically in the oxidized mechanism, when molecular oxygen is a stoichiometric co-reactant and dissociates on the TiO_2(110) surface. The implications for catalysis will be discussed in Chapter 9.

8

Photocatalytic Selectivity Switch to C-C Scission: α-Methyl Ejection of tert-Butanol on TiO_2(110)

While a stoichiometric photochemical mechanism for alcohol oxidation via α-H elimination on r-TiO_2(110) is found in Chapter 7.2, the experiments with a tertiary alcohol were performed to examine the general validity of the mechanism. Contrary to what one might expect, the tertiary alcohol tert-butanol is not inert towards photo-oxidation, but readily ejects methyl radicals to form acetone. Most interestingly, also the regular thermal dehydration reaction pathway seems affected by the UV-irradiation, leading to an immediate desorption of the dehydration product isobutene below the expected thermal reaction temperature. This work has recently been published:[405] C.A. Walenta *et al.*, Phys. Chem. Chem. Phys., 2018 - Reproduced by permission of the PCCP Owner Societies.

Introduction

While photocatalysis is currently heavily studied in the context of energy production and storage, it is also an often used approach for the decomposition of organic pollutants.[79] In this regard, titania is one of the most often applied materials, as this substance offers a rich oxidation catalysis of organics. The underlying reaction pathways may also be exploited in other fields of chemistry as for example, biomass conversion to fuels or high-value chemicals. These chemical processes are still limited by a lack of selectivity and new reaction pathways are highly desired to be found.[406] In this regard, primary, secondary and tertiary alcohols are structural motives that are often found in the conversion of biomass. Furthermore, tert-butanol, which is studied in this work, is a common additive to fuels as a gasoline octane booster, although its effects on the environment are still under investigation.[407,408]. While titania exists in different modifications, rutile TiO_2(110) is by far the most researched surface.[79,102] While detailed mechanisms via α-H abstraction of alkoxy species are known for methanol[116,365], ethanol[305] and iso-propanol[409] on this surface, tertiary alcohols have hitherto been neglected in photocatalytic studies on single crystal surfaces. This may be because textbooks about organic chemistry usually state that tertiary alcohols are inert towards oxidation.[410] Nevertheless, attempts have been tried out to use platinum-loaded TiO_2 (P25) particles for the photochemical conversion

of tert-butanol.[411,412] It was shown that the alcohol can indeed be converted to a variety of products. However, the exact reaction pathways still remained elusive, which was also the case when this alcohol was added to steer the selectivity of the photooxidation towards aldehydes in a different study.[413]
The thermal chemistry of tert-butanol exhibits a dehydration pathway to isobutene via a concerted E2-elimination of water instead of an oxidation reaction.[293] Furthermore, Dohnalek and co-workers have only recently reported a new thermal reaction pathway of phenylmethanol to methylbenzene and benzylradicals, because the benzene ring stabilizes the radical species.[389] As in the case of tert-butanol an α-hydride elimination is disabled, similarly a direct deoxygenation occurs in the thermal reaction.[293] In this work, we study the photochemical reaction mechanism on the rutile reduced TiO_2(110) surface [r-TiO_2(110)] for tert-butanol. It is shown how thermal and photochemical reaction steps contribute to the selectivity of the overall reaction outcome.

Experimental

The experiments were carried out in an ultrahigh vacuum (UHV) apparatus equipped for photochemical measurements as described previously.[232,233] The cylindrical TiO_2(110) single crystal (Surface-net GmbH) is mounted on a 1 mm thick tantalum plate with tantalum clamps and a very thin gold foil to ensure good thermal conductivity. Crystal cleaning was accomplished by cycles of Ar^+-sputtering ($5.0 \cdot 10^{-6}$ mbar, 20 min, 100 K, 11.8 μA), annealing in oxygen ($1 \cdot 10^{-6}$ mbar, 820 K, 20 min) and vacuum annealing (820 K, 10 min) and no impurities were detected in the Auger electron spectra. The defect concentration of the reduced, blue crystal (denoted r-TiO_2(110)) was determined by H_2O temperature programmed desorption (TPD) to be about 6% $\pm$ 1%.[205] Thermal and photodesorption experiments were carried out in a line-of-sight geometry with respect to the quadrupol mass spectrometer (QMA 430, Pfeiffer Vacuum GmbH) with a distance of about 4 mm to the skimmer. UV illumination of the sample was accomplished by a frequency doubled OPO laser (GWU, premiScan ULD/400) that is pumped by the third harmonic of a Nd:YAG-Laser (Innolas Spitlight HighPower 1200, 7 ns pulse width, 20 Hz repetition rate). The as-generated light pulses (700 μJ per pulse, 242 nm) illuminate the sample entirely. Laser-induced thermal heating effects were not observed and tert-butanol did not show any absorption in the UV-vis spectra in the spectral region of the illumination. Tert-butanol (2-methyl-2-propanol, Sigma-Aldrich, $\geqslant$ 99.5%) and tert-butanol-OD (2-methyl-2-propan(ol-d), Sigma Aldrich, 99 atom % D) were cleaned by pump-thaw cycles and dosed via background dosing. The coverages are referenced to the number of Ti^{4+}-sites, for which a monolayer is normalized to the H_2O desorption yield from all Ti-sites (1 ML $\equiv 5.2 \cdot 10^{14}$ sites/cm^{-2}). Further experimental details including product identification, cracking pattern correction and ionization sensitivities are given in the supporting information.

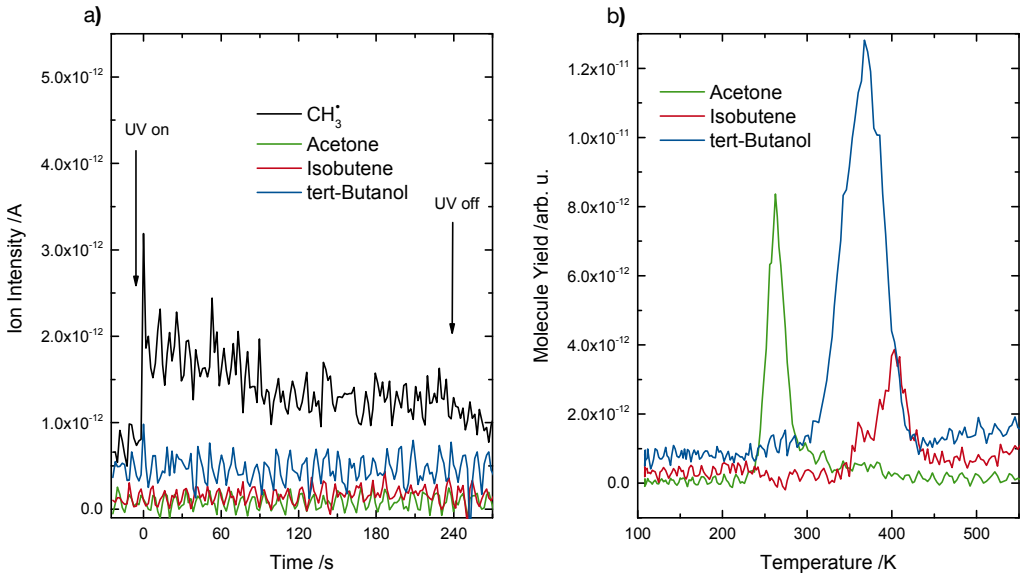

Figure 8.1. a) Isothermal photodesorption yield vs time for 0.18 ML tert-butanol-OD at 100 K on a r-TiO_2(110) surface. When the sample is irradiated with UV light, a CH_3-radical is ejected from the tert-butanol, but further molecules neither from thermal- nor photochemical-reactions do not desorb. In the right panel (b), a post-irradiation TPD experiment is shown after 20 min of UV illumination. The photo product acetone is observed around 270 K as well as the thermal dehydration product isobutene and unreacted tert-butanol. Adapted from[405] - Reproduced by permission of the PCCP Owner Societies.

Results and Discussion

While the photochemical reaction behavior of tertiary alcohols has so far not been investigated on single crystalline surfaces, the thermal reaction pathway of tert-butanol is already quite well understood. In good agreement with the literature[293,374], it is found that tert-butanol reacts via dehydration to isobutene, which occurs at around 425 K. In experiments with the deuterated tert-butanol-OD, HDO is identified as a by-product at the reaction temperature of 425 K (Fig. 8.6). The coverage dependent molecule yields (Fig. 8.8) show that the thermal reactivity levels off after the coverage of all Ti-sites on the surface.[293] When the n-type semiconductor r-TiO_2(110)-surface, which has been previously covered with 0.18 ML of tert-butanol, is illuminated with UV light, photon-generated holes reach the surface and methyl-radical ejection is observed at 100 K (Fig. 8.1a). While a similar photochemical methyl-ejection from organic compounds has been observed previously for ketones[108,255–257,414,415] and acetaldehyde[416] on oxidized TiO_2(110) [o-TiO_2(110)] or in an oxygen atmosphere[396], this pathway has so far not been identified for the reaction of alcohols. This signal is indeed a methyl-radical as verified by a comparison of the masses 15 and 16 (Fig. 8.9).

As for tertiary alcohols the usual photochemical reaction pathway[106,116,305,365] via the abstraction of an α-H is intrinsically excluded, the reaction with photoholes instead initiates the cleavage of a C-C bond. More detailed insights into the reaction pathways are

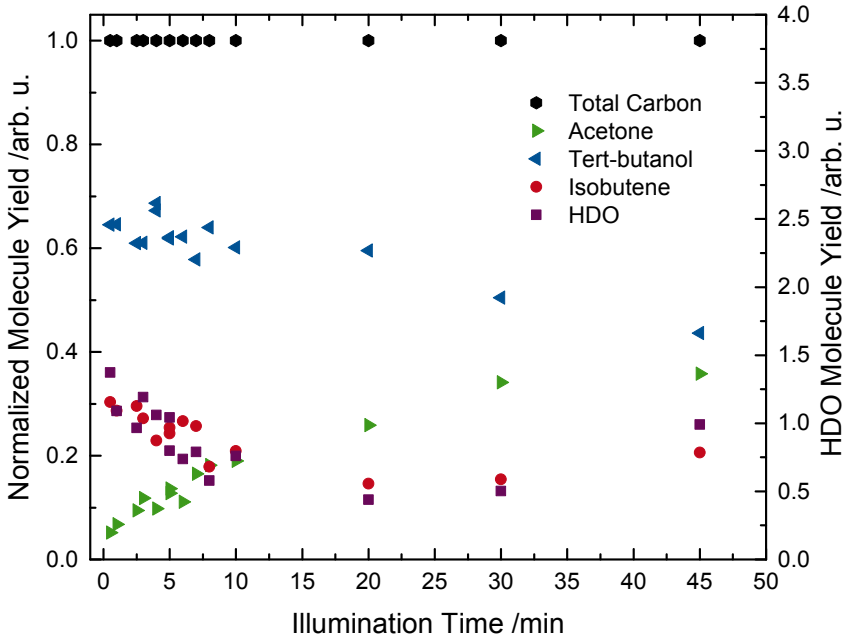

Figure 8.2. Normalized integrated molecule yields vs illumination time. Each of the data points represents the integrated molecule yields from a consecutive post-irradiation TPD run. Prior to this illumination, the r-TiO_2(110) surface is exposed to 0.18 ML tert-butanol-OD at 100 K. The carbon balance is closed, because coking is not observed in the experiments. With increasing UV illumination time, the photochemical yield of acetone increases, while both the isobutene and t-butanol yields are extenuated. After 30 min, the photoreaction saturates. Note, that the HDO yields are not scaled to the carbon mass balance. Due to isotopic exchange of water with alcohol groups[250], one refrains from a quantitative relation. However, the trend of the 425 K water feature shows a scaling with the isobutene yield. Adapted from[405] - Reproduced by permission of the PCCP Owner Societies.

obtained by subsequent post-irradiation TPD experiments (see Fig. 8.1b for 20 min illumination). These experiments reveal the formation of three different species: Acetone is identified as the resulting product from the photocatalytic methyl radical ejection. In addition, unreacted tert-butanol and isobutene, which is also generated in the thermal reaction (Fig. 8.6), are detected. Auger electron spectroscopy after the TPD experiments (data not shown) indicates that neither the alcohols nor the ketones result in a coking of the TiO_2(110) surface and, consequently, the carbon balance can be closed.

While other reaction products are not observed, their ratio of acetone/isobutene/tert-butanol significantly changes over illumination times at 100 K (Fig. 8.2). With an increasing illumination duration, the acetone production increases, while both the tert-butanol and the isobutene yields diminish. Finally, the acetone production saturates after about 30 min, yielding 36% for an initial tert-butanol coverage of 0.18 ML.

This amounts to a conversion of 0.065 ML of tert-butanol. Alkoxy species have previously been found to be the photoactive species.[116,365,417,418] While the actual active site for photooxidation still remains under discussion, we follow the interpretation of Henderson, who reports that methoxy formation occurs either on defects, co-adsorbed oxy-

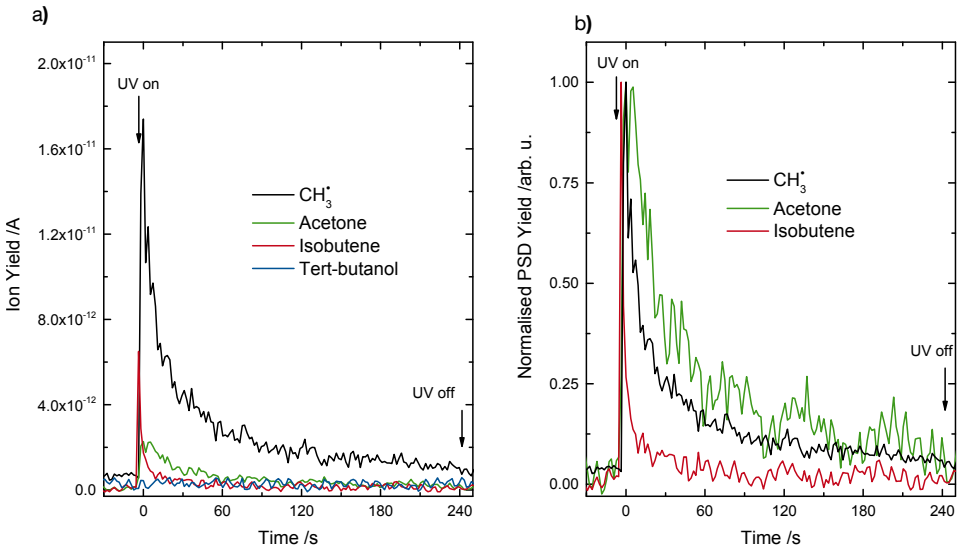

Figure 8.3. a) Isothermal photodesorption yield vs time for 0.18 ML of tert-butanol-OD at 293 K on a r-TiO_2(110) surface. When the sample is irradiated with UV light, CH_3-radical ejection is observed similar to the experiment at cryogenic conditions. Furthermore, the photoreaction product acetone also desorbs under illumination at this temperature. In addition, isobutene formation and desorption is observed at 293 K. In panel b), the normalized PSD yields from the same experiment as in a) are shown for a qualitative comparison of decay rates. All decay-rates follow a multi-exponential behavior. The acetone signal shows a small delay with respect to the methyl-radical ejection and then a slightly slower decay, which is attributed to a thermal desorption behavior after the photoreaction to acetone. The isobutene decay is faster then the methyl-ejection, which may be attributed to a photochemical desorption as observed in literature.[133] Adapted from[405] - Reproduced by permission of the PCCP Owner Societies.

gen adatoms or terminal OH groups.[417] As on the r-TiO_2(110)-surface, only defects occur in significant amounts, we assign the tert-butoxy formation to occur predominantly in bridge-bonding oxygen (BBO) defects, as attributed by the saturation value, which is in excellent agreement with the concentration of BBO-vacancies of 0.06 $\pm$ 0.01 ML on the r-TiO_2(110)-surface as determined by water-TPD.[205] Furthermore, STM images of 2-butanol reveal the butoxy formation only occurs in the defect.[419]

Interestingly, in the present work and the previously mentioned studies, some thermal dehydration-reactivity of the alcohol is still observed in the TPD after the photoproduct-accumulation experiment at cryogenic temperatures. As the thermal reaction has been attributed by Dohnalek and co-workers to also take place in the BBO-vacancies, these alkenes stem either from diffusion of the alcohol into the cleared BBO-vacancies during the TPD experiments. The thermal reaction pathway is not expected to be strongly affected by the photoreaction. This is also supported by the behavior of the isobutene signal for different illumination times (Fig. 8.2), for which a drop from about 30% to only somewhat below 20% is observed.

In a subsequent experiment, the photoreaction was investigated at 293 K (Fig. 8.3a). This particular temperature was chosen, as on the one hand significant desorption of tert-

butanol is not expected to occur. On the other hand, desorption of acetone shall be enabled according to the post-irradiation TPD experiments (Fig. 8.1b) and the desorption behavior reported in the literature.[409,420] Similar as in Figure 8.1, methyl radical ejection is observed from tert-butanol, while the desorption of tert-butanol is indeed completely suppressed. In addition, some acetone desorption is observed, although with significantly lower intensity during the beginning of the illumination. Unexpectedly, desorption of isobutene is also observed under UV illumination. While it has been shown that this molecule can even be photodesorbed below 100 K on the r-TiO_2(110) surface[133], it is detected at least 50 K below its first desorption feature in the tert-butanol TPD experiment (Fig. 8.6). When the resulting decay curves are normalized to their maximum value (Fig. 8.3b), the kinetics of the different processes can readily be compared with each other. All desorption traces show multi-exponential decay kinetics, which is generally found for photochemical processes on TiO_2 indicating complex reaction pathways.[96,131]
However, the individual decay curves are significantly different from each other, which is depending on respective desorbing species: While isobutene clearly exhibits the fastest reaction kinetics, the ejection of methyl is somewhat faster than the acetone formation and desorption. This behavior indicates that different mechanisms play a role, which are a combination of thermal and photochemical processes. The photochemistry at 100 K and 293 K as well as the thermal reactivity enable detailed insights into the different reaction mechanisms: The methyl radical ejection observed in all isothermal UV-illumination experiments is clearly a photon-induced reaction. However, this reaction is less efficient at 100 K than at 293 K, which demonstrates that at least one reaction step, only accessible by thermal chemistry, is of importance. To study the temperature dependency further, PSD experiments of 0.18 ML tert-butanol are carried out at several temperatures between 239 K and 330 K (Fig. 8.10). The analysis of this data shows (Figure 8.4), that at 239 K about equal amounts of isobutene and acetone are formed. An increase in the temperature of the photoreaction is enhancing the formation of both products. However, while for isobutene only a modest increase in the yield is detected, the signal of acetone strongly rises. We attribute this observation to originate from the superposition of two different effects, which are an enhanced thermal desorption of acetone and the diffusion of tert-butanol to the photoactive site. The changes in product yields are further reflected in the selectivity of the photoreaction (Figure 8.4b). While at low temperatures about 50% selectivity toward acetone is found, this value increases to over 80% at room temperature and above.
The absence of distinct low-energy structure as the η^2(C,O)-enolate for aldehydes and ketones[255,256,396] suggest that the transfer of the hole immediately leads to the abstraction of a methyl group regardless of the exact adsorption geometry in the defect. While this process rules out temperature-induced geometric transformations, diffusion of the alcohol molecules into the defects plays an important role for the reactivity. This is supported by STM studies, which show that alcohol molecules are also bound on TiO_2 rows even when BBO vacancies are still accessible.[419,421] Furthermore, the accompanied produc-

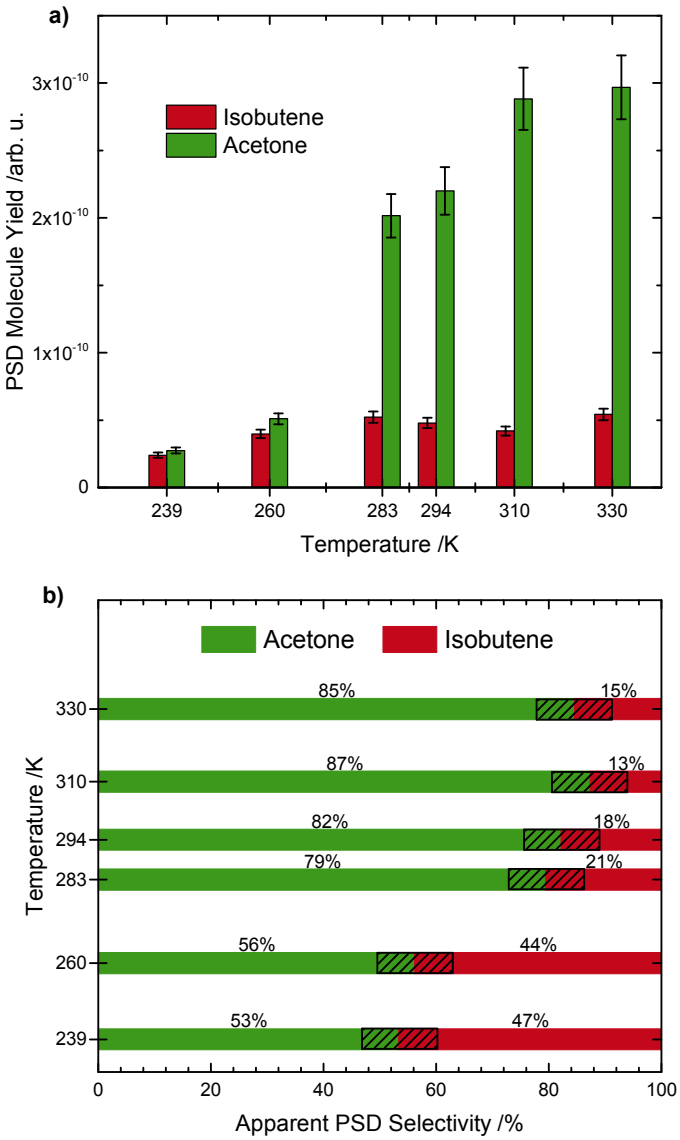

Figure 8.4. Figure a) resembles the integrated molecule yields of the first 100 s including all correction factors (see supplementary data) for the different PSD yields from Figure 8.10. For higher temperatures, the overall reaction yield is increased. In Figure b), the selectivities based on the integral yields are displayed. For higher temperatures, an enhanced apparent PSD selectivity towards acetone is obtained. Adapted from [405] - Reproduced by permission of the PCCP Owner Societies.

tion of acetone (eq. 8.2) is also found to be slow at 100 K and the yield only saturates after 30 min of illumination.

$$\underset{\text{tert-butanol}}{(CH_3)_3COH} + Vac_{BBO} + O_{BBO} \longrightarrow (CH_3)_3CO{-}Vac_{BBO} + OH_{BBO} \tag{8.1}$$

$$(CH_3)_3CO{-}Vac_{BBO} + OH_{BBO} \xrightarrow{h\nu} \underset{\text{acetone}}{C_3H_6O} + CH_3^{\cdot}\uparrow + Vac_{BBO} + OH_{BBO} \tag{8.2}$$

On the other hand, the resulting increase in methyl ejection at 293 K is not only increased due to a higher diffusion rate of the alcohol molecules into defects that remained empty, but also by a clearance of the defect by the thermal desorption of acetone. This subsequent desorption step of the ketone is also reflected by a slower decay of the acetone signal with respect to the methyl one, as for the latter this thermal reaction step does not occur.

In comparison with the products originating from methyl ejection, the desorption of isobutene is a very fast process, which is clearly evidenced by the rapid decay in the signal (Fig. 8.3b). While a very fast photodesorption behavior on the n-type semiconductor may be attributed to a photohole induced charge redistribution on the surface, the reaction is obviously temperature-dependent, as the formation of this molecule does not occur at 100 K. This temperature-dependence suggests, that a barrier to an activated transition state for the H_2O-elimination of tert-butanol exists, which can already be overcome at lower temperatures than the complete thermal reaction to isobutene. UV illumination seems to propel the consecutive chemical reaction steps and, as the desorption is not thermally hindered, the fastest kinetics of all observed products results. In the thermal reaction pathway the production of isobutene by water-elimination has previously been attributed to be an E2-type reaction via a 5-membered cyclic structure involving the BBO-vacancy.[293] Thus, it seems reasonable that this transition state is only formed after a certain temperature, while the formal abstraction of water is eventually done by the photoreaction (eq 8.5).

$$\underset{\text{tert-butanol}}{(CH_3)_3COH} + Vac_{BBO} + O_{BBO} \longrightarrow (CH_3)_3CO{-}Vac_{BBO} + OH_{BBO} \tag{8.3}$$

$$(CH_3)_3CO{-}Vac_{BBO} + OH_{BBO} \xrightarrow{\Delta T} \underset{\text{isobutene}}{C_4H_8} + H_2O + Vac_{BBO} + O_{BBO} \tag{8.4}$$

$$(CH_3)_3CO{-}Vac_{BBO} + OH_{BBO} \xrightarrow{h\nu} \underset{\text{isobutene}}{C_4H_8} \uparrow + H_2O + Vac_{BBO} + O_{BBO} \tag{8.5}$$

Both reactions, the formation of acetone by methyl ejection and the production of isobutene by dehydration, comprise thermal as well as photochemical steps, which are summarized in Figure 8.5.

The water-free conditions also demonstrate, that such photoreactions do not necessarily need to occur via the generation of OH-radical and a subsequent oxidation of the alcohol. Instead, a direct hole transfer to the organic molecule is observed. This mechanism may also work under aqueous conditions, as long as defects are not blocked or oxygen ad-atoms exist on the semiconductor. In addition, our findings also explain perfectly the detected products from a previous study concerning the photooxidation of tert-butanol on co-catalyst loaded TiO_2 (Degussa P25) in a reactor at 373 K.[411,412] In line with our observations, acetone was also identified as the main reaction product from the photoreaction, while isobutene was the sole thermal decomposition product. Based on our study, we related these properties to originate from the peculiar chemistry of TiO_2.

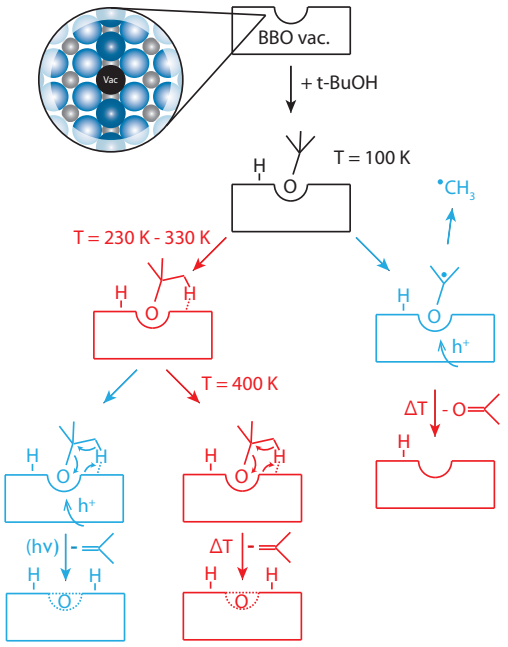

Figure 8.5. Photochemical (blue) and thermal (red) reaction pathways of tert-butanol on the r-TiO_2(110) surface. When the photo-holes react at cryogenic conditions with tert-butanol, methyl ejection is observed. Consecutively, a thermal desorption of acetone is observed. When the photo-reaction is initiated at room temperature, thermally formed isobutene is observed at lower temperatures than expected from the reaction temperature. The isobutene is either photo-desorbed in the illumination case or thermally desorbed. Reproduced from [405] - Reproduced by permission of the PCCP Owner Societies.

Conclusions

In summary, we have shown that the photooxidation for alcohols without an α-H moiety opens up new mechanistic pathways such as the splitting of C-C-bonds. In general, all photochemical processes observed can be associated with BBO-vacancies sites. Similar to ketones, the photooxidation of tertiary alcohols (i.e. tert-butanol) is attributed to be initiated by photoholes, which travel to the alcohol species to enable the ejection of a methyl radical. As the photochemical product evolution saturates at an amount, which can directly be related to the defect concentration, it is evidenced that the reaction occurs directly at the BBO-vacancy site. Increased reaction kinetics for the methyl ejection at higher temperatures suggest that diffusion and the clearance of defects play an important role in the reaction rate. While at 100 K only the reaction pathway to the formation of acetone occurs, an additional one is open for the illumination at 293 K. At this temperature, irradiation facilitates the formation of isobutene originating from a dehydration of the alcohol. However, the desorption of isobutene is observed at surprisingly low temperatures, as the thermal desorption is generally believed to take place immediately after the isobutene formation. [133,293] The temperature-dependent behavior of this reaction can be attributed to a cyclic transition state involving the BBO-vacancy [293], and a redistribution of charges upon illumination, which may facilitate the reaction and product desorption.

For all reaction channels, it is evident that both, thermal as well as photochemical effects are important for the yield of a particular product. Furthermore, it is demonstrated that even a seemingly simple system such as rutile and a tertiary alcohol offers a rich chemistry with two different reaction pathways, dehydrogenation and dehydration, which can be tuned by the judicious choice of the proper reaction parameters.

Supplementary Data

During the thermal and photo-desorption experiments, the potential products were monitored with several masses: Isobutene with masses 56, 41 and 39; acetone with 58 and 43, tert-butanol-OD with 59, 31 and 32. The methyl-radical was detected during the experiments on mass 15. Further molecules and corresponding masses including H_2 (2), HD (3), CH_4 (16), H_2O (18), HDO (19), CO (28), CO_2 (44) were recorded, but found to be insignificant with the exception of water (see Fig. 8.6). To quantify the results, the coverages of tert-butanol normalized to the H_2O-TPD of a monolayer according to the convention in literature.[374] The tert-butanol-OD was quantified using masses 31 and 32, because some isotope exchange could not be avoided in the gas line and on the single crystal. Isobutene and acetone were quantified using masses 56 and 58 as well as by considering the fragmentation of tert-butanol and the respective other molecules. For the

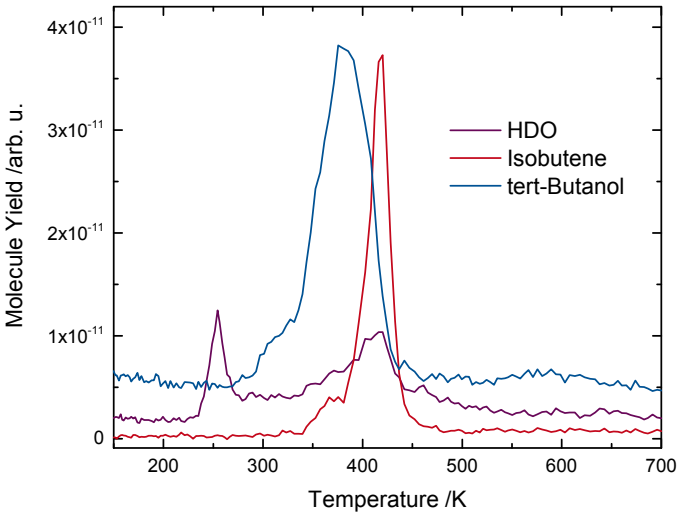

Figure 8.6. TPD of 0.45 ML tert-butanol-OD on r-TiO_2(110). Tert-butanol desorbs from the lattice sites, while a dehydration pathway to isobutene is observed around 425 K, which is in agreement with previous studies.[285,293] Additionally, the HDO (m/z = 19) was also monitored and two peaks occur: One is attributed to the direct dehydration pathway of tert-butanol-OD at 425 K, for which HDO is the by-product. In addition, another peak is observed around 250 K, which is attributed to the desorption from BBO-sites. I arises from water adsorption from the background and some dissociative adsorption, since some exchange to background adsorption from water is obtained. Adapted from[405] - Reproduced by permission of the PCCP Owner Societies.

quantification, all molecule yields were corrected for their fragmentation pattern, their transmission through the QMS and their ionization cross sections.[422–424]

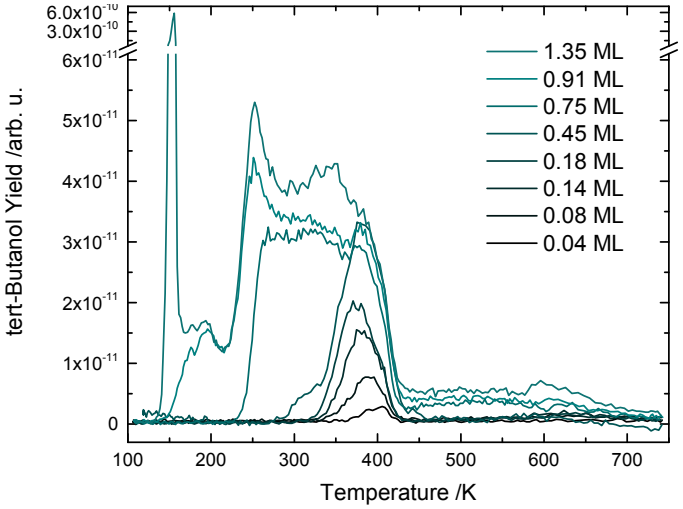

Figure 8.7. Coverage-dependent TPD series of tert-butanol-OD on r-TiO_2(110). At small coverages, a desorption feature at around 400 K arises, that is attributed to tert-butanol binding to Ti-lattice sites. With higher coverages, this feature saturates and a shoulder is growing to a peak at 250 K, which is assigned to the desorption from BBO surface atoms. Another feature appearing below 200 K is attributed to multilayer desorption. The coverages are referenced to the coverage determination of Dohnalek and co-workers and in very good agreement with their work.[374]

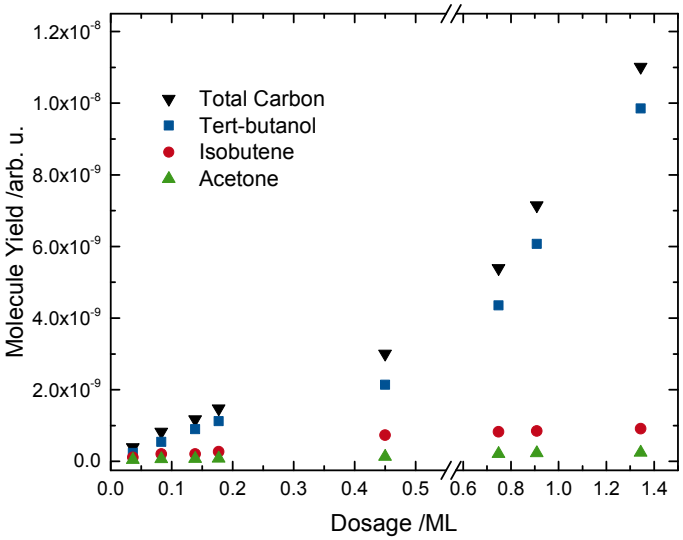

Figure 8.8. Integrated amounts of tert-butanol-OD and isobutene for different coverages. While tert-butanol is shown in blue squares, the amount of isobutene is given in red circles. Although not present from thermal TPD, the acetone baseline is shown in green triangles. Auger electron spectroscopy and previous studies[374] indicate, that there are no carbon deposits for all aliphatic alcohols on r-TiO_2(110). Hence, the carbon mass balance can be closed, which is addressed by black triangles showing the total carbon dosage by addition of the carbon containing desorbing molecules. Note, that the dosage axis is broken, to display more data points. Adapted from[405] - Reproduced by permission of the PCCP Owner Societies.

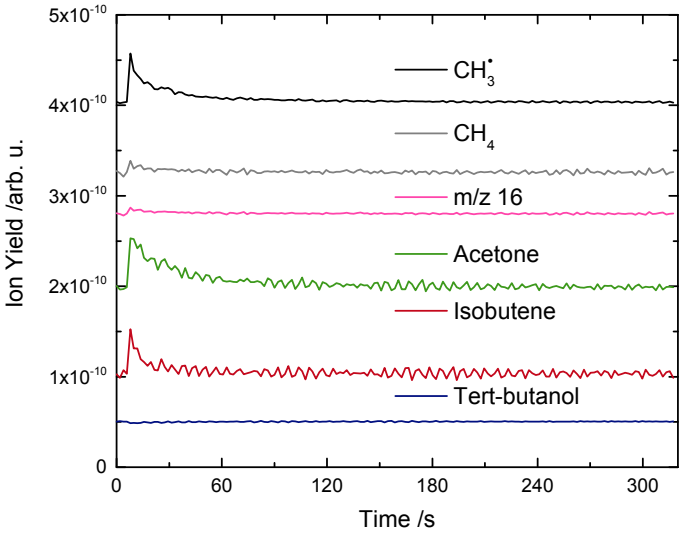

Figure 8.9. Isothermal photodesorption yield vs time for 0.18 ML of tert-butanol at 295 K on the r-TiO_2(110) surface. Note, that for the explicitly stated molecules the cracking pattern contributions and ionization sensitivities are accounted for. The traces are offset for clarity. The signal of m/z = 15 is more than 8 times as much as for m/z = 16. This clearly indicates, that a methyl radical is ejected during the photoreaction, while only traces amounts of methane are observed. The pink trace represents the raw data for mass 16. The different signal to noise ratios in this data set stem from the scaling by the above mentioned correction factors from cracking pattern and ionization coefficients. Adapted from [405] - Reproduced by permission of the PCCP Owner Societies.

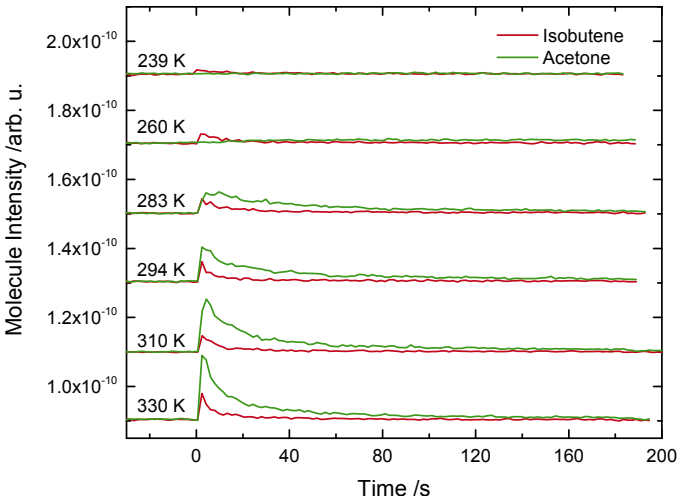

Figure 8.10. Isothermal photodesorption yield vs time for 0.18 ML of tert-butanol at different temperatures on the r-TiO_2(110) surface. The UV illumination is started at 0 s and ended after 180 s. For all temperatures, some desorption of both isobutene and acetone is observed, while no tert-butanol desorbs upon irradiation. By increasing the temperature, both the overall apparent desorption and the selectivity towards acetone are increased. The traces are offset for clarity. Reproduced from [405] - Reproduced by permission of the PCCP Owner Societies.

"When all think alike, then no one is thinking."

The Stakes of Diplomacy - Walter Lippmann

9

The Mechanism of H_2 Evolution from Methanol on $Pt_x/TiO_2(110)$

Abstract

As the conduction band edge of rutile TiO_2 is close to the reduction potential of hydrogen, there is a long-lasting discussion, whether molecular hydrogen can be evolved from this semiconductor. Our study on methanol photoreforming in the ultra-high vacuum reveals that photocatalysts comprising a $TiO_2(110)$ single crystal decorated with platinum clusters indeed enable the evolution of H_2. This is attributed to a new type of mechanism, in which the co-catalyst acts as a recombination center for hydrogen and not as a reduction site of a photoreaction. This mechanism is an alternative pathway to the commonly used photoelectrochemical type mechanism, and must particularly be considered for systems, in which the reducible semiconductors enable the surface diffusion of hydrogen species.

Introduction

Hydrogen generated from renewable feedstocks is envisioned to act as a potential fuel for clean transportation.[22,425,426] In the last decade research focusing on increasing the efficiency of hydrogen production has tremendously been intensified by following both conventional and novel approaches.[427–429] Photocatalytic water splitting facilitated by co-catalyst loaded semiconductor particles is one promising way for clean hydrogen production. Recently, such systems have been reported to exceed efficiencies of over 1% in a scalable solar-to-hydrogen production.[430] Surprisingly, detailed mechanistic insights are still scarce despite of the intense research efforts undertaken in the past. Such knowledge, however, may be vital for the development of devices, which economically outperform electrolyzers driven by a solar cell. So far, there is general agreement that two different effects contribute to the hydrogen evolution rate, the charge carrier dynamics

and the chemical reactions. For the latter, both partial reactions are usually treated somewhat independently from each other, following the concepts of photoelectrocatalysis. For most of the systems it is believed that the oxidation reaction is the rate-determining step, while the evolution of hydrogen occurs on a much faster time scale. The latter is usually viewed as a two-electron reduction of H^+. If such a separate picture of both half-reactions is valid, the choice of particular semiconductor materials is subject to certain restrictions, for example the position of the band edges with respect to the electrochemical potential of the two half-reactions. In this regard, there is still a lively discussion whether rutile is capable of enabling the evolution of molecular hydrogen or if its conduction band edge is too low in energy.[325,431] Evidenced by the study of the photocatalysis of methanol as model reaction, we show that H_2 evolution is indeed possible on a rutile single crystal decorated with small platinum clusters as co-catalysts. Experiments under well-defined conditions and in comparison with the bare semiconductor reveal the exact reaction mechanism, which does not occur along the (generally expected) reduction of H^+ by photoelectrons. The mechanism also explains, why only very little amounts of co-catalyst already facilitate efficient H_2 formation.[314] We believe that this mechanism has to be considered in other photocatalytic systems, in particular for those that enable hydrogen surface diffusion.

Results and Discussion

The photochemical behavior of methanol[116,206,365,417,418,421,432–434] and other aliphatic alcohols[395,396,403,409] on bare TiO_2(110) is already heavily investigated, which makes them excellent systems for studying the hydrogen evolution reaction. As alcohols are known to efficiently facilitate the hole-reaction, they have vastly been used in different studies as hole-scavenger in the past.[17] From studies in UHV it is known that on a reduced titania crystal the main photochemical reaction pathway is a disproportionation reaction yielding formaldehyde and the hydroxylated semiconductor (see Eq. 9.1).[417]

$$CH_3OH{-}Ti_{surf} + O_{br} \xrightarrow{h\nu} CH_2O\uparrow + Ti_{surf} + 2\,OH_{br} \tag{9.1}$$

At best only very small amounts of molecular hydrogen are detected.[206] As the semiconductor stays significantly hydroxylated until the desorption of water at elevated temperature (above 300 K), catalyst poisoning is observed.
In contrast, the deposition of small platinum clusters on the semiconductor completely changes the behavior (see Fig. 9.1). While the rate constant of the formaldehyde production, which is reflected in the respective decay curve, remains the same, strong production of molecular hydrogen is observed. The kinetics of this hydrogen production are very similar to the formaldehyde production, which suggests that the latter is the rate-determining step and that hydrogen diffusion and recombination is much faster. Contrary to the reaction on the bare semiconductor, catalyst poisoning is not observed after the deposition of Pt clusters. Besides a conditioning of the co-catalyst in the first cycle,

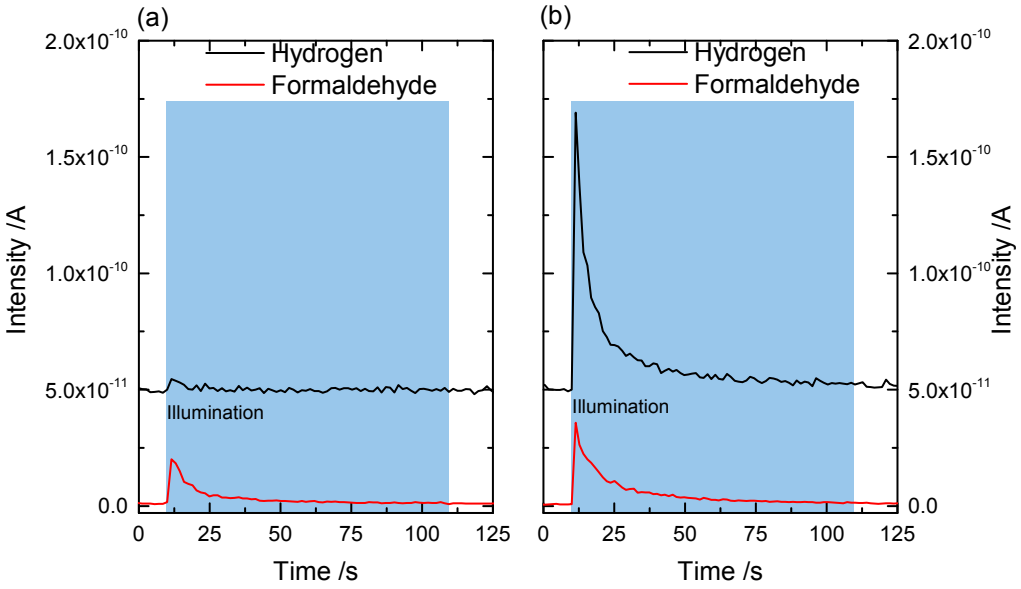

Figure 9.1. Isothermal photochemical reaction of 1 L of methanol on r-TiO_2(110) (a) and on Pt_x/TiO_2(110) (b) at 260 K. Upon UV illumination (shown in a blue background), methoxy species are photo-oxidized to formaldehyde, which desorbs thermally. In (a) only trace amounts of H_2 are formed upon illumination, while the catalyst poisoning is observed in subsequent runs (see Fig. 9.7 and Fig. 9.8). The Pt-loaded photocatalyst (b) shows an almost identical decay curve for formaldehyde desorption, but significant production of H_2 is additionally visible during illumination.

due to its reaction with the methanol, the kinetics stay the same in subsequent cycles (see Figure 9.13).

The comparison of the photocatalytic reaction behavior of the bare semiconductor with the Pt-loaded one leads to the following reaction mechanism, which is illustrated in Figure 9.2. From the alcohol chemistry on the bare semiconductor it is known that methoxy species are formed in titania defects, acting as photoactive centers for a hole-mediated αH abstraction.[116,417] Upon co-catalyst loading, this photoreaction mechanism remains unaltered, as evidenced by the unchanged apparent rate constant of formaldehyde production. However, the appearance of the intense H_2 signal demonstrates that the role of the co-catalyst is to enable the recombination of hydrogen atoms of the hydroxylated TiO_2 crystal (Eq. 9.2 and 9.3).

$$CH_3OH{-}Ti_{surf} + O_{br} \xrightarrow{h\nu} CH_2O\uparrow + Ti_{surf} + 2\,OH_{br} \tag{9.2}$$

$$Ti_{surf} + 2\,OH_{br} \xrightarrow{Pt_x} H_2\uparrow + Ti_{surf} + 2O_{br} \tag{9.3}$$

While the desorption of H_2 may be facilitated by the recombination of photoholes at or in the vicinity of the co-catalysts, an electron-consuming reduction of H^+ can be excluded due to the conservation of charges. The comparison of Eq. 9.2 and 9.3 with Eq. 9.1 demonstrates that the release of H_2 occurs via the recombination of hydrogen atoms on the co-catalyst, which can already by facilitated thermally (see Fig. 9.14). As the contri-

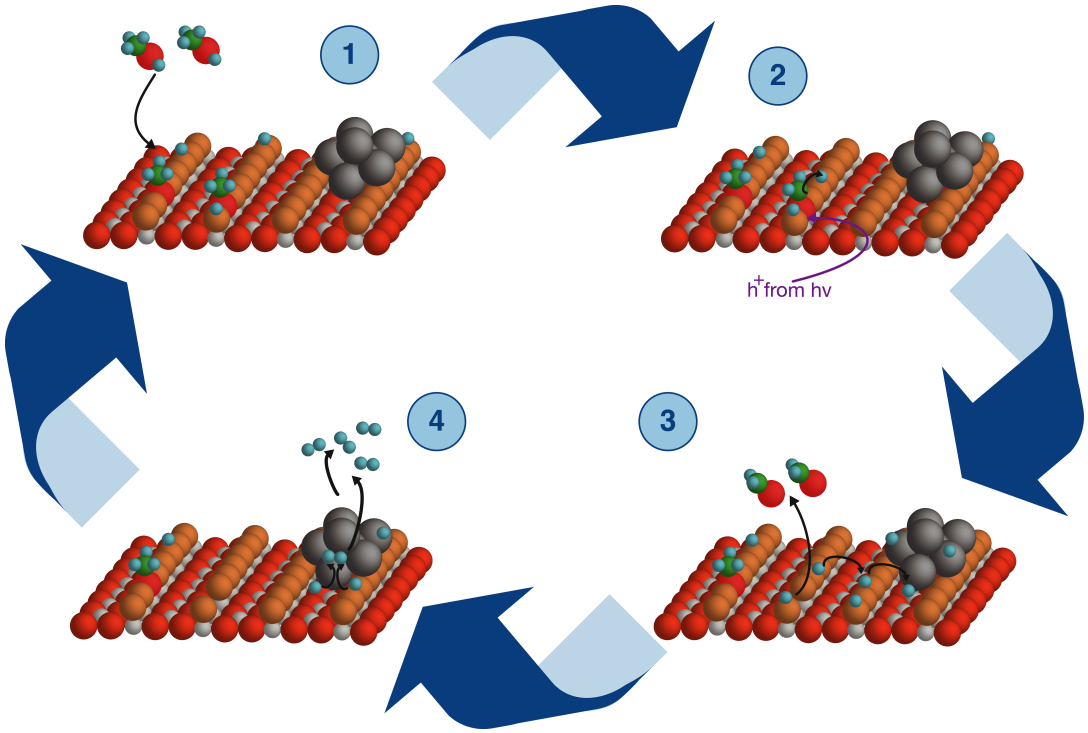

Figure 9.2. Scheme of the mechanism of photocatalytic methanol conversion at 260 K at a co-catalyst loaded r-TiO_2(110)-surface on an atomic scale. The reaction takes place in a bridge-bonding oxygen (BBO) vacancy, in which the thermally formed methoxy species (1) gets oxidized by photoholes[116,418] (2) and the formaldehyde desorbs (3). The formed atomic hydrogen diffuses on the surface (3), recombines at a co-catalyst and thermally desorbs (4), facilitating an overall charge neutral disproportionation reaction, which is triggered by the irreversible photo-oxidation step.

bution of photogenerated electrons is not required for yielding the respective products, the overall reaction is in fact a hole-mediated disproportion reaction of the alcohol rather than two different redox reactions, with the first step being the same as Eq. 9.1. This mechanism is also in good agreement with findings from semiconductor physics. As the TiO_2 single crystal represents a bulk oxide n-type semiconductor, surface band bending must strongly be considered, which is different to nano-structured systems. On an n-type semiconductor, photoholes highly tend to migrate to the surface, while photogenerated electrons preferentially move towards the bulk. A consumption of these photoholes causes a flattening of the semiconductor bands, which results in an increased rate of defect regeneration by corresponding photoelectrons. The resulting neutral charge balance is fully compatible with the mechanism described above.

The absence of poisoning in Pt_x/TiO_2(110) enables to perform the reaction under steady-state conditions (Fig. 9.3a) and to determine the turnover frequency (TOF) of the photocatalyst. Surprisingly, it is found that higher coverages of co-catalysts only lead to very small changes in the TOF (Fig. 9.3b). In this regard, changing the Pt loading over almost two orders of magnitude (from 0.02% to 1% of a monolayer) only leads to a 2-fold increase in the TOF. If a typical spherical rutile nanoparticle of 20 nm in diameter is considered,

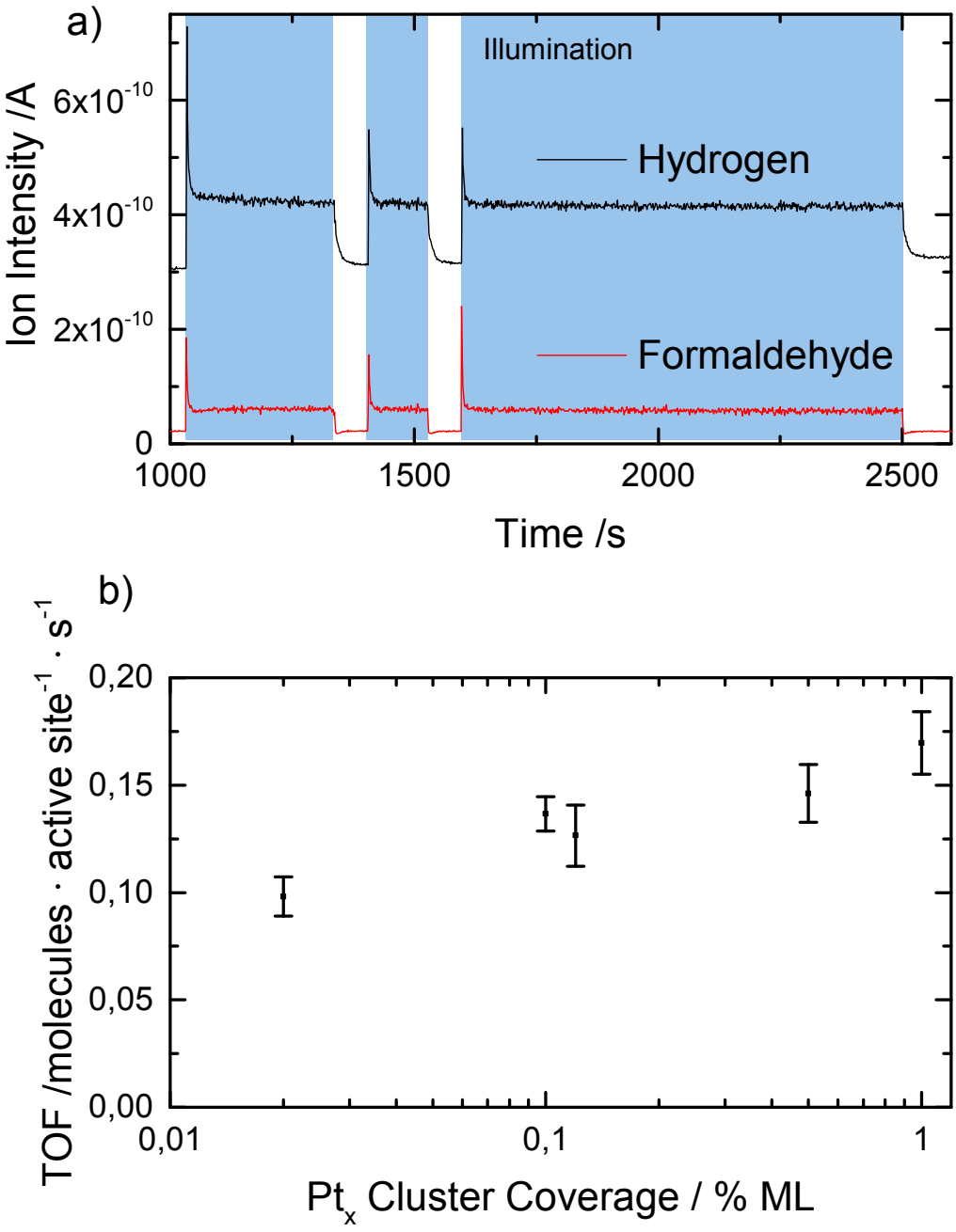

Figure 9.3. Photocatalytic conversion of methanol on Pt-loaded r-TiO_2(110). In a), the photocatalytic conversion of methanol to formaldehyde and hydrogen is shown. The reaction immediately starts with UV illumination and also stops immediately in the dark. In b), the cluster coverage is varied on the semiconductor and the reaction even occurs with an appreciable TOF for a Pt cluster coverage of 0.02% of a monolayer.

this coverage amounts to weight loadings of less than 0.01 to over 0.3 w% of platinum (assuming the bulk density of rutile TiO_2 and Pt_{15} as the average cluster size). Indeed, in a recent study of colloidal systems it was reported that very little amounts of platinum loading already result in high hydrogen production rates.[314]

With the hole-mediated disproportionation reaction mechanism, a straightforward interpretation of this observation can readily be given: As the platinum co-catalysts only act as recombination centers for hydrogen, charge carrier dynamics do not significantly influence the reaction step of hydrogen formation. Instead, the migration of hydrogen atoms to the co-catalysts plays a crucial role. In this regard, it has only recently been shown that the diffusion of hydrogen is efficiently facilitated over large distances on TiO_2, which has been attributed to the redox properties of the semiconductor.[435] As a result, the distance of the co-catalyst to the center of photoreaction is not of paramount importance for the H_2 evolution rate. Interestingly, the photocatalytic reaction is not dependent on the energy of the incident light as observed for the O_2-PSD[95] (Fig. 9.11). Further, no difference in amount or in the kinetics of the onset or the trail for the photoreforming products is observed, when the sample is irradiated continuously or with ns-laser pulses (Fig. 9.4). This further indicates, that the chemical kinetics dominate in this reaction regime and that the charge carrier dynamics seem negligible. The co-catalyst coverage dependence again demonstrates, how strongly formaldehyde formation is governing the overall reaction rate. As the density of oxygen vacancies, which were previously identified as active sites for the hole-mediated reaction, is about 6% (see Fig. 3.5), it is over two orders of magnitude higher than the lowest cluster coverage. Therefore, the vital role of these de-

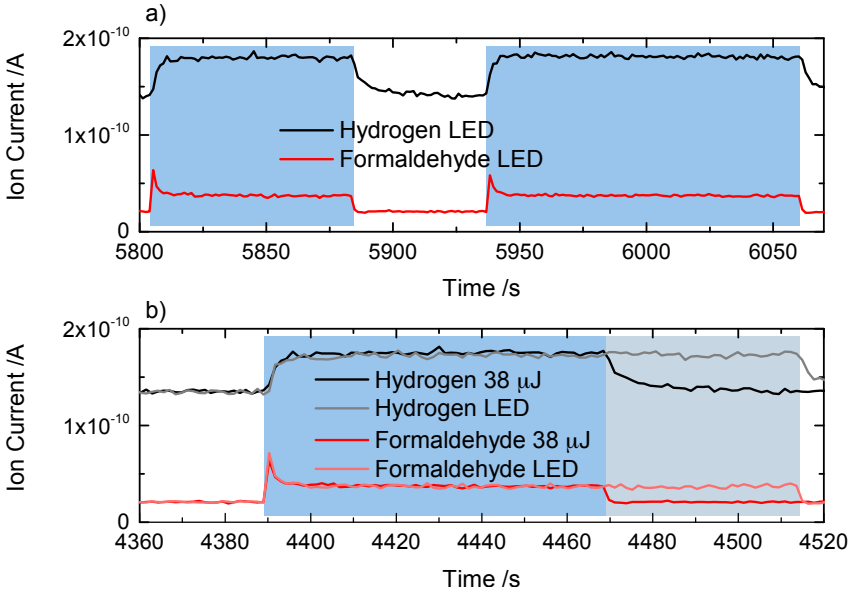

Figure 9.4. Photocatalytic experiments depending on wavelength and illumination conditions with $Pt_x/TiO_2(110)$ and a cluster coverage of 1% is shown in a background of $1 \cdot 10^{-7}$ mbar methanol. In a), the light source is exchanged from the ns-Laser with 20 Hz to a continuous light source. In this case, this light source is a UV-LED that emits light around 367 nm (see Fig. 9.12 for details), well above the band gap value for rutile TiO_2 of 3.0 eV. The photocatalytic reaction of methanol shows the same behavior as in Fig. 9.3 and Fig. 9.11. In panel (b), a direct comparison of the LED to laser excitation is shown, while the pulse energy of the laser is only 38 µJ at 241.8 nm and the characteristics show no appreciable difference.

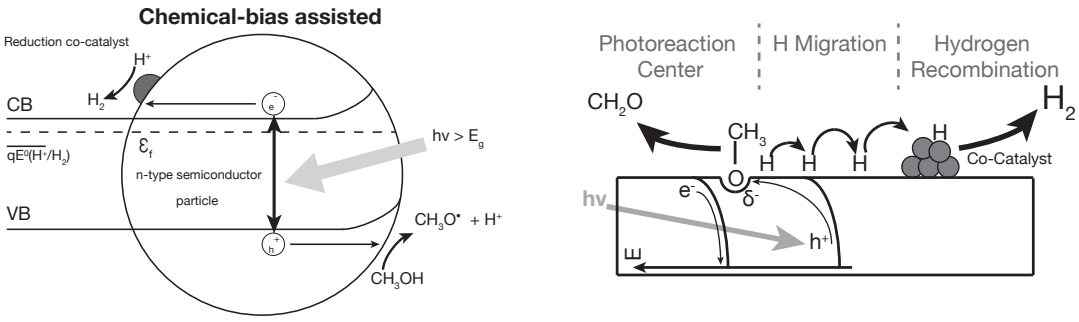

(a) **Photoelectrochemical-Type Mechanism** **(b)** **Photocatalytic Reaction Mechanism**

Figure 9.5. Different mechanistic pathways for photocatalyic reactions. In the left part, the conventional model (adapted from Domen and coworkers [17,428]) based on photoelectrochemisty is displayed. In this picture, H_2 evolution consumes two photoelectrons on the HER co-catalyst, while the other half-cell reaction is facilitated by two photoholes. The band edge positions have to align to the chemical standard reduction potentials to facilitate the photoelectrochemical reaction. In the right panel, the photocatalytic mechanism is shown. By light absorption, the methoxy species is photooxidized by one hole in the partially negatively charged defect, leading to formaldehyde desorption from the photoreaction center. The co-generated H-atoms migrate on the surface to the co-catalysts (in this case Pt clusters), which act as a recombination centers, rather than reduction sites for protons from solution. As the dissociative adsorption of methanol already occurs thermally in the dark on the semiconductor, only one photon is needed for the photocatalytic reaction in case of TiO_2. Depending on the reaction, the catalyst material and the reaction conditions, one of these two mechanisms may serve as a correct description for the reaction pathway.

fects in the reaction rate makes the avoidance of their blocking essential. Whether the defects are preserved may also depend on the method of co-catalyst preparation. In this study, clusters are randomly distributed on the surface due to the applied deposition method. [436,437]

The photon-stimulated desorption of oxygen, which is a powerful tool to probe the concentration of accessible BBO-defects [207], further confirms this assumption as it does not significantly change after cluster deposition and even catalysis (see Fig. 9.15). For example, this is different to the formation of clusters via the evaporation of metals on the semiconductor with subsequent annealing, which was found to strongly inhibit the photooxidation of CO in case of Pt [129] or the O_2 photodesorption in case of gold [114]. This is a clear indication that the migration to or the formation of metal centers in or near defects will inhibit the formation of the oxidized product and, thus, the entire reaction.

In summary, some important consequences result from these findings.

The new mechanism, which differs from the generally adopted photoelectrochemical picture, (see Figure 9.5) is an alternative possibility for the evolution of molecular hydrogen. While the established pathway still may be dominant in certain systems, the new mechanism extends the range of possible semiconductor materials. In particular, hydroxyl-forming oxides may be potential candidates and their conduction band edges do not

necessarily have to match the reduction potential of hydrogen, as it is illustrated here in the case for rutile decorated with co-catalysts.[431]
The amount of co-catalyst for the H_2 evolution has only a very weak influence on the TOF. While vital for the formation of molecular hydrogen, a coverage of 0.02% (which amounts to a loading of 0.01 w% for typical 20 nm rutile particles) result in a considerable strong H_2 signal. This effect can readily be explained with the reaction mechanism: As the co-catalysts only enables hydrogen recombination, its loading only plays a minor role in comparison to the formation of formaldehyde, which is the rate-determining step.
As oxygen vacancies enable the αH abstraction, it is vital that the co-catalyst does not block them. Consequently, the procedure of co-catalyst preparation may be essential for the photoreaction yield.[438] The optimal preparation procedure may differ for different metals, depending on the metal mobility on the semiconductor.[436]
The mechanism also illustrates that there may exist intrinsic differences of photocatalysis in comparison to photoelectrocatalysis other than the absence of voltage. These differences may be associated with disadvantages (e.g. significant contributions of the back reaction), but also with advantages as both half-reactions are not strictly separated from each other.

Experimental Methods

All experiments were performed in an ultra-high vacuum apparatus[305] with an attached laser-vaporization cluster source. A rutile TiO_2(110) single crystal (Surface-net GmbH) was cleaned by several cycles of sputtering (Ar, 1.0 keV, $7 \cdot 10^{-6}$ mbar) and annealing at 850 K in vacuum, which results in an atomically flat surface, while the crystal shows a light blue color indicating a slightly reduced surface.[99] Over the course of the experiments, the crystal was sputtered (same conditions), annealed in oxygen atmosphere ($1 \cdot 10^{-6}$ mbar, 820 K) for 20 min and vacuum annealed at 820 K for 10 min. This recipe is known to result in a clean surface with a constant bridge-bonding oxygen (BBO) vacancy concentration (6%±1 in this case).[99,305] The Pt (99.95% purity, ESG Edelmetalle, Germany) clusters are generated by a laser vaporization source coupled with a quadrupole mass spectrometer (Extrel, USA). In this work, the quadrupole mass spectrometer was operated with the AC-potential only, acting as an ion guide.[439,440] The resulting size-distribution is then determined by the pressure and voltage settings and kept constant over the course of the experiments.[440] The Pt clusters are deposited on the r-TiO_2(110) surface under soft-landing conditions (< 1eV/atom in kinetic energy). The resulting catalyst is therefore named Pt_x/TiO_2(110) in the following. The cluster size distribution is checked before every experiment and determined by a mass scan over all sizes. The resulting mass spectrum is displayed in Figure 9.6. The clusters are deposited randomly on the surface and show no preferential adsorption as evidenced by Kelvin Probe Force Microscopy and STM.[436,437,441]

Table 9.1. Cluster coverages used in this work on the TiO_2(110) surface.

% ML /cm^{-2}	Number of clusters /e $\cdot$ nm^{-2}	Number of clusters /e $\cdot$ cm^{-2}
0.02	0.003	$3 \cdot 10^{11}$
0.10	0.015	$1.2 \cdot 10^{12}$
0.12	0.018	$1.8 \cdot 10^{12}$
0.50	0.075	$7.5 \cdot 10^{12}$
1.00	0.150	$1.5 \cdot 10^{13}$

Between the experiments, a few cycles in sputtering, lasting in total more than 1 h, were employed to facilitate a clean surface. The surface purity is verified by D_2 and H_2O TPD, since also the smallest contamination of Pt clusters on the surface leads to a desorption feature in Hydrogen in a TPD between 200 K and 300 K. Methanol (Chromasolv, $\geqslant$99.9% purity) and Methanol-d_3 (Sigma Aldrich, 99.8 atom % D) are cleaned via several pump-freeze cycles and either dosed at cryogenic temperatures or via a constant background, while all relevant masses are monitored with a QMS.

For the photocatalytic measurements, the catalyst is prepared and moved to the QMS. The pulse energy of the laser is monitored and the reactant is dosed at cryogenic conditions, unless stated otherwise. The crystal is heated to the reaction temperature and then the UV-illumination is started. To determine turnover-frequencies (TOFs), the catalyst is exposed to a continuous background of a certain methanol pressure and the UV illumination is facilitated and blocked. Areas of constant photoconversion of methanol to H_2 (m/z=2) and formaldehyde (m/z=30) are chosen and both signals are integrated over time. For both species, transmission of the calibrated QMS, ionization cross sections and cracking pattern contributions are taken into account. The following integral area is normalized by the integral of a methanol TPD peak of the Ti-lattice sites (1 ML = $5.2 \cdot 10^{14}$).[374]

To calculate the TOF or site time yield (STY), this integral is divided by the number of active sites for formaldehyde production (0.06 ML, in this case for the BBO-vacancies[205] (see Fig. 3.5)) to yield a number of molecules per active site per second. Stoichiometry was checked for every catalytic experiment (see Fig. 9.9). This TOF is possibly still limited by mass transport, but pressures higher than $4 \cdot 10^{-7}$ mbar were not investigated to ensure the proper detection by QMS. The apparent quantum yield (AQY) can be calculated by relating the number of evolved molecules per second to the photon flux:[43,428]

$$\mathrm{AQY}(\%) = \frac{\text{Product Molecules } (s^{-1})}{\text{Photons } (s^{-1})} \cdot 100 \tag{9.4}$$

In this work, the amount of product molecule (either formaldehyde or hydrogen) is divided by the number of incident photons from the laser. In the classical picture, two charges are needed to oxidize methanol to formaldehyde as well as reduce protons to H_2.[41,42,428] For the lowest photon fluxes (compare to Fig. 9.10), a quantum yield of 3.2%

is obtained, while in the saturation regime (see Fig. 9.10), the quantum yield is about 0.11%.

Supplementary information

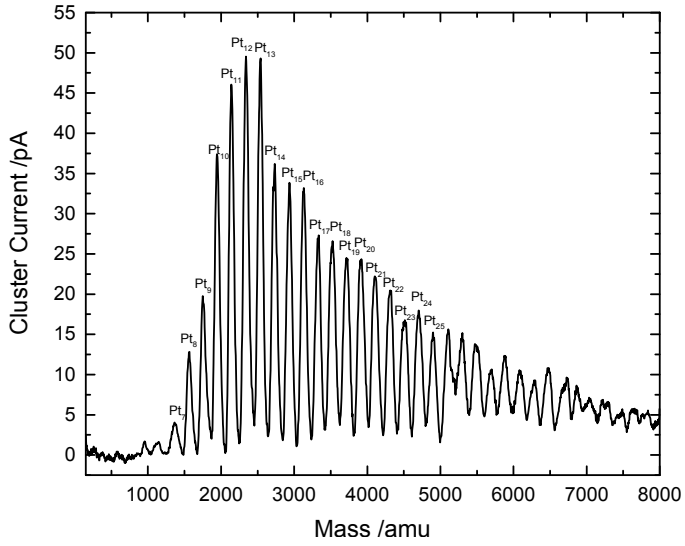

Figure 9.6. Mass spectrum of the cluster size distribution of Pt clusters from the laser vaporization source. The spectrum is taken after the quadrupole mass filter and shows a size-distribution of Pt_7 up to Pt_{32}. When depositing in the ion guide mode, all masses lower than Pt_8 are discarded. The clusters show a log-normal distribution and have a size about 1 nm in diameter.[440]

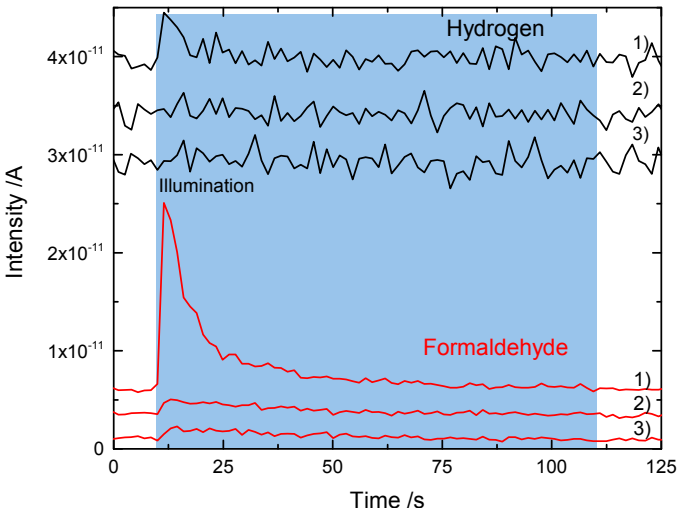

Figure 9.7. Isothermal photoreaction of methanol on the r-TiO_2(110) surface at 260 K while H_2 and formaldehyde are detected by the masses 2 and 30 respectively. In the first experiment (1), 1 of methanol is adsorbed on the crystal at cryogenic temperatures and then the crystal temperature is set to 260 K. The blue box in the figure indicates the illumination. Upon UV excitation of the n-type semiconductor, the photoholes travel to the surface and oxidize methoxy to formaldehyde.[116,417,418] At this temperature, the thermal desorption of formaldehyde is observed [118,365,442] accompanied by trace amounts of H_2.[206] After the first run, the hydroxylation of the semiconductor leads to site-blocking of the reactive sites.[305] This is shown by a consecutive coverage of the catalyst after (1) at cryogenic temperature by 1 L of Methanol. In the next started photoreaction at 260 K in(2), only a very small signal is obtained for formaldehyde and hydrogen is not obtained at all. This also holds true for further coverages as shown in traces (3).

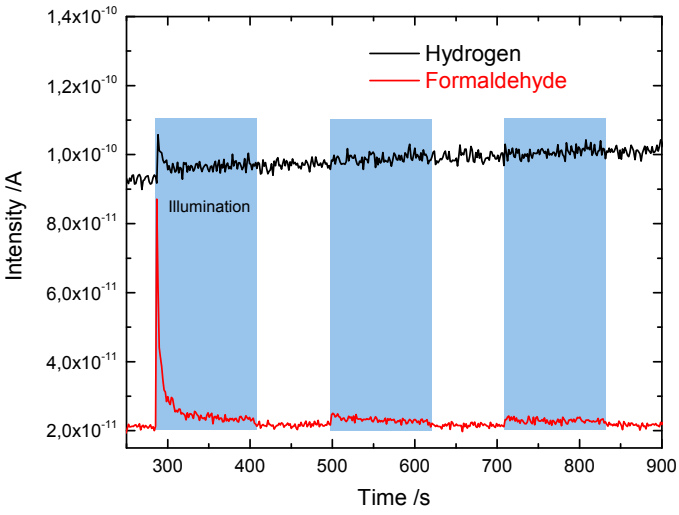

Figure 9.8. Isothermal experiment at 260 K on a r-TiO_2(110)-surface in a constant methanol background of $1 \cdot 10^{-7}$ mbar. In agreement with Fig. 9.7, upon the first irradiation formaldehyde and some trace amounts of hydrogen desorb.[206] Upon the second and third illumination, only a very small conversion of formaldehyde is obtained, since most sites are blocked by hydroxyls. No appreciable hydrogen signal is obtained during those irradiations.

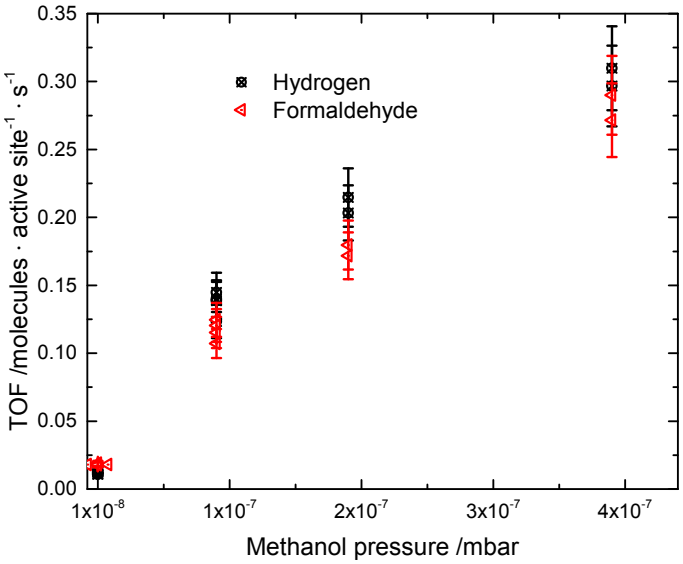

Figure 9.9. Methanol pressure-dependent TOF for Pt_x cluster on r-TiO_2(110) for photocatalytic conversion. The cluster coverage is 0.1% Pt clusters per (TiO2)(110) surface atom and the experiment is run at 260 K. The reaction stoichiometry is independent of the pressure. Every circle and triangle resembles a photocatalytic experiment. To ensure the integrity of the ultra-high vacuum and a proper quantitative detection with the QMS, pressure higher than $4 \cdot 10^{-7}$ mbar are not investigated.

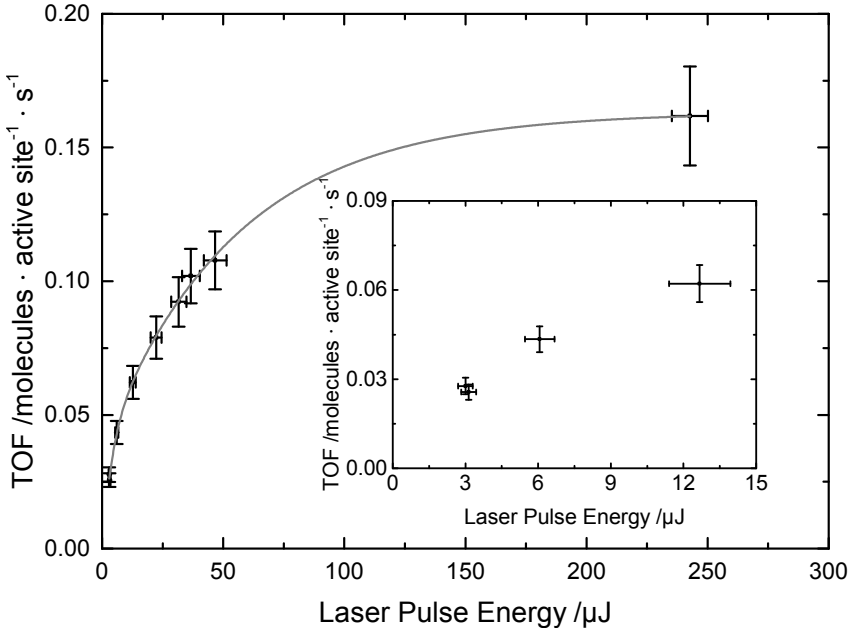

Figure 9.10. Turnover Frequency of formaldehyde in a background of $1 \cdot 10^{-7}$ mbar methanol in dependence on the incident laser pulse energy at 260 K. A typical pulse energy of 250 µJ is obtained when the OPO-Laser is operated at 241.8 nm. The grey line is only a guide to the eye to show that the photoreaction saturates. The error bars are determined by the standard deviation of the laser power as measured, while the error bars in the TOF are 10%, except for the one at 250 µJ, which is a standard deviation of four measurements. The inset shows the low energy area, where a linear dependence on the laser power is obtained.

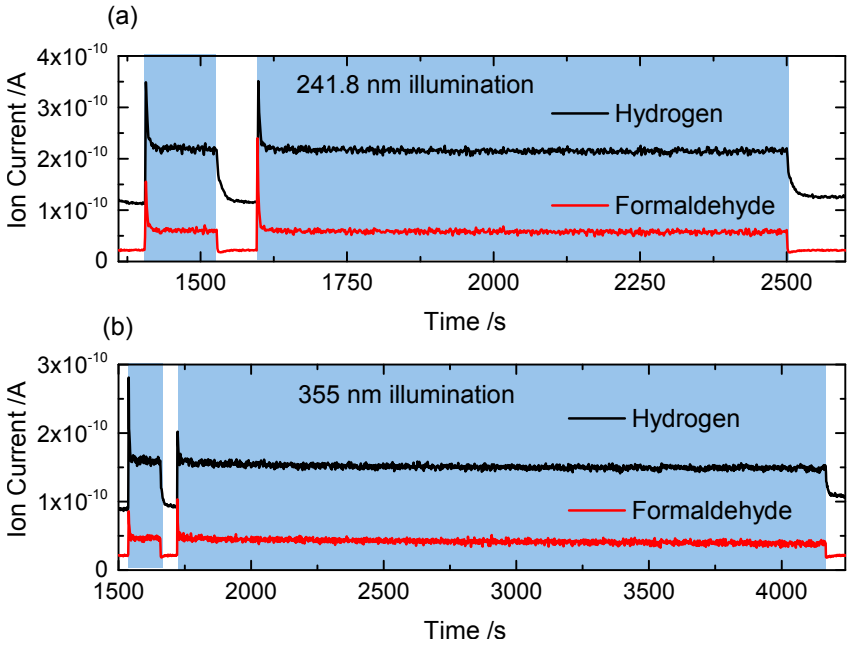

Figure 9.11. Photocatalytic experiments depending on wavelength and illumination conditions with $Pt_x/TiO_2(110)$ and a cluster coverage of 1% is shown in a background of $1 \cdot 10^{-7}$ mbar methanol. In (a), the sample is illuminated with 250 µJ at 241.8 nm, and with illumination the reaction starts immediately. The reaction stops immediately, when the light is switched off and also runs constant. In panel b), the pulse energy is also held constant at 250 µJ, but the wavelength is changed to 355 nm. The same amounts of hydrogen and formaldehyde are obtained, also in the second illumination over a time of 45 min.

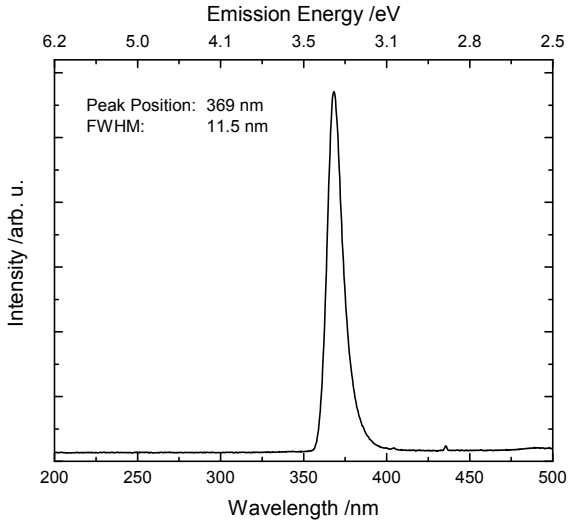

Figure 9.12. Characteristics of the light emission of the UV-LED. The emission is centered around 369 nm with a full-width half maximum of 11.5 nm.

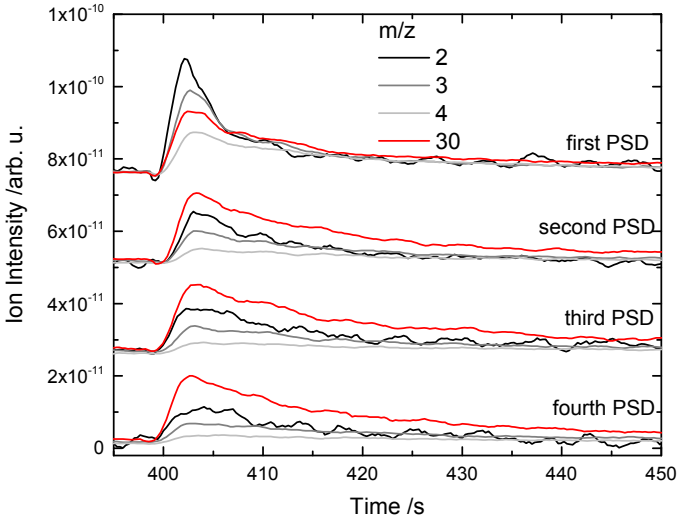

Figure 9.13. Consecutive photocatalytic experiments with methanol on Pt_x/r-TiO_2(110). The Pt coverage is 0.75% cluster per surface atom and the reaction is carried out at 260 K after adsorption of 1L methanol-d_3. In contrast to Fig. 9.7, no catalyst poisoning is observed after an initial conditioning of the catalyst. Formaldehyde is measured with mass 30, while all hydrogen species are measured on the masses 2, 3 and 4. Between the cycles, the surface is recovered with 1 L of methanol-d_3. In the first experiments, more H_2 is observed, which is attributed to dissociative methanol adsorption and an unknown degree of pre-hydroxylation of the semiconductor. In all runs, the formaldehyde intensity and kinetic decay stays the same and after the conditioning in the first shot, the same holds true for all hydrogen traces.

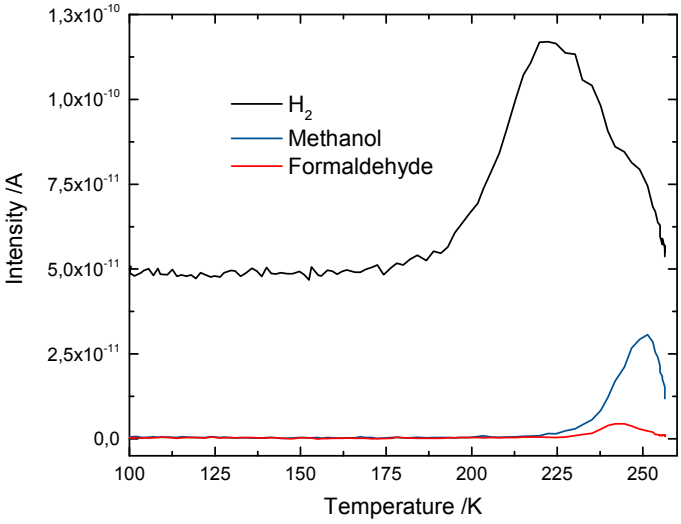

Figure 9.14. TPD of Methanol in a background of $1 \cdot 10^{-7}$ mbar on 0.1% Ptx/TiO2(110) from 100 K to the reaction temperature at 260 K. After the oversaturation of the surface at cryogenic temperatures, some methanol desorption occurs around 250 K as it is expected from TPD data. Hydrogen desorption from the Pt clusters is observed, too. As methanol adsorbs dissociatively on the TiO_2(110), which is known from STM studies[400], the abstracted hydrogen atoms thermally recombine at the Pt clusters and desorb.

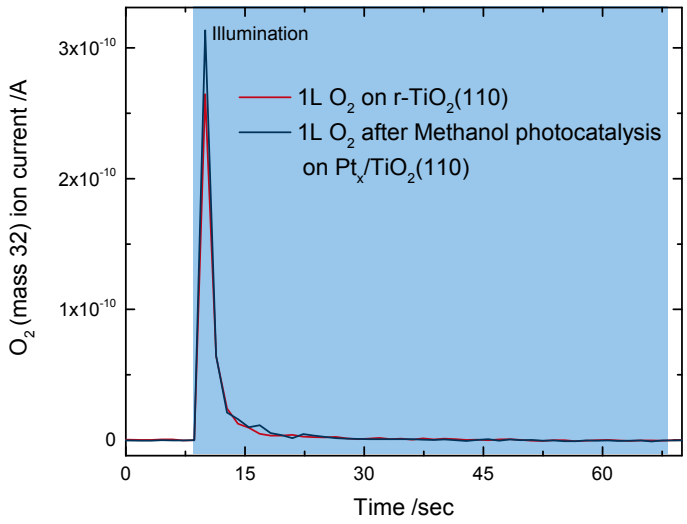

Figure 9.15. O_2-PSD at 100 K of the r-TiO_2(110)-surface and the Pt_x/TiO_2(110) catalyst after 2 h of photocatalysis. The red trace represents a O_2 PSD from bare surface, that is in excellent agreement with literature.[132,210] After the catalytic experiment, the methanol background is turned off and the sample was illuminated for another 15 min to deplete all the methanol from BBO-vacancies. After illumination is turned off, the sample was cooled down to 100 K and exposed to oxygen, to fill the BBO-defect sites. Upon UV illumination, the same intensity and kinetics for the O_2 PSD are observed as for the bare sample, indicating that the amount of defect sites stays constant and that the methanol at least in the BBO-vacancies was completely converted.

"An investment in knowledge pays the best interest."

- Benjamin Franklin

10

Tuning the Selectivity of Photoreactions: Temperature Control in Water-Free Alcohol Reforming TiO_2(110)-Supported Pt Clusters

10.1. Results

While the previous Chapter 9 focussed on the H_2-evolution and the co-catalyst, this chapter shifts the focus on the oxidation pathway of the photocatalytic alcohol disproportionation reactions. The validity of the presented mechanism will be evaluated further by changing the reactant to other alcohols such as ethanol, tert-butanol, cyclohexanol and benzylalcohol.

10.1.1. Methanol

First, the photo-reforming of methanol is revisited. Previous work on rutile TiO_2(110) observed methylformate as a further photo-coupling product from the photo-oxidation of methanol both on the r-TiO_2(110)[117,443] and o-TiO_2(110)[365] surfaces and on TiO_2 nanowires[366]. While quite clear at a first glance, the studies are in disagreement to that of Phillips *et al.*, who only observe the reaction on o-TiO_2(110).[365] Further, formaldehyde disproportionation can be ruled out as a mechanistic pathway, but there is no consensus which intermediate is involved in the second photo-oxidation step.[117,365,443,444]

To establish the basic photo-oxidation pathways on bare TiO_2(110), both the reduced and oxidized surfaces are investigated with the methodology presented in the previous Chapters 7.2 and 8. PI-TPD of methanol on r-TiO_2(110) irradiated for 15 min with UV light shows the formation of the photo-oxidation product formaldehyde, which desorbs around 260 K. Additionally, a small feature around 240 K of methylformate is detected, that is assigend to the consecutive photo-coupling product (see Fig. 10.1). All other features result from thermal chemistry and are well-known.[200,445] PI-TPDs after various

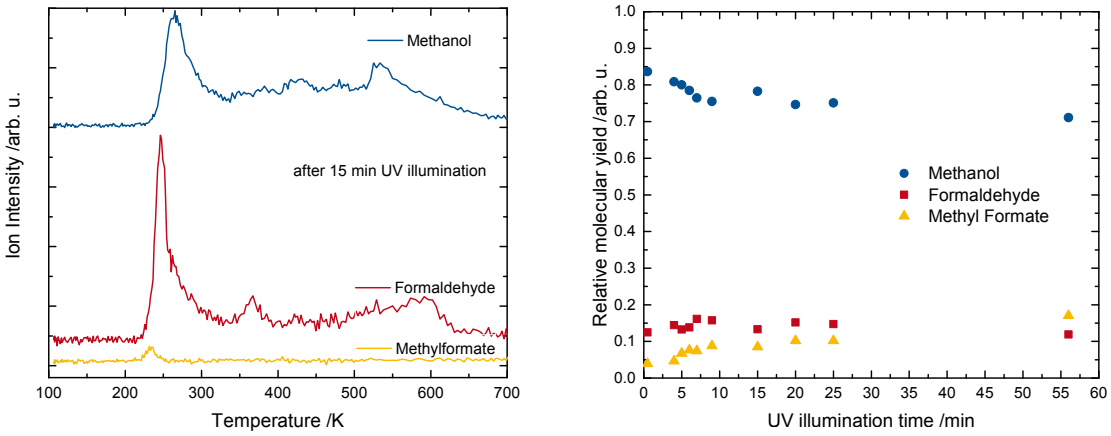

(a) PI-TPD on r-TiO_2(110). **(b)** PI-TPD Yields on r-TiO_2(110).

Figure 10.1. (a) Post-irradiation TPD experiment of 1 L methanol is shown after 15 min of UV illumination on r-TiO_2(110). The features in formaldehyde and methylformate around 240 K result from the photo-oxidation of methanol by photo-holes from the n-type semiconductor. The high temperature formaldehyde feature results from a disproportionation with methanol at high temperatures in the cleared BBO vacancies, while still molecular methanol desorption is observed around 270 K.
(b) Normalized integrated molecule yields vs illumination time on r-TiO_2(110). Each of the data points represents the integrated molecule yields from a consecutive post-irradiation TPD run. Prior to this illumination, the r-TiO_2(110) surface is exposed to 1 L methanol at 100 K. Since no coking is observed for the experiments by AES and in previous studies[445], the carbon mass balance can be closed. Even for the shortest UV irradiation, about 13% of methanol are converted to formaldehyde. The formaldehyde production saturates about at about 16% and then diminishes with the rise in methylformate. The yield of the consecutive photo-coupling product methylformate is even more increased after 55 min of illumination.

illumination times (Fig. 10.1(b)) show that the conversion to formaldehyde is very fast in this time range[1], and somehow is saturated around 0.15% of the methanol coverage. Significant methylformate formation is observed after more than 5 min and the formation increases even at 55 min of illumination time at cryogenic conditions, which corroborates the results from Yang's group.[117]
For the o-TiO_2(110) surface, the photo-products formaldehyde and methylformate are also observed around 250 K (see Fig. 10.2(a)), which is in excellent agreement with the work from Friend's group.[365] All other features are known to result from thermal chemistry and are already well established.[116,200,445] The behavior of the formation of photo-products (see Fig. 10.2(b)) from PI-TPDs is very similar to the one on r-TiO_2(110) (see Fig. 10.1(b)). Namely, formaldehyde is formed even at the shortest investigated time to about 20% of the initial methanol coverage and methylformate is observed for all illumination times and rises with longer illumination. As discussed earlier (see Chapter 3.3.1.2),

[1] Note, that illumination times shorter than a few seconds are not easily achieved. The use of a pulsed laser for illumination offers in principle the possibilty for single-shot experiments with just one pulse. Such experiments might be of further use to give accurate quantum efficiencies down to the sub-monolayer level.[183]

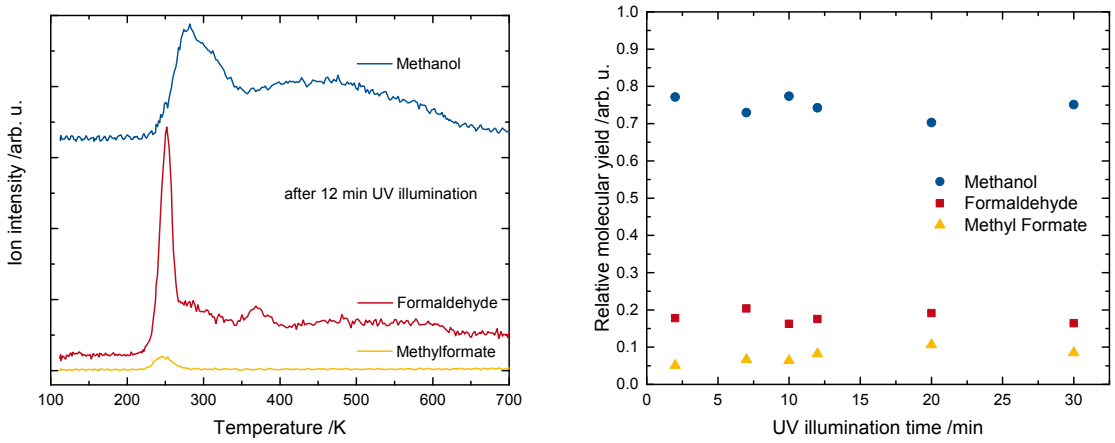

(a) PI-TPD on o-TiO_2(110) **(b) PI-TPD Yields on o-TiO_2(110).**

Figure 10.2. (a) Post-irradiation TPD experiment of 1 L methanol is shown after 12 min of UV illumination on o-TiO_2(110). The features in formaldehyde and methylformate around 250 K result from the photo-oxidation of methanol by photo-holes from the n-type semiconductor. The high temperature formaldehyde feature significantly diminishes, since most methoxys are already photo-oxidized. The methanol feature around 270 K is assigned to molecular desorption, while a very broad feature is obtained for the high temperature species, which can be attributed to the lack of definition on the so-prepared o-TiO_2(110) surface.
(b) Normalized integrated molecule yields vs illumination time on o-TiO_2(110). Each of the data points represents the integrated molecule yields from a consecutive post-irradiation TPD run. Prior to this illumination, the o-TiO_2(110) surface is exposed to 1 L methanol at 100 K. Since coking is not observed for the experiments by AES and in previous studies[445], the carbon mass balance can be closed. Even for the shortest UV irradiation, about 18% of methanol are converted to formaldehyde. The formaldehyde production saturates at about 22% while more methylformate is formed with increased illumination time. The kinetics are less obvious due to significant deviations from the expected trends. This is due to the more undefined surface preparation (annealing and cooling down in oxygen atmosphere to 300 K[404], see also chapter 3.3.1.2) with regard to the r-TiO_2(110) surface, which could lead to oxidized interstitials on the surface.

the o-TiO_2(110) surface obtained by this preparation method[404] is less defined than the r-TiO_2(110) surface, which can also be seen in the data points in Figure 10.2(b). Therefore, it is refrained from a quantitative analysis here, but, qualitatively, the photo-oxidation of methoxy to formaldehyde and the consecutive photo-oxidation and -coupling to methylformate are observed on both crystal surfaces.

To investigate this reaction pathway under catalytic conditions, methylformate is also monitored during photocatalytic experiments of 1% Pt_x on r-TiO_2(110). As can be seen in Figure 10.3, small amounts of methylformate are formed upon illumination at 262 K. A further investigation of the reaction temperature shows that for temperatures above 265 K, the methylformate formation is negligible and the reaction selectivity towards formaldehyde approaches almost 100%. This changes for temperatures below 260 K, where substantial methylformate evolution is observed, yielding a selectivity of 57% and

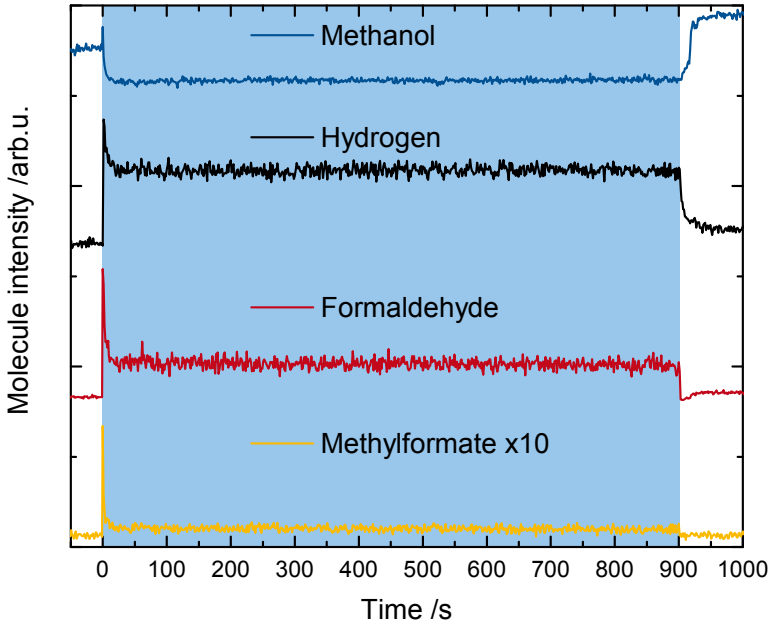

Figure 10.3. Products from a photocatalytic experiment of 1% Pt_x clusters on the r-TiO_2(110) surface. The methanol background is set to $7 \cdot 10^{-8}$ mbar and the UV excitation is performed at 241.8 nm with a pulse energy of 195 µJ and the reaction temperature is 262 K. Methanol, hydrogen, formaldehyde and methylformate are identified by the masses 32, 2, 30 and 60 respectively. The methylformate trace is multiplied by 10 for a better visibility.

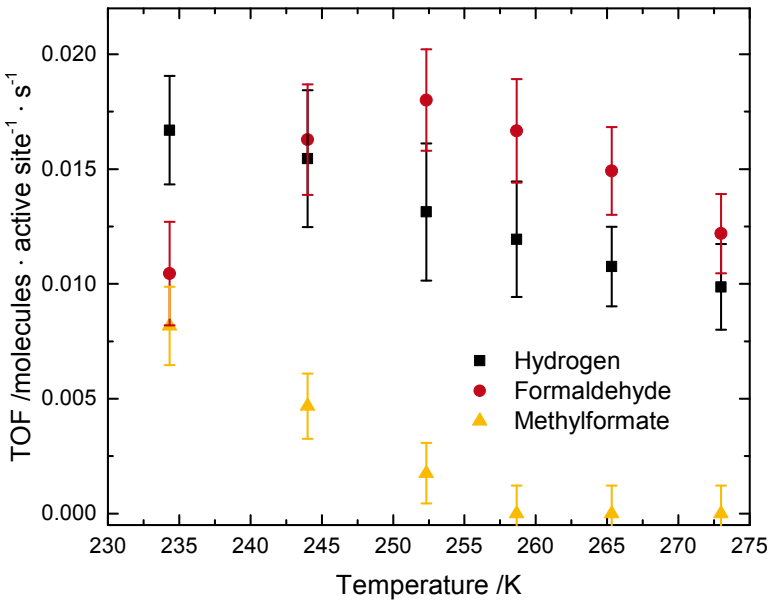

Figure 10.4. Temperature-dependent TOFs for the photocatalytic conversion of methanol on Pt_x/r-TiO_2(110) in a background of $1 \cdot 10^{-8}$ mbar. The reaction is highly selective towards formaldehyde above 260 K. At lower temperatures, the methylformate formation as a consecutive photo-oxidation product is observed, while the formaldehyde yield diminishes.

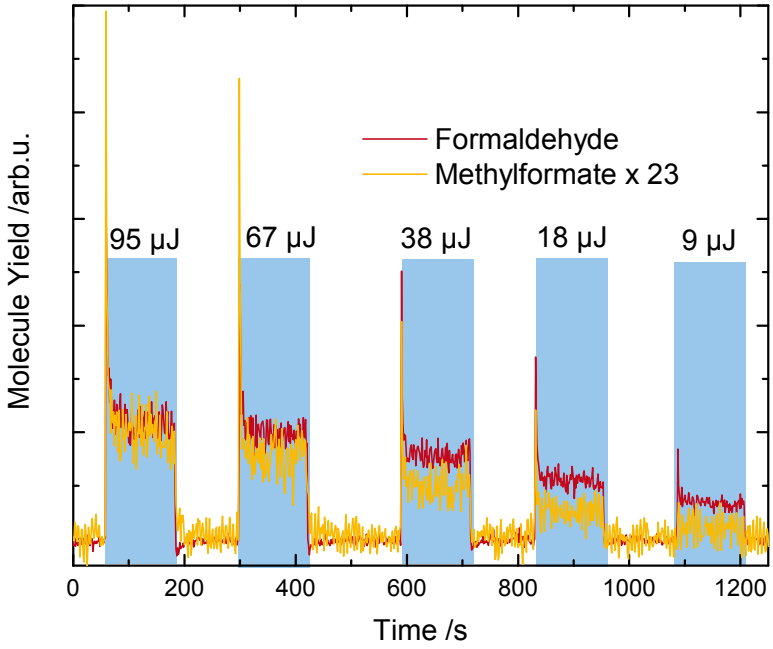

Figure 10.5. Photocatalytic experiment in a methanol background on Pt_x/r-TiO_2(110) with different UV illumination intensities. The methylformate trace is multiplied by 23 to ensure a better visibility. With a declining UV intensity, the formation of methylformate is decreased to a larger extent than the one of formaldehyde, proving that the formation of methylformate occurs via a second photo-oxidation in catalytic conditions.

43% for formaldehyde and methylformate, respectively. To confirm that the methylformate is indeed a consecutive photo-oxidation product, the yield of formaldehyde and methylformate is displayed in dependence of the UV-irradiation intensity in Figure 10.5. While both product yields are diminished by lower light intensities, the methylformate yield is decreased to a higher extent than the formaldehyde yield, leaving a clear indication that the consecutive photo-oxidation and coupling is dependent on a second photon. Thus, a solely thermal reaction pathway can be excluded.

10.1.2. Ethanol, Benzaldehyde and Cyclohexanol

Ethanol is chosen as the next higher homologue alcohol, since it offers an additional thermal dehydration chemistry on TiO_2(110).[285,293] Further it is also relevant as a potential renewable feedstock for thermal[34,429,446–448] and photocatalytic hydrogen production.[33,81,149,168,169,315,449–451] Cyclohexanol is a representative of a secondary alcohol with relatively bulky steric demand and benzaldehyde is of industrial relevance.[452] The corresponding benzylalcohol shows an interesting thermal deoxygenation chemistry at elevated temperatures.[389]

First, the selectivity for the catalytic ethanol photo-oxidation is displayed in Figure 10.6, while the reaction to acetaldehyde and hydrogen is stoichiometric (data not shown). In agreement with previous single crystal studies,[305,397,453] no further photo-oxidation product was found (marked in yellow). Surprisingly, the acetaldehyde formation does not show a clear temperature dependence above 200 K, while the main desorption feature was previously assigned to 225 K.[305] No further oxidation products like acetic acid or other coupling products like diethyl ether are found, so a selectivity of 100% is obtained for the photoreforming of ethanol.

As a secondary alcohol, the photoreforming of cyclohexanol is investigated on Pt_x/r-TiO_2(110) as shown in Figure 10.7(a). As evidenced by the pressure series, both cyclohexanone and hydrogen are evolved in stoichiometric amounts at the reaction temperature of 280 K. No further oxidation or ring-opening products are observed at these conditions.

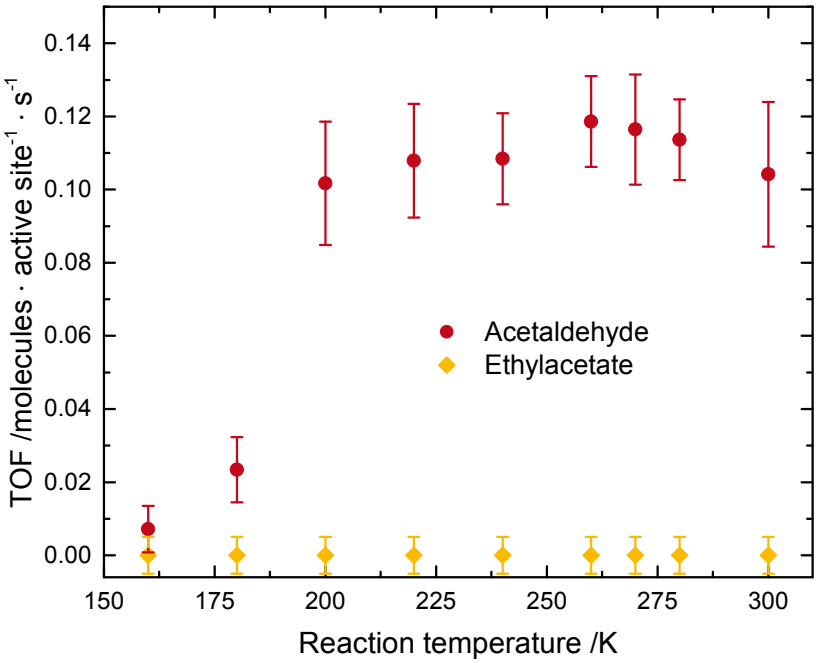

Figure 10.6. The temperature-dependent TOFs for $7 \cdot 10^{-8}$ mbar ethanol on 1% Pt_x/r-TiO_2(110) show that in the investigated temperature range no photo-oxidative coupling product is formed at all. The acetaldehyde production is independent of the temperature between 200 and 300 K and only below 200 K a depletion in the acetaldehyde yield is observed.

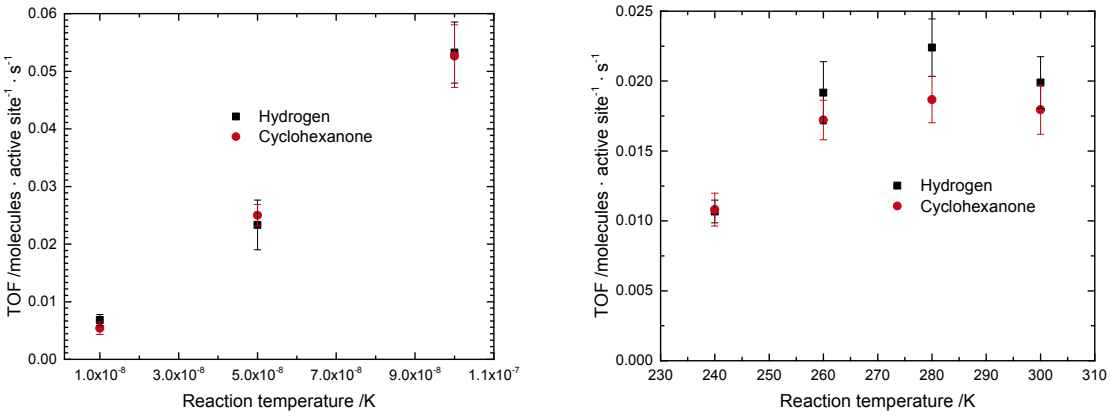

(a) Pressure-dependent TOFs **(b) Temperature-dependent TOFs**

Figure 10.7. (a) Pressure series of cyclohexanol background pressure for photoreforming on 1% Pt_x/r-TiO_2(110) at 280 K. The reaction is stoichiometric towards the cyclohexanone and molecular hydrogen.
(b) Temperature-dependent TOFs for $1 \cdot 10^{-8}$ mbar cyclohexanol on 1%Pt_x/r-TiO_2(110). The reaction seems saturated around 280 K and only at 240 K a reduced TOF is observed.

The temperature-dependent TOFs are shown in Figure 10.7(b). A plateau is observed from 240 K to 300 K and the TOF is only lessened, when the reaction temperature is below 260 K.
Further, benzylalcohol photoreforming is investigated in dependence of the benzylalcohol pressure (Fig. 10.8(a)). Hydrogen and benzaldehyde are observed as stoichiometric products. To further clarify, whether the selectivity is controlled thermally, the temperature dependent TOFs are investigated (Fig. 10.8(b)) No deoxygenation product like

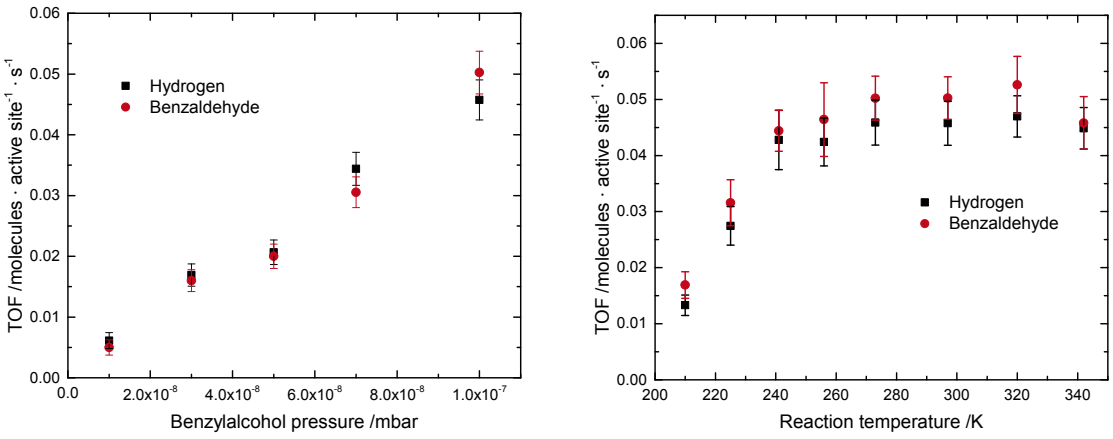

(a) Pressure-dependent TOFs **(b) Temperature-dependent TOFs**

Figure 10.8. (a) Pressure series of benzylalcohol background pressure for photoreforming on 1% Pt_x/r-TiO_2(110) at 280 K. The reaction is stoichiometric towards the benzaldehyde and molecular hydrogen. (b) Temperature-dependent TOFs for $5 \cdot 10^{-8}$ mbar cyclohexanol on 1%Pt_x/r-TiO_2(110). The reaction seems saturated around room temperature and only below 240 K a decrease in the TOF is observed.

toluene are observed that would stem from a thermal reaction channel.[389] Only around 240 K, trace amounts of mass 92 are observed, that could be indicative of the photo-oxidative coupling product benzyl benzoate. However, the raw data signal is barely distinguishable from the background noise, which is why it is refrained from a quantitative evaluation here.

10.1.3. tert-Butanol

As already examined previously (see chap. 8), tert-butanol is interesting mainly from a mechanistic point of view. Since it is a tertiary alcohol, no αH-species can dissociate by the photo-oxidation reaction. Instead, both acetone and isobutene formation have been observed at room temperature with the accompanying by-products methyl-radicals, molecular hydrogen and water, respectively (see Fig. 10.9). The largest amount of direct photo-oxidation of tert-butanol to acetone is obtained at 320 K, accompanied by a stoichiometric methyl-radical ejection and $^1/_2$ H_2 per converted alcohol. Note, that mass 15 is indeed an ejected methyl-radical and not methane as confirmed previously (see Fig. 8.9). Additionally, a second photo-reaction channel is observed as in the previous chapter 8: the dehydration of tert-butanol to isobutene and H_2O;

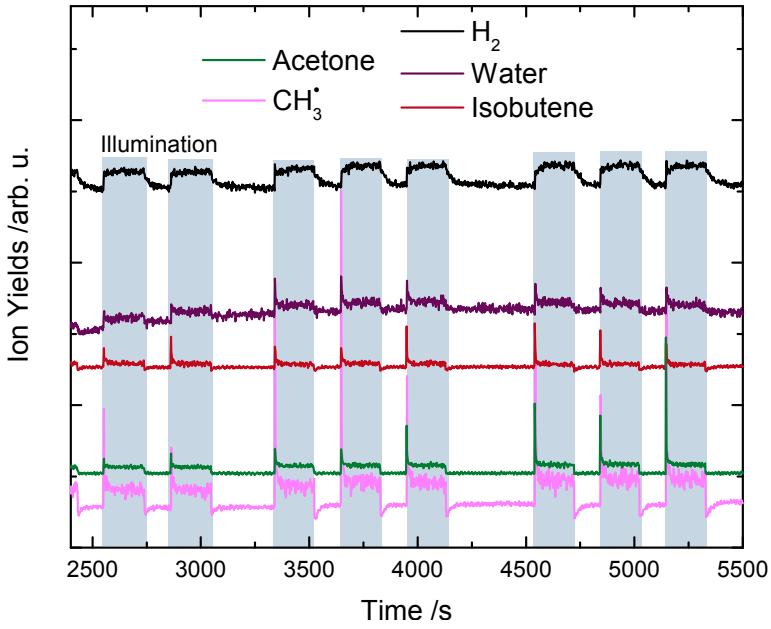

Figure 10.9. Products from a photocatalytic experiment of 1% Pt_x clusters on the r-TiO_2(110) surface in a background of $1 \cdot 10^{-7}$ mbar tert-butanol at 300 K. All relevant molecules are shown and most interestingly, water desorption is also observed upon UV-illumination. Every UV illumination is marked with a light blue box.

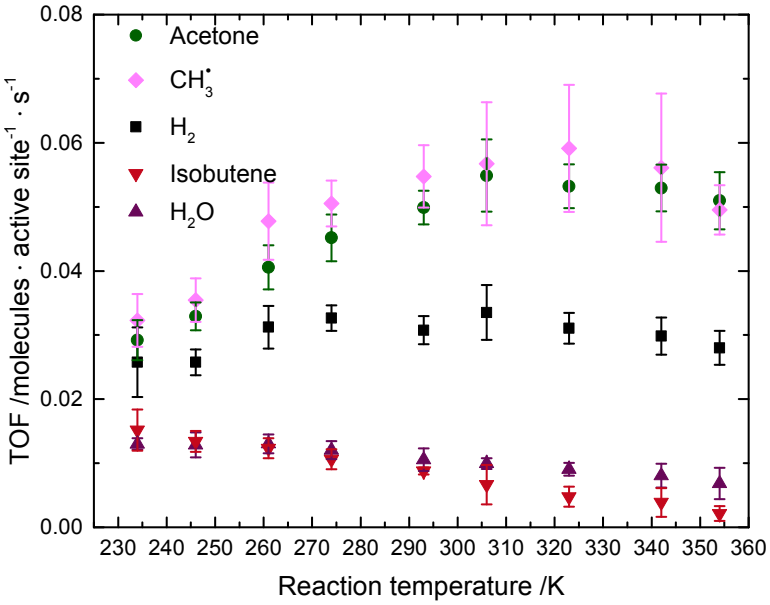

Figure 10.10. Temperature-dependent TOFs for $1 \cdot 10^{-7}$ mbar tert-butanol on 1% Pt_x/r-TiO_2(110). Below room temperature, the TOFs for the photo-oxidation products acetone, H_2 and the methyl-radical rise, until a saturation is observed that carries on until 350 K. Additionally, a second photo-reaction channel is observed, namely the formation of isobutene and water. This reaction channel is relevant especially for temperatures around and below 300 K and it diminishes with a rise in the reaction temperature. Interestingly, water is also formed catalytically even in the presence of platinum and no poisoning is observed.

Both stoichiometric products desorb upon UV-illumination. However, the highest yield is obtained for the coldest investigated temperature and with a rise in reaction temperature, the isobutene and water yields diminish. The selectivity towards acetone is largest at 354 K with 96% and the smallest value is obtained for 234 K with 65% for acetone and 35% for isobutene, respectively.

10.2. Discussion

The results above show that the presented mechanism in Chapter 9 is of general validity, since all investigated alcohols can be oxidized photocatalytically with the desired molecular H_2 as by-product. In the following, molecular mechanisms are presented for all photoreforming reactions.

10.2.1. Photoactive Intermediates and Reaction Sites

The active species and active sites of alcohol photoreforming on the TiO_2(110) surface are still under discussion in literature.[104,116,305,365,394,395,397,402,403,417,418,421,434,443,444,454] For the active species, there are basically two general lines of interpretation: The groups of Yang and Huang share the idea, that the O-H bond cleavage (either homo- or heterolytic) of the alcohol involves a photon-generated hole[104,397,443,454], while the group of Friend and

Henderson's work suggest that the thermally formed alkoxy species are the photoactive ones.[116,365,417,421] Henderson in particular emphasizes explicitly, that the molecular methanol species on TiO_2(110) surfaces are photo-inactive[417] and the thermally formed methoxy species get photo-oxidized.[116] In this regard, the author tends to follow the interpretation of Henderson's work, where only alkoxy species are photoactive on the surface.[2]

Regarding the active site for photo-oxidation, even less is known, mostly because of the lack of in-situ spectroscopic methods with the sensitivity to the subtle differences in sites. Likewise, there are two general lines of interpretation for the photochemical results:

The first line of interpretation is mostly based on thermal chemistry. Many previous STM[308,400,419,455] and TPD studies[285,286,293,456] show clearly that the alcohol adsorbs dissociatively on r-TiO_2(110) in the BBO-vacancy, forming the alkoxy species and surface hydroxyl. As discussed above, the alkoxy are presumably the photoactive species that get oxidized by the photo-hole.[116] Therefore, the justifiable assumption can be made, that the photoreactivity is somehow limited by the number of BBO-vacancies, if the conversion to the photo-product fits the amount of BBO-vacancies as in chapters 8 and 7.2.[305] Note that in the PI-TPD of those studies, still some thermal reaction products are found at high temperatures. This can easily be rationalized, since in general the photo-oxidation products (aldehydes and ketones) desorb at lower temperatures[305,365,396] and clear the defect, when the alcohol is still to some degree on the surface and can repopulate the BBO-vacancies, which in turn then show the high temperature reactivity from the thermal studies to varying extent.[305,397] Yang specifically speculates in a review[104] that the actual amount of photoactive sites is governed by the density of subsurface defects, since the sample history seems to play a role for the ethanol photo-oxidation. Further evidence for the photo-active BBO vacancies is the O_2-PSD, that was believed to take place out of the defect[120,124,207] and defect-mediated in its direct vicinity,[99,457] while in contrary a more recent study identified regular Ti_{5c}-sites as the active sites by STM.[131] In the other line of argumentation, a regular Ti_{5c}-site is deemed to bw the photoactive adsorption site, although the chemical environment of the site itself might be different (such as O-adatoms or terminal hydroxyls in regular Ti_{5c}-sites).[3] The basis of this argumentation is often an oxidative surface preparation (o-TiO_2(110)), where the alkoxy formation is believed to take place on a Ti_{5c}-site at the resulting O-adatoms on the surface.[116,365,402,417,445] The surface itself remains controversial (see Chapter 3.3.1.2), as contradicting STM studies[101,217–219] show that not all BBO vacancies can be filled and, in turn, even more O-adatoms can be formed from molecular oxygen dissociation in regular Ti troughs.[218] On the o-TiO_2(110) surface however, a surface only covered by methoxy-species can be prepared by judicious choice of the adsorption temperatures. Consequently, those methoxy species get photo-oxidized to formaldehyde.[116] Making the assumption, that most of the vacancies are blocked and quantifying the converted

[2] This interpretation is also used in the previous chapters 7.2, 8 and 9.

[3] For trimethyl acetic acid BBO-vacancies were found to inhibit the photo-oxidation.[458]

methoxys to be significantly larger than the initial BBO-vacancy concentration, it is clear that the reaction can in principle also take place on Ti_{5c}-sites. This has also been observed by STM for ethanol by Besenbacher's group, since the population of surface sites before and after the photoreaction showed, that the ethoxys are photo-oxidized more efficiently, while the ones in BBO vacancies react to a lesser extent.[402] A similar assignment of photoreactivity to Ti_{5c}-sites for methanol by Friend's group for o-TiO_2(110).[365,459] Although unclear under illumination conditions, alcohol diffusion[421,460] seems only to be relevant at temperatures of 200 K and higher. Regardless of the surface preparation, Henderson states that the methoxy formation is only initiated by defects, oxygen adatoms or terminal OH groups, but not on the regular surface.[417] Following the longstanding discussion of the degree of water dissociation on TiO_2(110)[215,461,462], Ren's group showed spectroscopically by SFG that methanol can also dissociate to some degree on regular lattice sites.[463,464] To conclude this discussion of the reactive site, the following points seem reasonable: Alkoxy species can be formed thermally on all kinds of defects and maybe to some extent also on regular surface sites. Alkoxy is definitely an intermediate in the photo-oxidation of alcohols, that gets oxidized by a hole to the respective aldehyde or ketone. The oxidized surface (o-TiO_2(110)) offers way more kinds of defects and those are only quantifiable by an tremendous amount of STM studies to get an integral, statistically relevant picture of the surface. Therefore, it is somewhat less defined then the r-TiO_2(110) surface with its BBO-vacancies.[4] For all photoreactive studies only a certain amount of reactant in the range of 5% to 20% is converted.[104,116,117,305,409] For the further interpretation of the results, the authors follows the accepted point of view, that the alkoxy formation occurs thermally and that the photoreaction is somehow in the defect or in its vicinity, and therefore scales with the defect concentration.

It is the author's belief, that the underlying governing factor might be the surface states of the n-type semiconductor. Assuming a constant band-bending, the amount of negatively charged surface states on a n-type semiconductor scales with the bulk doping level[231], which is, in this case, the overall degree of bulk reduction of the semiconductor.[99,466,467] This is in great accordance with the observation of Yang, that the sample history plays a role in the photo-activity.[104] Preparing the oxidized surface presumably creates more surface alterations in form of O adatoms or terminal OH groups by contamination, than expected from a stoichiometric reaction of oxygen with the initial BBO-vacancies.[101,218] These defects all can stabilize charges from other adsorbates, that might lead to a higher band-bending.[98,115] A recent study of the O_2-PSD showed, that even noble gases have a significant influence on the photo-activity of TiO_2(110), which stresses the point of a local assessment of electrostatic potentials of the chemical environment even more.

[4] Ti-interstitials may occur on both surface preparations, but are usually a minority species and only of reactive relevance at elevated temperatures.[465]

10.2.2. A Detailed Mechanistic Picture for Alcohol Reforming

Based on the results and the mechanism of Chapter 9, the overall reaction equation of photocatalytic methanol reforming can be described as the following:

$$CH_3OH + Pt_x/TiO_2 \xrightarrow{h\nu} CH_2O\uparrow + H_2\uparrow + Pt_x/TiO_2 \tag{10.1}$$

However, the mechanistic picture, that can be drawn for the results is much more detailed (see Fig. 10.11). It consists of eight steps, from dissociative adsorption of methanol in the

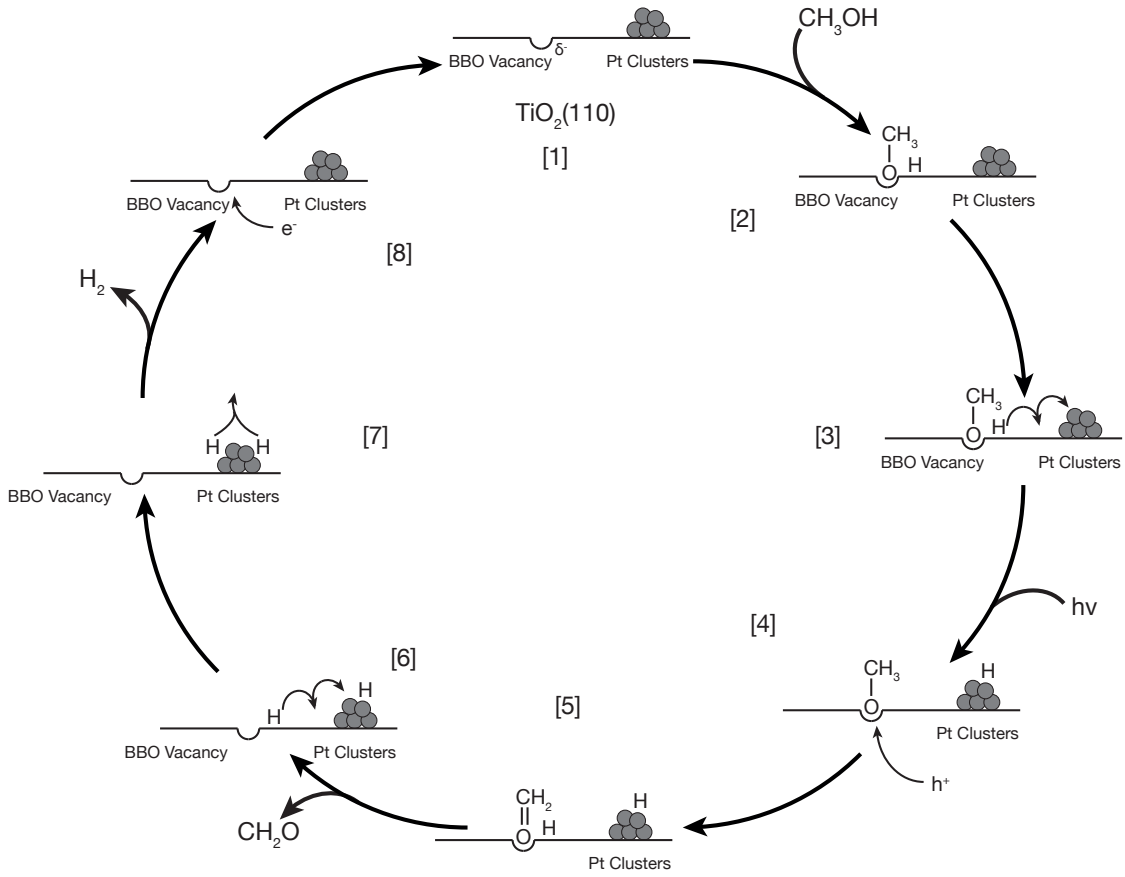

Figure 10.11. The scheme displays a catalytic cycle consisting of elementary steps in the photocatalytic alcohol reforming of methanol to formaldehyde and hydrogen. First, the bare catalyst [1] adsorbs methanol, which adsorbs dissociatively in the BBO vacancies [2]. The abstracted hydrogen atom can then easily diffuse on the surface at the reaction temperatures and presumably to a Pt cluster [3]. When the catalyst is irradiated with UV-light, a photo-generated hole and electron are formed. In the n-type semiconductor, the hole travels to the surface [4], where it can oxidize a methoxy species by αH abstraction to form formaldehyde [5]. The formaldehyde can then thermally desorb and the remaining hydrogen atom can also diffuse on the surface [6]. Two hydrogen atoms can thermally recombine at the Pt cluster [7] to form molecular hydrogen, that desorbs at the reaction temperature. Also charge conservation is obtained, since the defect site is replenished by a photon-generated electron [8] to yield the bare catalyst. Note, that the elementary steps do not necessarily need to occur in this order.

BBO-vacancies to the photo-oxidation of the methoxy to formaldehyde, that eventually desorbs, while the hydrogen atoms liberated in the process can thermally recombine at a platinum cluster and desorb. The charge balance is conserved, since the electron is needed to recharge the defects; else, a flattening of the bands would occur, leading to a drop in photocatalytic reactivity. Theoretical work on a Pt_{13} cluster on a TiO_2 surface shows, that the barriers for the charge carrier diffusion are significantly changed upon H adsorption and strongly depend on the charge density of the adsorbate H and the Pt cluster.[468]

When the reaction conditions are changed to lower temperatures, methylformate as an additional photo-product is observed. This is in good agreement with previous photochemical studies the bare TiO_2(110) surface.[117,365,443] The reaction can be described by the following equation, starting from the intermediate photo-product formaldehyde.

$$CH_3OH + CH_2O + Pt_x/TiO_2 \xrightarrow{h\nu} HCOOCH_3\uparrow + H_2\uparrow + Pt_x/TiO_2 \tag{10.2}$$

The total reaction equation from methanol can be written as follows:

$$2CH_3OH + Pt_x/TiO_2 \xrightarrow{h\nu} HCOOCH_3\uparrow + 2H_2\uparrow + Pt_x/TiO_2 \tag{10.3}$$

The exact nature of the photo-coupling mechanism is still under discussion,[117,365,443,444] but either formaldehyde gets further oxidized by a hole to a formyl species, which then couples with a methoxy or the intermediate species involve the formation of a hemiacetal. In both reaction pathways, a hole photo-oxidizes an intermediate, which is in good agreement with our results (Fig. 10.5). The observed temperature dependence is attributed to the thermal desorption behavior of the first photo-product formaldehyde. If the thermal desorption is hindered for formaldehyde at lower reaction temperatures like 235 K, a second hole can oxidize the formaldehyde leading to methylformate formation. At elevated temperatures in turn, the desorption is faster than a second photo-oxidation reaction.

For ethanol, cyclohexanol and benzylalcohol high selectivities towards hydrogen and the aldehydes and the respective ketone are observed. The proposed reaction model can therefore be generalized for primary and secondary alcohols to the following set of reaction equations:

$$R_2CHOH + TiO_2 \longrightarrow R_2CHO_{ad}/TiO_2 + H_{ad}/TiO_2 \tag{10.4}$$

$$R_2CHO_{ad}/TiO_2 \xrightarrow{h\nu} R_2C{=}O\uparrow + H_{ad}/TiO_2 \tag{10.5}$$

$$2H_{ad}/TiO_2 \xrightarrow{\text{Diffusion}} 2H_{ad}/Pt_x \longrightarrow H_2\uparrow + Pt_x \tag{10.6}$$

The overall reaction equation results in:

$$R_2CHOH \xrightarrow[Pt_x/TiO_2]{h\nu} R_2C{=}O\uparrow + H_2\uparrow \tag{10.7}$$

The unifying idea of this reaction scheme is the αH abstraction of the alkoxy species, that occurs exclusively for the investigate primary and secondary alcohols. The rests R can range from two hydrogen atoms in the case for methanol two a chain of 5 carbon atoms in a 6-membered ring for cyclohexanol. The absence of a further photo-oxidation in general then results in a selectivity of 100%. If further photo-oxidation products are obtained, the judicious selection of the reaction temperature above the desorption temperature of the aldehyde yields very high selectivities up to 100% in the case for methanol.
For the tertiary alcohol tert-butanol, no αH abstraction is possible, but methyl ejection is observed (see Fig. 10.10). The mechanistic picture, however, breaks down for the photo-oxidation channel of tert-butanol to acetone:

$$\underset{\text{tert-butanol}}{(CH_3)_3COH} + TiO_2 \longrightarrow (CH_3)_3CO_{ad}/TiO_2 + H_{ad}TiO_2 \tag{10.8}$$

$$(CH_3)_3CO_{ad}/TiO_2 \xrightarrow{h\nu} \underset{\text{acetone}}{(CH_3)_2C{=}O}\uparrow + CH_3^{\cdot}\uparrow \tag{10.9}$$

$$H_{ad}/TiO_2 \xrightarrow{\text{Diffusion}} H_{ad}/Pt_x \longrightarrow \frac{1}{2}H_2\uparrow + Pt_x \tag{10.10}$$

Although similar to the generalized mechanism presented above, no recombination of the methyl-radical species with the hydrogen is observed. This behavior might drastically change in solution, since those methyl radicals are known to recombine for example in multilayers of water adsorbed on top of them.[108] Further, the so-called photothermal reaction pathway is observed at all investigated temperatures under catalytic conditions:

$$\underset{\text{tert-butanol}}{(CH_3)_3COH} + Vac_{BBO} + O_{BBO} \longrightarrow (CH_3)_3CO{-}Vac_{BBO} + OH_{BBO} \tag{10.11}$$

$$(CH_3)_3CO{-}Vac_{BBO} + OH_{BBO} \xrightarrow{\Delta T} \underset{\text{isobutene}}{C_4H_8} + H_2O + Vac_{BBO} + O_{BBO} \tag{10.12}$$

$$(CH_3)_3CO{-}Vac_{BBO} + OH_{BBO} \xrightarrow{h\nu} \underset{\text{isobutene}}{C_4H_8}\uparrow + H_2O + Vac_{BBO} + O_{BBO} \tag{10.13}$$

This pathway is the same as described in Chapter 8 and does not involve the Pt clusters. As previously discussed, the crucial thermal intermediate (the 5-membered transition state) must be formed at lower temperatures than the observed reaction temperature of 425 K. Note that in all the work in Chapter 8, no desorption of water upon illumination was observed. Since all the other reaction products were recorded in a similar manner, the water desorption upon illumination may be either an effect of catalytic conditions or the platinum clusters on the surface. For a detailed assessment of the desorption behavior of water, more studies are needed.

The overall photoreforming reaction equations for tert-butanol can be described as the combination of the photo-oxidation to acetone and the photothermal reaction pathway to isobutene:

$$\underset{\text{tert-butanol}}{2(CH_3)_3COH} \xrightarrow[Pt_x/TiO_2]{h\nu} \underset{\text{acetone}}{(CH_3)_2C{=}O\uparrow} \underset{\text{isobutene}}{C_4H_8\uparrow} + \frac{1}{2}H_2\uparrow + CH_3^{\cdot}\uparrow + H_2O\uparrow \qquad (10.14)$$

Tert-butanol is the only investigated reactant, that shows two parallel photo-reaction pathways. The selectivity is again temperature dependent ranging from 65% towards acetone at 234 K to 96% towards acetone at 354 K. This selectivity stems from an increase in the acetone conversion with temperature, while the isobutene formation slowly decreases.

10.2.3. Mechanistic Consequences for Applied Systems

The results show that from alcohol-reforming of primary and secondary alcohols, water-free aldeyhdes and ketones can be obtained with highest selectivity. tert-Butanol as a tertiary alcohol is an exception, since both reaction pathways to acetone and isobutene involve a photon as shown previously (see Chapter 8). By the control of the temperature, it is also possible to tune the selectivity towards acetone close to 100%. These high selectivities result on one hand from the selective photo-oxidation process on the TiO_2(110) and on the other hand from the reaction control in the gas-phase. Under these conditions, readsorption of the products is highly unlikely, which makes consecutive reactions less likely. The case of the consecutive photo-coupling to methylformate clearly showed, that by preventing the thermal desorption of formaldehyde intentionally, a further photo-oxidation product was observed. In addition, the reaction conditions are anaerobic, which has a strong influence on the oxidation pathways. Further oxidation in aerobic conditions on TiO_2(110) was observed for formaldehyde[118], acetaldehyde[395,396,398,403] and acetone[253,255–257,416,469], which, in combination with photo-decomposition of organic molecules in general[79], leads to the conclusion that in aerobic conditions a total oxidation of alcohols is indeed possible. Consequently, this is accompanied with a decrease in selectivity. The observed reaction pathways and selectivities for tert-butanol under catalytic conditions are in good agreement with previous studies on the photo-oxidation of tert-butanol on co-catalyst loaded TiO_2 (P25) at 373 K in the gas-phase, where acetone was the main product and trace amounts of isobutene[5] were observed.[411,412] In further studies on alcohol reforming on Pd- and Pt-loaded TiO_2 powders, the hydrogen evolution from tert-butanol was very sluggish.[152,158]

In aqueous solution, a major contribution to photo-oxidation pathways is attributed to indirect hole transfer from $OH^{\cdot}$ radicals.[79,159,160,169,385] Those are in particular believed to be responsible for C-C scission steps and other for the formation of other (radical) intermediates.[31,159] Furthermore, complete oxidation[29,153,168,173,178,470] and reduction products[31,32,168], CO_2 and CH_4 respectively, are also commonly observed. It is clear from

[5] Those were found to stem from a thermal reaction pathway.[412]

the presented mechanistic findings, that they are capable of explaining the products in gas-phase photocatalysis[471,472], but in solution other competitive pathways including oxygen and hydroxyl-radicals might dominate the product distribution. In this regard, a deliberate choice of reactor design, the catalyst and reaction parameters is a prerequisite for highly selective photo-reforming of alcohols.

11

Single-Atom Photocatalysis of Methanol on $Pt_1/TiO_2(110)$ - Co-Catalysts at the Lowest Size-Limit

In this preliminary (and still ongoing) work, the role of the co-catalyst is explored. While in the previous chapters, the co-catalyst was always a distribution of Pt clusters, in this part, the co-catalyst is chosen to be Pt atoms. Those are known to be randomly distributed on r-TiO_2(110) as evidenced by previous AFM study by the group of Onishi[436] and S-TEM work by Shibata[473], which shows also a variety of adsorption sites for Pt atoms. The thermal stability of single atoms on various supports has stimulated quite some academic research recently,[316,319,474,475] since the catalytically active atoms are the lowest possible size-limit for metal catalysts.[476] Single Pt atoms have been shown to be a co-catalyst in photocatalytic hydrogen evolution in general[477,478] and also specifically when

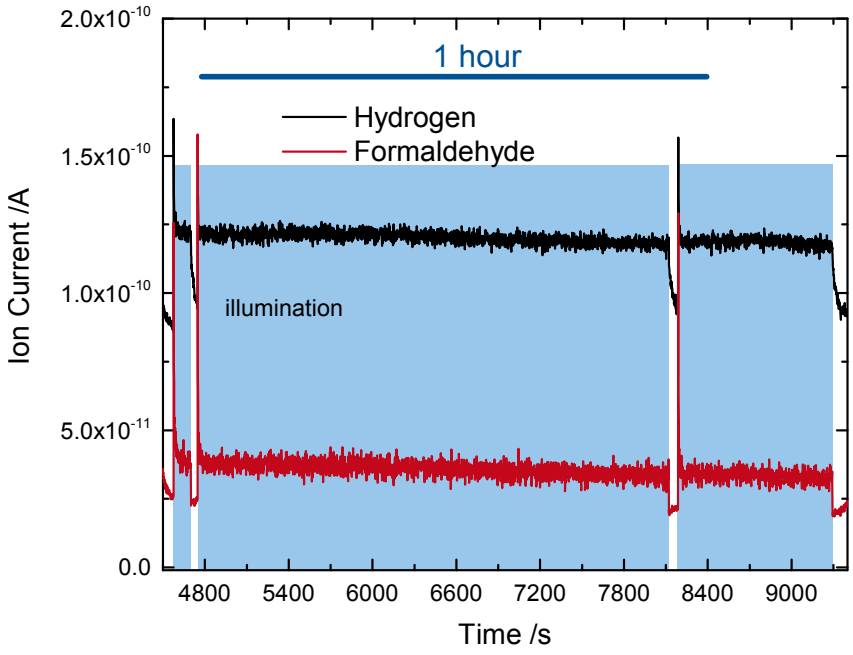

Figure 11.1. Products from a photocatalytic experiment of 1% Pt_1 on the r-TiO_2(110) surface. The UV excitation (shown in light blue) is performed at 241.8 nm with a pulse energy of 218 µJ, the methanol background is set to $1 \cdot 10^{-7}$ mbar and and the reaction temperature is 262 K. Hydrogen and formaldehyde are identified by the masses 2 and 30 respectively and raw data is displayed here.

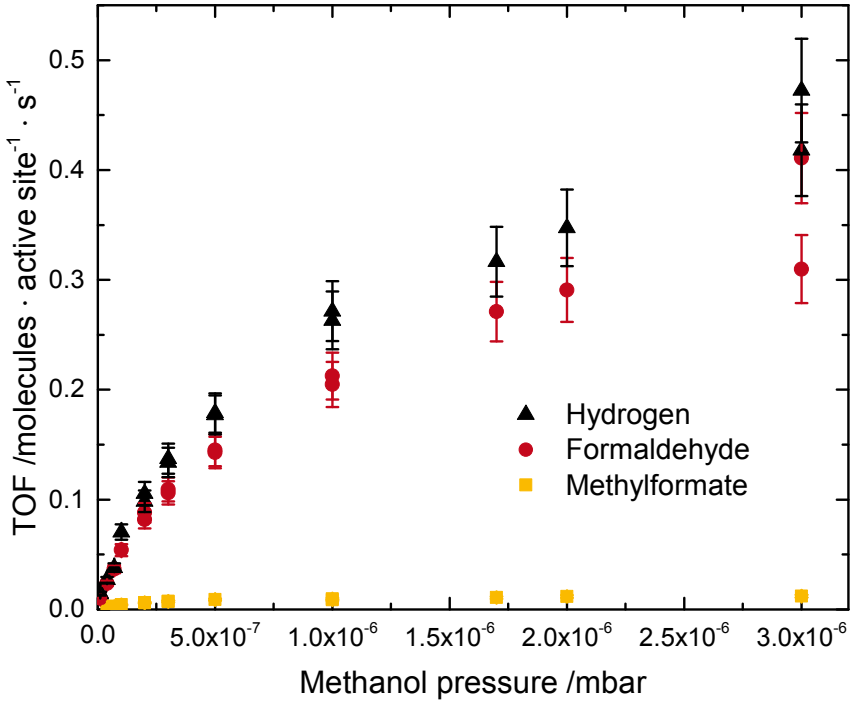

Figure 11.2. Methanol pressure-dependent TOF for Pt_1 on r-TiO_2(110) for photocatalytic conversion. The cluster coverage is 1.0% Pt atoms per TiO_2(110) surface atom and the experiment is run at 260 K. The reaction stoichiometry is independent of the pressure. Every circle, triangle and square resembles a photocatalytic experiment. The data points suggest some saturation at higher pressures, although the value remains unclear.

being supported on TiO_2.[479] Figure 11.1 shows that the photocatalyst is stable for over one hour in a methanol background at 262 K. The slight decay in both curves is observed with a slight decrease in background methanol pressure over the whole time of illumination from $1 \cdot 10^{-7}$ mbar to $9.6 \cdot 10^{-8}$ mbar. Interestingly, a single Pt atom can act as an active site for hydrogen recombination, since the bare r-TiO_2(110) surface does not evolve significant amounts of molecular hydrogen (see Figures 9.7 and 9.8). Further measurements and in-situ characterization methods are needed to confirm that the Pt_1 is really the active species for H_2-evolution, since a possible adsorbate induced diffusion[480] and sintering[481] can not be ruled out.[1] The pressure-dependent TOFs for methanol reforming have been investigated (Fig. 11.2) and a maximal value of 0.4 molecules per active site and second is achieved. The data points suggest, that the gas-phase alcohol reforming somehow saturates, although the exact value is not clear. Methylformate is produced as well on the Pt_1/TiO_2(110) catalyst, but its yield is negligible at higher pressures.
Additionally, the TOF-dependence on the incident light is displayed in Figure 11.3. In analogy to the previous measurements (Fig. 9.10) a saturation is observed around 200 µJ pulse energy. A significant TOF is observed for all pulse energies down to 3 µJ per pulse, which equivales to 0.06 mW/cm^2.

[1] The TOF might not be a good indicator, since differences in two orders of magnitude in cluster coverage did only change the TOF of the photoreaction by a factor of 2 (see Fig. 9.3(b)).

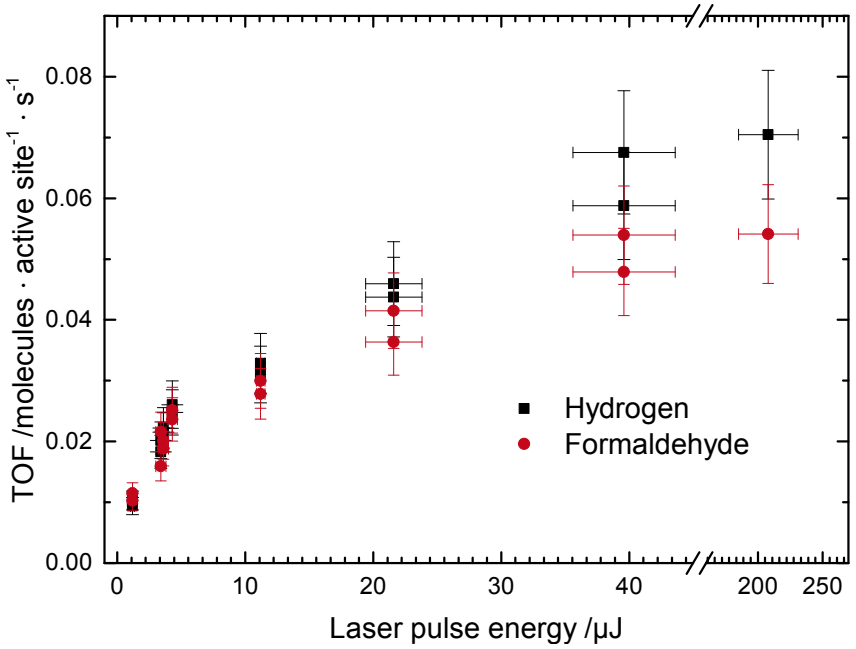

Figure 11.3. Turnover frequencies of formaldehyde and molecular hydrogen in a background of $1 \cdot 10^{-7}$ mbar methanol in dependence on the incident laser pulse energy for 1% Pt_1 on the r-TiO_2(110) at 261 K. A typical pulse energy of 230 µJ is obtained, when the OPO-Laser is operated at 241.8 nm. The error bars are determined by the standard deviation of the laser power, while the error bars in the TOF are 10%. Note, that the pulse energy axis is broken for a better visibility.

In summary, these preliminary results show the remarkable activity of Pt atoms on the r-TiO_2(110) surface and further suggest, that tuning the size of the co-catalyst might be not as important for gas-phase photocatalysis, since one Pt-atom is presumably enough for the recombination and desorption of molecular hydrogen on this surface. This is especially valid for gas-phase reactions, where product readsorption and the undesired backreaction [74–76] do not significantly contribute due to the low pressures in this reaction regime.

12

O_2-PSD from differently prepared TiO_2(110)

The photon-stimulated desorption of O_2 is a commonly used technique to probe the photochemistry of the TiO_2(110) surface.[96,97,123–126,131,132,211,213,416] A very detailed description of known mechanism and the active species can be found elsewhere.[79,131] Especially co-adsorption of organic molecules has been investigated systematically[120,125,132], while the effect of the surface preparation has usually been ignored previously. The O_2-PSD is studied as a model reaction for e.g. the electronic properties of photochemical and photocatalytic systems.[114,115,211]

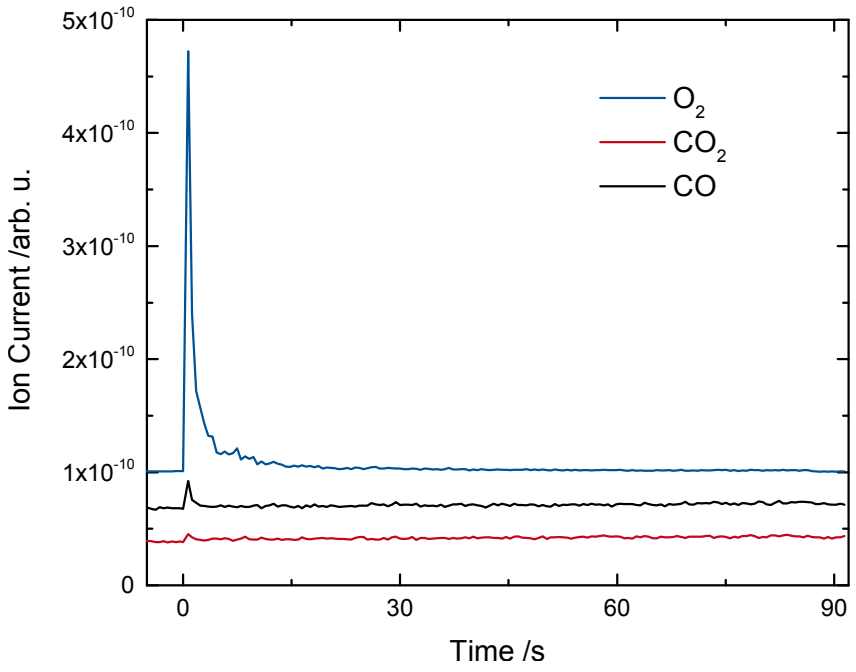

Figure 12.1. O_2-PSD from 1 L molecular oxygen the r-TiO_2(110) surface. Upon UV illumination, a desorption signal of molecular oxygen is obtained (similar to Fig. 3.6). The trace follows a multi-exponential decay, as reported previously.[482] Desorption signals from traces representing CO_2 and CO are also found, that are attributed to background adsorption of CO and its photo-oxidation.[128,129] The UV illumination (242 nm, 600µJ pulse energy) is started at 0 seconds.

12.1. Effect of surface preparation

For a systematic comparison, the three well characterized surface terminations of the TiO_2(110) (described in Chapter 3.3.1) are investigated. On the r-TiO_2(110) surface, three signals upon UV-illumination at 100 K are obtained. The one for molecular oxygen originates most likely from the PSD of an O_2-species on the regular Ti_{5c}-sites from the surface.[131] This study from Henderson found, that the active species is most likely not a O_2^--species on the surface as believed previously[95,97,120], but rather an η^2-O_2^{2-}-species.[131] The active site of the O_2-PSD is assigned to a regular Ti_{5c}-site[131], rather than the BBO vacancy.[95] Further desorbing species from the PSD results from a contamination with CO from the background: The trace amounts of CO_2 formation have been identified as a photo-oxidation product from adsorbed CO and O_2.[128,129] The PSD from CO has only recently been reported to occur from point defects on the TiO_2(110) surface.[281]
To investigate the effect of the surface preparation on the O_2-PSD, the PSD of 1 L of molecular oxygen at 100 K is investigated on the r-TiO_2(110), o-TiO_2(110) and h-TiO_2(110) surfaces (Fig. 12.2).
A previous study with ammonia on the three surface terminations showed that the highest Lewis acidity of the Ti_{5c}-sites is obtained on the r-TiO_2(110) surface. In contrast, it is believed on the o-TiO_2(110) surface that the surface charge is eliminated upon oxidation and the charge is assigned to the electronegative O-adatoms.[101,220,483,484] In contrast, upon hydroxylation, the BBO-vacancy sites are blocked chemically by hydroxyl forma-

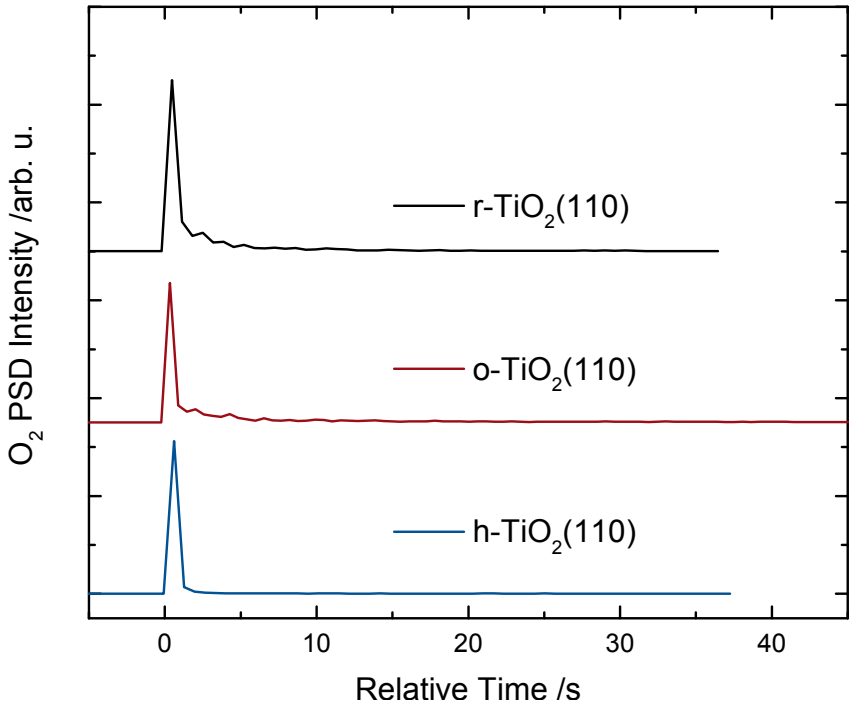

Figure 12.2. O_2-PSD from 1 L molecular oxygen on r-TiO_2(110), o-TiO_2(110) and h-TiO_2(110) at 100 K. A PSD for molecular oxygen of comparable intensity is observed for all surface preparations. The traces are offset for clarity.

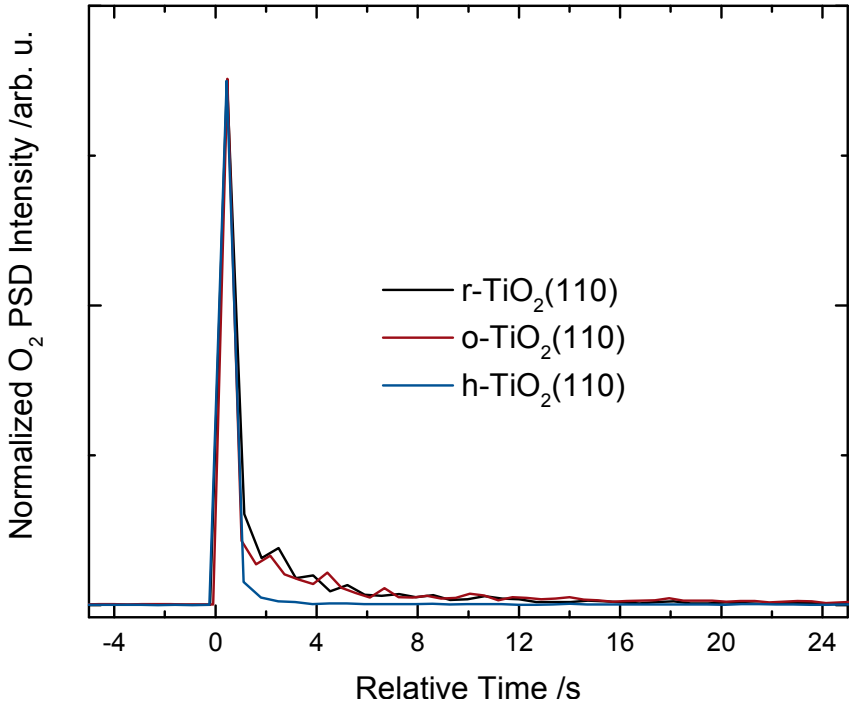

Figure 12.3. Normalized O_2-PSD from 1 L molecular oxygen on r-TiO_2(110), o-TiO_2(110) and h-TiO_2(110) at 100 K. It can be seen, that decay kinetic for the O_2-PSD from the hydroxylated surface may differ from the other ones, but a better time resolution would be needed for a quantitative evaluation.

tion, but remain negatively charged as on the r-TiO_2(110) surface.[220,483,484] The observed PSD intensity for all 3 different surfaces are very similar (Fig. 12.2). This indicates, that the active site is present on all of those surface terminations, which is in good agreement with previous work.[131] Petrik *et al.* compared the intensity of the O_2-PSD from a r-TiO_2(110) with the one from a hydroxylated TiO_2(110) surface.[132] While the exact hydroxylation conditions are not clearly stated, the observed initial intensity is 40% lower than for r-TiO_2(110) surface. The integral amounts of O_2 photodesorption for both terminations look very similar, though. The integral yields of molecular oxygen for the three surface terminations are similar within the experimental error. This indicates, that the O_2-PSD is not affected by a removal of the surface states by a preoxidation of the crystal and also does not occur directly from the BBO-vacancy, since the hydroxylated surface shows also a similar amount.

The study of Petrik *et al.* found that the band bending model can not fully explain the observed differences in the O_2-PSD with co-adsorbates, since also co-adsorption of rare gases also affects the O_2-PSD, while no charge is donated from the rare gases to the semiconductor.[132] Therefore, they stress the importance of the local changes in the electrostatic potential of the surface instead of the very common macroscopic picture. While most studies here focus on the integral desorption yield, photochemical dissociation of molecular oxygen is the other reaction pathway under illumination. The nature of the underlying mechanisms on an atomic scale are still elusive, both the photophysics leading

to the desorption as well as the photochemistry of the dissociation of molecular oxygen. Further studies are needed, but an analysis of the decay kinetics of the desorption of molecular oxygen in very well defined conditions and preparations seems an appropriate way to disentangle the fundamental mechanisms on the surface.

12.2. Effect of Pt-loading

Further measurements of the O_2-PSD are carried out on the r-TiO_2(110) supported Pt clusters, since they have attracted a lot of attention over last years.[102,240,436,441,485–491] The Pt cluster coverage is 1% of a monolayer and size distribution is the same Figures 9.6 and A.6.

In Figure 12.4, the PSDs of 1 L oxygen from the r-TiO_2(110) surface and the Pt_x/r-TiO_2(110) hybrid material are presented. On both, r-TiO_2(110)(a) and Pt_x/r-TiO_2(110), oxygen desorbs upon UV-illumination. The error bars in the measurements represent an experimental uncertainty of 4 measurements. This means, that if the measurements are performed four times, the highest data point will be within the error bar. Clearly, at this time resolution of the measurements, the highest intensity strongly depends on the timing of the mass 32 measurements and the laser illuminating the sample. The limited number of data points also render a fitting of the multi-exponential decay an arbitrary task. The intensity of the PSD on the Pt co-catalyst loaded sample is significantly decreased. While in this value, both the kinetics and the number of active sites are superimposed, the PSDs are normalized to qualitatively analyze the decay rates. This is illustrated in Figure 12.5.

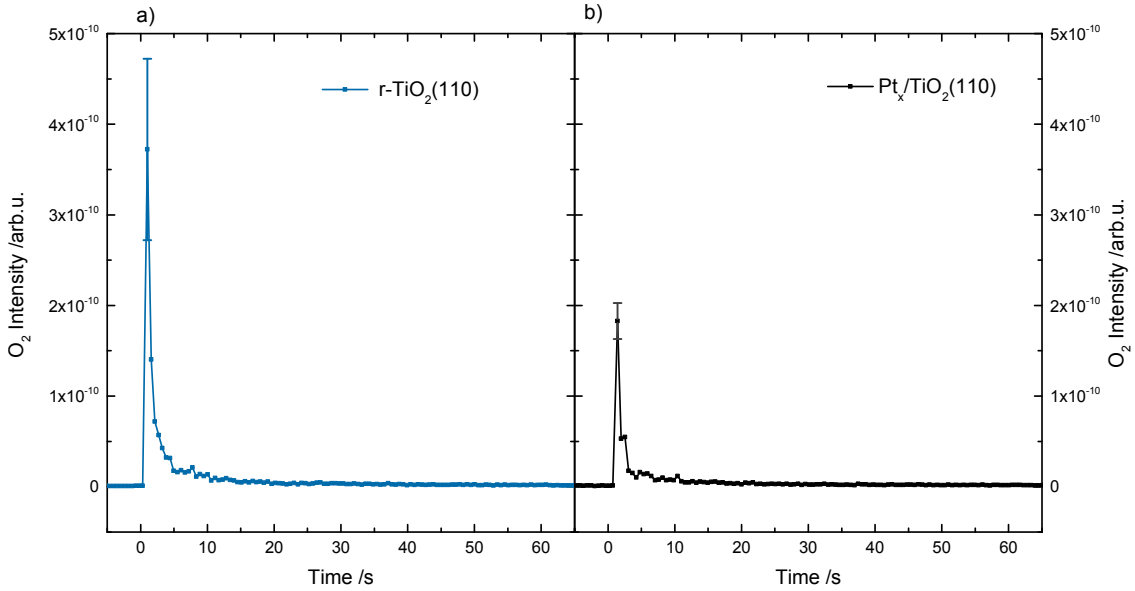

Figure 12.4. O_2-PSD from 1 L molecular oxygen on r-TiO_2(110)(a) and on the Pt_x/r-TiO_2(110)(b) at 100 K. For both surfaces, a PSD signal of oxygen is obtained. The respective error bar at the highest intensity of the molecular oxygen peak represents the experimental uncertainty of the peak intensity of four measurements at this time resolution.

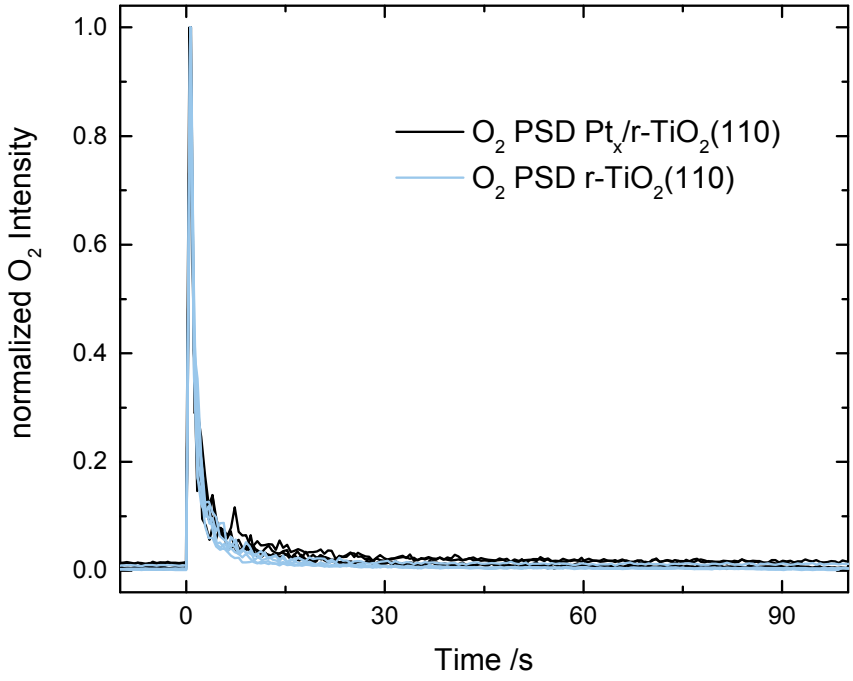

Figure 12.5. Normalized O_2-PSD from 1 L molecular oxygen on r-TiO_2(110) and on the Pt_x/r-TiO_2(110) at 100 K. The decay kinetics are the same within the experimental uncertainty.

The kinetics of all the performed measurements are normalized and show no appreciable difference in these experimental conditions. It seems, that the multi-exponential decay consists of a very fast process with a time constant of a few seconds, and an additional slower one in the range of several seconds up to a minute.

The effect of a metal deposited on the O_2-PSD has been studied once before for the deposition of Au atoms on the r-TiO_2(110) surface.[114] Zhang *et al.* investigated the O_2-PSD in the dependence of the Au atom coverage. Their main finding was a decrease in the initial PSD yield upon higher metal loadings. Their decay kinetics, however, look fairly similar as in the measurements here. The authors of the study attribute the phenomenon to a depression of the photo-induced hole transport rate from the bulk to the surface of the semiconductor. They even predict a downward band-bending for higher Au_1 coverages by DFT. However, if the band bending is so strongly affected by the presumably positively charged gold atoms, one would expect an effect in the decay kinetics of the PSD as well. Furthermore, the possibility of site-blocking and sintering by mobile Au atoms on the surface cannot be ruled out.[492,493]

Pt clusters on oxide supports can also be significantly charged (up to about 2 e^- per cluster), as previous DFT results showed.[236] Although the effect of the Pt co-catalyst are rather of an empiric nature, these results may give the impetus for further studies of the influence of metal loading on basic photochemical processes. While the molecular mechanism presumably does not differ from the bare TiO_2(110) semiconductor, the metal (in this case Pt) is expected to significantly alter the electronic processes upon illumination as shown for other n-type semiconductors.[494] Size selected clusters therefore are

the ideal model system, since they are uniform in distribution and the cluster coverage can be investigated separately from size-effects. Furthermore, XPS, FT-IR measurements and theory may give more insights into the charge state of the cluster on the surface and of the surface itself.[495–498] A combination of these results for the O_2-PSD and its decay kinetics with electronic measurements such as KPFM, CPD and photocurrents of the same or comparable samples will further the understanding of underlying mechanisms of photocatalysis by the unraveling the nature of the governing parameters.

13
Conclusion and Outlook

In this work it is shown how the *surface science approach* can contribute to a more profound understanding of photocatalysis. By the clear assignment of reactive sites both for thermal and photochemical reactions, mechanisms on a molecular scale can be found for both photochemical and photo-thermal reactions. By altering the properties of the semiconductor (e.g. by doping or surface oxidation), the influence on model reactions can be studied successfully. These mechanistic details are a fundamental prerequisite for understanding photocatalytic reactions as shown for alcohol reforming on TiO_2(110) supported platinum clusters. By the combined knowledge of single crystal studies of the photoreaction pathways and the observations under catalytic conditions, a new mechanism is found for the photocatalytic H_2 formation and the observed selectivity for the photo-oxidation reactions was found to depend crucially on the temperature. The plausible correlation of adsorption states, thermal and photochemical products under single coverage and catalytic conditions, with experiments under ambient conditions is of great importance to improve our understanding of fundamental surface chemistry on photocatalytic materials. The findings include details for the semiconductor properties, surface properties and thermal and photochemical reaction mechanisms.

By CO-adsorption, the influence of the bulk doping level on the adsorption properties on the surface is shown for MBE-grown **n-type GaN(0001)**. While the saturation coverage of physisorbed CO is found to be smaller for higher dopant levels, this effect is observed to be independent for the degree of oxidation of the GaN(0001) surface. The latter, however, is a crucial factor governing the photoactivity of the GaN(0001) films towards a **photon-stimulated desorption of CO**.
Ethanol is used as a second probe molecule for the GaN samples. The MOCVD-grown **GaN(0001)** surface shows a remarkable reactivity towards **ethanol dehydrogenation** as the major reaction pathway and dehydration as the minor one without formation of carbon deposits. In contrast to many studies on oxides, as i.e. TiO_2(110), **molecular hydrogen formation** is observed from the GaN samples. Furthermore, ethanol is used as a chemical probe to investigate the **effects of surface oxidation on the reactivity**. Indeed it is found that the reactivity is not observed upon full oxidation of the surface layer, while ethanol still adsorbs dissociatively. By a comparison of the reactivity with $Ga_2O_3(\bar{2}01)$ single crystal, it is observed that the adsorption properties on the oxidized GaN(0001) surface are similar to the clean MBE-grown GaN(0001) sample, while the suppression of the reactivity is assigned to the oxide layer. The results on GaN(0001) already show,

that the observed adsorption properties and reactivity is governed by a delicate balance of bulk electronic influences, the chemical nature of the surface structure and electric charges at the surface (surface states), that can be removed upon oxidation.
In Chapter 6 it is shown that the **ozone preparation of α-Fe_2O_3(0001)** in the ultra-high vacuum leads to the surface termination observed in an ambient atmosphere and water. The thermal reactivity of the typical photochemical hole scavengers methanol and ethanol is benchmarked and three distinct adsorption states are observed for both alcohols. The most strongly bound alkoxy species disproportionate in a high temperature reaction channel to the yield the alcohol and the aldehyde, respectively. While commonly used in photocatalysis, no photoreactivity is observed for ethanol under the investigated conditions.
The experimental improvement of the apparatus has lead to the addition of an OPO laser as a UV light source, a load lock with a sample transfer holder, a molecular beam doser and the **cluster source**. The latter allows for the synthesis of TiO_2(110) supported Pt clusters, that are used as co-catalyst for photocatalysis.
As a prerequisite for understanding photochemical mechanisms on the **TiO_2(110)** surface, the **thermal chemistry of ethanol** is studied in a quantitative way and the bridge bonding oxygen vacancies are found to be the reactive sites. The O_2-PSD is investigated over the whole work, to further the understanding of the effects of surface termination and the presence of a co-catalyst on a **photochemical probe reaction**.
By a judicious choice of illumination length and temperature, the **molecular mechanism of ethanol photo-oxidation** iss unravelled. The photo-generated hole oxidizes an ethoxy species in a defect to acetaldehyde, while the hydrogen atoms eventually desorb as stoichiometric water formation. The photoreactivity eventually vanishes by a site-blocking (steric and/or electronic) of the formed hydroxyls, that desorb as water at higher temperatures, leading to a formal reduction of the surface. This hydroxylation leads to a poisoning for the photo-oxidation of alcohols.
To avoid the poisoning of the TiO_2(110) catalyst, Pt clusters are deposited as a co-catalyst and a photocatalytic reaction is found for methanol under conditions. The findings (see chapter 9) lead to the formulation of a **new photocatalytic mechanism for hydrogen formation** from alcohol photo-oxidation. The hydrogen evolution does not take place by the reduction of a proton from solution, but by the thermal formation and consecutive desorption of molecular hydrogen from the Pt clusters. This mechanism of the H_2 formation occurs even on the smallest co-catalysts investigated in this work, Pt atoms. The oxidation reaction is driven by the photoholes from the n-type semiconductor takes place on the semiconductor without the involvement of the co-catalyst and is a one photon process. Based on band-bending of the n-type semiconductor, charge conservation, the investigated reaction conditions and the observed reaction products, the reduction of protons by photoelectrons can be ruled out as the mechanism of hydrogen evolution.
An investigation of photocatalytic reforming of other alcohols, such as ethanol, cyclohexanol, tert-butanol and benzylalcohol, further confirmed established mechanism of the hydrogen evolution reaction and unravels a **new reaction pathways of alcohol pho-**

tochemistry. In addition to the photo-oxidation, a **new photo-thermal mechanism** is found, for which the originally thermal dehydration of tert-butanol to isobutene is observed below the thermal reaction temperature upon UV illumination in addition to the photo-oxidation of tert-butanol to acetone via a methyl radical ejection.
Furthermore, the **reaction temperature** is found to be crucial for the observed **selectivity of the photo-oxidation** products in this work. While the photo-oxidiation reaction on TiO_2(110) supported Pt clusters is found to be highly selective for cyclohexanol, ethanol and benzylalcohol, for methanol and tert-butanol, consecutive and parallel reaction channels are found in agreement with previous single crystal studies. The selectivity of the reaction pathways depends crucially on the reaction temperature. The consecutive photoreaction to methylformate can be explained by a thermally hindered desorption of formaldehyde, that gets photo-oxidized further, while the photo-oxidation of tert-butanol and the photo-thermal dehydration are found to be parallel reactions under catalytic conditions.

In the future, this unique apparatus offers many different possibilities for the investigation of photocatalytic systems in very well defined conditions. Fundamentally interesting directions include the study the effects upon co-catalyst loading on very simple model reactions like to O_2 or CO PSD, in order to gain a deeper understanding of the electronic effects stemming from the catalyst and from co-adsorbates on the photochemical reactions. Another very interesting direction is the search for a co-catalyst for the oxidation side of a photocatalytic reaction, most prominently for water-splitting. A promising approach is the deposition of a model co-catalyst material, which are known to be oxygen evolution catalysts under ambient conditions, such as a Ru_xO_y or Ni_xO_y. For these clusters their cluster size and chemical composition can be tuned for a maximal oxygen evolution from adsorbed water. This will also expand then the semiconductor materials that can be studied under catalytic conditions, since the oxidation reaction does no longer take place on the semiconductor itself, other than observed in this work. An intriguing investigation includes the use of bimodal co-catalysts, namely a size-selected metal oxide cluster for the oxidation reaction and very small metallic clusters for the hydrogen evolution. This offers a wide parameter space of two co-catalyst loadings, different preparation conditions of the surface and, furthermore, of all bulk semiconductor properties such as the charge carrier concentrations and the band gap.

Bibliography

[1] Fujishima, A.; Honda, K. *Nature* **1972**, *238*, 37 – 38.

[2] Serpone, N.; Emeline, A. V. *J. Phys. Chem. Lett.* **2012**, *3*, 673–677.

[3] Friedmann, D.; Hakki, A.; Kim, H.; Choi, W.; Bahnemann, D. *Green Chem.* **2016**, *18*, 5391–5411.

[4] Chen, X.; Shen, S.; Guo, L.; Mao, S. S. *Chem. Rev. (Washington, DC, U.S.)* **2010**, *110*, 6503–6570.

[5] Panayotov, D. A.; Morris, J. R. *Surf. Sci. Rep.* **2016**, *71*, 77–271.

[6] Osterloh, F. E. *ACS Energy Lett.* **2017**, *2*, 445–453.

[7] Tran, P. D.; Wong, L. H.; Barber, J.; Loo, J. S. C. *Energy Environ. Sci.* **2012**, *5*, 5902 – 5918.

[8] Teoh, W. Y.; Scott, J. A.; Amal, R. *J. Phys. Chem. Lett.* **2012**, *3*, 629 – 639.

[9] Service, R. F. *Science* **2002**, *297*, 2189 – 2190.

[10] Takanabe, K. *ACS Catal.* **2017**, *11*, 8006–8022.

[11] Barber, J. *Phil. Trans. R. Soc. A* **2007**, *365*, 1007–1023.

[12] Niemantsverdriet, J. W.; Chorkendorff, I. *Concepts of Modern Catalysis and Kinetics*, 2nd ed.; Wiley-VCH, 2007.

[13] Kim, D.; Sakimoto, K. K.; Hong, D.; Yang, P. *Angew. Chem. Int. Ed.* **2015**, *54*, 3259–3266.

[14] Eberle, D. U.; von Helmolt, D. R. *Energy Environ. Sci.* **2010**, *3*, 689–699.

[15] Mathias, M. F.; Makharia, R.; Gasteiger, H. A.; Conley, J. J.; Fuller, T.; Gittleman, C. J.; Kocha, S. S.; Miller, D. P.; Mittelsteadt, C. K.; Xie, T.; Yan, S. G.; Yu, P. T. *Electrochem. Soc. Interface* **2005**, 24 – 35.

[16] Gasteiger, H. A.; Markovic, N. M. *Science* **2009**, *324*, 48 – 49.

[17] Fabian, D. M.; Hu, S.; Singh, N.; Houle, F. A.; Hisatomi, T.; Domen, K.; Osterloh, F. E.; Ardo, S. *Energy Environ. Sci.* **2015**, *8*, 2825–2850.

[18] Faunce, T. A.; Lubitz, W.; Rutherford, A. W. B.; MacFarlane, D.; Moore, G. F.; Yang, P.; Nocera, D. G.; Moore, T. A.; Gregory, D. H.; Fukuzumi, S.; Yoon, K. B.; Armstrong, F. A.; Wasielewski, M. R.; Styring, S. *Energy Environ. Sci.* **2013**, *6*, 695 – 698.

[19] Vesborg, P. C. K.; Jaramillo, T. F. *RSC Adv.* **2012**, *2*, 7933–7947.

[20] Gray, H. B. *Nat. Chem.* **2009**, *1*, 7.

[21] McKone, J. R.; Lewis, N. S.; Gray, H. B. *Chemistry of Materials* **2014**, *26*, 407 – 414.

[22] Turner, J. A. *Science* **2004**, *305*, 972–974.

[23] Yuliati, L.; Yoshida, H. *Chem. Soc. Rev.* **2008**, *37*, 1592–1602.

[24] Sastre, F.; Oteri, M.; Corma, A.; Garcia, H. *Energy Environ. Sci.* **2013**, *6*, 2211–2215.

[25] Sastre, F.; Puga, A. V.; Liu, L.; Corma, A.; García, H. *J. Am. Chem. Soc.* **2014**, *136*, 6798–6801.

[26] Yuliati, L.; Itoh, H.; Yoshida, H. *Chem. Phys. Lett.* **2008**, *452*, 178–182.

[27] Habisreutinger, S. N.; Schmidt-Mende, L.; Stolarczyk, J. K. *Angew. Chem. Int. Ed.* **2013**, *52*, 7372–7408.

[28] Zhou, X.; Liu, R.; Sun, K.; Chen, Y.; Verlage, E.; Francis, S. A.; Lewis, N. S.; Xiang, C. *ACS Energy Lett.* **2016**, *1*, 764–770.

[29] Chiarello, G. L.; Aguirre, M. H.; Selli, E. *J. Catal.* **2010**, *273*, 182–190.

[30] Christoforidis, K. C.; Fornasiero, P. *ChemCatChem* **2017**, *9*, 1523–1544.

[31] Cargnello, M.; Gasparotto, A.; Gombac, V.; Montini, T.; Barreca, D.; Fornasiero, P. *Eur. J. Inorg. Chem.* **2011**, *28*, 4309–4323.

[32] Murdoch, M.; Waterhouse, G. I. N.; Nadeem, M.; Metson, J. B.; Keane, M. A.; Howe, R. F.; Llorca, J.; Idriss, H. *Nat Chem* **2011**, *3*, 489 – 492.

[33] Jovic, V.; Al-Azri, Z.; Chen, W.-T.; Sun-Waterhouse, D.; Idriss, H.; Waterhouse, G. I. *Top. Catal.* **2013**, *56*, 1139–1151.

[34] Navarro, R. M.; Sanchez-Sanchez, M. C.; Alvarez-Galvan, M. C.; Valle, F. d.; Fierro, J. L. G. *Energy Environ. Sci.* **2009**, *2*, 35–54.

[35] Shimura, K.; Yoshida, H. *Energy Environ. Sci.* **2011**, *4*, 2467–2481.

[36] Agustina, T.; Ang, H.; Vareek, V. *J. Photochem. Photobiol., C* **2005**, *6*, 264–273.

[37] Ilie, M.; Cojocaru, B.; Parvulescu, V. I.; Garcia, H. *Int. J. Hydrogen Energy* **2011**, *36*, 15509–15518.

[38] Sasaki, Y.; Nemoto, H.; Saito, K.; Kudo, A. *J. Phys. Chem. C* **2009**, *113*, 17536–17542.

[39] Lewis, N. S. *Science* **2016**, *351*.

[40] Greg Wilson, S. K.; Werner, M. https://www.nrel.gov/pv/assets/images/efficiency-chart.png, checked on January 25th, 2018.

[41] Ohtani, B. *J. Photochem. Photobiol., C* **2010**, *11*, 157–178.

[42] Ohtani, B. *Chem. Lett.* **2008**, *37*, 216–229.

[43] Kudo, A.; Miseki, Y. *Chem. Soc. Rev.* **2009**, *38*, 253 – 278.

[44] Kato, H.; Asakura, K.; Kudo, A. *J. Am. Chem. Soc.* **2003**, *125*, 3082–3089.

[45] Hara, M.; Kondo, T.; Komoda, M.; Ikeda, S.; N. Kondo, J.; Domen, K.; Hara, M.; Shinohara, K.; Tanaka, A. *Chem. Commun.* **1998**, *3*, 357–358.

[46] Zou, Z.; Ye, J.; Sayama, K.; Arakawa, H. *Nature* **2001**, *414*, 625 – 627.

[47] Maeda, K.; Teramura, K.; Domen, K. *J. Catal.* **2008**, *254*, 198–204.

[48] Mubeen, S.; Lee, J.; Singh, N.; Kramer, S.; Stucky, G. D.; Muskovits, M. *Nat. Nanotechnol.* **2013**, *8*, 247.

[49] Maeda, K.; Lu, D.; Domen, K. *Chem.—Eur. J.* **2013**, *19*, 4986–4991.

[50] Sasaki, Y.; Iwase, A.; Kato, H.; Kudo, A. *J. Catal.* **2008**, *259*, 133–137.

[51] Asai, R.; Nemoto, H.; Jia, Q.; Saito, K.; Iwase, A.; Kudo, A. *Chem. Commun.* **2014**, *50*, 2543–2546.

[52] Liu, J.; Liu, Y.; Liu, N.; Han, Y.; Zhang, X.; Huang, H.; Lifshitz, Y.; Lee, S.-T.; Zhong, J.; Kang, Z. *Science* **2015**, *347*, 970–974.

[53] Xu, J.; Pan, C.; Takata, T.; Domen, K. *Chem. Commun.* **2015**, *51*, 7191–7194.

[54] Pan, C.; Takata, T.; Nakabayashi, M.; Matsumoto, T.; Shibata, N.; Ikuhara, Y.; Domen, K. *Angew. Chem. Int. Ed.* **2015**, *54*, 2955–2959.

[55] Yang, J.; Jiang, P.; Yue, M.; Yang, D.; Cong, R.; Gao, W.; Yang, T. *J. Catal.* **2017**, *345*, 236–244.

[56] Gao, L.; Li, Y.; Ren, J.; Wang, S.; Wang, R.; Fu, G.; Hu, Y. *Appl. Catal., B: Environ.* **2017**, *202*, 127–133.

[57] Wang, Q.; Hisatomi, T.; Ma, S. S. K.; Li, Y.; Domen, K. *Chem. Mat.* **2014**, *26*, 4144–4150.

[58] Maeda, K.; Takata, T.; Hara, M.; Saito, N.; Inoue, Y.; Kobayashi, H.; Domen, K. *J. Am. Chem. Soc.* **2005**, *127*, 8286 – 8287.

[59] Higashi, M.; Abe, R.; Teramura, K.; Takata, T.; Ohtani, B.; Domen, K. *Chem. Phys. Lett.* **2008**, *452*, 120–123.

[60] Abe, R.; Higashi, M.; Domen, K. *J. Am. Chem. Soc.* **2010**, *132*, 11828–11829.

[61] Miseki, Y.; Fujiyoshi, S.; Gunji, T.; Sayama, K. *Catal. Sci. Technol.* **2013**, *3*, 1750–1756.

[62] Abe, R.; Shinmei, K.; Koumura, N.; Hara, K.; Ohtani, B. *J. Am. Chem. Soc.* **2013**, *135*, 16872–16884.

[63] Kobayashi, R.; Tanigawa, S.; Takashima, T.; Ohtani, B.; Irie, H. *J. Phys. Chem. C* **2014**, *118*, 22450–22456.

[64] Nakada, A.; Nishioka, S.; Vequizo, J. J. M.; Muraoka, K.; Kanazawa, T.; Yamakata, A.; Nozawa, S.; Kumagai, H.; Adachi, S.-i.; Ishitani, O.; Maeda, K. *J. Mater. Chem. A* **2017**, *5*, 11710–11719.

[65] Goto, Y. et al. *Joule* **2018**,

[66] Hamann, C. H.; Vielstich, W. *Elektrochemie*, 4th ed.; Wiley-VCH, 2005.

[67] Young, K. M. H.; Klahr, B. M.; Zandi, O.; Hamann, T. W. *Catal. Sci. Technol.* **2013**, *3*, 1660–1671.

[68] Seitz, L. C.; Dickens, C. F.; Nishio, K.; Hikita, Y.; Montoya, J.; Doyle, A.; Kirk, C.; Vojvodic, A.; Hwang, H. Y.; Norskov, J. K.; Jaramillo, T. F. *Science* **2016**, *353*, 1011–1014.

[69] Niishiro, R.; Takano, Y.; Jia, Q.; Yamaguchi, M.; Iwase, A.; Kuang, Y.; Minegishi, T.; Yamada, T.; Domen, K.; Kudo, A. *Chem. Commun.* **2017**, *53*, 629–632.

[70] Stoerzinger, K. A.; Diaz-Morales, O.; Kolb, M.; Rao, R. R.; Frydendal, R.; Qiao, L.; Wang, X. R.; Halck, N. B.; Rossmeisl, J.; Hansen, H. A.; Vegge, T.; Stephens, I. E. L.; Koper, M. T. M.; Shao-Horn, Y. *ACS Energy Lett.* **2017**, *2*, 876–881.

[71] Grimaud, A.; Diaz-Morales, O.; Han, B.; Hong, W. T.; Lee, Y.-L.; Giordano, L.; Stoerzinger, K. A.; Koper, M. T. M.; Shao-Horn, Y. *Nat Chem* **2017**, *9*, 457–465.

[72] Zachaus, C.; Abdi, F. F.; Peter, L. M.; van de Krol, R. *Chem. Sci.* **2017**, *8*, 3712–3719.

[73] Pan, C.; Takata, T.; Khine Ma, S. S.; Ueda, K.; Minegishi, T.; Nakabayashi, M.; Matsumoto, T.; Shibata, N.; Ikuhara, Y.; Domen, K. *J. Mater. Chem. A* **2016**, *4*, 4544–4552.

[74] Maeda, K.; Xiong, A.; Yoshinaga, T.; Ikeda, T.; Sakamoto, N.; Hisatomi, T.; Takashima, M.; Lu, D.; Kanehara, M.; Setoyama, T.; Teranishi, T.; Domen, K. *Angew. Chem. Int. Ed.* **2010**, *122*, 4190 – 4193.

[75] Maeda, K.; Teramura, K.; Lu, D.; Saito, N.; Inoue, Y.; Domen, K. *Angew. Chem. Int. Ed.* **2006**, *118*, 1521–3757.

[76] Berto, T. F.; Sanwald, K. E.; Byers, J. P.; Browning, N. D.; Gutiérrez, O. Y.; Lercher, J. A. *J. Phys. Chem. Lett.* **2016**, *7*, 4358–4362.

[77] Zhou, X.; Dong, H.; Ren, A.-M. *Phys. Chem. Chem. Phys.* **2016**, *18*, 11111–11119.

[78] Ohtani, B.; Prieto-Mahaney, O.; Li, D.; Abe, R. *J. Photochem. Photobiol., A* **2010**, *216*, 179–182.

[79] Henderson, M. A. *Surf. Sci. Rep.* **2011**, *66*, 185 – 297.

[80] Kho, Y. K.; Iwase, A.; Teoh, W. Y.; Mädler, L.; Kudo, A.; Amal, R. *J. Phys. Chem. C* **2010**, *114*, 2821 – 2829.

[81] Connelly, K. A.; Idriss, H. *Green Chem.* **2012**, *14*, 260 – 280.

[82] Ohtani, B. *Front. Chem.* **2017**, *5*, 79.

[83] Nitta, A.; Takashima, M.; Murakami, N.; Takase, M.; Ohtani, B. *Electrochim. Acta* **2017**,

[84] Nitta, A.; Takase, M.; Takashima, M.; Murakami, N.; Ohtani, B. *Chem. Commun.* **2016**, *52*, 12096–12099.

[85] Marsh, A. L.; Ribeiro, F. H.; Somorjai, G. A. In *Handbook of Heterogeneous Catalysis*, 2nd ed.; Ertl, G., Knözinger, H., Schüth, F., Weitkamp, J., Eds.; Wiley-VCH, 2008.

[86] Ertl, G. In *Reactions at Solid Surfaces*; Ertl, G., Ed.; 1; John Wiley & Sons, 2009; Vol. 1.

[87] Zaera, F. *J. Phys. Chem. B* **2002**, *106*, 4043–4052.

[88] Zaera, F. *Phys. Chem. Chem. Phys.* **2013**, *15*, 11866–12003.

[89] Brandt, K.; Chiu, M. E.; Watson, D. J.; Tikhov, M. S.; Lambert, R. M. *J. Phys. Chem. C* **2012**, *116*, 4605–4611.

[90] Böcklein, S.; Günther, S.; Wintterlin, J. *Angew. Chem. Int. Ed.* **2013**, *52*, 5518–5521.

[91] Stoltze, P.; Nørskov, J. K. *Phys. Rev. Lett.* **1985**, *55*, 2502–2505.

[92] Norskov, J. K.; Abild-Pedersen, F.; Studt, F.; Bligaard, T. *Proc. Natl. Acad. Sci. U.S.A.* **2011**, *108*, 937 – 943.

[93] Somorjai, G. A.; Kliewer, C. J. *React. Kinet. Catal. Lett.* **2009**, *96*, 191–208.

[94] Linsebigler, A. L.; Lu, G.; Yates, J. T. *Chem. Rev. (Washington, DC, U.S.)* **1995**, *95*, 735 – 758.

[95] Thompson, T. L.; Yates, J. T. *Top. Catal.* **2005**, *35*, 197 – 210.

[96] Thompson, T. L.; Yates, J. T. *Chem. Rev. (Washington, DC, U.S.)* **2006**, *106*, 4428 – 4453.

[97] Yates Jr., J. T. *Surf. Sci.* **2009**, *603*, 1605 – 1612.

[98] Zhang, Z.; Yates, J. T. *Chem. Rev. (Washington, DC, U.S.)* **2012**, *112*, 5520–5551.

[99] Diebold, U. *Surf. Sci. Rep.* **2003**, *48*, 53 – 229.

[100] Lun Pang, C.; Lindsay, R.; Thornton, G. *Chem. Soc. Rev.* **2008**, *37*, 2328–2353.

[101] Dohnalek, Z. and Lyubinetsky, I. and Rousseau, R., *Prog. Surf. Sci.* **2010**, *85*, 161–205.

[102] Pang, C. L.; Lindsay, R.; Thornton, G. *Chem. Rev. (Washington, DC, U.S.)* **2013**, *113*, 3887–3948.

[103] Hussain, H.; Tocci, B.; Woolcot, T.; Torrelles, X.; Pang, C. L.; Humphrey, D. S.; Yim, C. M.; Grinter, D. C.; Cabailh, G.; Bikonda, O.; Lindsay, R.; Zegenhagen, J.; Michaelides, A.; Thonrton, G. *Nat Mater* **2016**, *16*, 461.

[104] Guo, Q.; Zhou, C.; Ma, Z.; Ren, Z.; Fan, H.; Yang, X. *Chem. Soc. Rev.* **2015**,

[105] Walker, A. V.; Yates, J. T. *J. Phys. Chem. B* **2000**, *104*, 9038–9043.

[106] Setvin, M.; Shi, X.; Hulva, J.; Simschitz, T.; Parkinson, G. S.; Schmid, M.; Di Valentin, C.; Selloni, A.; Diebold, U. *ACS Catal.* **2017**, 7081–7091.

[107] Henderson, M.; White, J.; Uetsuka, H.; Onishi, H. *J. Catal.* **2006**, *238*, 153–164.

[108] Shen, M.; Henderson, M. A. *J. Phys. Chem. C* **2011**, *115*, 5886–5893.

[109] Henderson, M. A. *J. Phys. Chem. C* **2015**,

[110] Chambers, S.; Williams, J.; Henderson, M.; Joly, A.; Varela, M.; Pennycook, S. *Surf. Sci.* **2005**, *587*, 197–207.

[111] Henderson, M. A. *J. Phys. Chem. C* **2014**,

[112] Heeskens, D.; Aghaei, P.; Kaluza, S.; Strunk, J.; Muhler, M. *phys. status solidi (b)* **2013**, *250*, 1107–1118.

[113] Atsumi, S.; Hanai, T.; Liao, J. C. *Nature* **2008**, *451*, 86–89.

[114] Zhang, Z.; Tang, W.; Neurock, M.; Yates, J. T. *J. Phys. Chem. C* **2011**, *115*, 23848–23853.

[115] Zhang, Z.; Yates, J. T. *J. Phys. Chem. Lett.* **2010**, *1*, 2185–2188.

[116] Shen, M.; Henderson, M. A. *J. Phys. Chem. Lett.* **2011**, *2*, 2707–2710.

[117] Guo, Q.; Xu, C.; Yang, W.; Ren, Z.; Ma, Z.; Dai, D.; Minton, T. K.; Yang, X. *J. Phys. Chem. C* **2013**, *117*, 5293–5300.

[118] Cremer, T.; Jensen, S. C.; Friend, C. M. *J. Phys. Chem. C* **2014**, *118*, 29242–29251.

[119] Xiong, F.; Yin, L.-L.; Wang, Z.; Jin, Y.; Sun, G.; Gong, X.-Q.; Huang, W. *J. Phys. Chem. C* **2017**, *121*, 9991–9999.

[120] Thompson, T. L.; Yates, J. T. *J. Phys. Chem. B* **2005**, *109*, 18230–18236.

[121] Henderson, M. A.; Lyubinetsky, I. *Chem. Rev.* **2013**, *113*, 4428 – 4455.

[122] Petrik, N. G.; Kimmel, G. A. *J. Phys. Chem. Lett.* **2010**, *1*, 1758–1762.

[123] Petrik, N. G.; Kimmel, G. A. *J. Phys. Chem. C* **2011**, *115*, 152–164.

[124] Petrik, N. G.; Kimmel, G. A. *J. Phys. Chem. Lett.* **2011**, *2*, 2790–2796.

[125] Petrik, N. G.; Kimmel, G. A. *Phys. Chem. Chem. Phys.* **2014**, *16*, 2338–2346.

[126] Wang, Z.-T.; Deskins, N. A.; Lyubinetsky, I. *J. Phys. Chem. Lett.* **2012**, *3*, 102–106.

[127] Petrik, N. G.; Kimmel, G. A. *J. Phys. Chem. Lett.* **2013**, *4*, 344–349.

[128] Linsebigler, A.; Lu, G.; Yates, J. T. *J. Phys. Chem.* **1996**, *100*, 6631–6636.

[129] Linsebigler, A.; Rusu, C.; Yates, J. T. *J. Am. Chem. Soc.* **1996**, *118*, 5284–5289.

[130] Zhang, Z.; Yates, J. T. *J. Am. Chem. Soc.* **2010**, *132*, 12804–12807.

[131] Henderson, M. A.; Shen, M.; Wang, Z.-T.; Lyubinetsky, I. *J. Phys. Chem. C* **2013**, *117*, 5774–5784.

[132] Petrik, N. G.; Kimmel, G. A.; Shen, M.; Henderson, M. A. *Surf. Sci.* **2016**, *652*, 183–189.

[133] Henderson, M. A. *J. Phys. Chem. C* **2013**, *117*, 14113 – 14124.

[134] Henderson, M. A. *J. Phys. Chem. C* **2013**, *117*, 23840 – 23847.

[135] Maeda, K. *J. Photochem. Photobiol., C* **2011**, *12*, 237–268.

[136] Nadeem, M.; Murdoch, M.; Waterhouse, G.; Metson, J.; Keane, M.; Llorca, J.; Idriss, H. *J. Photochem. Photobiol., A* **2010**, *216*, 250 – 255.

[137] Takanabe, K. In *Solar Energy for Fuels*; Tüysüz, H., Chan, K. C., Eds.; Springer International Publishing, 2016; Chapter Solar Water Splitting Using Semiconductor Photocatalysts Powders, pp 73–103.

[138] Ohtani, B. *Catalysts* **2013**, *3*, 942–953.

[139] Valdés, Á.; Qu, Z.-W.; Kroes, G.-J.; Rossmeisl, J.; Nørskov, J. K. *J. Phys. Chem. C* **2008**, *112*, 9872 – 9879.

[140] Oberhofer, H.; Reuter, K. *J. Chem. Phys.* **2013**, *139*, 044710–1 – 044710–5.

[141] Maeda, K.; Domen, K. *J. Phys. Chem. Lett.* **2010**, *1*, 2655 – 2661.

[142] Berr, M. J.; Schweinberger, F. F.; Döblinger, M.; Sanwald, K. E.; Wolff, C.; Breimeier, J.; Crampton, A. S.; Ridge, C. J.; Tschurl, M.; Heiz, U.; Jäckel, F.; Feldmann, J. *Nano Lett.* **2012**, *12*, 5903 – 5906.

[143] Schweinberger, F. F.; Berr, M. J.; Döblinger, M.; Wolff, C.; Sanwald, K. E.; Crampton, A. S.; Ridge, C. J.; Jäckel, F.; Feldmann, J.; Tschurl, M.; Heiz, U. *J. Am. Chem. Soc.* **2013**, *135*, 13262 – 13265.

[144] Simon, T.; Bouchonville, N.; Berr, M. J.; Vaneski, A.; Adrovic, A.; Volbers, D.; Wyrwich, R.; Döblinger, M.; Susha, A. S.; Rogach, A. L.; Jäckel, F.; Stolarczyk, J. K.; Feldmann, J. *Nat Mater* **2014**, *13*, 1013–1018.

[145] Stegbauer, L.; Schwinghammer, K.; Lotsch, B. V. *Chem. Sci.* **2014**, *5*, 2789–2793.

[146] Kim, T. W.; Choi, K.-S. *Science* **2014**, *343*, 990–993.

[147] Negishi, Y.; Matsuura, Y.; Tomizawa, R.; Kurashige, W.; Niihori, Y.; Takayama, T.; Iwase, A.; Kudo, A. *J. Phys. Chem. C* **2015**, *119*, 11224–11232.

[148] Garcia-Esparza, A. T.; Shinagawa, T.; Ould-Chikh, S.; Qureshi, M.; Peng, X.; Wei, N.; Anjum, D. H.; Clo, A.; Weng, T.-C.; Nordlund, D.; Sokaras, D.; Kubota, J.; Domen, K.; Takanabe, K. *Angew. Chem. Int. Ed.* **2017**, *56*, 5780–5784.

[149] Chen, W.-T.; Chan, A.; Sun-Waterhouse, D.; Moriga, T.; Idriss, H.; Waterhouse, G. I. *J. Catal.* **2015**, *326*, 43–53.

[150] Ocana, I. R.; Beltram, A.; Jaen, J. J. D.; Adami, G.; Montini, T.; Fornasiero, P. *Inorg. Chim. Acta* **2015**, *431*, 197–205.

[151] Yang, Y.; Chang, C.-H.; Idriss, H. *Appl. Catal., B: Environ.* **2006**, *67*, 217–222.

[152] Bahruji, H.; Bowker, M.; Davies, P. R.; Al-Mazroai, L. S.; Dickinson, A.; Greaves, J.; James, D.; Millard, L.; Pedrono, F. *J. Photochem. Photobiol., A* **2010**, *216*, 115–118.

[153] Bowker, M. *Green Chem.* **2011**, *13*, 2235–2246.

[154] Olah, G. A. *Angew. Chem. Int. Ed.* **2006**, *44*, 2636–2639.

[155] Olah, G. A. *Angew. Chem. Int. Ed.* **2013**, *52*, 104–107.

[156] Meyer, A.; Renken, A. *Chem. Eng. Technol.* **1990**, *13*, 145–140.

[157] Guan, Y.; Hensen, E. J. *Appl. Catal., A* **2009**, *361*, 49–56.

[158] Al-Azri, Z. H.; Chen, W.-T.; Chan, A.; Jovic, V.; Ina, T.; Idriss, H.; Waterhouse, G. I. *J. Catal.* **2015**, *329*, 355–367.

[159] Sanwald, K. E.; Berto, T. F.; Eisenreich, W.; Gutiérrez, O. Y.; Lercher, J. A. *J. Catal.* **2016**,

[160] Sanwald, K. E.; Berto, T. F.; Eisenreich, W.; Jentys, A.; Gutiérrez, O. Y.; Lercher, J. A. *ACS Catal.* **2017**,

[161] Kennedy, J.; Bahruji, H.; Bowker, M.; Davies, P. R.; Bouleghlimat, E.; Issarapanacheewin, S. *J. Photochem. Photobiol., A* **2018**,

[162] Kundu, S.; Vidal, A. B.; Nadeem, M. A.; Senanayake, S. D.; Idriss, H.; Liu, P.; Rodriguez, J. A.; Stacchiola, D. *J. Phys. Chem. C* **2013**, *117*, 11149–11158.

[163] Beltram, A.; Romero-Ocana, I.; Jaen, J. J. D.; Montini, T.; Fornasiero, P. *Appl. Catal., A* **2016**, *518*, 167–175.

[164] Luken, A.; Muhler, M.; Strunk, J. *Phys. Chem. Chem. Phys.* **2015**, *17*, 10931–10397.

[165] Gazsi, A.; Bánsági, T.; Solymosi, F. *Catal. Lett.* **2009**, *131*, 33–41.

[166] Bashir, S.; Idriss, H. *Catal. Sci. Technol.* **2017**, *7*, 5301–5320.

[167] Primo, A.; Corma, A.; Garcia, H. *Phys. Chem. Chem. Phys.* **2011**, *13*, 886–910.

[168] Puga, A. V.; Forneli, A.; García, H.; Corma, A. *Adv. Funct. Mater.* **2014**, *24*, 241–248.

[169] Nishimoto, S.-i.; Ohtani, B.; Kagiya, T. *J. Chem. Soc., Faraday Trans. 1* **1985**, *81*, 2467–2474.

[170] Yamakata, A.; Ishibashi, T.-a.; Onishi, H. *J. Phys. Chem. B* **2003**, *107*, 9820–9823.

[171] Nadeem, A.; Waterhouse, G.; Idriss, H. *Catal. Today* **2012**, *182*, 16–24.

[172] Nadeem, M. A.; Majeed, I.; Waterhouse, G. I. N.; Idriss, H. *Catal. Struct. React.* **2015**, *1*, 61–70.

[173] Chen, T.; Feng, Z.; Wu, G.; Shi, J.; Ma, G.; Ying, P.; Li, C. *J. Phys. Chem. C* **2007**, *111*, 8005–8014.

[174] Li, R.; Li, C. *Photocatalytic Water Splitting on Semiconductor-Based Photocatalysts*; Advances in Catalysis; Academic Press, 2017.

[175] Su, R. et al. *ACS Nano* **2014**, *8*, 3490–3497.

[176] Amirav, L.; Alivisatos, A. P. *J. Phys. Chem. Lett.* **2010**, *1*, 1051–1054.

[177] Escobedo, S.; Serrano, B.; Calzada, A.; Moreira, J.; de Lasa, H. *Fuel* **2016**, *181*, 438–449.

[178] Naldoni, A.; D'Arienzo, M.; Altomare, M.; Marelli, M.; Scotti, R.; Morazzoni, F.; Selli, E.; Santo, V. D. *Appl. Catal., B: Environ.* **2013**, *130-131*, 239–248.

[179] Ismail, A. A.; Al-Sayari, S. A.; Bahnemann, D. *Catal. Today* **2013**, *209*, 2–7.

[180] Liu, N.; Zhou, X.; Nguyen, N. T.; Peters, K.; Zoller, F.; Hwang, I.; Schneider, C.; Miehlich, M. E.; Freitag, D.; Meyer, K.; Fattakhova-Rohlfing, D.; Schmuki, P. *ChemSusChem* **2017**, *10*, 62–67.

[181] Schreiber, P. Determination of the sensitivity of a TOF-MS with REMPI for the analysis of isomers in UHV: a case study on benzene/Pt(111). Master's Thesis, 2014.

[182] Winbauer, A.; Kollmannsberger, S. L.; Walenta, C. A.; Schreiber, P.; Kiermaier, J.; Tschurl, M.; Heiz, U. *Anal. Chem.* **2016**, *88*, 5392–5397.

[183] Kiermaier, J. Entwicklung und Aufbau einer Apparatur zur Bestimmung der photokatalytischen Eigenschaften von halbleiterbasierten Modellsystem im Ultrahochvakuum - Photodesorption von Sauerstoff auf (110)-TiO_2-Einkristallen. Ph.D. thesis, Technische Universität München, 2013.

[184] Winbauer, A. REMPI-ToF als isomerenselektive Analysemethode in der heterogenen Katalyse. Ph.D. thesis, Technische Universität München, 2014.

[185] Palmberg, P. W.; Riach, G. E.; Weber, R. E.; MacDonald, N. C. *Handbook of Auger Electron Spectroscopy - A Reference Book of Standard Data for Identification and Interpretation of Auger Electron Spectropscopy Data.*; Physical Electronics Industries Inc.: 7317 South Washington Avenue, Edina, Minnesota 55435, 1972.

[186] Moulder, J. F.; Stickle, W. F.; Sobol, P. E.; Bomben, K. D. In *Handbook of X-Ray Photoelectron Spectroscopy*; Chastian, J., Ed.; Perkin Elmer Corporation Physical Electronics Division: 6509 Flying Cloud Drive, Eden Prairie, Minnesota 55344, United States of America, 1992.

[187] Niemantsverdriet, J. W. *Spectroscopy in Catalysis*; Wiley-VCH Verlag GmbH & Co. KGaA, 2007.

[188] John T. Yates, J. *Experimental Innovations in Surface Science*, 2nd ed.; Springer International Publishing, 2015.

[189] Czanderna, A. W., Powell, C. J., Madey, T. E., Hercules, D. M., Jr., J. T. Y., Eds. *Specimen Handling, Preparation, and Treatments in Surface Characterization*; Springer US, 1998; Vol. 4.

[190] Bozack, M. J.; Muehlhoff, L.; Russell, J. N.; Choyke, W. J.; Yates, J. T. *J. Vac. Sci. Technol., A* **1987**, *5*, 1–8.

[191] Winkler, A.; Yates, J. T. *J. Vac. Sci. Technol., A* **1988**, *6*, 2929–2932.

[192] Riedel, J. N. Ethylene hydrogenation on Pt catalyst surfaces under UHV conditions. Internship Repot, 2012.

[193] Crampton, A. S. Systematic UHV Study of Ethylene Hydrogenation on Supported, Size-Selected Clusters. Ph.D. thesis, Technische Universität München, 2015.

[194] Schweinberger, F. F. Catalysis with supported size-selected Pt clusters Fundamental UHV and applied ambient experiments. Ph.D. thesis, Technische Universität München, 2013.

[195] Smentkowski, V. S.; Yates, J. T. *J. Vac. Sci. Technol., A* **1996**, *14*, 260 – 265.

[196] Röhrl, M. H. Towards photocatalysis on GaN thin films in the UHV. Bachelor's Thesis, 2015.

[197] Ambacher, O.; Brandt, M. S.; Dimitrov, R.; Metzger, T.; Stutzmann, M.; Fischer, R. A.; Miehr, A.; Bergmaier, A.; Dollinger, G. *J. Vac. Sci. Technol., B* **1996**, *14*, 3532–3542.

[198] Heiz, U.; Vanolli, F.; Trento, L.; Schneider, W.-D. *Rev. Sci. Instrum.* **1997**, *68*, 1986–1994.

[199] König, M. Scanning Probe Microscopy of size-selected, supported clusters: The cluster-support interaction. Ph.D. thesis, Technische Universität München, 2015.

[200] Courtois, C. The Mechanisms of Photocatalytic Hydrogen Production from Methanol on TiO_2(110) Supported Pt Cluster. Master's Thesis, 2017.

[201] Courtois, C. Towards Metal Cluster-Semiconductor Hybrid Materials in Photocatalysis. Internship Report, 2016.

[202] Vetter, K.-M. Implementing a Cluster Source for Metal Cluster-Semiconductor Hybrid Materials. Internship Report, 2017.

[203] Jablonka, K. M. Towards Studies on Metal-Cluster/Semiconductor-Hybridmaterials for Photocatalysis . Bachelor's Thesis, 2017.

[204] Henderson, M. A.; Shen, M. *Top. Catal.* **2017**, 1–6.

[205] Henderson, M. A. *Langmuir* **1996**, *12*, 5093–5098.

[206] Xu, C.; Yang, W.; Guo, Q.; Dai, D.; Chen, M.; Yang, X. *J. Am. Chem. Soc.* **2013**, *135*, 10206–10209.

[207] Rusu, C. N.; Yates, J. T. *Langmuir* **1997**, *13*, 4311–4316.

[208] Herman, G. S.; Dohnálek, Z.; Ruzycki, N.; Diebold, U. *J. Phys. Chem. B* **2003**, *107*, 2788–2795.

[209] Yanagisawa, Y.; Ota, Y. *Surf. Sci. Lett.* **1991**, *254*, L433–L436.

[210] Lu, G.; Linsebigler, A.; Yates, J. T. *J. Chem. Phys.* **1995**, *102*, 3005–3008.

[211] Diwald, O.; Thompson, T. L.; Goralski, E. G.; Walck, S. D.; Yates, J. T. *J. Phys. Chem. B* **2004**, *108*, 52 – 57.

[212] Møller, P. J.; Lazneva, E. F.; Komolov, A. S.; Komolov, S. A. *Surf. Sci.* **1998**, *395*, 82–87.

[213] Sporleder, D.; Wilson, D. P.; White, M. G. *J. Phys. Chem. C* **2009**, *113*, 13180–13191.

[214] Henderson, M. A.; Epling, W. S.; Perkins, C. L.; Peden, C. H. F.; Diebold, U. *J. Phys. Chem. B* **1999**, *103*, 5328 – 5337.

[215] Diebold, U. *J. Chem. Phys.* **2017**, *147*, 040901.

[216] Li, M.; Hebenstreit, W.; Gross, L.; Diebold, U.; Henderson, M.; Jennison, D.; Schultz, P.; Sears, M. *Surf. Sci.* **1999**, *437*, 173–190.

[217] Lira, E.; Hansen, J. Ø.; Huo, P.; Bechstein, R.; Galliker, P.; Lægsgaard, E.; Hammer, B.; Wendt, S.; Besenbacher, F. *Surf. Sci.* **2010**, *604*, 1945–1960.

[218] Du, Y.; Deskins, N. A.; Zhang, Z.; Dohnalek, Z.; Dupuis, M.; Lyubinetsky, I. *Phys. Chem. Chem. Phys.* **2010**, *22*, 6337–6344.

[219] Hansen, J. Ø.; Matthiesen, J.; Lira, E.; Lammich, L.; Wendt, S. *Surf. Sci.* **2017**, *666*, 113–122.

[220] Kim, B.; Li, Z.; Kay, B. D.; Dohnalek, Z.; Kim, Y. K. *Phys. Chem. Chem. Phys.* **2012**, *14*, 15060–15065.

[221] Gottschalch, V.; Mergenthaler, K.; Wagner, G.; Bauer, J.; Paetzelt, H.; Sturm, C.; Teschner, U. *phys. status solidi a* **2009**, *206*, 243–249.

[222] Ueda, N.; Hosono, H.; Waseda, R.; Kawazoe, H. *Appl. Phys. Lett.* **1997**, *70*, 3561–3563.

[223] Mohamed, M.; Unger, I.; Janowitz, C.; Manzke, R.; Galazka, Z.; Uecker, R.; Fornari, R. *Journal of Physics: Conference Series* **2011**, *286*, 012027.

[224] Janowitz, C.; Scherer, V.; Mohamed, M.; Krapf, A.; Dwelk, H.; Manzke, R.; Galazka, Z.; Uecker, R.; Irmscher, K.; Fornari, R.; Michling, M.; Schmeißer, D.; Weber, J. R.; Varley, J. B.; de Walle, C. G. V. *New J. Phys.* **2011**, *13*, 085014.

[225] Bermudez, V. *Surf. Sci. Rep.* **2017**, *72*, 147–315.

[226] Eller, B. S.; Yang, J.; Nemanich, R. J. *J. Vac. Sci. Technol., A* **2013**, *31*, 050807.

[227] Wu, C. I.; Kahn, A.; Taskar, N.; Dorman, D.; Gallagher, D. *J. Appl. Phys.* **1998**, *83*, 4249–4252.

[228] Prabhakaran, K.; Andersson, T. G.; Nozawa, K. *Appl. Phys. Lett.* **1996**, *69*, 3212–3214.

[229] Zhou, J.; Reddic, J.; Sinha, M.; Ricker, W.; Karlinsey, J.; Yang, J.-W.; Khan, M.; Chen, D. *Appl. Surf. Sci.* **2002**, *202*, 131–138.

[230] Eller, B. S.; Yang, J.; Nemanich, R. J. *J. Electronic Materials* **2014**, *43*, 4560–4568.

[231] Kollmannsberger, S. L.; Walenta, C. A.; Winnerl, A.; Weiszer, S.; Pereira, R. N.; Tschurl, M.; Stutzmann, M.; Heiz, U. *J. Phys. Chem. C* **2017**, *121*, 8473–8479.

[232] Kollmannsberger, S.; Walenta, C. A.; Winnerl, A.; Knoller, F.; Pereira, R. N.; Tschurl, M.; Stutzmann, M.; Heiz, U. *J. Chem. Phys.* **2017**, *147*, 124704.

[233] Walenta, C.; Kollmannsberger, S.; Winnerl, A.; Weiszer, S.; Pereira, R. N.; Tschurl, M.; Stutzmann, M.; Heiz, U. *J. Phys. Chem. C* **2017**, *121*, 16293–16298.

[234] Heiz, U.; Sanchez, A.; Abbet, S.; Schneider, W.-D. *J. Am. Chem. Soc.* **1999**, *121*, 3214–3217.

[235] Crampton, A. S.; Rötzer, M. D.; Landman, U.; Heiz, U. *ACS Catal.* **2017**,

[236] Crampton, A. S.; Rötzer, M. D.; Ridge, C. J.; Schweinberger, F. F.; Heiz, U.; Yoon, B.; Landman, U. *Nat Commun* **2016**, *7*.

[237] Crampton, A. S.; Rötzer, M. D.; Schweinberger, F. F.; Yoon, B.; Landman, U.; Heiz, U. *Angew. Chem. Int. Ed.* **2016**,

[238] Tang, X.; Bumueller, D.; Lim, A.; Schneider, J.; Heiz, U.; Ganteför, G.; Fairbrother, D. H.; Bowen, K. H. *J. Phys. Chem. C* **2014**,

[239] Watanabe, Y.; Isomura, N. *J. Vac. Sci. Technol., A* **2009**, *27*, 1153–1158.

[240] Watanabe, Y.; Wu, X.; Hirata, H.; Isomura, N. *Catal. Sci. Technol.* **2011**, *1*, 1490–1495.

[241] Kaden, W. E.; Wu, T.; Kunkel, W. A.; Anderson, S. L. *Science* **2009**, *326*, 826–829.

[242] Kaden, W. E.; Kunkel, W. A.; Kane, M. D.; Roberts, F. S.; Anderson, S. L. *J. Am. Chem. Soc.* **2010**, *132*, 13097–13099.

[243] Baxter, E. T.; Ha, M.-A.; Cass, A. C.; Alexandrova, A. N.; Anderson, S. L. *ACS Catal.* **2017**, 3322–3335.

[244] Tong, X.; Benz, L.; Kemper, P.; Metiu, H.; Bowers, M. T.; ; Buratto, S. K. *J. Am. Chem. Soc.* **2005**, *127*, 13516–13518.

[245] Kemper, P.; Kolmakov, A.; Tong, X.; Lilach, Y.; Benz, L.; Manard, M.; Metiu, H.; Buratto, S. K.; Bowers, M. T. *Int. J. Mass Spectrom.* **2006**, *254*, 202–209.

[246] Tyo, E. C.; Vajda, S. *Nat Nano* **2015**, *10*, 577–588.

[247] Vajda, S.; White, M. G. *ACS Catal.* **2015**, *5*, 7152–7176.

[248] Yang, B.; Liu, C.; Halder, A.; Tyo, E. C.; Martinson, A. B. F.; Seifert, S.; Zapol, P.; Curtiss, L. A.; Vajda, S. *J. Phys. Chem. C* **2017**,

[249] Li, Z.; Kay, B. D.; Dohnalek, Z. *Phys. Chem. Chem. Phys.* **2013**, *15*, 12180–12186.

[250] Chen, L.; Li, Z.; Smith, R. S.; Kay, B. D.; Dohnálek, Z. *J. Am. Chem. Soc.* **2014**, *136*, 5559–5562.

[251] Rusu, C. N.; ; J. T. Yates, J. *J. Phys. Chem. B* **2000**, *104*, 1729–1737.

[252] White, J. M.; Henderson, M. A. *J. Phys. Chem. B* **2005**, *109*, 12417 – 12430.

[253] Wilson, D. P.; Sporleder, D.; White, M. G. *J. Phys. Chem. C* **2012**, *116*, 16541–16552.

[254] Petrik, N. G.; Kimmel, G. A. *J. Phys. Chem. Lett.* **2010**, *1*, 2508–2513.

[255] Petrik, N. G.; Henderson, M. A.; Kimmel, G. A. *J. Phys. Chem. C* **2015**, *119*, 12273–12282.

[256] Petrik, N. G.; Henderson, M. A.; Kimmel, G. A. *J. Phys. Chem. C* **2015**, *119*, 12262–12272.

[257] Kershis, M. D.; Wilson, D. P.; White, M. G. *J. Chem. Phys.* **2013**, *138*, 204703.

[258] Wilson, D. P.; Sporleder, D. P.; White, M. G. *J. Phys. Chem. C* **2013**, *117*, 9290–9300.

[259] Shur, M. S. *Solid-State Electron.* **1998**, *42*, 2131–2138.

[260] Morkoç, H.; Mohammad, S. N. *Science* **1995**, *267*, 51–55.

[261] Nanishi, Y. *Nat. Photon.* **2014**, *8*, 884.

[262] Kamimura, J.; Bogdanoff, P.; Abdi, F. F.; Lähnemann, J.; van de Krol, R.; Riechert, H.; Geelhaar, L. *J. Phys. Chem. C* **2017**, *121*, 12540–12545.

[263] Jung, H. S.; Hong, Y. J.; Li, Y.; Cho, J.; Kim, Y.-J.; Yi, G.-C. *ACS Nano* **2008**, *2*, 637–642.

[264] Park, J. Y.; Kim, S. M.; Lee, H.; Nedrygailov, I. I. *Acc. Chem. Res.* **2015**, *48*, 2475–2483.

[265] Baur, B.; Steinhoff, G.; Hernando, J.; Purrucker, O.; Tanaka, M.; Nickel, B.; Stutzmann, M.; Eickhoff, M. *Appl. Phys. Lett.* **2005**, *87*.

[266] Bermudez, V. *Surf. Sci.* **2002**, *499*, 124–134.

[267] Bermudez, V. *Langmuir* **2003**, *19*, 6813–6819.

[268] Karrer, U.; Ambacher, O.; Stutzmann, M. *Appl. Phys. Lett.* **2000**, *77*, 2012–2014.

[269] Bermudez, V. *Chem. Phys. Lett.* **2000**, *317*, 290–295.

[270] Bermudez, V.; Long, J. *Surf. Sci.* **2000**, *450*, 98–105.

[271] Long, J. P.; Bermudez, V. M. *Phys. Rev. B* **2002**, *66*, 121308–121311.

[272] Schäfer, S.; Wyrzgol, S. A.; Lercher, J. A.; Stutzmann, M.; Sharp, I. D. *ChemCatChem* **2013**, *5*, 3224–3227.

[273] Reiner, M.; Pietschnig, R.; Ostermaier, C. *ACS Appl. Mater. Interfaces* **2015**, *7*, 23124–23131.

[274] Bartoš, I.; Romanyuk, O.; Houdkova, J.; Paskov, P. P.; Paskova, T.; Jiříček, P. *J. Appl. Phys.* **2016**, *119*.

[275] Schultz, T.; Schlesinger, R.; Niederhausen, J.; Henneberger, F.; Sadofev, S.; Blumstengel, S.; Vollmer, A.; Bussolotti, F.; Yang, J.-P.; Kera, S.; Parvez, K.; Ueno, N.; Müllen, K.; Koch, N. *Phys. Rev. B* **2016**, *93*, 125309.

[276] Duan, T. L.; Pan, J. S.; Ang, D. S. *ECS J. Solid State Sci. Technol.* **2016**, *5*, 514–517.

[277] Winnerl, A.; Garrido, J. A.; Stutzmann, M. *Appl. Phys. Lett.* **2017**, *110*, 101602.

[278] Winnerl, A.; Garrido, J. A.; Stutzmann, M. *J. Appl. Phys.* **2017**, *122*, 045302.

[279] Winnerl, A.; Pereira, R. N.; Stutzmann, M. *Phys. Rev. B* **2015**, *91*, 075316–075327.

[280] Bermudez, V. M. *J. Appl. Phys.* **1996**, *80*, 1190–1200.

[281] Mu, R.; Dahal, A.; Wang, Z.-T.; Dohnálek, Z.; Kimmel, G. A.; Petrik, N. G.; Lyubinetsky, I. *J. Phys. Chem. Lett.* **2017**,

[282] Idriss, H.; Seebauer, E. *J. Mol. Catal. A: Chem.* **2000**, *152*, 201–212.

[283] Martono, E.; Hyman, M. P.; Vohs, J. M. *Phys. Chem. Chem. Phys.* **2011**, *13*, 9880–9886.

[284] Farfan-Arribas, E.; Madix, R. J. *J. Phys. Chem. B* **2002**, *106*, 10680–10692.

[285] Kim, Y. K.; Kay, B. D.; White, J. M.; Dohnálek, Z. *J. Phys. Chem. C* **2007**, *111*, 18236–18242.

[286] Gamble, L.; Jung, L. S.; Campbell, C. T. *Surf. Sci.* **1996**, *348*, 1–16.

[287] Vohs, J.; Barteau, M. *Surf. Sci.* **1989**, *221*, 590–608.

[288] Lee, A. F.; Gawthrope, D. E.; Hart, N. J.; Wilson, K. *Surf. Sci.* **2004**, *548*, 200–208.

[289] Shekhar, R.; Barteau, M. A. *Catal. Lett.* **1995**, *31*, 221–237.

[290] Sturm, J.; Lee, C.; Bijkerk, F. *Surf. Sci.* **2013**, *612*, 42–47.

[291] Gates, S.; Russell, J.; Yates, J. *Surf. Sci.* **1986**, *171*, 111–134.

[292] Lagerstedt, O.; Monemar, B. *Phys. Rev. B* **1979**, *19*, 3064–3070.

[293] Kim, Y.; Kay, B. D.; White, J.; Dohnálek, Z. *Catal. Lett.* **2007**, *119*, 1–4.

[294] Halevi, B.; Vohs, J. M. *Catal. Lett.* **2006**, *111*, 1–4.

[295] Kwak, G.; Yong, K. *J. Phys. Chem. C* **2008**, *112*, 3036–3041.

[296] Yates Jr, J. T.; Madey, T. E. *J. Chem. Phys.* **1971**, *54*, 4969–4978.

[297] Dulub, O.; Boatner, L. A.; Diebold, U. *Surf. Sci.* **2002**, *519*, 201–217.

[298] Kresse, G.; Dulub, O.; Diebold, U. *Phys. Rev. B* **2003**, *68*, 245409.

[299] Dulub, O.; Diebold, U.; Kresse, G. *Phys. Rev. Lett.* **2003**, *90*, 016102.

[300] Bellitto, V.; Thoms, B.; Koleske, D.; Wickenden, A.; Henry, R. *Surf. Sci.* **1999**, *430*, 80–88.

[301] Northrup, J. E. *Phys. Rev. B* **2008**, *77*, 045313.

[302] Van de Walle, C. G.; Neugebauer, J. *Phys. Rev. Lett.* **2002**, *88*, 066103.

[303] Bermudez, V. *Surf. Sci.* **2004**, *565*, 89–102.

[304] Ptasinska, M.; Piechota, J.; Krukowski, S. *J. Phys. Chem. C* **2015**, *119*, 11563–11569.

[305] Walenta, C. A.; Kollmannsberger, S. L.; Kiermaier, J.; Winbauer, A.; Tschurl, M.; Heiz, U. *Phys. Chem. Chem. Phys.* **2015**, *17*, 22809–22814.

[306] Wendt, S.; Matthiesen, J.; Schaub, R.; Vestergaard, E. K.; Lægsgaard, E.; Besenbacher, F.; Hammer, B. *Phys. Rev. Lett.* **2006**, *96*, 066107–066111.

[307] Hammer, B. and Wendt, S. and Besenbacher, F., *Top. Catal.* **2010**, *53*, 423 – 430.

[308] Hansen, J. Ø.; Huo, P.; Martinez, U.; Lira, E.; Wei, Y. Y.; Streber, R.; Lægsgaard, E.; Hammer, B.; Wendt, S.; Besenbacher, F. *Phys. Rev. Lett.* **2011**, *107*, 136102–136106.

[309] Li, S.-C.; Chu, L.-N.; Gong, X.-Q.; Diebold, U. *Science* **2010**, *328*, 882 – 884.

[310] Shekhar, R.; Jensen, K. F. *Surf. Sci.* **1997**, *381*, L581–L588.

[311] Fujino, T.; Katayama, M.; Inudzuka, K.; Okuno, T.; Oura, K.; Hirao, T. *Appl. Phys. Lett.* **2001**, *79*, 2716–2718.

[312] Gombac, V.; Sordelli, L.; Montini, T.; Delgado, J. J.; Adamski, A.; Adami, G.; Cargnello, M.; Bernal, S.; Fornasiero, P. *J. Phys. Chem. A* **2010**, *114*, 3915–3925.

[313] Garbarino, G.; Wang, C.; Valsamakis, I.; Chitsazan, S.; Riani, P.; Finocchio, E.; Flytzani-Stephanopoulos, M.; Busca, G. *Appl. Catal., B: Environ.* **2015**, *174-175*, 21–34.

[314] Wang, K.; Wei, Z.; Ohtani, B.; Kowalska, E. *Catal. Today* **2017**, *303*, 327–333.

[315] Wahab, A.; Bashir, S.; Al-Salik, Y.; Idriss, H. *Appl. Petrochem. Res.* **2014**, *4*, 55–62.

[316] Kyriakou, G.; Boucher, M. B.; Jewell, A. D.; Lewis, E. A.; Lawton, T. J.; Baber, A. E.; Tierney, H. L.; Flytzani-Stephanopoulos, M.; Sykes, E. C. H. *Science* **2012**, *335*, 1209–1212.

[317] Shan, J.; Lucci, F. R.; Liu, J.; El-Soda, M.; Marcinkowski, M. D.; Allard, L. F.; Sykes, E. C. H.; Flytzani-Stephanopoulos, M. *Surf. Sci.* **2016**, *650*, 121–129.

[318] Shan, J.; Janvelyan, N.; Li, H.; Liu, J.; Egle, T. M.; Ye, J.; Biener, M. M.; Biener, J.; Friend, C. M.; Flytzani-Stephanopoulos, M. *Appl. Catal., B: Environ.* **2017**, *205*, 541–550.

[319] Flytzani-Stephanopoulos, M. *Chin. J. Catal.* **2017**, *38*, 1432–1442.

[320] Ohno, T.; Bai, L.; Hisatomi, T.; Maeda, K.; Domen, K. *J. Am. Chem. Soc.* **2012**, *134*, 8254 – 8259.

[321] Kibria, M. G.; Zhao, S.; Chowdhury, F. A.; Wang, Q.; Nguyen, H. P. T.; Trudeau, M. L.; Guo, H.; Mi, Z. *Nat Commun* **2014**, *5*, 3825.

[322] Kida, T.; Minami, Y.; Guan, G.; Nagano, M.; Akiyama, M.; Yoshida, A. *J. Mater. Sci.* **2006**, *41*, 3527 – 3534.

[323] Hayashi, T.; Deura, M.; Ohkawa, K. *Jap. J. Appl. Phys.* **2012**, *51*, 112601.

[324] Qun-qing Hao and Zhi-qiang Wang and Dong-xu Dai and Chuan-yao Zhou and Xue-ming Yang, *Chin. J. Chem. Phys.* **2017**, *30*, 1–5.

[325] Chen, S.; Wang, L.-W. *Chem. Mat.* **2012**, *24*, 3659–3666.

[326] Smith, A. R.; Feenstra, R. M.; Greve, D. W.; Shin, M. S.; Skowronski, M.; Neugebauer, J.; Northrup, J. E. *J. Vac. Sci. Technol., B* **1998**, *16*, 2242–2249.

[327] Tarsa, E. J.; Heying, B.; Wu, X. H.; Fini, P.; DenBaars, S. P.; Speck, J. S. *J. Appl. Phys.* **1997**, *82*, 5472–5479.

[328] Winnerl, A. Electronic Processes at the GaN Surface. Ph.D. thesis, Technische Universität München, 2017.

[329] Hashizume, T.; Ootomo, S.; Oyama, S.; Konishi, M.; Hasegawa, H. *J. Vac. Sci. Technol., B* **2001**, *19*, 1675–1681.

[330] Oliver, R.; Nörenberg, C.; Martin, M.; Crossley, A.; Castell, M.; Briggs, G. *Appl. Surf. Sci.* **2003**, *214*, 1–10.

[331] Watkins, N. J.; Wicks, G. W.; Gao, Y. *Appl. Phys. Lett.* **1999**, *75*, 2602–2604.

[332] Hollinger, G.; Skheyta-Kabbani, R.; Gendry, M. *Phys. Rev. B* **1994**, *49*, 11159–11167.

[333] Branda, M. M.; Collins, S. E.; Castellani, N. J.; Baltanás, M. A.; Bonivardi, A. L. *J. Phys. Chem. B* **2006**, *110*, 11847–11853.

[334] Bermudez, V. M. *Langmuir* **2008**, *24*, 12943–12952.

[335] Garcia, M. A.; Wolter, S. D.; Kim, T.-H.; Choi, S.; Baier, J.; Brown, A.; Losurdo, M.; Bruno, G. *Appl. Phys. Lett.* **2006**, *88*, 013506.

[336] Lorenz, P.; Gutt, R.; Haensel, T.; Himmerlich, M.; Schaefer, J. A.; Krischok, S. *phys. status solidi C* **2010**, *7*, 169–172.

[337] Fu, X.; Wang, H.; Zhang, J.; Li, Z.; Cui, S.; Zhang, L. *J. Appl. Phys.* **2015**, *118*.

[338] Parkinson, G. S. *Surf. Sci. Rep.* **2016**, *71*, 272–365.

[339] Kuhlenbeck, H.; Shaikhutdinov, S.; Freund, H.-J. *Chem. Rev.* **2013**, *113*, 3986–4034.

[340] Chen, C. T.; Cahan, B. D. *J. Opt. Soc. Am.* **1981**, *71*, 932–934.

[341] Cesar, I.; Sivula, K.; Kay, A.; Zboril, R.; Grätzel, M. *J. Phys. Chem. C* **2009**, *113*, 772–782.

[342] Baltrusaitis, J.; Hu, Y.-S.; McFarland, E. W.; Hellman, A. *ChemSusChem* **2014**, *7*.

[343] Kay, A.; Cesar, I.; Grätzel, M. *J. Am. Chem. Soc.* **2006**, *128*, 15714–15721.

[344] Shelton, T. L.; Harvey, N.; Wang, J.; Osterloh, F. E. *Appl. Catal., A* **2016**, *521*, 168–173.

[345] Hahn, N. T.; Ye, H.; Flaherty, D. W.; Bard, A. J.; Mullins, C. B. *ACS Nano* **2010**, *4*, 1977–1986.

[346] Lin, Y.; Zhou, S.; Sheehan, S. W.; Wang, D. *J. Am. Chem. Soc.* **2011**, *133*, 2398–2401.

[347] Zhu, Y.; Schultz, A. M.; Rohrer, G. S.; Salvador, P. A. *J. Am. Cheram. Soc.* **2016**, *99*, 2428–2435.

[348] Nguyen, M.-T.; Seriani, N.; Piccinin, S.; Gebauer, R. *J. Chem. Phys.* **2014**, *140*, 064703.

[349] Nguyen, M.-T.; Piccinin, S.; Seriani, N.; Gebauer, R. *ACS Catal.* **2015**, *5*, 715–721.

[350] Yatom, N.; Neufeld, O.; Caspary Toroker, M. *J. Phys. Chem. C* **2015**, *119*, 24789–24795.

[351] Zhang, X.; Klaver, P.; van Santen, R.; van de Sanden, M. C. M.; Bieberle-Hütter, A. *J. Phys. Chem. C* **2016**, *120*, 18201–18208.

[352] Zhang, X.; Cao, C.; Bieberle-Hütter, A. *J. Phys. Chem. C* **2016**, *120*, 28694–28700.

[353] Zandi, O.; Hamann, T. W. *Nat Chem* **2016**, *8*, 778–783.

[354] Lad, R. J.; Henrich, V. E. *Surf. Sci.* **1988**, *193*, 81–93.

[355] Condon, N.; Leibsle, F.; Lennie, A.; Murray, P.; Parker, T.; Vaughan, D.; Thornton, G. *Surf. Sci.* **1998**, *397*, 278–287.

[356] Shaikhutdinov, S.; Weiss, W. *Surf. Sci.* **1999**, *432*, 627–634.

[357] Kim, C.-Y.; Escuadro, A.; Bedzyk, M.; Liu, L.; Stair, P. *Surf. Sci.* **2004**, *572*, 239–246.

[358] Henderson, M. A.; Joyce, S. A.; Rustad, J. R. *Surf. Sci.* **1998**, *417*, 66–81.

[359] Henderson, M. A. *Geochim. Cosmochim. Acta* **2003**, *67*, 1055–1063.

[360] Henderson, M. A. *Surf. Sci.* **2010**, *604*, 1197–1201.

[361] Henderson, M. A. *J. Phys. Chem. C* **2011**, *115*, 23527–23534.

[362] Kraushofer, F.; Jakub, Z.; Bichler, M.; Hulva, J.; Drmota, P.; Weinold, M.; Schmid, M.; Setvin, M.; Diebold, U.; Blaha, P.; Parkinson, G. S. *J. Phys. Chem. C* **2018**, *122*, 1657–1669.

[363] Li, Z.; Potapenko, D. V.; Rim, K. T.; Flytzani-Stephanopoulos, M.; Flynn, G. W.; Osgood, R. M.; Wen, X.-D.; Batista, E. R. *J. Phys. Chem. C* **2015**, *119*, 1113–1120.

[364] Gamba, O.; Hulva, J.; Pavelec, J.; Bliem, R.; Schmid, M.; Diebold, U.; Parkinson, G. S. *Top. Catal.* **2017**, *60*, 420–430.

[365] Phillips, K. R.; Jensen, S. C.; Baron, M.; Li, S.-C.; Friend, C. M. *J. Am. Chem. Soc.* **2013**, *135*, 574–577.

[366] Crampton, A. S.; Cai, L.; Janvelyan, N.; Zheng, X.; Friend, C. M. *J. Phys. Chem. C* **2017**,

[367] Weiss, W.; Ritter, M. *Phys. Rev. B* **1999**, *59*, 5201–5213.

[368] Weiss, W.; Ranke, W. *Prog. Surf. Sci.* **2002**, *70*, 1–151.

[369] Tang, Y.; Qin, H.; Wu, K.; Guo, Q.; Guo, J. *Surf. Sci.* **2013**, *609*, 67–72.

[370] Genuzio, F.; Sala, A.; Schmidt, T.; Menzel, D.; Freund, H.-J. *J. Phys. Chem. C* **2014**, *118*, 29068–29076.

[371] Henderson, M. A.; Otero-Tapia, S.; Castro, M. E. *Faraday Discuss.* **1999**, *114*, 313 – 329.

[372] Pratt, A.; Graziosi, P.; Bergenti, I.; Prezioso, M.; Dediu, A.; Yamauchi, Y. *Rev. Sci. Instrum.* **2014**, *85*.

[373] Jensen, S. C.; Friend, C. M. *Top. Catal.* **2013**, *56*, 1377–1388.

[374] Li, Z.; Smith, R. S.; Kay, B. D.; Dohnálek, Z. *J. Phys. Chem. C* **2011**, *115*, 22534–22539.

[375] Zandi, O.; Hamann, T. W. *J. Phys. Chem. Lett.* **2014**, *5*, 1522–1526.

[376] Klahr, B.; Gimenez, S.; Zandi, O.; Fabregat-Santiago, F.; Hamann, T. *ACS Appl. Mater. Interfaces* **2015**, *7*, 7653–7660.

[377] Sivula, K.; Le Formal, F.; Grätzel, M. *ChemSusChem* **2011**, *4*.

[378] Sivula, K. *The Journal of Physical Chemistry Letters* **2013**, *4*, 1624 – 1633.

[379] Osterloh, F. E. *Chem. Soc. Rev.* **2013**, *42*, 2294–2320.

[380] Zandi, O.; Hamann, T. W. *Phys. Chem. Chem. Phys.* **2015**, *17*, 22485–22503.

[381] Joly, A. G.; Williams, J. R.; Chambers, S. A.; Xiong, G.; Hess, W. P.; Laman, D. M. *J. Appl. Phys.* **2006**, *99*.

[382] Barroso, M.; Pendlebury, S. R.; Cowan, A. J.; Durrant, J. R. *Chem. Sci.* **2013**, *4*, 2724–2734.

[383] Bora, D. K.; Braun, A.; Constable, E. C. *Energy Environ. Sci.* **2013**, *6*, 407–425.

[384] Bartelt, N. C.; Nie, S.; Starodub, E.; Bernal-Villamil, I.; Gallego, S.; Vergara, L.; McCarty, K. F.; de la Figuera, J. *Phys. Rev. B* **2013**, *88*, 235436.

[385] Berto, T. F.; Sanwald, K. E.; Eisenreich, W.; Gutiérrez, O. Y.; Lercher, J. A. *J. Catal.* **2016**, *338*, 68–81.

[386] Acharya, D. P.; Yoon, Y.; Li, Z.; Zhang, Z.; Lin, X.; Mu, R.; Chen, L.; Kay, B. D.; Rousseau, R.; Dohnálek, Z. *ACS Nano* **2013**, *7*, 10414 – 10423.

[387] Chen, L.; Li, Z.; Smith, R. S.; Kay, B. D.; Dohnálek, Z. *J. Phys. Chem. C* **2014**, *118*, 15339–15347.

[388] Chen, L.; Li, Z.; Smith, R. S.; Kay, B. D.; Dohnálek, Z. *J. Phys. Chem. C* **2014**, *118*, 23181–23188.

[389] Chen, L.; Smith, R. S.; Kay, B. D.; Dohnalek, Z. *ACS Catal.* **2017**, *7*, 2002–2006.

[390] Henderson, M. A. *Surf. Sci.* **1999**, *419*, 174–187.

[391] Li, M.; Hebenstreit, W.; Diebold, U.; Tyryshkin, A. M.; Bowman, M. K.; Dunham, G. G.; Henderson, M. A. *J. Phys. Chem. B* **2000**, *104*, 4944–4950.

[392] Li, Z.; Fang, Z.; Kelley, M. S.; Kay, B. D.; Rousseau, R.; Dohnalek, Z.; Dixon, D. A. *J. Phys. Chem. C* **2014**, *118*, 4869–4877.

[393] Henrich, V. E.; Cox, P. A. *The Surface Science of Metal Oxides*; Cambridge University Press (April 26, 1996), 1996; Vol. 2.

[394] Muir, J. N.; Choi, Y.; Idriss, H. *Phys. Chem. Chem. Phys.* **2012**, *14*, 11910–11919.

[395] Nadeem, A. M.; Muir, J. M. R.; Connelly, K. A.; Adamson, B. T.; Metson, B. J.; Idriss, H. *Phys. Chem. Chem. Phys.* **2011**, *13*, 7637 – 7643.

[396] Kershis, Matthew D. and White, Michael G., *Phys. Chem. Chem. Phys.* **2013**, *15*, 17976–17892.

[397] Ma, Z.; Guo, Q.; Mao, X.; Ren, Z.; Wang, X.; Xu, C.; Yang, W.; Dai, D.; Zhou, C.; Fan, H.; Yang, X. *J. Phys. Chem. C* **2013**, *117*, 10336–10344.

[398] Zehr, R.; Henderson, M. *Surf. Sci.* **2008**, *602*, 2238–2249.

[399] Wendt, S.; Schaub, R.; Matthiesen, J.; Vestergaard, E.; Wahlström, E.; Rasmussen, M.; Thostrup, P.; Molina, L.; Lægsgaard, E.; Stensgaard, I.; Hammer, B.; Besenbacher, F. *Surf. Sci.* **2005**, *598*, 226 – 245.

[400] Zhang, Z.; Bondarchuk, O.; White, J. M.; Kay, B. D.; Dohnálek, Z. *J. Am. Chem. Soc.* **2006**, *128*, 4198–4199.

[401] Zhang, Z.; Bondarchuk, O.; Kay, B. D.; White, J. M.; Dohnálek, Z. *J. Phys. Chem. B* **2006**, *110*, 21840–21845.

[402] Hansen, J. Ø.; Bebensee, R.; Martinez, U.; Porsgaard, S.; Lira, E.; Wei, Y.; Lammich, L.; Li, Z.; Idriss, H.; Besenbacher, F.; Hammer, B.; Wendt, S. *Sci. Rep.* **2016**, *6*, 21990.

[403] Jayaweera, P. M.; Quah, E. L.; Idriss, H. *J. Phys. Chem. C* **2007**, *111*, 1764 – 1769.

[404] Pan, J.-M.; Maschhoff, B. L.; Diebold, U.; Madey, T. E. *J. Vac. Sci. Technol., A* **1992**, *10*, 2470 – 2476.

[405] Walenta, C. A.; Kollmannsberger, S. L.; Courtois, C.; Tschurl, M.; Heiz, U. *Phys. Chem. Chem. Phys.* **2018**,

[406] Rinaldi, R.; Schüth, F. *Energy Environ. Sci.* **2009**, *2*, 610–626.

[407] Frusteri, F.; Arena, F.; Bonura, G.; Cannilla, C.; Spadaro, L.; Blasi, O. D. *Appl. Catal., A* **2009**, *367*, 77–83.

[408] Rahmat, N.; Abdullah, A. Z.; Mohamed, A. R. *Renewable and Sustainable Energy Reviews* **2010**, *14*, 987–1000.

[409] Brinkley, D.; Engel, T. *J. Phys. Chem. B* **1998**, *102*, 7596 – 7605.

[410] Vollhardt, K. P. C.; Schore, N. E. In *Organische Chemie*, 4th ed.; Butenschön, H., Ed.; Wiley-VCH Verlag GmbH & Co. KGaA, Weinheim, 2005; Vol. 1; pp 339–342.

[411] Preis, S.; Falconer, J. *Water Sci. Technol.* **2004**, *49*, 141–145.

[412] Preis, S.; Falconer, J. L.; del Prado Asensio, R.; Santiago, N. C.; Kachina, A.; Kallas, J. *Appl. Catal., B: Environ.* **2006**, *64*, 79–87.

[413] Augugliaro, V.; Kisch, H.; Loddo, V.; López-Muñoz, M. J.; Márquez-Álvarez, C.; Palmisano, G.; Palmisano, L.; Parrino, F.; Yurdakal, S. *Appl. Catal., A* **2008**, *349*, 182–188.

[414] Zehr, R. T.; Henderson, M. A. *Phys. Chem. Chem. Phys.* **2010**, *12*, 8085–8092.

[415] Henderson, M. A. *Surf. Sci.* **2008**, *602*, 3188–3193.

[416] Henderson, M. A. *J. Phys. Chem. C* **2008**, *112*, 11433 – 11440.

[417] Shen, M.; Henderson, M. A. *J. Phys. Chem. C* **2012**, *116*, 18788–18795.

[418] Kolesov, G.; Vinichenko, D.; Tritsaris, G. A.; Friend, C. M.; Kaxiras, E. *J. Phys. Chem. Lett.* **2015**, *6*, 1624–1627.

[419] Zhang, Z.; Bondarchuk, O.; Kay, B. D.; White, J. M.; Dohnálek, Z. *J. Phys. Chem. C* **2007**, *111*, 3021–3027.

[420] Henderson, M. A. *J. Phys. Chem. B* **2004**, *108*, 18932–18941.

[421] Shen, M.; Acharya, D. P.; Dohnálek, Z.; Henderson, M. A. *J. Phys. Chem. C* **2012**, *116*, 25465–25469.

[422] Hudson, J. E.; Hamilton, M. L.; Vallance, C.; Harland, P. W. *Phys. Chem. Chem. Phys.* **2003**, *5*, 3162–3168.

[423] Linstrom, P., Mallard, W., Eds. *NIST Chemistry WebBook, NIST Standard Reference Database Number 69*, retrieved December 12, 2017 ed.; National Institute of Standards and Technology: Gaithersburg MD, 20899, 2017.

[424] Bull, J. N.; Harland, P. W.; Vallance, C. *J. Phys. Chem. A* **2012**, *116*, 767–777.

[425] Dionigi, F.; Vesborg, P. C. K.; Pedersen, T.; Hansen, O.; Dahl, S.; Xiong, A.; Maeda, K.; Domen, K.; Chorkendorff, I. *Energy Environ. Sci.* **2011**, *4*, 2937 – 2942.

[426] Seh, Z. W.; Kibsgaard, J.; Dickens, C. F.; Chorkendorff, I.; Nørskov, J. K.; Jaramillo, T. F. *Science* **2017**, *355*.

[427] Maeda, K.; Teramura, K.; Lu, D.; Takata, T.; Saito, N.; Inoue, Y.; Domen, K. *Nature* **2006**, *440*, 295 – 295.

[428] Hisatomi, T.; Kubota, J.; Domen, K. *Chem. Soc. Rev.* **2014**,

[429] Navarro, R. M.; Peña, M. A.; Fierro, J. L. G. *Chem. Rev. (Washington, DC, U.S.)* **2007**, *107*, 3952–3991.

[430] Wang, Q.; Hisatomi, T.; Jia, Q.; Tokudome, H.; Zhong, M.; Wang, C.; Pan, Z.; Takata, T.; Nakabayashi, M.; Shibata, N.; Li, Y.; Sharp, I. D.; Kudo, A.; Yamada, T.; Domen, K. *Nat Mater* **2016**, *15*, 611–615.

[431] Esch, T. R.; Bredow, T. *Surf. Sci.* **2017**, *664*, 20–27.

[432] Zhang, J.; Peng, C.; Wang, H.; Hu, P. *ACS Catal.* **2017**, *7*, 2374–2380.

[433] Chu, W.; Saidi, W. A.; Zheng, Q.; Xie, Y.; Lan, Z.; Prezhdo, O. V.; Petek, H.; Zhao, J. *J. Am. Chem. Soc.* **2016**, *138*, 13740–13749.

[434] Wei, D.; Jin, X.; Huang, C.; Dai, D.; Ma, Z.; Li, W.-X.; Yang, X. *J. Phys. Chem. C* **2015**, *119*, 17748–17754.

[435] Karim, W.; Spreafico, C.; Kleibert, A.; Gobrecht, J.; VandeVondele, J.; Ekinci, Y.; van Bokhoven, J. A. *Nature* **2017**, *541*, 68–71.

[436] Sasahara, A.; Pang, C. L.; Onishi, H. *J. Phys. Chem. B* **2006**, *110*, 17584–17588.

[437] Isomura, N.; Wu, X.; Watanabe, Y. *J. Chem. Phys.* **2009**, *131*.

[438] Haselmann, G. M.; Eder, D. *ACS Catal.* **2017**, *7*, 4668–4675.

[439] Kunz, S.; Hartl, K.; Nesselberger, M.; Schweinberger, F.; Kwon, G.; Hanzlik, M.; Mayrhofer, K.; Heiz, U.; Arenz, M. *Phys. Chem. Chem. Phys.* **2010**, *12*, 10288–10291.

[440] Crampton, A. S.; Rötzer, M. D.; Schweinberger, F. F.; Yoon, B.; Landman, U.; Heiz, U. *J. Catal.* **2016**, *333*, 51–58.

[441] Simon Bonanni and Kamel Aït-Mansour and Harald Brune and Wolfgang Harbich, *ACS Catalysis* **2011**, *1*, 385–389.

[442] Yuan, Q.; Wu, Z.; Jin, Y.; Xiong, F.; Huang, W. *J. Phys. Chem. C* **2014**, *118*, 20420–20428.

[443] Yuan, Q.; Wu, Z.; Jin, Y.; Xu, L.; Xiong, F.; Ma, Y.; Huang, W. *J. Am. Chem. Soc.* **2013**, *135*, 5212–5219.

[444] Lang, X.; Wen, B.; Zhou, C.; Ren, Z.; Liu, L.-M. *J. Phys. Chem. C* **2014**, *118*, 19859–19868.

[445] Henderson, Michael A. and Otero-Tapia, Sary and E. Castro, Miguel, *Faraday Discuss.* **1999**, *114*, 313–329.

[446] Benito, M.; Sanz, J.; Isabel, R.; Padilla, R.; Arjona, R.; Daza, L. *J. Power Sources* **2005**, *151*, 11–17.

[447] Haryanto, A.; Fernando, S.; Murali, N.; Adhikari, S. *Energy Fuels* **2005**, *19*, 2098–2106.

[448] Zhang, B.; Tang, X.; Li, Y.; Xu, Y.; Shen, W. *Int. J. Hydrogen Energy* **2007**, *32*, 2367–2373.

[449] Chen, W.-T.; Jovic, V.; Sun-Waterhouse, D.; Idriss, H.; Waterhouse, G. I. *Int. J. Hydrogen Energy* **2013**, *38*, 15036–15048.

[450] Taboada, E.; Angurell, I.; Llorca, J. *J. Catal.* **2014**, *309*, 460–467.

[451] Bonmatí, E.; Casanovas, A.; Angurell, I.; Llorca, J. *Top. Catal.* **2015**, *58*, 77–84.

[452] Pina, C. D.; Falletta, E.; Rossi, M. *J. Catal.* **2008**, *260*, 384–386.

[453] Ma, Z.; Zhou, C.; Mao, X.; Ren, Z.; Dai, D.; Yang, X. *Chin. J. Chem. Phys.* **2013**, *26*, 1–7.

[454] Zhou, C. et al. *Chem. Sci.* **2010**, *1*, 575–580.

[455] Zhang, Z.; Rousseau, R.; Gong, J.; Kay, B. D.; Dohnálek, Z. *J. Am. Chem. Soc.* **2009**, *131*, 17926–17932.

[456] Bondarchuk, O.; Kim, Y. K.; White, J. M.; Kim, J.; Kay, B. D.; Dohnalek, Z. *J. Phys. Chem. C* **2007**, *111*, 11059 – 11067.

[457] Henderson, M. A.; Epling, W. S.; Perkins, C. L.; Peden, C. H. F.; Diebold, U. *J. Phys. Chem. B* **1999**, *103*, 5328–5337.

[458] Wang, Z.-T.; Deskins, N. A.; Henderson, M. A.; Lyubinetsky, I. *Phys. Rev. Lett.* **2012**, *109*, 266103.

[459] Wang, L.-C.; Stowers, K. J.; Zugic, B.; Biener, M. M.; Biener, J.; Friend, C. M.; Madix, R. J. *Catal. Sci. Technol.* **2015**, *5*, 1299–1306.

[460] Huo, P.; Hansen, J. Ø.; Martinez, U.; Lira, E.; Streber, R.; Wei, Y.; Lægsgaard, E.; Hammer, B.; Wendt, S.; Besenbacher, F. *J. Phys. Chem. Lett.* **2012**, *3*, 283–288.

[461] Bikondoa, O.; Pang, C. L.; Ithnin, R.; Muryn, C. A.; Onishi, H.; Thornton, G. *Nat Mater* **2006**, *5*, 189–192.

[462] Wang, Z.-T.; Wang, Y.-G.; Mu, R.; Yoon, Y.; Dahal, A.; Schenter, G. K.; Glezakou, V.-A.; Rousseau, R.; Lyubinetsky, I.; Dohnálek, Z. *Proc. Natl. Acad. Sci. U.S.A.* **2017**,

[463] Liu, S.; an Liu, A.; Wen, B.; Zhang, R.; Zhou, C.; Liu, L.-M.; Ren, Z. *J. Phys. Chem. Lett.* **2015**, *6*, 3327–3334.

[464] Liu, A.-a.; Liu, S.; Zhang, R.; Ren, Z. *J. Phys. Chem. C* **2015**, *119*, 23486–23494.

[465] Clawin, P. M.; Friend, C. M.; Al-Shamery, K. *Chem.—Eur. J.* **2014**, *20*, 7665–7669.

[466] Hasiguti, R. R.; Yagi, E. *Phys. Rev. B* **1994**, *49*, 7251–7256.

[467] Yagi, E.; Hasiguti, R. R.; Aono, M. *Phys. Rev. B* **1996**, *54*, 7945–7956.

[468] Wang, D.; Liu, Z.-P.; Yang, W.-M. *ACS Catal.* **2017**, *7*, 2744–2752.

[469] Henderson, M. A. *J. Phys. Chem. B* **2005**, *109*, 12062 – 12070.

[470] Wu, G.; Chen, T.; Zong, X.; Yan, H.; Ma, G.; Wang, X.; Xu, Q.; Wang, D.; Lei, Z.; Li, C. *J. Catal.* **2008**, *253*, 225–227.

[471] Noda, K.; Hattori, M.; Amari, K.; Kobayashi, K.; Horiuchi, T.; Matsushige, K. *Jap. J. Appl. Phys.* **2007**, *46*, L749.

[472] Hattori, M.; Noda, K.; Kobayashi, K.; Matsushige, K. *phys. status solidi C* **2011**, *8*, 549–551.

[473] Chang, T.-Y.; Tanaka, Y.; Ishikawa, R.; Toyoura, K.; Matsunaga, K.; Ikuhara, Y.; Shibata, N. *Nano Lett.* **2014**, *14*, 134–138.

[474] Parkinson, G. S. *Chin. J. Catal.* **2017**, *38*.

[475] Novotný, Z. c. v.; Argentero, G.; Wang, Z.; Schmid, M.; Diebold, U.; Parkinson, G. S. *Phys. Rev. Lett.* **2012**, *108*, 216103.

[476] Yang, X.-F.; Wang, A.; Qiao, B.; Li, J.; Liu, J.; Zhang, T. *Acc. Chem. Res.* **2013**, *46*, 1740–1748.

[477] Li, X.; Bi, W.; Zhang, L.; Tao, S.; Chu, W.; Zhang, Q.; Luo, Y.; Wu, C.; Xie, Y. *Adv. Mater.* **2016**, *28*, 2427–2431.

[478] Cheng, N.; Stambula, S.; Wang, D.; Banis, M. N.; Liu, J.; Riese, A.; XIao, B.; Li, R.; Sham, T.-K.; Liu, L.-M.; Botton, G. A.; Sun, X. *Nat Commun* **2016**, *7*, 13638.

[479] Xing, J.; Chen, J. F.; Li, Y. H.; Yuan, W. T.; Zhou, Y.; Zheng, L. R.; Wang, H. F.; Hu, P.; Wang, Y.; Zhao, H. J.; Wang, Y.; Yang, H. G. *Chem.—Eur. J.* **2014**, *20*, 2138.2144.

[480] Parkinson, G. S.; Novotny, Z.; Argentero, G.; Schmid, M.; Pavelec, J.; Kosak, R.; Blaha, P.; Diebold, U. *Nat. Mater.* **2013**, *12*, 724.

[481] Bliem, R.; van der Hoeven, J. E. S.; Hulva, J.; Pavelec, J.; Gamba, O.; de Jongh, P. E.; Schmid, M.; Blaha, P.; Diebold, U.; Parkinson, G. S. *Proc. Natl. Acad. Sci. U.S.A.* **2016**, *113*, 8921–8926.

[482] Thompson, T. L.; Yates, J. T. *J. Phys. Chem. B* **2006**, *110*, 7431 – 7435.

[483] Wendt, S.; Sprunger, P. T.; Lira, E.; Madsen, G. K. H.; Li, Z.; Hansen, J. Ø.; Matthiesen, J.; Blekinge-Rasmussen, A.; Lægsgaard, E.; Hammer, B.; Besenbacher, F. *Science* **2008**, *320*, 1755–1759.

[484] Yim, C. M.; Pang, C. L.; Thornton, G. *Phys. Rev. Lett.* **2010**, *104*, 036806.

[485] Bonanni, S.; Aït-Mansour, K.; Harbich, W.; Brune, H. *J. Am. Chem. Soc.* **2012**, *134*, 3445–3450.

[486] Bonanni, S.; Aït-Mansour, K.; Hugentobler, M.; Brune, H.; Harbich, W. *Eur. Phys. J. D* **2011**, *63*, 241–249.

[487] Bonanni, S.; Aït-Mansour, K.; Harbich, W.; Brune, H. *J. Am. Chem. Soc.* **2014**, *136*, 8702–8707.

[488] Rieboldt, F.; Helveg, S.; Bechstein, R.; Lammich, L.; Besenbacher, F.; Lauritsen, J. V.; Wendt, S. *Phys. Chem. Chem. Phys.* **2014**, *16*, 21289–21299.

[489] Gan, S.; Liang, Y.; Baer, D. R.; Sievers, M. R.; Herman, G. S.; Peden, C. H. F. *J. Phys. Chem. B* **2001**, *105*, 2412–2416.

[490] Tenney, S. A.; He, W.; Ratliff, J. S.; Mullins, D. R.; Chen, D. A. *Top. Catal.* **2011**, *54*, 42–55.

[491] Rieboldt, F.; Vilhelmsen, L. B.; Koust, S.; Lauritsen, J. V.; Helveg, S.; Lammich, L.; Besenbacher, F.; Hammer, B.; Wendt, S. *J. Chem. Phys.* **2014**, *141*, 214702.

[492] Matthey, D.; Wang, J. G.; Wendt, S.; Matthiesen, J.; Schaub, R.; Lægsgaard, E.; Hammer, B.; Besenbacher, F. *Science* **2007**, *315*, 1692 – 1696.

[493] Mellor, A.; Humphrey, D.; Yim, C. M.; Pang, C. L.; Idriss, H.; Thornton, G. *J. Phys. Chem. C* **2017**,

[494] Winnerl, A.; Pereira, R. N.; Stutzmann, M. *J. Appl. Phys.* **2015**, *118*.

[495] Moseler, M.; Walter, M.; Yoon, B.; Landman, U.; Habibpour, V.; Harding, C.; Kunz, S.; Heiz, U. *J. Am. Chem. Soc.* **2012**, *134*, 7690–7699.

[496] Yoon, B.; Landman, U.; Habibpour, V.; Harding, C.; Kunz, S.; Heiz, U.; Moseler, M.; Walter, M. *J. Phys. Chem. C* **2012**, *116*, 9594–9607.

[497] Yoon, B.; Häkkinen, H.; Landman, U.; Wörz, A. S.; Antonietti, J.-M.; Abbet, S.; Judai, K.; Heiz, U. *Science* **2005**, *307*, 403–407.

[498] Wörz, A. S.; Heiz, U.; Cinquini, F.; Pacchioni, G. *J. Phys. Chem. C* **2005**, *109*, 18418–18426.

[499] Kartouzian, A.; Thämer, M.; Heiz, U. *phys. status solidi (b)* **2010**,

[500] Dohnálek, Z.; Kim, J.; Bondarchuk, O.; White, J. M.; Kay, B. D. *J. Phys. Chem. B* **2006**, *110*, 6229–6235.

[501] Chen, L.; Smith, R. S.; Kay, B. D.; Dohnálek, Z. *Surf. Sci.* **2016**, *650*, 83–92.

[502] Xu, B.; Haubrich, J.; Freyschlag, C. G.; Madix, R. J.; Friend, C. M. *Chem. Sci.* **2010**, *1*, 310–314.

[503] Rodríguez-Reyes, J. C. F.; Teplyakov, A. V.; Brown, S. D. *Surf. Sci.* **2010**, *604*, 2043–2054.

[504] Harrison, A. G.; Jones, E. G.; Gupta, S. K.; Nagy, G. P. *Can. J. Chem.* **1966**, *44*, 1967–1973.

[505] Tian, C.; Vidal, C. *Chem. Phys. Lett.* **1998**, *288*, 499–503.

[506] Gupta, D.; Antony, B. *J. Chem. Phys.* **2014**, *141*, 054303.

[507] Hudson, J. E.; Weng, Z. F.; Vallance, C.; Harland, P. W. *Int. J. Mass Spectrom.* **2006**, *248*, 42–46.

[508] Peng, X.; Viswanathan, R.; Jr., G. H. S.; Stair, P. C. *Rev. Sci. Instrum.* **1992**, *63*, 3930–3935.

List of Abbreviations

AES	Auger Electron Spectroscopy
AFM	Atomic Force Microscopy
AQY	Apparent Quantum Yield
E-TEM	Environmental Transmission Electron Microscopy
L	Langmuir
LEED	Low Energy Electron Diffraction
MBE	Molecular Beam Epitaxy
ML	Monolayer
MOCVD	Metal Organic Chemical Vapor Deposition
OPO	Optic Parametric Oscillator
PI-TPD	Post Irradtion-Temperature Programmed Desorption
PSD	Photon Stimulated Desorption
QMS	Quadrupole Mass Spectrometer
SCR	Space Charge Region
SHG	Second Harmonic Generation
SPM	Scanning Probe Microscopy
STEM	Scanning Transmission Electron Microscopy
STH	Solar to Hydrogen
STM	Scanning Tunneling Microscopy
STY	Site Time Yield
TEM	Transmission Electron Microscopy
TOF	Turn Over Frequency
TPD	Temperature Programmed Desorption
UHV	Ultra High Vacuum
XPS	X-ray Photoelectron Spectroscopy

List of Figures

1.1. Selection of reported quantum yields for photocatalytic water splitting . . 2
1.2. Selection of reported total amounts of H_2 and O_2 from photocatalytic water splitting . . . 3

2.1. Band-bending in semiconductors in "dark" and illumination conditions. . 6
2.2. Fate of charge carriers in semiconductors for photocatalysis. 7
2.3. Short circuit model for photocatalytic water-splitting. 10

3.1. Scheme of the experimental setup. 12
3.2. TiO_2 single crystal sample holder 13
3.3. First and second generation GaN sample holders. 14
3.4. Auger electron spectrum of r-TiO_2(110) 17
3.5. H_2O-TPD on r-TiO_2(110) 17
3.6. O_2-PSD from r-TiO_2(110). 18
3.7. Auger electron spectrum of o-TiO_2(110) 19
3.8. Auger electron spectrum of $Ga_2O_3(\bar{2}01)$ 20
3.9. Auger electron spectrum of a MBE-grown GaN(0001) 21
3.10. Auger electron spectrum of a MOCVD-grown GaN(0001) 21
3.11. Measurement principle for TPD experiments 23
3.12. Measurement principle for PSD experiments 24
3.13. Measurement principle for photocatalytic experiments 24

4.1. CO adsorption on differently doped n-type GaN(0001). 26
4.2. Scheme of the CO PSD from n-type GaN(0001). 27

5.1. TPD mass traces for ethanol in MOCVD-grown GaN(0001). 29
5.2. Coverage series of ethanol on MOCVD-grown GaN(0001). 30
5.3. Acetaldehyde and ethylene yields from ethanol TPDs on MOCVD-grown GaN(0001). 30
5.4. Hydrogen yields from ethanol TPDs on MOCVD-grown GaN(0001). . . . 31
5.5. Water traces for ethanol TPDs on MOCVD-grown GaN(0001). 32
5.6. Molecule yields from ethanol TPDs on MOCVD-grown GaN(0001). 32
5.7. Selectivities for selected TPD experiments. 33
5.8. Ethanol photochemistry on MOCVD-grown GaN(0001). 35
5.9. Scheme of the surface reactivity of GaN, oxidized GaN and Ga_2O_3. 37

6.1. Auger electron spectrum of α-Fe_2O_3(0001). 41
6.2. LEED and surface representations of different α-Fe_2O_3(0001) crystal terminations. 42
6.3. Ozone and oxygen TPDs of α-Fe_2O_3(0001). 42
6.4. Methanol TPD from α-Fe_2O_3(0001) 43

6.5. Molecule yields from methanol on α-Fe_2O_3(0001) 44
6.6. Ethanol TPD from α-Fe_2O_3(0001) 45
6.7. Molecule yields from ethanol on α-Fe_2O_3(0001) 45
6.8. Photochemical experiments of ethanol on α-Fe_2O_3(0001). 46
6.9. TPDs with different illumination of ethanol on α-Fe_2O_3(0001). 47

7.1. Ethanol TPD from r-TiO_2(110). 49
7.2. Ethanol coverage series on r-TiO_2(110). 50
7.3. Reaction products from ethanol TPDs on r-TiO_2(110). 51
7.4. Hydrogen traces for ethanol TPDs from r-TiO_2(110). 51
7.5. Water traces for ethanol TPDs from r-TiO_2(110). 52
7.6. Integrated molecule yields from ethanol TPD experiments. 53
7.7. Ethanol TPD experiments with and without prior UV illumination. 55
7.8. Isothermal photoreaction of ethanol on r-TiO_2(110). 56
7.9. Water traces from ethanol TPD experiments with and without prior UV illumination. 57
7.10. Integral yields of acetaldehyde and water from ethanol photo-oxidation experiments. 57
7.11. Molecular mechanism of the ethanol photo-oxidation on r-TiO_2(110). . . . 58
7.12. Ethanol TPD after UV illumination from o-TiO_2(110). 60

8.1. Isothermal photoreaction and PI-TPD from tert-butanol on r-TiO_2(110). . . 64
8.2. Molecule yields from different photoreaction of tert-butanol on r-TiO_2(110). 65
8.3. Isothermal photoreaction and normalized decay kinetics from tert-butanol on r-TiO_2(110). 66
8.4. Photoreactions of tert-butanol on r-TiO_2(110) at different temperatures. . . 68
8.5. Thermal, photo-thermal and photochemical reaction pathways of tert-butanol on r-TiO_2(110). 70
8.6. TPD of tert-butanol-OD on r-TiO_2(110). 71
8.7. TPD coverage series of tert-butanol on r-TiO_2(110). 72
8.8. Integrated molecule yields from tert-butanol coverages on r-TiO_2(110). . . 73
8.9. Identification of photoreaction products of tert-butanol on r-TiO_2(110). . . 74
8.10. Photoreaction of tert-butanol on r-TiO_2(110) at different temperatures. . . 74

9.1. Photoreaction of methanol on r-TiO_2(110) and Pt_x/TiO_2(110). 77
9.2. The mechanism of methanol photoreforming on Pt_x/TiO_2(110). 78
9.3. Photocatalytic reforming on Pt_x/TiO_2(110). 79
9.4. Dependence on the excitation of methanol photoreforming. 80
9.5. Comparison between two photochemical mechanisms. 81
9.6. Cluster mass spectrum of Pt clusters. 84
9.7. Photochemistry of methanol on r-TiO_2(110). 85
9.8. Photochemistry on TiO_2(110) in a methanol background. 85
9.9. Stoichiometry of methanol photoreforming. 86

9.10. Illumination intensity dependent photocatalytic formaldehyde production. 86
9.11. Effect of the photon energy on methanol photoreforming. 87
9.12. Output of the used UV-LED. 87
9.13. Catalyst conditioning of methanol photocatalysis on Pt_x/r-TiO_2(110). . . . 88
9.14. Thermal desorption productions before the photocatalytic reaction temperature. 88
9.15. O_2-PSD on bare r-TiO_2(110) and Pt_x/TiO_2(110) after photoreforming. . . . 89

10.1. Methanol photo-oxidation on r-TiO_2(110). 91
10.2. Methanol photo-oxidation on o-TiO_2(110). 92
10.3. Photoreforming of methanol on Pt_x/r-TiO_2(110). 93
10.4. Pressure dependent TOFs for methanol photoreforming on Pt_x/r-TiO_2(110). 93
10.5. Illumination dependence of photocatalytic formaldehyde and methylformate formation on Pt_x/r-TiO_2(110). 94
10.6. TOFs for ethanol photoreforming on Pt_x/r-TiO_2(110). 95
10.7. Photoreforming of cyclohexanol on Pt_x/r-TiO_2(110). 96
10.8. Photoreforming of benzylalcohol on Pt_x/r-TiO_2(110). 96
10.9. Photoreforming of tert-butanol on Pt_x/r-TiO_2(110). 97
10.10. Temperature dependent photoreaction products of tert-butanol on Pt_x/r-TiO_2(110). 98
10.11. Catalytic cycle for methanol reforming on Pt_x/r-TiO_2(110). 101

11.1. Photocatalytic methanol reforming on Pt_1/r-TiO_2(110). 106
11.2. Methanol pressure-dependent TOF on Pt_1/r-TiO_2(110). 107
11.3. Illumination-dependent TOF for Pt_1/r-TiO_2(110). 108

12.1. O_2-PSD from r-TiO_2(110). 109
12.2. O_2-PSD from differently prepared TiO_2(110). 110
12.3. Normalized O_2-PSD from differently prepared TiO_2(110). 111
12.4. O_2-PSD from r-TiO_2(110) and Pt_x/r-TiO_2(110). 112
12.5. Normalized O_2-PSD from r-TiO_2(110) and Pt_x/r-TiO_2(110). 113

A.1. Drawing of the cluster source flange. 153
A.2. 3D-rendering of the cluster source flange. 154
A.3. Explosion drawing of the octupole assembly. 154
A.4. Drawing of the quadrupole bender and its mounting. 155
A.5. Rendering of a cross-section of the cluster apparatus. 156
A.6. Cluster mass scan for Pt clusters. 158
A.7. Cluster mass scan for Pt_1. 158

B.1. Example for the fragmentation correction for a TPD. 160

Acknowledgements

First and foremost, I want to thank Prof. Dr. Ulrich Heiz: you gave me the opportunity to work in this exciting and challenging project. I really appreciated the scientific freedom during all the projects and the chance to follow up on every promising idea. I cherish the scientific environment you envisioned and created in your group and want to thank you for always supporting me. Thank you for all the trust, Ueli!
Furthermore, I want to thank Prof. Dr. Martin Stutzmann for the particularly successful collaboration, sharing your tremendous knowledge of semiconductors and for being part of my thesis committee. I also want to thank Prof. Dr. Bettina Lotsch for being part of my thesis committee.
I am very indebted to Dr. Martin Tschurl for the excellent supervision of the projects, your drive to really grasp scientific issues and for countless hours of scientific discussions on blackboards, that always led to better conclusions. Further, I want to thank my lab mate Sebastian Kollmannsberger for all the effort he put into the projects together with me, your meticulous solutions to problems, being a great rival in sportive lab competitions and your constant drive and scrutiny in data analysis. I especially want to thank you both, not only for being excellent colleagues, but also great friends.
Furthermore, I acknowledge at this point the Zeidler Forschungsstiftung for granting Sebastian and me the opportunity to use the resources of the UnternehmerTUM MakerSpace GmbH, which enabled the manufacture of parts of the sample holder within the PhotoPlus project.
I also want to thank Carla for her commitment to the projects and her hard work, especially towards the end of my time here. It was a pleasure to add you to our morning coffee circle and I think the future of the lab holds great things for you.
I want to thank Dr. Rui Pereira for all the scientific discussions within the collaborative project, all the things I was able to learn from him about semiconductor physics, careful reading of publications and the long discussion about what constitutes an adsorption site. I further want to acknowledge Dr. Andrea Winnerl and Saskia Weiszer for the AFM characterizations of the GaN films during the project's beginning.
Furthermore, I want to thank Dr. Friedrich Esch for his inspiring curiosity and his never ending enthusiasm for almost any scientific topic and coffee.
I want to thank the doctors Philipp Heister, Tobias Lünskens, Martin Thämer and Aras Kartouzian for introducing me into cluster science during my undergraduate studies, their fascination with spectroscopy and lasers and the opportunity for meaningful scientific contributions. I further want to thank Dr. Sebastian Kunz, whose enthusiasm for science drew me to the group in the first place.
I also want to thank doctors Josef Kiermaier and Andreas Winbauer, who put so much work in building the core of the apparatus and maintaining it in excellent conditions. Further I thank Prof. Sebastian Günther for being helpful with every question concerning

vacuum and Dr. Florian Schweinberger for having an open ear and sharing his knowledge of cluster sources with me.
I further want to thank Prof. Dr. Cynthia Friend for hosting me as a visiting research scholar and her whole group for the welcoming atmosphere during my time abroad. I want to thank Dr. Andrew "Drew" Crampton for the fruitful collaboration, the many discussions about science and life in general and all the efforts around the collaboration. I further want to thank the Nanosystems Initiative Munich for granting me the travel grant, that made this collaboration possible. Especially, Peter and Christoph are acknowledged for their dedication in the work of the NIM graduate program.
I further want to acknowledge the whole group for making this a great place to work and do science. I especially acknowledge Jan, Marian, Fabian and Basti, who joined the group in parallel with me, for all the discussions about scientific and non-scientific topics. I also appreciated the help of Michael Eckinger for the planning of the cluster source and transfer chamber.
Furthermore, I want to express my gratitude to the mechanical workshop for realizing demanding and precise works concerning the apparatus and helping with all the obstacle repairs that came up. Further, the electronic workshop, Gerd in particular, is acknowledged for help with Friday afternoon emergencies. Many thanks go to Max Wiedemann, without whom trouble-shooting electronic parts would not have been feasible.
I also want to thank Carla Courtois, Patrick Schreiber, Kim Vetter, Moritz Eder, Sophie Mader, Michael Röhrl, Jeryl Yep, Nicolas Hadisurya and Kevin Jablonka, who did either their master's thesis, research internship or bachelor's thesis in the lab.

I further have to thank my family, especially my parents Andrea and Christian and my sister Theresa for their endless support. In this regard, I also want to thank my in-laws. I could not ask for a more caring and loving environment in my life. I further want to acknowledge my friends, especially Kierbaum, Basti, Xaver, Gaucho and Dom and furthermore Korbinian, Yvonne, Marita and Resa. Finally, I deeply thank my wife Lena for her never ending encouragement and loving support. I am certain, that you are one of the main reasons I went into science and am now and the end of dissertation. I am very curious, what future holds for us.

List of Publications

Publications and prepared manuscripts based on insights from this thesis:

S.L. Kollmannsberger†, C.A. Walenta†, C. Courtois, M. Tschurl, U. Heiz, Thermal Control of Selectivity in Photocatalytic Water-free Alcohol Reforming, *to be submitted*, See Chapter 10

C.A. Walenta†, A.S. Crampton†, U. Heiz, C.M. Friend, Ozone Preparation and alcohol reactivity of α-Fe_2O_3(0001), *to be submitted*, See Chapter 6

C.A. Walenta†, S.L. Kollmannsberger†, C. Courtois, R. N. Pereira, M. Stutzmann, M. Tschurl, U. Heiz, Why Co-Catalyst Loaded Rutile Facilitates Photocatalytic Hydrogen Evolution, *submitted*, See Chapter 9

C.A. Walenta†, S.L. Kollmannsberger†, C. Courtois, M. Tschurl, U Heiz, Photocatalytic Selectivity Switch to C-C Scission: α-Methyl Ejection of tert-Butanol on TiO_2(110), *Phys. Chem. Chem. Phys.*, **2018**, just accepted, See Chapter 8

S.L. Kollmannsberger†, C.A. Walenta†, A. Winnerl, F. Knoller, R.N. Pereira, M. Tschurl, M. Stutzmann, U. Heiz, Ethanol Surface Chemistry on MBE-grown GaN(0001), GaO_x/GaN(0001) and $Ga_2O_3(\bar{2}01)$, *J. Chem. Phys.*, **2017**, 147, 124704, See Chapter 5.2

C.A. Walenta†, S.L. Kollmannsberger†, A. Winnerl, R.N. Pereira, M. Tschurl, M. Stutzmann, U. Heiz, Anhydrous Ethanol Dehydrogenation on MOCVD-Grown GaN(0001), *J. Phys. Chem. C*, **2017**, 121, 16293-16298, See Chapters 5.1 and 7.1

S.L. Kollmannsberger†, C.A. Walenta†, A. Winnerl, S. Weiszer, R.N. Pereira, M. Tschurl, M. Stutzmann, U. Heiz, Doping-dependent Adsorption and Photon-stimulated Desorption of CO on GaN(0001), *J. Phys. Chem. C*, **2017**, 121, 8473-8479, See Chapter 4

C.A. Walenta†, S.L. Kollmannsberger†, J. Kiermaier, A. Winbauer, M. Tschurl and U. Heiz, Ethanol Photocatalysis on Rutile TiO_2(110): the Role of Defects and Water, *Phys. Chem. Chem. Phys.*, **2015**, 17, 22809-22814; See Chapter 7.2

---

† The authors contributed equally to this work.

Other Publications:

T. Lünskens, C.A. Walenta, P. Heister, A. Kartouzian and U. Heiz, Surface Oxidation of Supported, Size-Selected Silver Clusters, *J. Cluster. Sci.*, **2017**, 28, 3185-3192

A. Winbauer, S.L. Kollmannsberger, C.A. Walenta, J. Kiermaier, M. Tschurl, U. Heiz, Isomer-Selective Detection of Aromatic Molecules in Temperature-Programmed Desorption for Model Catalysis, *Anal. Chem.*, **2016**, 88, 5392-5397

T. Lünskens, P. Heister, M. Thämer, C.A. Walenta, A. Kartouzian and U. Heiz, Plasmons in Supported Size-Selected Silver Nanoclusters, *Phys. Chem. Chem. Phys.*, **2015**, 17, 17541-17544

Appendices

A

Further Experimental Details

A.1. The Cluster Source

In this chapter, some illustrative drawings of the cluster source are presented. The source itself (Figures A.1 and A.2) is very similar to other ones used earlier.[199,499] An explosion drawing of the skimmer and the octupole unit is shown in Figure A.3. The quadrupole bender (Fig. A.4) is mounted in a new way, that offers more possibilities for geometrical adjustments. In Figure A.5, a rendered view of the cluster source from the top perspective is depicted.

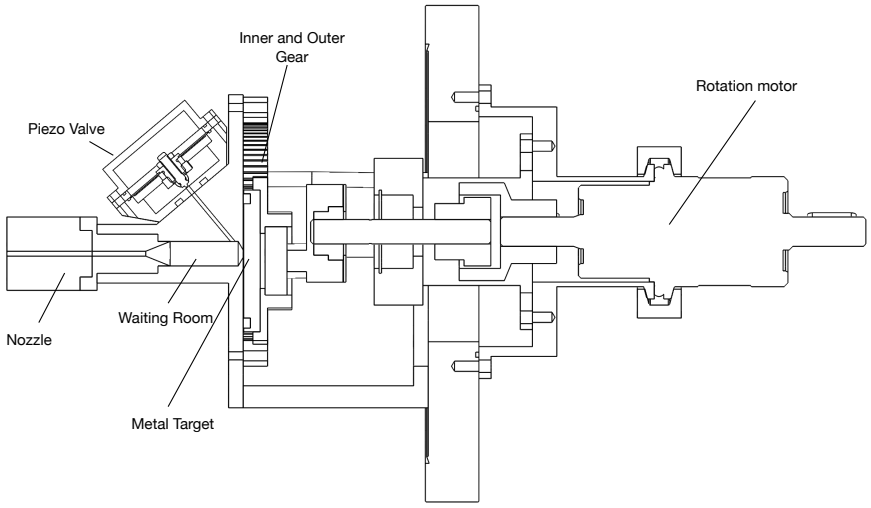

Figure A.1. A cross-sectional drawing of the cluster source flange. The metal target is pressed with a spring around the rotation axis in the outer gear. The piezo valve is fixed to the point of ablation, with a small volume called "Waiting Room". The as-generated clusters then expand through the nozzle into the vacuum.

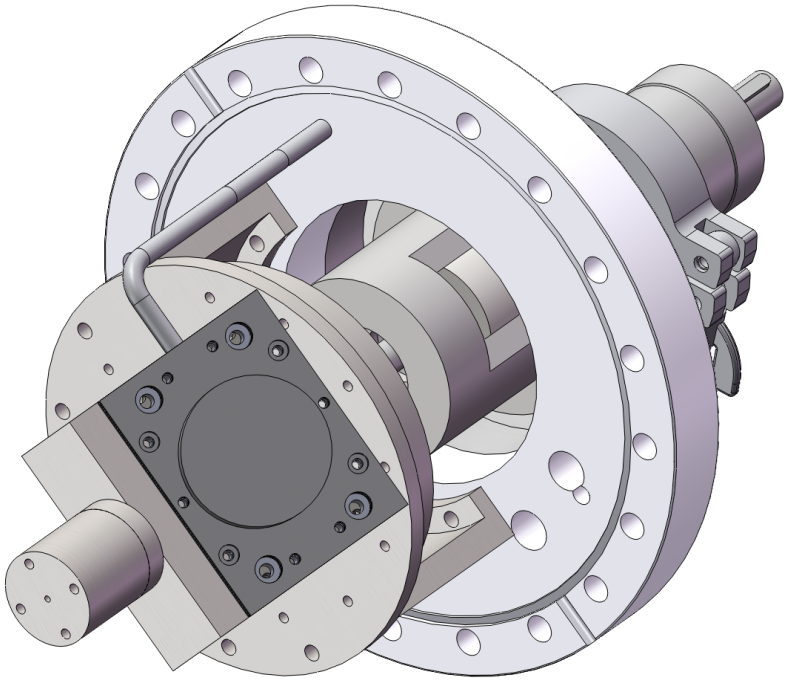

Figure A.2. Rendering of the cluster source assembly flange with the gas input into the vacuum. The piezo valve is mounted on top of the cluster source and sealed by a Viton ring.

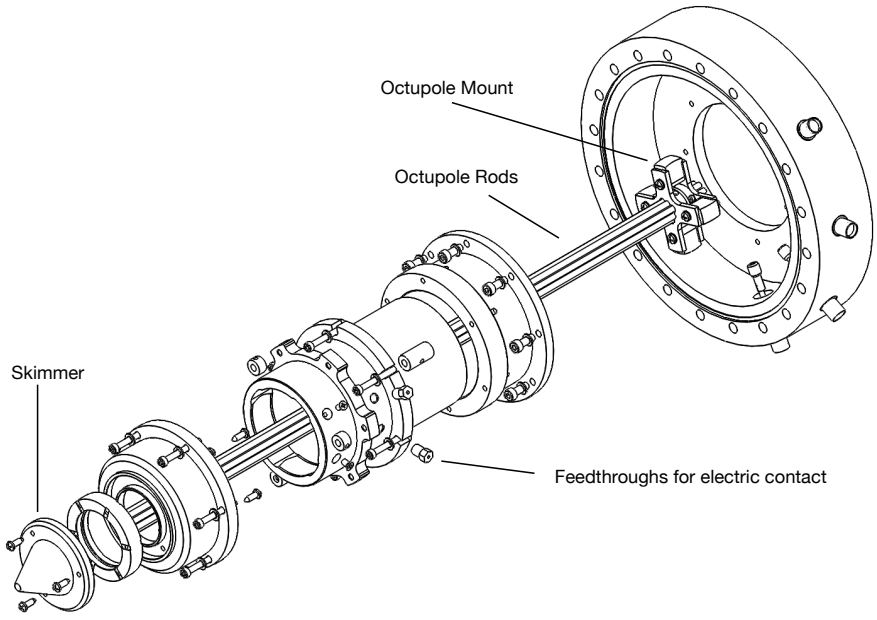

Figure A.3. Explosion drawing of the octupole assembly. The skimmer is shown in the left bottom part of the drawing and the isolated first holder

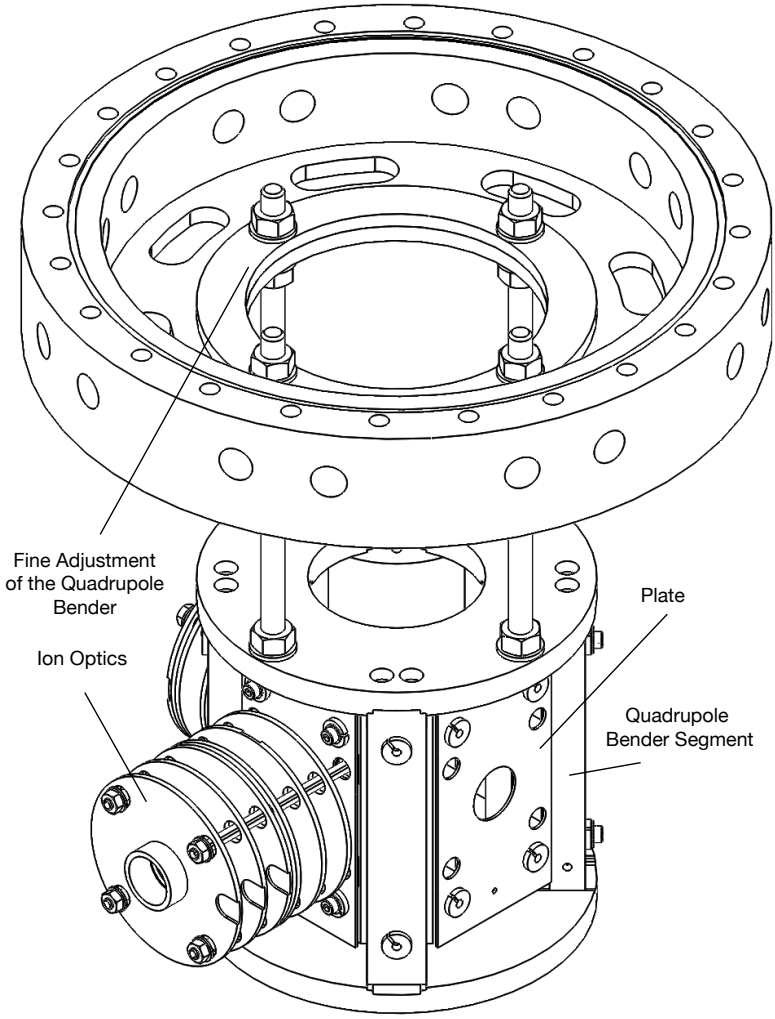

Figure A.4. Drawing of the quadrupole bender and its mounting. By adjusting the threaded rod, the position in the bender chamber and angles can be adjusted precisely.

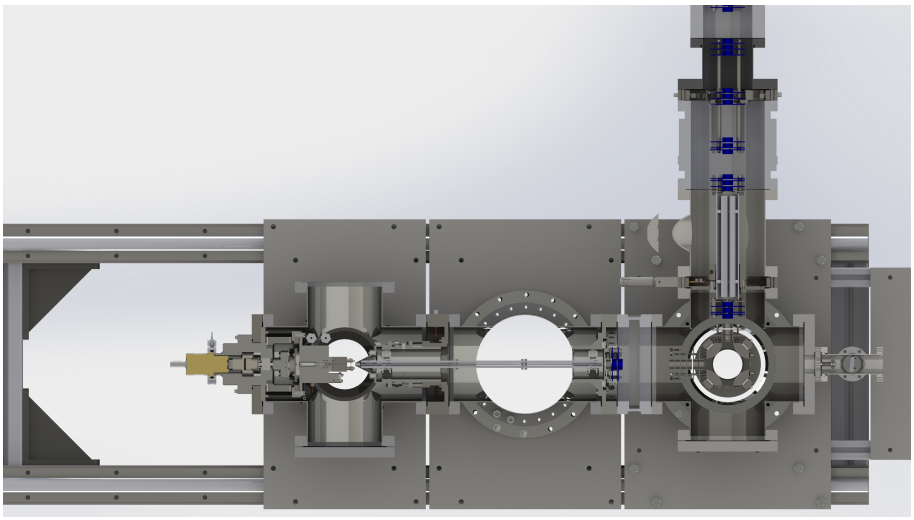

Figure A.5. Rendering of a cross-section of the cluster apparatus from a top viewpoint. Note, that the ion optics after the quadrupole mass filter are shown in a simplified way.

Table A.1. List of settings for the cluster source - part I.

Variable	Value
He-backinge pressure	7 bar
Piezo voltage	300 V
Piezo pulse width	400 µs
Piezo pulse delay	-200 µs [a]
Pressure in source chamber	1.1 mbar
Skimmer	13 V
Octupole DC	23 V
Octupole Frequency	2.11734 MHz
Octupole Guide 1	-160 V
Octupole Guide 2	-9 V
Octupole Guide 3	-310 V
Octupole Guide 4	-7 V
Bender Lense 1	-113 V
Bender Lense 2	-16 V
Bender Lense 3	-88 V
Bender Lense 4	-188 V
Bender Lense 5	-81 V
Bender Lense 6	-124 V
Plate In	-72 V
Quad A	-66 V
Quad B	-487 V
Plate Out	-55 V
Bender Lense 7	-210 V
Bender Lense 8	-120 V
QMS Lense 1	-3.6 V
QMS Lense 2	-22 V
QMS Lense 3	25 V
QMS Lense 4	-170 V
QMS Lense 5	–50 V
QMS Lense 6	-9 V
QMS Lense 7	-200 V
QMS Lense 8	-9 V
QMS Resolution	6.05
Bellow 1	-140 V
Bellow 2	-15 V
Bellow 3	-8 V
Bellow 4	-290 V
Bellow 5	-160 V
Bellow 6	-10 V
Bellow 7	-170 V
Bellow 8	-14 V
Bellow 9	-90 V
Bellow 10	-67 V
Bellow 11	-150 V
Main Chamber 1	-80 V
Main Chamber 2	-150 V
Main Chamber 3	-40 V
Main Chamber 4	-80 V
Main Chamber 5	-5 V
Main Chamber 6	-8 V
Main Chamber 7	-36 V

[a] This value is negative with respect to the laser pulse, since the valve has a opening time of about 200 µs, so the He reaches the target contemporaneous with the laser pulse.

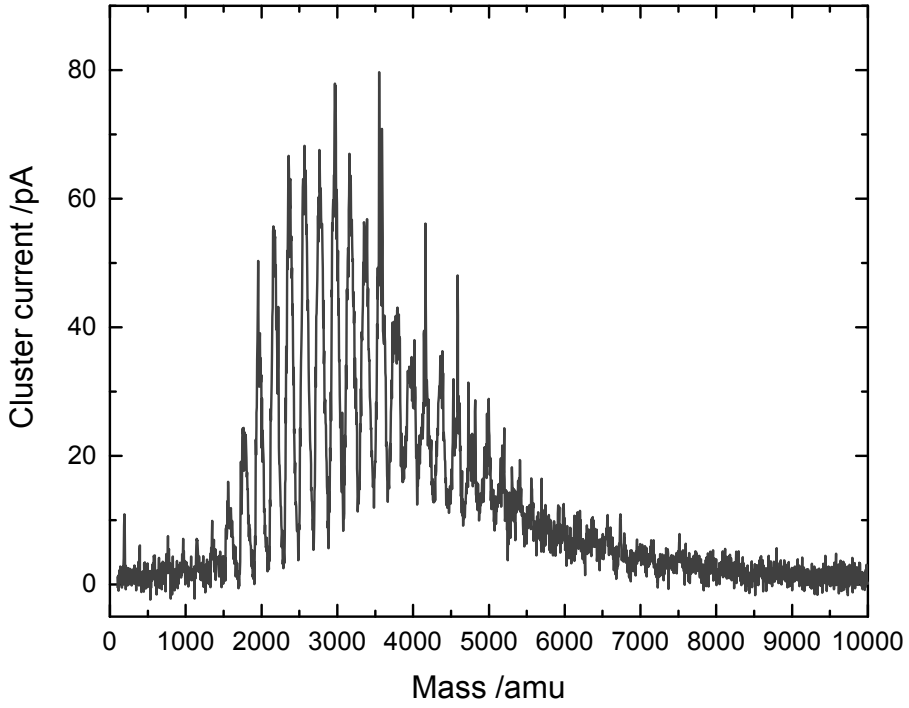

Figure A.6. A mass scan from 0 to 10000 amu for the generation of Pt clusters with the settings reported in the table A.1.

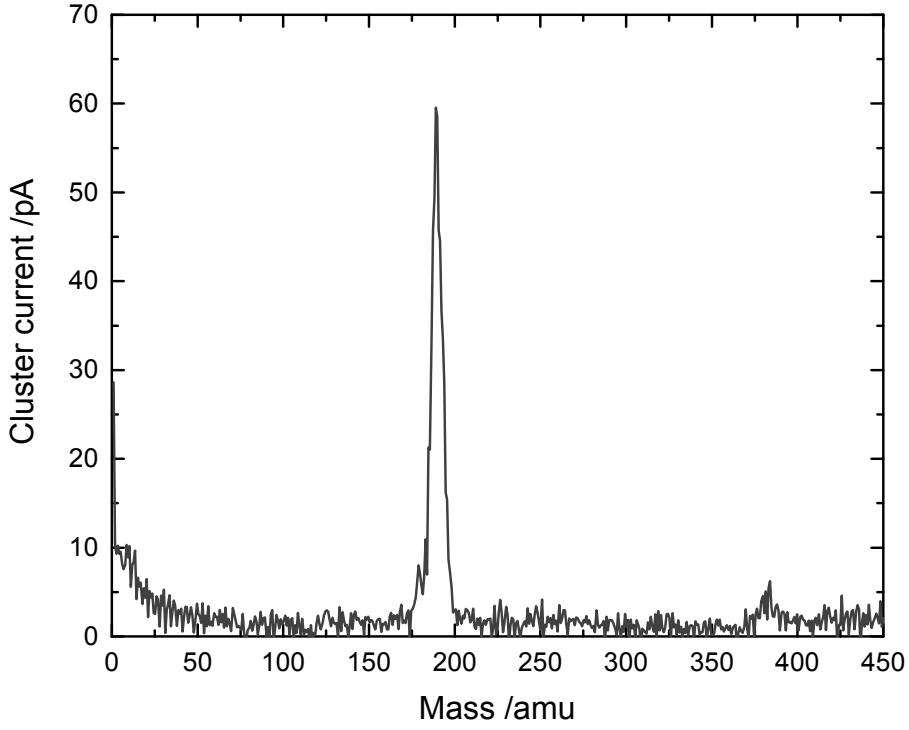

Figure A.7. A mass scan with for Pt atom with settings optimized for the atom.

A.2. Chemicals

A list of the chemicals used in this work is presented in table A.2.

Table A.2. A list of reactants and chemicals used in this work.

Substance	Supplier	Purity
Ammonia	Air Liquide	99.97% (3.8)
Argon	Air Liquide	99.9999% (6.0)
Benzylalcohol	Sigma-Aldrich	99,8%
Carbon Dioxide	Westfalen	99.999% (5.0)
Carbon Monoxide	Air Liquide	99.997% (4.7)
Cyclohexanol	Sigma-Aldrich	99%
Deuterium	Westfalen	99% (2.0)
Deuterium oxide	Sigma-Aldrich	99.9 atom % D
Ethanol	Sigma-Aldrich	$\geqslant$99.8%
Ethanol-OD	Sigma-Aldrich	98 % D
Ethanol-d_6	Sigma-Aldrich	$\geqslant$99.5 atom % D
Helium	Westfalen	99.996% (4.6)
Helium	Westfalen	99.9999% (6.0)
Methanol	Sigma-Aldrich	$\geqslant$99.9%
Methanol-d_3	Sigma-Aldrich	99.8 atom % D
Oxygen	Westfalen	99.999% (5.0)
Paraformaldehyde-d_2	Sigma-Aldrich	98 % D, 98%
Tert-butanol	Sigma-Aldrich	$\geqslant$99.5%
Tert-butanol-OD	Sigma-Aldrich	99 atom % D
Water	Milli-Q	$\geqslant$ 18.0 MΩ·cm

B

TPD and TOF Quantification

The deconvolution of the fragmentation patterns for TPD allows for the exact quantification of product formation of a TPD experiment. First, a known coverage is referenced to standard experiment. To calibrate for the ion current signal of a monolayer, a waterfall coverage plot with a clear peak assignment to lattice sites needs to be obtained without any interfering signals. Suitable molecules include H_2O[205,374,500], alcohols[374] or small hydrocarbons[501] on TiO_2(110). In all of these studies, the coverages of 1 ML of H_2O are defined to be 1 ML $\equiv 5.2 \cdot 10^{14}$ molecules/cm^{-2}. Most other coverages from experiments with molecular beam dosers are referenced to the one of water.[374,500]
This leads to a trace, where certain amount of reactant leads to a certain amount of ion current for that molecule. This will be used later for the TOF determination. A very

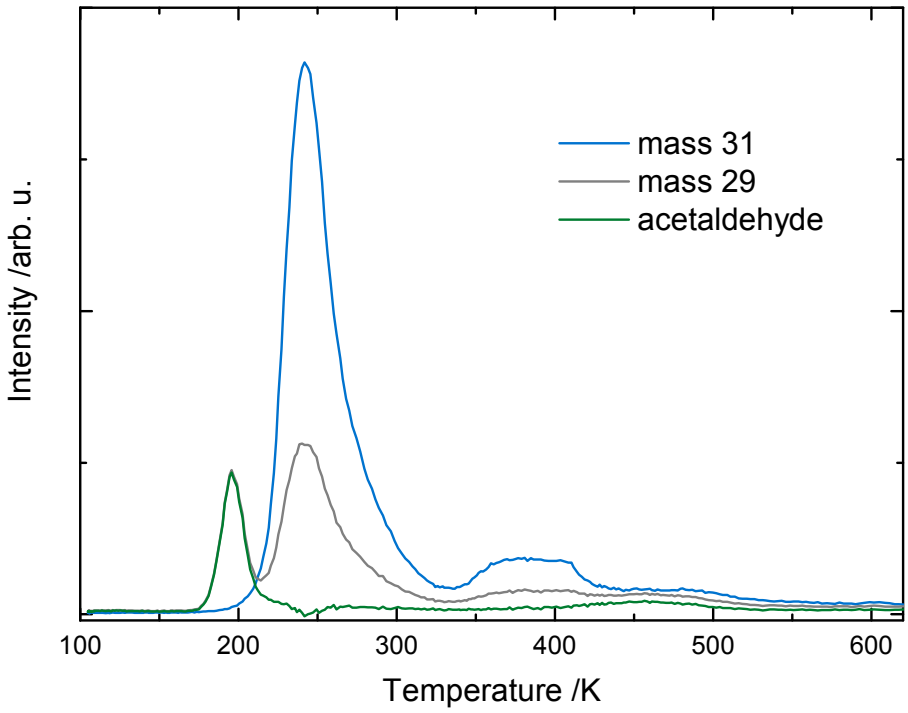

Figure B.1. Mass traces from a ethanol TPD experiment after 5 min of UV illumination at 100 K. Mass trace 31 is the main fragment from ethanol, while mass trace 29 is the main fragment of acetaldehyde, but occurs also in the ethanol fragmentation pattern. By subtracting the mass 29 trace with the factor of 0.33 from the ethanol cracking pattern, the acetaldehyde trace is obtained. This holds true, if no further fragments from other molecules are contributing to the respective trace.

simple example for the fragmentation pattern correction is the deconvolution of the acetaldehyde signal from an ethanol photochemistry experiment. Here, a PI-TPD of ethanol is shown in Figure B.1, in which some acetaldehyde is formed on the surface. Ethanol is identified by mass 31, acetaldehyde usually by mass 29. The latter exhibits 4 features, at 200 K, 250 K, 375 K and 450 K. However, two of them originate from the fragmentation pattern of ethanol. Therefore, the correction for acetaldehyde is presented as follows:

$$\text{acetadelhyde} = \text{trace } 29 - 0.33 \times \text{trace } 29 \tag{B.1}$$

However, this works only, if no further fragmentation from other molecules contributes to the fragmentation pattern. In general, obviously more fragment masses than molecules have to be available to be determined. While the analysis can be still performed by hand, it is advisable to have a certain mass trace as a control fragment to see whether the correction is performed correctly. For more complex systems, a Matlab Code from the Friend group is available publicly, that does an evaluation of the mass traces for molecules defined by the user.[502] Further development for the data analysis is also reported for heavily fragmenting model systems, without an educated guess by the user.[503]
While this fragmentation pattern correction is handy, the integrals from those signals are not directly the quantified molecule yields. In the photoreforming experiments, no coverage determination as described above was feasible for H_2 and formaldehyde. Therefore, the formed amount of i.e. hydrogen is integrated with respect to the baseline. This results in an value A_{raw} for the respective molecule. From this value, the corrected area A_{corr} for hydrogen can be determined by the following equation:

$$A_{corr} = \frac{A_{raw} \cdot FF \cdot T}{\sigma} \tag{B.2}$$

The corrected integral for hydrogen is then the product of the mathematic integration A_{raw}, the Fragmentation Factor FF obtained from the fragmentation pattern and a value for the transmission of the QMS T, divided by the ionization cross section σ (see table B.1). The obtained value is then related to the ion signal ($2.8313 \cdot 10^{-9}$) from 1 ML of methanol on r-TiO_2(110) from the coverage determination above. Furthermore, the amount of active sites needs to be known. In this case we assumed those to be the BBO vacancies with a density of 6% of a monolayer from TiO_2(110). The TOF is therefore:

$$TOF = \frac{A_{corr}}{2 \cdot 10^{-9} \cdot 0.06 \cdot t} \left(\frac{\text{molecules}}{\text{active site} \cdot s}\right) \tag{B.3}$$

This procedure gives stoichiometric values of the TOFs of all identified reaction products in this work. The transmission coefficient T is determined either experimentally by applying a certain background pressure of gases and correlating this to the pressure (with further factors considering the pressure determination with the ion gauge), or taking a typical function for a QMS, that is mainly an exponential decay toward higher masses.

Table B.1. Ionization Cross Sections used in this work.

Molecule	Ionization Cross Section / Å^2
Acetaldehyde	6.7 [424]
Acetone	9.0 [424]
Benzylaldehyde	20.1 [504]
Benzyl benzoate	39.06 [504]
Cycloehexanone	17.6 [504]
Ethanol	7.40 [422]
Ethylene	5.39 [505]
Formaldehyde	4.14 [506]
Hydrogen	1.021 [423]
Isobutene	11.889 [423]
Methanol	4.61 [424]
Methylformate	6.8 [507]
Methyl-Radical	2.99 [508]
Tert-butanol	13.41 [424]
Toluene	16.1 [504]
Water	2.275 [423]

C

Doping-Dependent Adsorption and Photon-Stimulated Desorption of CO on GaN(0001)

THE JOURNAL OF PHYSICAL CHEMISTRY C

Article

pubs.acs.org/JPCC

Doping-Dependent Adsorption and Photon-Stimulated Desorption of CO on GaN(0001)

Sebastian L. Kollmannsberger,[†,∥] Constantin A. Walenta,[†,‡,∥] Andrea Winnerl,[§] Saskia Weiszer,[§] Rui N. Pereira,[§] Martin Tschurl,[†] Martin Stutzmann,[§,‡] and Ueli Heiz*[,†,‡]

[†]Chair of Physical Chemistry, Department of Chemistry & Catalysis Research Center, Technische Universität München, Lichtenbergstr. 4, 85748 Garching, Germany

[‡]Nanosystems Initiative Munich, Schellingstr. 4, 80799 München, Germany

[§]Walter Schottky Institute and Physics Department, Technische Universität München, Am Coulombwall 4, 85748 Garching, Germany

Supporting Information

ABSTRACT: CO is used as a chemical probe molecule to elucidate the properties of differently n-type doped GaN(0001) surfaces under ultrahigh vacuum conditions. Doping-dependent sticking of CO is observed by temperature-programmed desorption, which is not influenced by the surface composition of the semiconductor substrates. By the excitation of the semiconductor with UV photons a low-temperature desorption of CO is stimulated. The absolute photon-stimulated desorption intensity strongly depends on the surface composition. However, the desorption kinetics do not significantly depend on the surface composition, semiconductor doping, or UV excitation wavelength. A model is introduced, which is based on the electronic characteristics of the GaN substrates and describes the doping-dependent adsorption as well as the photochemical behavior.

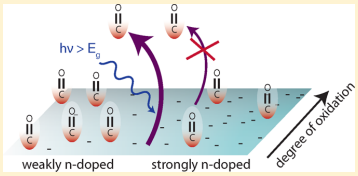

INTRODUCTION

Heterogeneous photocatalysis is believed to be a viable pathway to H_2 production from renewable energy sources and sunlight.[1−3] Since their discovery as suitable catalysts, group III−V materials such as gallium nitride (GaN) have proven to be stable heterogeneous photocatalysts when decorated with cocatalysts.[4−6] The most explored reactions in photocatalysis on GaN are the H_2 evolution from water[6−11] and the CO oxidation.[12−16]

Pure GaN is a semiconductor with an energy gap of 3.4 eV.[17] In contrast with other semiconductors used in photocatalysis such as ZnO and TiO_2, it can be n-type- as well as p-type-doped to alter the charge-carrier concentration and the sign of charge accumulated at the illuminated surface.[18] Additionally, solid solutions of GaN with other wurtzite-type structures such as ZnO can be prepared. Because in such systems the energy of the valence band edge is shifted upward with respect to ZnO, the band gap is moved into the visible part of the solar spectrum.[19,20] Despite these promising properties the surface chemistry even of bare GaN is not well known, which is different from other catalysts such as TiO_2.[21,22] Previous surface science studies mainly have focused on the building process during epitaxial growth[23−25] and surface reconstructions[26−28] for applications in devices.[29,30] However, a better understanding of the surface chemistry of the bare semiconductor helps in identifying and avoiding undesirable side reactions in heterogeneous (photo)catalysis. O_2 photon-stimulated desorption (PSD) from TiO_2(110) is a powerful tool to determine the photochemical activity of the bare semiconductor surface.[31,32] While the detailed mechanism of O_2 PSD from TiO_2 has been investigated during the last 30 years,[33−38] no other PSD experiments without a previous chemical reaction on semiconductors are known.

In metal nanoparticle/semiconductor hybrid materials it has been shown that the p-type or n-type doping has an influence on the charge state of the metal nanoparticle as well as on the charge carrier dynamics. Consequently, the reactivity during catalysis is also affected by semiconductor doping.[15,39] The common assumption of those studies is that the chemical properties of the semiconductor surface are doping-independent, as doping only alters the bulk charge-carrier concentration.

In this work, we present a ultrahigh vacuum (UHV) study of the effect of bulk semiconductor n-type doping on the CO adsorption on the GaN(0001) surface and investigate the PSD of CO from that surface.

EXPERIMENTAL SECTION

Different GaN samples were studied in the UHV using an apparatus that is equipped with standard methods for surface science to perform thermal and photochemical reaction studies. This apparatus is described in detail elsewhere.[40] The Si-doped GaN(0001) epitaxial layers with a thickness of ∼550 nm were deposited by plasma-induced molecular beam epitaxy (PIMBE). As substrates Fe-doped semi-insulating Ga-polar

Received: February 17, 2017
Revised: March 28, 2017
Published: March 31, 2017

DOI: 10.1021/acs.jpcc.7b01570
J. Phys. Chem. C 2017, 121, 8473−8479

GaN MOCVD templates (thickness 4 μm) on α-Al_2O_3(0001) from Lumilog were used. The samples were grown in the Ga-droplet regime. During the process, the substrate temperature was kept at 1143 K. The Ga source was heated to 1253 K, which corresponds to a beam equivalent pressure of 1.3×10^{-6} mbar. For the silicon doping, the source was operated at 1273 and 1373 K. The plasma source was operated at 300 W with a nitrogen flux of 0.15 sccm. These conditions were chosen because it is well known that atomically flat surfaces can be achieved in this way.[41] Furthermore, it is known that for the range of silicon dopant concentrations employed in this study the dopant profile in the homoepitaxial layers is constant because it has been confirmed by SIMS profiles.[42] The free electron concentration of all of these samples was determined by Hall effect measurements.[43] The GaN samples were cut to a rectangular shape with a size of 10 mm × 10 mm for being mounted onto a sample holder, which consists of a 1 mm thick tantalum plate with a 0.3 mm deep cutout of the size of the GaN sample. A thin (0.025 mm) gold foil is placed between the base plate of the sample holder and the semiconductor to ensure good thermal conductivity. The fixation of the semiconductor samples is achieved by two spot-welded 0.1 mm thick tantalum clamps. The heating of the sample is performed indirectly via resistive heating of two tungsten–rhenium wires (0.38 mm in diameter), which are mounted on the sides of the tantalum holder. This setup has been developed on the basis of TiO_2 sample holders.[40,44] Cooling of the sample to temperatures of around 100 K is achieved by contact to a reservoir of liquid nitrogen (LN_2). The temperature is measured by the calibrated readout of a twisted type-C thermocouple spot-welded to the bottom of the tantalum sample holder. The deviation of the temperature of the GaN surface to the base plate was determined to be <5 K over the entire temperature range. The in situ GaN treatment before measurements includes a single vacuum annealing to 800 K for 10 min and a cycle of Ar^+ sputtering at 80 K (0.5 keV, 1×10^{-6} mbar, $I_{sputter}$ = 2.0 μA) with a subsequent vacuum annealing flash to 800 K, so that no carbon contamination is observed with Auger electron spectroscopy (AES). The surface morphology and roughness were checked ex situ with atomic force microscopy (AFM) (Figure S1).

For the photochemical measurements a Nd:YAG-pumped dye laser (Spectra GCR 4, ~10 ns pulse length) (Lambda Physics) with a wavelength of 266.5 nm is used to excite electron–hole pairs close to the GaN surface. The laser spot is adjusted to illuminate the entire GaN sample. The intensity is set to a pulse energy of 600 μJ/pulse, so that no laser-induced thermal heating effects are observed. All PSD experiments were performed at LN_2 temperature.

RESULTS

Thermal Adsorption and Desorption. CO temperature-programmed desorption (TPD) measurements were performed on three differently doped MBE GaN samples to monitor the influence of doping on the adsorption effects at the GaN surface. Sample a is nominally undoped (5.2×10^{16} charge carriers (cc)/cm^3), sample b is weakly n-type doped ($1.3 \times 10^{18} \pm 1.2 \times 10^{16}$ cc/cm^3), and sample c is strongly n-type doped ($2.1 \times 10^{19} \pm 2.2 \times 10^{18}$ cc/cm^3).

Figure 1 presents a series of TPD spectra from various CO exposures on sample c ($2.1 \times 10^{19} \pm 2.2 \times 10^{18}$ cc/cm^3). For lower coverages only one desorption peak is observed at ~100 K. A second peak, which appears at ~225 K, is observed for

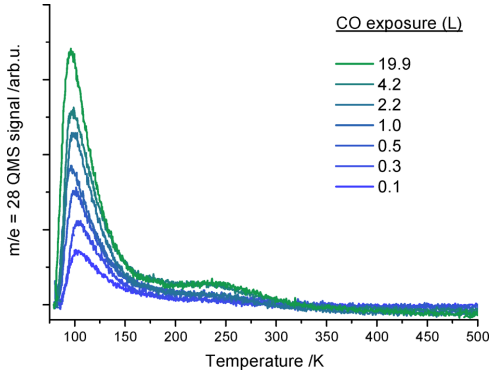

Figure 1. TPD spectra from various coverages of CO dosed on a GaN(0001) surface, sample c, at 80 K.

coverages of 1 langmuir (L) and more. Control experiments indicate that this feature originates from CO desorption from the sample holder. The low-temperature peak is assigned to thermal desorption of physisorbed CO from the GaN surface. Because the relative change in the desorption signal is low for high coverages a saturation behavior is already suggested. Hence it can be seen that no multilayer adsorption occurs in this temperature range. The CO desorption from a multilayer for a nonmetal is expected to occur at ~30 K.[45,46] The GaN samples with the lowest charge-carrier concentrations also show a similar behavior concerning the peak position. However, if the absolute integrals of the 100 K desorption peak at identical exposures are regarded, then a difference between the three GaN samples is observed. The resulting saturation graphs from exposures of 0.1 to 9.0 L are shown in Figure 2. The exposures were determined by background-corrected integration of the m/e = 28 signal of the quadrupole mass spectrometer (QMS) during dosage.

As shown in Figure 2, the total saturation coverage is decreasing with increasing n-type doping of the GaN samples. Furthermore, for the smallest exposures to CO, a steeper rise in

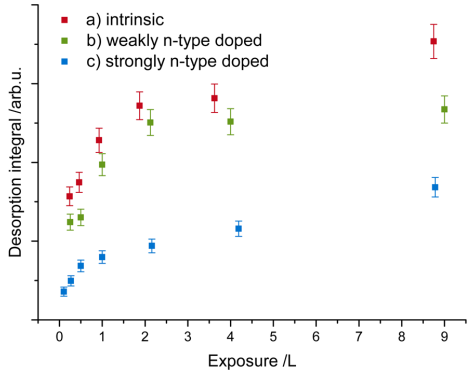

Figure 2. CO desorption integral series of three differently doped GaN samples from exposures of 0.1 to 9.0 L. The higher the charge carrier concentration, the slower the CO coverage rises and the lower is the maximum CO coverage.

DOI: 10.1021/acs.jpcc.7b01570
J. Phys. Chem. C 2017, 121, 8473–8479

the desorption integral is observed for weaker n-type-doped samples.

Photon-Stimulated Processes. After illumination of a 2.0 L CO-covered GaN surface by UV light at 80 K a considerably smaller thermal desorption signal is observed in TPD compared with that without previous illumination (Figure 3a). With the exception of the high-temperature feature due to the sample holder, the TPD signal decreases as a whole and not at a specific temperature. This indicates that all binding sites are affected similarly by the photostimulation. During the illumination process, desorption of CO occurs (Figure 3b), which stops within the time resolution of the desorption experiment when illumination ends. The absolute amount of CO desorbed via the PSD and the consecutive TPD quantitatively matches the regular desorption of 2.0 L in a "dark" only TPD experiment within the experimental accuracy.

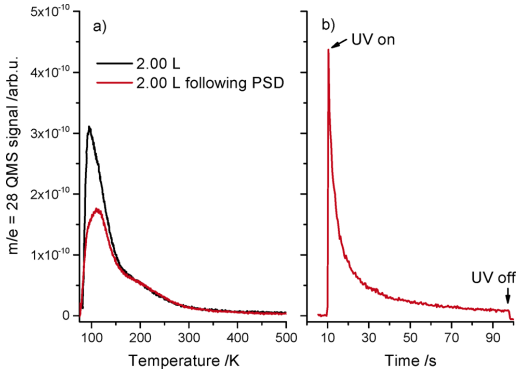

Figure 3. (a) TPD spectra of 2.0 L CO with and without UV illumination after CO exposure on a nonintentionally doped GaN(0001). The desorption following the illumination is considerably smaller than the "dark" one. (b) Photon-stimulated desorption spectra of CO at 80 K. UV excitation starts at 10 s and an immediate CO desorption is observed. Note that panels a and b have the same scale in the $m/e = 28$ QMS signal and that the sum of the integrated red curves matches the "dark" desorption quantitatively.

Figure 4 illustrates the normalized intensities of PSD curves for differently n-type-doped samples. It is found that no appreciable difference in the decay curves is observed, which shows that the photon-stimulated desorption kinetics does not change with the semiconductor doping. After an initial rise in intensity, the signal decay can be described by a sum of two stretched exponential functions, one with a fast time constant in the range of some seconds and one with a slow time constant about 1 order of magnitude higher. A change in the irradiation wavelength to 355 nm resulted in the same desorption kinetics (Figure S2). Furthermore, the kinetics were also found to be independent of the surface oxidation state. It is well known that intermediate gallium oxide species (GaO_x) and stoichiometric Ga_2O_3 are always present on GaN surfaces,[47] and even repeated AES measurements can oxidize the surface.[48] Long cycles of Ar^+ sputtering reduce the N/Ga ratio, and nitrogen vacancies are formed.[49,50] Oxygen impurities from the sputter gas or the background pressure lead to an oxidation of the free Ga surface species. The evolution of the surface oxidation can be tuned by the sputtering time and is determined by AES, corrected for the elemental sensitivities.[51] For the calculation of the percentage

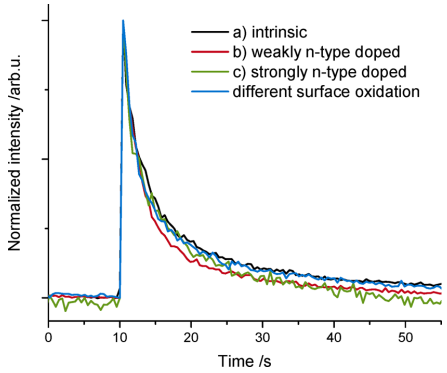

Figure 4. Intensity-normalized PSD signal of three differently doped GaN samples with the same surface oxidation as well as of a differently oxidized GaN surface. The various decay curves do not exhibit any significant differences. Hence the kinetics of the PSD is independent of doping and surface oxidation.

of respective atoms it is assumed that the oxidation occurs only at the surface, as it is described in the literature.[52]

In Figure 5a, it can be seen that the photoactivity decreases with a decrease in the N percentage on the surface. Figure 5b demonstrates the decline in PSD intensity with rising oxygen content. If the PSD intensity is plotted versus the N/O ratio (Figure 5c), then a sigmoidal curve with a linear transition region results. Thus it can be concluded that the presence of oxygen atoms and the decrease in nitrogen lead to a decrease in the PSD intensity. However, the kinetics of the PSD remain unaltered, and similarly the thermal desorption is also found to stay unaffected by the surface oxidation process (Figure 4).

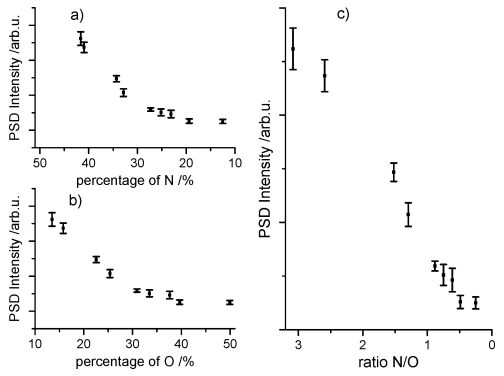

Figure 5. (a) Decrease in PSD intensity with decreasing percentage of nitrogen. (b) Decrease in PSD intensity with increasing percentage of oxygen. (c) Sigmoidal PSD intensity trend as a function of N/O ratio. All Ga, N, and O percentage values were obtained from AES measurements, corrected for the corresponding elemental sensitivities.[51] The percentage of gallium decreases from 45 to 38% with increasing O coverage in the indicated range.

DISCUSSION

Thermal CO Adsorption and Desorption. The binding of CO to GaN(0001) only occurs via physisorption, which is

DOI: 10.1021/acs.jpcc.7b01570
J. Phys. Chem. C 2017, 121, 8473−8479

indicated by the low desorption temperature of ~100 K (Figure 1). It is found that the sticking of CO is dependent on the dopant concentration. The intensity of the desorption signal for same dosages decreases with increasing n-type doping. The effect is significant but is not as pronounced as the change of the dopant concentration: An increase in the charge-carrier concentration by a factor of one thousand only results in a maximum decrease in the desorption signal by a factor of 2. While doping results in different electronic properties of the semiconductor, its surface morphology is preserved, as can be seen in the respective AFM images (Figure S1). The saturation coverage behavior shown in Figure 2 and the same desorption temperature of CO also allow us to exclude the formation of different surface defects for different doping levels. In such a case, a difference in the binding of CO to the surface would result, which would be reflected in different TPD peaks. However, such an effect is not observed. Furthermore, the sticking of CO does not significantly depend on the surface composition, as GaN samples with identical doping but different degrees of surface oxidation exhibit identical CO desorption characteristics in TPD experiments. To explain these effects, we propose the following adsorption model, which is sketched in Figure 6 and considers the dependence of the CO sticking on the semiconductor doping.

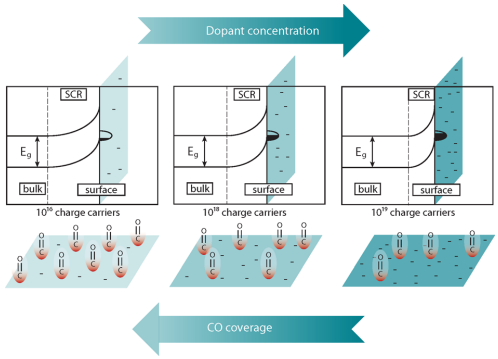

Figure 6. Influence of bulk doping on the CO adsorption on GaN(0001). Because samples with the same surface morphology are obtained by epitaxy, bulk doping only significantly affects the space charge region (SCR) below the GaN surface. Consequently a different degree of electron accumulation in the surface states is obtained. The occupation of surface states and the negative surface charges in the figure are for illustrative purposes only. A higher n-doping results in a higher negative charge density at the semiconductor's surface, which enables the adsorption of only a few electron donors such as CO. Therefore, less CO is bound on higher n-doped GaN samples, whereas on nonintentionally n-doped GaN the highest CO coverage is observed.

All of the investigated semiconductors are n-type and therefore exhibit accumulation of electrons in surface sites, which results in an upward band bending.[53] Moreover, from surface photovoltage experiments it is known that this band bending at the surface occurs in a very similar manner for all of the samples.[54] However, a different amount of doping results in a different depth of the space charge region (SCR) and a different degree of electron accumulation in the surface sites. From calculations similar to those previously reported,[54] performed with the nextnano software package,[55] we estimate that the surface charge density increases by about 1 order of magnitude when the doping is changed from the value of sample a (nominally undoped) to that of sample c (highly n-type-doped).

CO is considered to be an electron donor, and it is expected that the physisorbed molecule donates some negative charge to the semiconductor. Thus CO is expected to adsorb on surface sites sufficiently far away from the negatively charged, electronically active surface defects, which are responsible for the upward band bending. A similar phenomenon was observed for NH_3 on TiO_2(110), where the ammonia molecules are repelled by an increased number of negative surface states of the n-type semiconductor.[56] This is also in very good agreement with our simulations and shows that doping itself is indeed changing the surface charge density and thus the adsorption properties of the molecules. Consequently, on the surface of a highly n-doped GaN, where the density of negatively charged surface states is higher, less CO would be adsorbed in comparison with a nominally undoped GaN sample with less negative charge.

Photon-Stimulated Desorption of CO. Figure 3 shows that upon UV illumination a fraction of the adsorbed CO desorbs from the GaN(0001) surface. It is found that the kinetics of this process is not influenced by semiconductor doping, as it can be seen in Figure 4. Because the SCR changes with the degree of doping, it can be concluded that the size of the SCR does not significantly affect the desorption rate. Similarly, the same exponential decay is also observed for GaN surfaces with different degrees of oxidation. However, and in contrast with the CO adsorption, the presence of oxygen instead of nitrogen reduces the PSD intensity. As a consequence, it can be concluded that certain adsorption sites exist, which promote the photodesorption of CO (photoactive sites). These sites diminish for higher degrees of oxidation, which is accompanied by the release of nitrogen. As a result of the existence of these photoactive sites, only a fraction of CO can be photodesorbed, while the remaining molecules can only be removed from the GaN surface thermally (Figure 3). We note that it is observed that the photoactive sites are again accessible after the PSD, as subsequent dosing of CO without any thermal cleaning step results in the same PSD signal as before. Comparing the fast and the slow time constants of the PSD decay with previous photo decay and contact potential difference (CPD) measurements of GaN,[54] similar time constants of a few seconds and minutes are obtained. The CPD decay has been assigned to the transfer of photogenerated holes to the surface and subsequent capture in electron-filled surface sites,[54] leading to compensation of the negative charge accumulated at the surface. That the desorption process in PSD experiments is indeed a photochemical one, based on the extinction of charge transferred from CO to the semiconductor, is evidenced by the desorption behavior of CO_2, which has also been investigated. The TPD of CO_2 on GaN(0001) is very similar to that of CO (Figure S3), and desorption of both molecules is observed at roughly the same temperature. However, no photoinitiated desorption occurs for carbon dioxide. Consequently, local thermal effects originating from the recombination of charge carriers in the vicinity of the adsorbed molecules can be excluded for the PSD of CO, as these would also lead to the desorption of other weakly bound species, for example, CO_2. In general, upon illumination of an n-type semiconductor, holes move to the surface and neutralize the negatively charged electronic surface states. Immediately

DOI: 10.1021/acs.jpcc.7b01570
J. Phys. Chem. C 2017, 121, 8473−8479

after UV excitation, CO desorbs from the GaN surface (Figure 3b). Detailed mechanisms for photon-stimulated desorption on the atomic scale are still largely unknown and under discussion.[36,37,57−59] However, it is known that a charge redistribution at the surface alters the electrostatics of the molecule−surface interaction and gives rise to a PSD.[58] Under the assumption that CO binds with a negative partial charge redistribution to the GaN surface, the molecule−surface interaction can only be weakened when the charge donation is neutralized and consequently a PSD arises. Because in an illuminated n-type semiconductor only holes from the SCR move to the surface, only negative charge states in surface vicinity can be involved. In this picture minority and majority charge carriers may contribute to the atomic PSD mechanism.[59,60] Experimental data provide evidence that the CO PSD can also occur on p-doped GaN; however, only a very small quantity of CO can be photodesorbed (Figure S4). Consequently both electrons and holes seem to be able to activate the photon-stimulated desorption of CO.

CONCLUSIONS

We demonstrate for the model system CO on GaN(0001) that the adsorption of molecules on semiconductors can be doping-dependent. The change of the n-type doping of GaN results in different amounts of CO on the semiconductors' surface and eventually different saturation coverages. We introduce a model based on the electronic characteristics of the semiconductor, which is capable of explaining this effect qualitatively. With higher n-type doping less carbon monoxide can be adsorbed due to a higher density of negatively charged surface states. Furthermore, the first observation of a photodesorption on GaN is reported. It is found that the kinetics of the PSD are independent of the degree of doping or the surface oxidation state. However, the surface composition influences the PSD intensity, which is related to the existence of photoactive sites. The number of these sites can be reduced by a higher degree of oxidation of the GaN semiconductor surface. Furthermore, by a comparative study of CO_2, local thermal heating effects originating from charge-carrier recombination can be ruled out as the origin of the photon-stimulated desorption. We propose that the CO PSD is indeed a process based on the compensation of transferred charge density from the molecule to the semiconductor, which can be facilitated by electrons and holes.

ASSOCIATED CONTENT

Supporting Information

The Supporting Information is available free of charge on the ACS Publications website at DOI: 10.1021/acs.jpcc.7b01570.

AFM pictures of differently doped PIMBE GaN(0001) surfaces, CO PSD signals of different excitation wavelengths and intensities, TPD spectrum of CO_2 dosed on GaN, and CO PSD signal of the p-type doped GaN sample. (PDF)

AUTHOR INFORMATION

Corresponding Author

*E-mail: ulrich.heiz@mytum.de. Tel: +49 (0) 89 289 13391. Fax: +49 (0) 89 289 13389.

ORCID

Martin Tschurl: 0000-0001-6618-7312

Author Contributions

‖S.L.K. and C.A.W. contributed equally to this work.

Notes

The authors declare no competing financial interest.

ACKNOWLEDGMENTS

We thank the DFG through grants HE3435/22-1 and STU139/12-1 for financial support.

REFERENCES

(1) Shimura, K.; Yoshida, H. Heterogeneous Photocatalytic Hydrogen Production from Water and Biomass Derivatives. *Energy Environ. Sci.* **2011**, *4*, 2467−2481.

(2) Takanabe, K.; Domen, K. Toward Visible Light Response: Overall Water Splitting Using Heterogeneous Photocatalysts. *Green* **2011**, *1*, 313−322.

(3) Chen, X.; Shen, S.; Guo, L.; Mao, S. S. Semiconductor-Based Photocatalytic Hydrogen Generation. *Chem. Rev. (Washington, DC, U. S.)* **2010**, *110*, 6503−6570.

(4) Hayashi, T.; Deura, M.; Ohkawa, K. High Stability and Efficiency of GaN Photocatalyst for Hydrogen Generation from Water. *Jpn. J. Appl. Phys.* **2012**, *51*, 112601.

(5) Kida, T.; Minami, Y.; Guan, G.; Nagano, M.; Akiyama, M.; Yoshida, A. Photocatalytic Activity of Gallium Nitride for Producing Hydrogen from Water under Light Irradiation. *J. Mater. Sci.* **2006**, *41*, 3527−3534.

(6) Ohno, T.; Bai, L.; Hisatomi, T.; Maeda, K.; Domen, K. Photocatalytic Water Splitting Using Modified GaN:ZnO Solid Solution under Visible Light: Long-Time Operation and Regeneration of Activity. *J. Am. Chem. Soc.* **2012**, *134*, 8254−8259.

(7) Maeda, K.; Takata, T.; Hara, M.; Saito, N.; Inoue, Y.; Kobayashi, H.; Domen, K. GaN:ZnO Solid Solution as a Photocatalyst for Visible-Light-Driven Overall Water Splitting. *J. Am. Chem. Soc.* **2005**, *127*, 8286−8287.

(8) Maeda, K.; Teramura, K.; Lu, D.; Takata, T.; Saito, N.; Inoue, Y.; Domen, K. Photocatalyst Releasing Hydrogen from Water. *Nature* **2006**, *440*, 295−295.

(9) Maeda, K.; Xiong, A.; Yoshinaga, T.; Ikeda, T.; Sakamoto, N.; Hisatomi, T.; Takashima, M.; Lu, D.; Kanehara, M.; Setoyama, T.; et al. Photocatalytic Overall Water Splitting Promoted by Two Different Cocatalysts for Hydrogen and Oxygen Evolution under Visible Light. *Angew. Chem.* **2010**, *122*, 4190−4193.

(10) Lu, X.; Bandara, A.; Katayama, M.; Yamakata, A.; Kubota, J.; Domen, K. Infrared Spectroscopic Study of the Potential Change at Cocatalyst Particles on Oxynitride Photocatalysts for Water Splitting by Visible Light Irradiation. *J. Phys. Chem. C* **2011**, *115*, 23902−23907.

(11) Jung, H. S.; Hong, Y. J.; Li, Y.; Cho, J.; Kim, Y.-J.; Yi, G.-C. Photocatalysis Using GaN Nanowires. *ACS Nano* **2008**, *2*, 637−642.

(12) Ji, X. Z.; Somorjai, G. A. Continuous Hot Electron Generation in Pt/TiO_2, Pd/TiO_2, and Pt/GaN Catalytic Nanodiodes from Oxidation of Carbon Monoxide. *J. Phys. Chem. B* **2005**, *109*, 22530−22535.

(13) Park, J. Y.; Somorjai, G. A. Energy Conversion from Catalytic Reaction to Hot Electron Current with Metal-Semiconductor Schottky Nanodiodes. *J. Vac. Sci. Technol., B* **2006**, *24*, 1967−1971.

(14) Park, J. Y.; Renzas, J. R.; Hsu, B. B.; Somorjai, G. A. Interfacial and Chemical Properties of Pt/TiO_2, Pd/TiO_2, and Pt/GaN Catalytic Nanodiodes Influencing Hot Electron Flow. *J. Phys. Chem. C* **2007**, *111*, 15331−15336.

(15) Kim, S. M.; Lee, S. J.; Kim, S. H.; Kwon, S.; Yee, K. J.; Song, H.; Somorjai, G. A.; Park, J. Y. Hot Carrier-Driven Catalytic Reactions on Pt-CdSe-Pt Nanodumbbells and Pt/GaN under Light Irradiation. *Nano Lett.* **2013**, *13*, 1352−1358.

(16) Park, J. Y.; Baker, L. R.; Somorjai, G. A. Role of Hot Electrons and Metal-Oxide Interfaces in Surface Chemistry and Catalytic Reactions. *Chem. Rev. (Washington, DC, U. S.)* **2015**, *115*, 2781−2817.

(17) Khan, M. A.; Kuznia, J. N.; Olson, D. T.; Van Hove, J. M.; Blasingame, M.; Reitz, L. F. High-Responsivity Photoconductive

DOI: 10.1021/acs.jpcc.7b01570
J. Phys. Chem. C 2017, 121, 8473−8479

Ultraviolet Sensors Based on Insulating Single-Crystal GaN Epilayers. *Appl. Phys. Lett.* **1992**, *60*, 2917−2919.
(18) Long, J. P.; Bermudez, V. M. Band Bending and Photoemission-Induced Surface Photovoltages on Clean n- and p-GaN (0001) Surfaces. *Phys. Rev. B: Condens. Matter Mater. Phys.* **2002**, *66*, 121308−121311.
(19) Hirai, T.; Maeda, K.; Yoshida, M.; Kubota, J.; Ikeda, S.; Matsumura, M.; Domen, K. Origin of Visible Light Absorption in GaN-Rich $(Ga_{1-x}Zn_x)(N_{1-x}O_x)$ Photocatalysts. *J. Phys. Chem. C* **2007**, *111*, 18853−18855.
(20) Oshima, C.; Nishiyama, H.; Chatterjee, A.; Uchida, K.; Sato, K.; Inoue, Y.; Hisatomi, T.; Domen, K. Photocatalytic Activity of ZnO/$GaP_{1-x}N_x$ for Water Splitting. *J. Mater. Chem. A* **2015**, *3*, 18083−18089.
(21) Diebold, U. The Surface Science of Titanium Dioxide. *Surf. Sci. Rep.* **2003**, *48*, 53−229.
(22) Henderson, M. A. A Surface Science Perspective on TiO_2 Photocatalysis. *Surf. Sci. Rep.* **2011**, *66*, 185−297.
(23) Shekhar, R.; Jensen, K. F. Temperature Programmed Desorption Investigations of Hydrogen and Ammonia Reactions on GaN. *Surf. Sci.* **1997**, *381*, L581−L588.
(24) Xie, M. H.; Seutter, S. M.; Zhu, W. K.; Zheng, L. X.; Wu, H.; Tong, S. Y. Anisotropic Step-Flow Growth and Island Growth of GaN(0001) by Molecular Beam Epitaxy. *Phys. Rev. Lett.* **1999**, *82*, 2749−2752.
(25) Ambacher, O.; Brandt, M. S.; Dimitrov, R.; Metzger, T.; Stutzmann, M.; Fischer, R. A.; Miehr, A.; Bergmaier, A.; Dollinger, G. Thermal Stability and Desorption of Group III Nitrides Prepared by Metal Organic Chemical Vapor Deposition. *J. Vac. Sci. Technol., B: Microelectron. Process. Phenom.* **1996**, *14*, 3532−3542.
(26) Smith, A. R.; Feenstra, R. M.; Greve, D. W.; Neugebauer, J.; Northrup, J. E. Reconstructions of the GaN(000$\bar{1}$) Surface. *Phys. Rev. Lett.* **1997**, *79*, 3934−3837.
(27) Smith, A. R.; Feenstra, R. M.; Greve, D. W.; Shin, M. S.; Skowronski, M.; Neugebauer, J.; Northrup, J. E. Reconstructions of GaN(0001) and (000$\bar{1}$) Surfaces: Ga-rich Metallic Structures. *J. Vac. Sci. Technol., B: Microelectron. Process. Phenom.* **1998**, *16*, 2242−2249.
(28) Schulz, C.; Kuhr, S.; Geffers, H.; Schmidt, T.; Flege, J. I.; Aschenbrenner, T.; Hommel, D.; Falta, J. Cleaning of GaN($\bar{2}$110) Surfaces. *J. Vac. Sci. Technol., A* **2011**, *29*, 011013.
(29) Morkoç, H.; Mohammad, S. N. High-Luminosity Blue and Blue-Green Gallium Nitride Light-Emitting Diodes. *Science* **1995**, *267*, 51−55.
(30) Shur, M. S. GaN Based Transistors for High Power Applications. *Solid-State Electron.* **1998**, *42*, 2131−2138.
(31) Zhang, Z.; Yates, J. T. Electron-Mediated CO Oxidation on the TiO_2(110) Surface During Electronic Excitation. *J. Am. Chem. Soc.* **2010**, *132*, 12804−12807.
(32) Green, I. X.; Tang, W.; Neurock, M.; Yates, J. T. Insights into Catalytic Oxidation at the Au/TiO_2 Dual Perimeter Sites. *Acc. Chem. Res.* **2014**, *47*, 805−815.
(33) Yanagisawa, Y.; Ota, Y. Thermal and Photo-Stimulated Desorption of Chemisorbed Oxygen Molecules from Titanium Dioxide Surfaces. *Surf. Sci.* **1991**, *254*, L433−L436.
(34) Thompson, T. L.; Yates, J. T. Monitoring Hole Trapping in Photoexcited TiO_2(110) Using a Surface Photoreaction. *J. Phys. Chem. B* **2005**, *109*, 18230−18236.
(35) Petrik, N. G.; Kimmel, G. A. Electron- and Hole-Mediated Reactions in UV-Irradiated O_2 Adsorbed on Reduced Rutile TiO_2(110). *J. Phys. Chem. C* **2011**, *115*, 152−164.
(36) Petrik, N. G.; Kimmel, G. A.; Shen, M.; Henderson, M. A. Quenching of Electron Transfer Reactions through Coadsorption: A Study of Oxygen Photodesorption from TiO_2(110). *Surf. Sci.* **2016**, *652*, 183.
(37) Rusu, C. N.; Yates, J. T. Photochemistry of NO Chemisorbed on TiO_2(110) and TiO_2 Powders. *J. Phys. Chem. B* **2000**, *104*, 1729−1737.
(38) Shapira, Y.; McQuistan, R. B.; Lichtman, D. Relationship Between Photodesorption and Surface Conductivity in ZnO. *Phys. Rev. B* **1977**, *15*, 2163−2169.
(39) Winnerl, A.; Pereira, R. N.; Stutzmann, M. Kinetics of Optically Excited Charge Carriers at the GaN Surface: Influence of Catalytic Pt Nanostructures. *J. Appl. Phys.* **2015**, *118*, 155704.
(40) Walenta, C. A.; Kollmannsberger, S. L.; Kiermaier, J.; Winbauer, A.; Tschurl, M.; Heiz, U. Ethanol Photocatalysis on Rutile TiO_2(110): the Role of Defects and Water. *Phys. Chem. Chem. Phys.* **2015**, *17*, 22809−22814.
(41) Heying, B.; Averbeck, R.; Chen, L. F.; Haus, E.; Riechert, H.; Speck, J. S. Control of GaN Surface Morphologies Using Plasma-Assisted Molecular Beam Epitaxy. *J. Appl. Phys.* **2000**, *88*, 1855−1860.
(42) Schuster, F.; Winnerl, A.; Weiszer, S.; Hetzl, M.; Garrido, J. A.; Stutzmann, M. Doped GaN Nanowires on Diamond: Structural Properties and Charge Carrier Distribution. *J. Appl. Phys.* **2015**, *117*, 044307.
(43) Karrer, U.; Ambacher, O.; Stutzmann, M. Influence of Crystal Polarity on the Properties of Pt/GaN Schottky Diodes. *Appl. Phys. Lett.* **2000**, *77*, 2012−2014.
(44) Lu, G.; Linsebigler, A.; Yates, J. T. The Photochemical Identification of Two Chemisorption States for Molecular Oxygen on TiO_2(110). *J. Chem. Phys.* **1995**, *102*, 3005−3008.
(45) Schlichting, H.; Menzel, D. Techniques for Attainment, Control, and Calibration of Cryogenic Temperatures at Small Single-Crystal Samples under Ultrahigh Vacuum. *Rev. Sci. Instrum.* **1993**, *64*, 2013−2022.
(46) Dohnálek, Z.; Kimmel, G. A.; Joyce, S. A.; Ayotte, P.; Smith, R. S.; Kay, B. D. Physisorption of CO on the MgO(100) Surface. *J. Phys. Chem. B* **2001**, *105*, 3747−3751.
(47) Grabow, L.; Uhlrich, J.; Kuech, T.; Mavrikakis, M. Effectiveness of in situ NH_3 Annealing Treatments for the Removal of Oxygen from GaN Surfaces. *Surf. Sci.* **2009**, *603*, 387−399.
(48) King, S. W.; Barnak, J. P.; Bremser, M. D.; Tracy, K. M.; Ronning, C.; Davis, R. F.; Nemanich, R. J. Cleaning of AlN and GaN Surfaces. *J. Appl. Phys.* **1998**, *84*, 5248−5260.
(49) Ishikawa, H.; Kobayashi, S.; Koide, Y.; Yamasaki, S.; Nagai, S.; Umezaki, J.; Koike, M.; Murakami, M. Effects of Surface Treatments and Metal Work Functions on Electrical Properties at p-GaN/Metal Interfaces. *J. Appl. Phys.* **1997**, *81*, 1315−1322.
(50) Hunt, R.; Vanzetti, L.; Castro, T.; Chen, K.; Sorba, L.; Cohen, P.; Gladfelter, W.; Van Hove, J. M.; Kuznia, J.; Khan, M.; et al. Electronic Structure, Surface Composition and Long-Range Order in GaN. *Phys. B* **1993**, *185*, 415−421.
(51) Childs, K. D.; Carlson, B. A.; Vanier, L. A.; Moulder, J. F.; Paul, D. F.; Stickle, W. F.; Watson, D. G. *Handbook of Auger Electron Spectroscopy*; Physical Electronics Industries: Chanhassen, MN, 1995.
(52) Watkins, N. J.; Wicks, G. W.; Gao, Y. Oxidation Study of GaN Using X-ray Photoemission Spectroscopy. *Appl. Phys. Lett.* **1999**, *75*, 2602−2604.
(53) Zhang, Z.; Yates, J. T. Band Bending in Semiconductors: Chemical and Physical Consequences at Surfaces and Interfaces. *Chem. Rev. (Washington, DC, U. S.)* **2012**, *112*, 5520−5551.
(54) Winnerl, A.; Pereira, R. N.; Stutzmann, M. Kinetics of Optically Excited Charge Carriers at the GaN Surface. *Phys. Rev. B: Condens. Matter Mater. Phys.* **2015**, *91*, 075316−075327.
(55) Birner, S.; Zibold, T.; Andlauer, T.; Kubis, T.; Sabathil, M.; Trellakis, A.; Vogl, P. Nextnano: General Purpose 3-D Simulations. *IEEE Trans. Electron Devices* **2007**, *54*, 2137−2142.
(56) Kim, B.; Li, Z.; Kay, B. D.; Dohnalek, Z.; Kim, Y. K. The Effect of Oxygen Vacancies on the Binding Interactions of NH_3 with Rutile TiO_2(110)-1 × 1. *Phys. Chem. Chem. Phys.* **2012**, *14*, 15060−15065.
(57) Henderson, M. A. Visible Light Induced Photodesorption of NO from the α-Cr_2O_3(0001) Surface. *Surf. Sci.* **2012**, *606*, 505−509.
(58) Henderson, M. A.; Mu, R.; Dahal, A.; Lyubinetsky, I.; Dohnálek, Z.; Glezakou, V.-A.; Rousseau, R. Light Makes a Surface Banana-Bond Split: Photodesorption of Molecular Hydrogen from RuO_2(110). *J. Am. Chem. Soc.* **2016**, *138*, 8714−8717.

DOI: 10.1021/acs.jpcc.7b01570
J. Phys. Chem. C 2017, 121, 8473−8479

(59) Petrik, N. G.; Kimmel, G. A. Probing the Photochemistry of Chemisorbed Oxygen on TiO_2(110) with Kr and Other Co-Adsorbates. *Phys. Chem. Chem. Phys.* **2014**, *16*, 2338−2346.
(60) Linsebigler, A.; Lu, G.; Yates, J. T. CO Photooxidation on TiO_2(110). *J. Phys. Chem.* **1996**, *100*, 6631−6636.

DOI: 10.1021/acs.jpcc.7b01570
J. Phys. Chem. C 2017, 121, 8473−8479

Supporting information for: Doping-Dependent Adsorption and Photon-Stimulated Desorption of CO on GaN(0001)

Sebastian L. Kollmannsberger,[†,§] Constantin A. Walenta,[†,‡,§] Andrea Winnerl,[¶] Saskia Weiszer,[¶] Rui N. Pereira,[¶] Martin Tschurl,[†] Martin Stutzmann,[¶,‡] and Ueli Heiz[*,†,‡]

Chair of Physical Chemistry, Department of Chemistry & Catalysis Research Center, Technische Universität München, Lichtenbergstr. 4, 85748 Garching, Germany, Nanosystems Initiative Munich, Schellingstr. 4, 80799 München, Germany, and Walter Schottky Institute and Physics Department, Technische Universität München, Am Coulombwall 4, 85748 Garching, Germany

E-mail: ulrich.heiz@mytum.de

Phone: +49 (0) 89 289 13391. Fax: +49 (0) 89 289 13389

[*]To whom correspondence should be addressed

[†]Chair of Physical Chemistry, Department of Chemistry & Catalysis Research Center, Technische Universität München, Lichtenbergstr. 4, 85748 Garching, Germany

[‡]Nanosystems Initiative Munich, Schellingstr. 4, 80799 München, Germany

[¶]Walter Schottky Institute and Physics Department, Technische Universität München, Am Coulombwall 4, 85748 Garching, Germany

[§]The authors contributed equally to this work

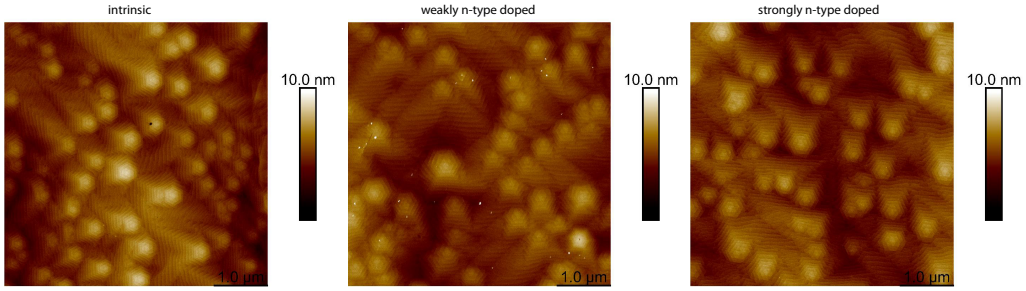

Figure S1: AFM images of differently doped PIMBE GaN(0001) surfaces. The images show that the surface morpholgy is unaffected by doping.

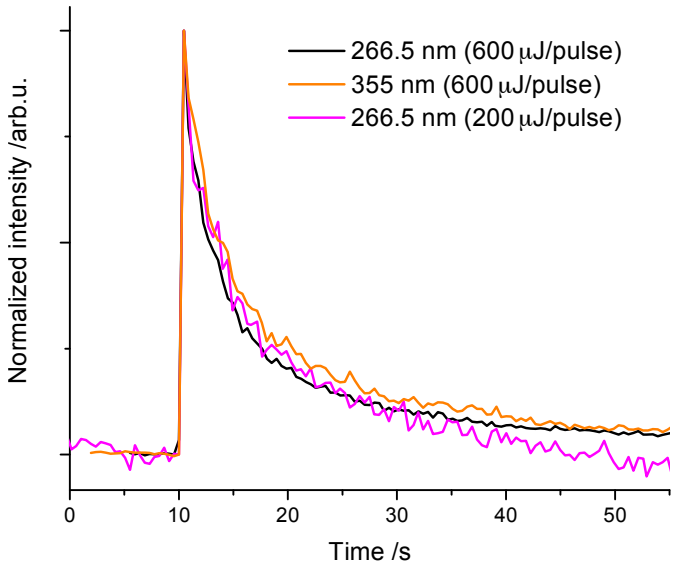

Figure S2: Intensity normalized PSD signal of different UV wavelength (266.5 nm or 355 nm) and UV intensities (200 μJ/pulse or 600 μJ/pulse). The decays show no appreciable differences, which indicates that the kinetics of the PSD do not change significantly with the variation of UV wavelength and UV intensity.

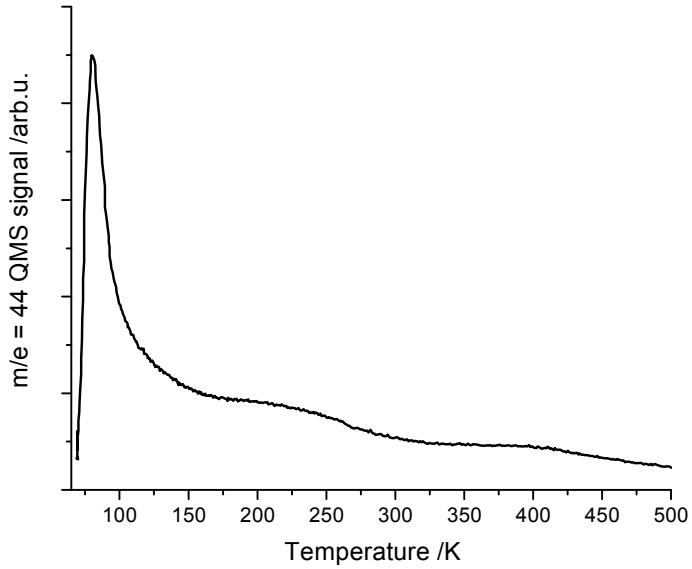

Figure S3: TPD spectrum from CO_2 dosed on a GaN(0001) surface. The low temperature peak is very similar to that of CO on GaN. Analogously, the small high temperature features originate from CO_2 desorption from the sample holder.

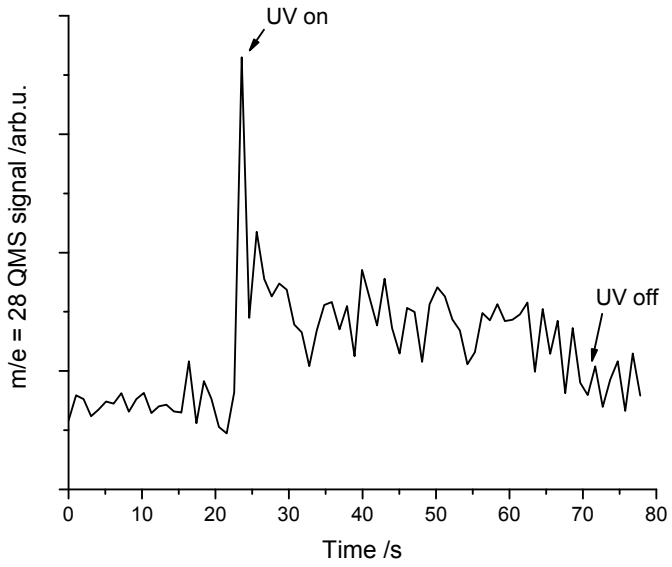

Figure S4: CO PSD spectrum of p-type GaN(0001). Note that the signal is comparably small since the surface has a low N/O ratio. The PSD is carried out at LN_2 temperature after 4 L CO exposure. By illumination with 266.5 nm UV light, a rise in the CO intensity is observed.

D

Ethanol Surface Chemistry on MBE-grown GaN(0001), GaO_χ/GaN(0001) and $Ga_2O_3(\bar{2}01)$

Reproduced from [S.L. Kollmannsberger, C.A. Walenta, et al., The Journal of Chemical Physics 147, 124704 (2017)], with the permission of AIP Publishing.

THE JOURNAL OF CHEMICAL PHYSICS **147**, 124704 (2017)

Ethanol surface chemistry on MBE-grown GaN(0001), GaO_x/GaN(0001), and $Ga_2O_3(\bar{2}01)$

Sebastian L. Kollmannsberger,[1,a)] Constantin A. Walenta,[1,2,a)] Andrea Winnerl,[3] Fabian Knoller,[1] Rui N. Pereira,[3] Martin Tschurl,[1] Martin Stutzmann,[2,3] and Ueli Heiz[1,2,b)]

[1]*Chair of Physical Chemistry, Department of Chemistry and Catalysis Research Center, Technische Universität München, Lichtenbergstrasse 4, 85748 Garching, Germany*

[2]*Nanosystems Initiative Munich (NIM), Schellingstr. 4, 80799 Munich, Germany*

[3]*Walter Schottky Institute and Physics Department, Technische Universität München, Am Coulombwall 4 85748 Garching, Germany*

(Received 4 July 2017; accepted 8 September 2017; published online 28 September 2017)

In this work, ethanol is used as a chemical probe to study the passivation of molecular beam epitaxy-grown GaN(0001) by surface oxidation. With a high degree of oxidation, no reaction from ethanol to acetaldehyde in temperature-programmed desorption experiments is observed. The acetaldehyde formation is attributed to a mechanism based on α-H abstraction from the dissociatively bound alcohol molecule. The reactivity is related to negatively charged surface states, which are removed upon oxidation of the GaN(0001) surface. This is compared with the $Ga_2O_3(\bar{2}01)$ single crystal surface, which is found to be inert for the acetaldehyde production. These results offer a toolbox to explore the surface chemistry of nitrides and oxynitrides on an atomic scale and relate their intrinsic activity to systems under ambient atmosphere. *Published by AIP Publishing.* https://doi.org/10.1063/1.4994141

I. INTRODUCTION

Mimicking nature and driving a heterogeneous photocatalytic or photoelectrochemical reaction have become a major scientific and also industrial interest.[1–5] In order to harvest a maximum of sunlight, semiconductors with optimized band positions are tailored via alloying and doping.[6–8] However, these materials are quite complex, with multiple elements in the compound.[8–10] An emerging group of such materials is alloys or solid solutions of oxides and nitrides, in general called oxy-nitrides.[11–15] While the bulk properties of these materials have been tailored for their use in photo(electro-)catalysis, their surface chemistry is largely unknown. In the last decade, many of these materials have been investigated in electrocatalytic, photocatalytic, and photo-electrocatalytic studies, although mostly with limited efficiencies.[16–19] Temperature-programmed desorption (TPD) studies in general have allowed for a more detailed investigation of surface reaction pathways and specific intermediates.[20–22] Due to the interest in alcohols as a potential hydrogen carrier and its importance in both photocatalysis[23] and electrocatalysis,[18,24] ethanol is the ideal molecule to investigate the surface reaction on oxynitride compounds. GaN and solid solutions of GaN:ZnO and GaN:InN have attracted much interest in the last years as stable materials in photo(electro)catalysis.[25–31] However, the surface chemistry of these materials has not been widely studied.[32] In this study, we investigate the ethanol surface chemistry of plasma-induced molecular beam epitaxy (PIMBE) grown GaN(0001) with different degrees of surface oxidation. Furthermore, a $Ga_2O_3(\bar{2}01)$ single crystal is studied in order to compare our findings with results from a sample with a similar chemical surface composition.

II. EXPERIMENTAL

GaN(0001) is grown by plasma-induced molecular beam epitaxy (PIMBE) to a thickness of about 550 nm on Fe-doped semi-insulating Ga-polar GaN MOCVD (metal-organic chemical vapor deposition) templates (thickness 4 μm) on α-Al_2O_3(0001) from Lumilog.[33,34] The samples are non-intentionally doped Ga-face samples that show a free electron concentration of about 5×10^{16} cm^{-3} as determined by Hall measurements. The MBE (molecular beam epitaxy)-grown n-type GaN(0001) samples are etched 30 s in concentrated HCl and rinsed with Milli-Q water twice. Two MBE grown GaN(0001) samples and one Ga_2O_3 single crystal were used.

Prior to TPD measurements, one of the MBE grown samples [denoted GaN(0001) sample] was treated in cycles of Ar^+-sputtering (0.5 keV, 1×10^{-6} mbar, $I_{sputter}$ = 2.0 μA, 100 K) for 15 min and 10 min, each time with a subsequent annealing step (800 K, 15 min). The other MBE sample [denoted GaO_x/GaN(0001)] was Ar^+-sputtered for a total time of 50 min, again with consecutive annealing steps. In detail, five cycles of 5-20 min of sputtering (same conditions as above) followed by 800 K annealing were carried out. By these procedures, all carbon and chlorine contaminations were removed.

Furthermore, varying sputter time leads to a different surface oxidation[34–36] as free Ga surface species are easily oxidized by oxygen or water from the residual background.[37,38] The surface constitution was confirmed by Auger Electron Spectroscopy (AES) measurements. The $Ga_2O_3(\bar{2}01)$ single

[a)]S. L. Kollmannsberger and C. A. Walenta contributed equally to this work.
[b)]Author to whom correspondence should be addressed: ulrich.heiz@mytum.de. Tel.: +49 (0)89 289 13391. Fax: +49 (0)89 289 13389.

crystal (Tamura Cooperation, Tokyo, Japan) was chosen, since it is the natural growth direction of gallium oxide on (0001) facets.[39] The treatment before measurements includes 40 min Ar^+-sputtering (1.0 keV, 5×10^{-6} mbar, $I_{sputter}$ = 10.0 μA, 100 K), 30 min O_2 annealing (800 K, 2×10^{-6} mbar), and 30 min vacuum annealing at 800 K. The subsequent AES spectra did not show any contaminants.

The load lock compatible sample holder is of home-built design and fully made of tantalum. It is capable of heating and cooling samples between 100 K and 1000 K. Since in the upper most level two tantalum sheets are used to clamp the sample to the mount, also materials grown on electrical insulating substrates (i.e. sapphire) can be used. The temperature is measured with a spotwelded type-C thermocouple,[40] and the temperature difference between the measurement point on the back of the tantalum heating plate and the top of a sample grown on sapphire was determined to be less than 10 K over the entire thermal desorption run. The chamber consists of a quadrupole mass spectrometer (QMS, QMA 430, Pfeiffer Vacuum GmbH) with a skimmer that is differentially pumped, a molecular beam doser, a sputter gun (IQE 11/35, SPECS GmbH), and an Auger Electron Spectrometer (AES, CMA 100, Omicron Nanotechnology GmbH). In this setup, a typical base pressure of 8.0×10^{-11} mbar is achieved.

The purification of ethanol (absolute, HPLC grade, ≥99.8%, Sigma-Aldrich) was performed by several pump-freeze cycles. The ethanol molecules were adsorbed on the sample at 110 K. TPD experiments were performed using a constant heating rate of 1.2 K/s to 700 K. The cracking pattern correction of acetaldehyde accounts for fragment intensities of all desorbing products. The monolayer coverage is normalized to the integral of the highest coverage that shows no desorption of physisorbed ethanol.

X-ray photoelectron spectroscopy (XPS) was performed in a commercial system (Specs GmbH) using monochromatized Al Kα radiation (= 1486.6 eV) to avoid an overlap of the Ga LMM Auger lines with the C 1s peak. Spectral fitting was performed using the Casa XPS analysis software and OriginPro. The curves were fitted using a Shirley background.

III. RESULTS

To elucidate the influence of gallium oxide surface species on the reactivity of ethanol to acetaldehyde, differently oxidized surfaces of PIMBE-grown GaN(0001) surfaces and a $Ga_2O_3(\bar{2}01)$ single crystal are investigated. The morphology of the PIMBE-grown GaN samples and the $Ga_2O_3(\bar{2}01)$ crystal was studied by *ex situ* AFM as shown in Figs. S1 and S2 of the supplementary material. The morphology is in very good agreement with the literature for the GaN(0001) epitaxial films[41–43] as well as for the $Ga_2O_3(\bar{2}01)$ single crystal.[44]

The chemical compositions after the cleaning cycles were confirmed by *in situ* AES (Fig. S3 of the supplementary material). A detailed description of the determination of oxidation values from AES can be found in Table S1 of the supplementary material. It is clearly evident that the different sample preparation leads to different surface compositions for the two MBE-grown GaN(0001) samples. On the GaN(0001) sample, 0.18 ML of "native oxide" is observed.[45,46] XPS was also carried out on GaN(0001) to validate the cleaning cycle. The spectra in Fig. S4 of the supplementary material confirm the removal of residual carbon under the applied sputter conditions and indicate the oxidation of the sample. For the oxidized sample GaO_x/GaN(0001), a strong surface oxidation with 1.05 ML of "native oxide" is determined and in good agreement with the literature.[46] A successful cleaning from all contaminants was obtained for $Ga_2O_3(\bar{2}01)$. Furthermore, for the Ga_2O_3 single crystal, an oxygen rich first layer and a stoichiometric second layer are calculated from AES measurements. The oxygen content of the samples does not change with TPD runs.

In Fig. 1(a), the desorption characteristics of ethanol from a MBE-grown GaN(0001) surface are shown. It can be seen that the desorption maximum, appearing for low coverages at around 380 K, is shifting to lower temperatures (≈225 K) for higher coverages, until it saturates at 0.72 ML. Such a

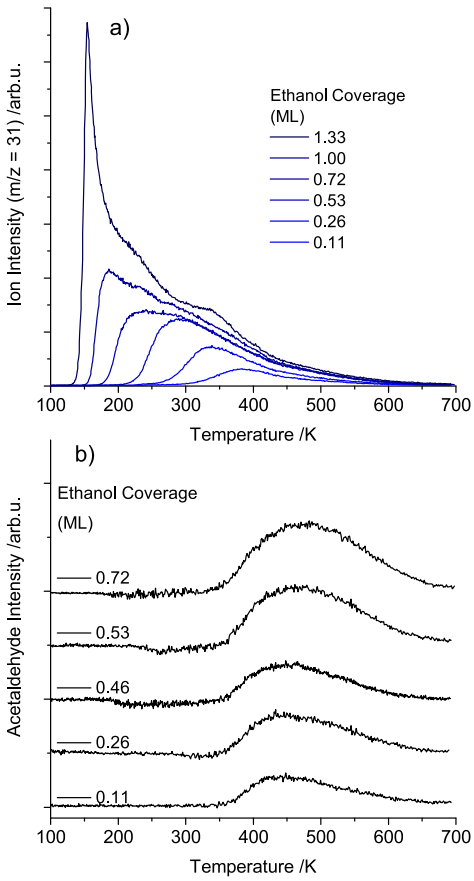

FIG. 1. TPD spectra from various coverages of ethanol dosed with a molecular beam doser on a MBE-grown GaN(0001) surface at 110 K (a). Fragmentation-corrected TPD spectra of the reaction product acetaldehyde (b). For the lowest coverage, the main desorption feature of ethanol appears at around 380 K and shifts to lower temperatures (≈225 K) with higher coverages. At coverages exceeding 0.72 ML, a second ethanol desorption peak at 180 K is observed. For the highest coverage, a sharp desorption maximum occurs at 150 K, which can be assigned to desorption of physisorbed ethanol. The desorption peak of acetaldehyde appears at 470 K. The acetaldehyde yield saturates at around 0.53 ML of initial ethanol dosage.

desorption behavior can be attributed to second-order desorption kinetics, which mostly result from dissociative adsorption.[47–49] For the 1 ML coverage, a second low temperature peak at 180 K arises. For the highest coverage, a desorption peak at around 150 K can be assigned to desorption of physisorbed ethanol. The surface constitution was checked with AES before and after ethanol TPDs and showed no coking. Figure 1(b) shows the acetaldehyde yield from various ethanol coverages. The traces are corrected for fragmentation of desorbing hydrocarbons. The acetaldehyde desorption peak [Fig. 1(b)] occurs at around 470 K and the maximum yield is reached for 0.53 ML of adsorbed ethanol, since a higher initial ethanol dosage shows no increase in the acetaldehyde yield. In Fig. 2, the desorption features of ethanol from surface-oxidized GaO_x/GaN(0001) are given. The ethanol desorption maximum for the lowest coverage occurs at significantly higher temperatures compared to GaN(0001) and at a similar temperature (≈500 K) at which acetaldehyde is formed on GaN(0001). The shift of the leading edge of the desorption feature is similar to the ethanol desorption on the less oxidized sample. For the highest coverage, the desorption edge appears at around 280 K, and the multilayer feature can be assigned to the peak at 150 K. The product evaluation reveals that no acetaldehyde is produced on the surface oxidized GaN sample.

For $Ga_2O_3(\bar{2}01)$, the resulting ethanol TPD is shown in Fig. 3. As the sticking of ethanol is strongly reduced on Ga_2O_3 in comparison to GaN-based samples, a significantly higher dosage must be applied in order to achieve similar coverages. The $Ga_2O_3(\bar{2}01)$ surface exhibits a peak maximum at around 300 K for the lowest coverage. This maximum is increasing in intensity for higher coverages until another peak evolves at 250 K, indicating desorption from another site with lower binding energy. The peak at around 150 K, which rises for coverages exceeding 1 ML, can be assigned to desorption of physisorbed ethanol from the multilayer. Just like the strongly surface-oxidized GaN sample, the Ga_2O_3 surface shows no

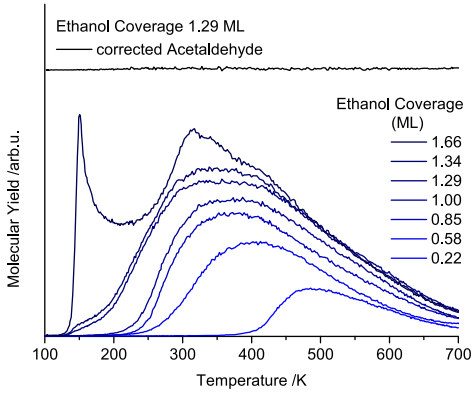

FIG. 2. Ethanol TPD spectra dosed with a molecular beam doser from GaO_x/GaN(0001) in the lower part and desorption yield of acetaldehyde at 1.29 ML in the upper part. For the lowest coverage, the peak maximum is located at around 500 K. With rising coverage, the leading edge shifts to 280 K for the saturated monolayer. For the highest coverages, physisorption of ethanol is observed at around 150 K. The acetaldehyde trace shows that no dehydrogenation products are formed.

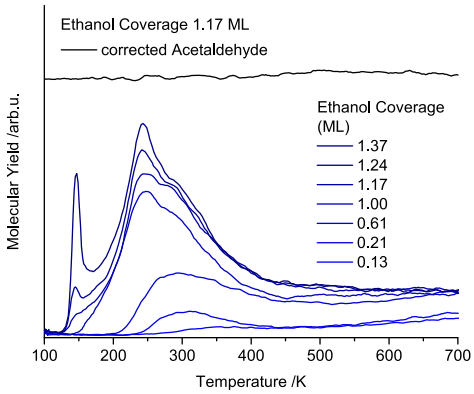

FIG. 3. Ethanol TPD spectra (smoothed) with Langmuir dosing from $Ga_2O_3(\bar{2}01)$ in the lower part and desorption yield of acetaldehyde at 1.17 ML in the upper part. For the lowest coverage, the peak maximum is located at around 300 K. With rising coverage, the desorption feature shifts to 250 K for the saturated monolayer. For coverages bigger than 1 ML, physisorption of ethanol is observed as can be seen from the peak at around 150 K. The high background at high temperatures originates from ethanol desorption from the sample holder, which is due to a combination of Langmuir dosing and a significantly reduced sticking of ethanol on Ga_2O_3 in comparison to GaN-based samples. No acetaldehyde formation is observed.

reactivity to produce acetaldehyde from ethanol, as can be seen in the upper part in Fig. 3. A larger background at higher temperatures is observed, which originates from ethanol desorption from the sample holder caused by the Langmuir dosing. It shall be mentioned that reaction pathways to products other than acetaldehyde are not observed for all samples studied. In this regard, conversion to CO or CO_2 (the CO traces are given in Fig. S5 in the supplementary material) does not occur, and very little amount of ethylene production is only visible on GaN(0001) (see Fig. S6 in the supplementary material).

IV. DISCUSSION

The surface reaction of ethanol to acetaldehyde on the MBE-grown GaN(0001) surface (Fig. 1) can be interpreted by the following mechanisms. In analogy to this study and others on metal oxides,[50,51] this reactivity is always accompanied by a metal bound ethanolate intermediate,

$$CH_3CH_2OH + N_{surf} + Ga_{surf} \longrightarrow CH_3CH_2O - Ga_{surf} + NH_{surf}. \quad (1)$$

This intermediate is also supported by two additional evidences: First, the shift of the leading edge to lower temperatures with increasing coverages is generally attributed to a second-order desorption kinetics from a dissociative adsorption.[47–49] Furthermore, the acetaldehyde desorption is observed at higher temperatures than the ethanol one, indicating a more strongly bound ethanolate intermediate.[50] The dehydrogenation reaction is a formal α-H abstraction,

$$CH_3CH_2O - Ga_{surf} + N_{surf} \longrightarrow CH_3CHO + Ga_{surf} + NH_{surf}. \quad (2)$$

On the GaO_x/GaN(0001) surface, the thickness of the oxide layer obtained from the quantitative AES amounts to one complete monolayer of GaO_x on the GaN(0001) surface because it

is known that the oxide growth takes place layer-by-layer and only on the surface.[52,53] As observed in Fig. 2, the reactivity of ethanol vanishes completely and acetaldehyde production is not observed. The shift of the leading edge of the high temperature ethanol desorption peak indicates that the adsorption is dissociative.

Compared to the GaN(0001) surface, ethanol desorption takes place at higher temperatures. However, on the thin oxide film, no reactivity towards acetaldehyde is observed. This indicates that on GaN(0001) the surface nitrogen has a key role in the abstraction of α-H to facilitate the dehydrogenation reaction, whereas on the oxide this reaction channel is excluded. Consequently, the strongly bound ethoxy intermediates recombine with the proton to form ethanol.

In order to represent the gallia chemistry, the $Ga_2O_3(\bar{2}01)$ surface was studied (Fig. 3). No reaction of ethanol towards acetaldehyde was observed, similar to the reactivity of the oxidized GaO_x/GaN(0001) surface. However, for the bulk oxide, the adsorption properties of ethanol on the $Ga_2O_3(\bar{2}01)$ surface are changed, as ethanol desorbs at significantly lower temperatures of around 300 K. Furthermore, no distinct shift of the leading edge is observed and, in combination with the lower desorption temperature, a molecular adsorption for ethanol is likely to occur. This is in good agreement with findings for methanol adsorption on pristine Ga_2O_3 surfaces on powders and in theoretical studies.[54,55] The adsorption property for high ethanol coverages of $Ga_2O_3(\bar{2}01)$ is similar to the GaN(0001) and the GaO_x/GaN(0001) surfaces, as all surfaces exhibit a multilayer feature at around 150 K.

To explain the difference in the reaction behavior of the oxide surfaces to GaN(0001), the different properties of the semiconductors have to be considered. All samples are n-type semiconductors, and thus, negative charges populate the surface states.[43] By oxidation of GaN to GaO_x/GaN(0001), these surface states are removed as shown by photoelectron spectroscopies[56] and electrochemistry.[57] This effect is attributed to be responsible for the blocking of the dehydrogenation pathway for ethanol. While the removal of surface states explains that α-H abstraction does not take place on GaO_x/GaN(0001), the ethoxy species does not even occur on $Ga_2O_3(\bar{2}01)$. However, the formation of such a more strongly bound ethoxy intermediate is generally a prerequisite for a subsequent chemical reaction.[50,51]

V. CONCLUSION

In this work, AES, XPS, *ex situ* AFM, and TPD are used to investigate the influence of surface oxides on the reactivity of ethanol on MBE-grown GaN(0001). A thin GaO_x film on the GaN(0001) surface completely passivates the reactivity of ethanol to acetaldehyde. This demonstrates that the local chemical environment is responsible for the reactivity of ethanol. This can also be rationalized by the removal of the semiconductor's surface states upon oxidation.[56] The measurements on the $Ga_2O_3(\bar{2}01)$ single crystal confirm the missing reactivity for ethanol on gallia but also show that the adsorption properties of the molecule are influenced significantly by the bulk material. In contrast to the thin film, only non-dissociative molecular adsorption is observed on the $Ga_2O_3(\bar{2}01)$ single crystal. However such an ethoxy formation is in general the initial step for a subsequent alcohol conversion.

SUPPLEMENTARY MATERIAL

See supplementary material for AFM images from the MBE-grown GaN(0001) surface and the $Ga_2O_3(\bar{2}01)$ single crystal, AES spectra of a MBE-grown GaN(0001) sample, an oxidized sample GaO_x/GaN(0001), and a Ga_2O_3 single crystal, a detailed description of the determination of "native oxide" proportion from AES measurements, and a XPS of the O 1s, the N 1s, the Ga 3d, and the C 1s signals. TPD traces representing the production of CO and ethylene for all three samples.

ACKNOWLEDGMENTS

The authors thank the DFG for financial support through Grant Nos. HE3435/22-1 and STU139/12-1. C.A.W. and S.L.K. thank the Zeidler Forschungsstiftung for a grant for the UnternehmerTUM MakerSpace GmbH, which enabled the manufacture of parts of the sample holder within the framework of the PhotoPlus start-up project.

[1] H. B. Gray, Nat. Chem. **1**, 7 (2009).
[2] P. D. Tran, L. H. Wong, J. Barber, and J. S. C. Loo, Energy Environ. Sci. **5**, 5902 (2012).
[3] W. Y. Teoh, J. A. Scott, and R. Amal, J. Phys. Chem. Lett. **3**, 629 (2012).
[4] T. A. Faunce, W. Lubitz, A. W. B. Rutherford, D. MacFarlane, G. F. Moore, P. Yang, D. G. Nocera, T. A. Moore, D. H. Gregory, S. Fukuzumi *et al.*, Energy Environ. Sci. **6**, 695 (2013).
[5] D. Kim, K. K. Sakimoto, D. Hong, and P. Yang, Angew. Chem., Int. Ed. **54**, 3259 (2015).
[6] K. Takanabe and K. Domen, Green **1**, 313 (2011).
[7] F. E. Osterloh, Chem. Soc. Rev. **42**, 2294 (2013).
[8] C. Pan, T. Takata, S. S. Khine Ma, K. Ueda, T. Minegishi, M. Nakabayashi, T. Matsumoto, N. Shibata, Y. Ikuhara, and K. Domen, J. Mater. Chem. A **4**, 4544 (2016).
[9] Q. Wang, T. Hisatomi, Q. Jia, H. Tokudome, M. Zhong, C. Wang, Z. Pan, T. Takata, M. Nakabayashi, N. Shibata *et al.*, Nat. Mater. **15**, 611 (2016).
[10] Y. Goto, J. Seo, K. Kumamoto, T. Hisatomi, Y. Mizuguchi, Y. Kamihara, M. Katayama, T. Minegishi, and K. Domen, Inorg. Chem. **55**, 3674 (2016).
[11] T. Hirai, K. Maeda, M. Yoshida, J. Kubota, S. Ikeda, M. Matsumura, and K. Domen, J. Phys. Chem. C **111**, 18853 (2007).
[12] K. Maeda and K. Domen, J. Phys. Chem. C **111**, 7851 (2007).
[13] M. Higashi, K. Domen, and R. Abe, J. Am. Chem. Soc. **134**, 6968 (2012).
[14] C. Pan, T. Takata, M. Nakabayashi, T. Matsumoto, N. Shibata, Y. Ikuhara, and K. Domen, Angew. Chem., Int. Ed. **54**, 2955 (2015).
[15] Z. Pan, T. Hisatomi, Q. Wang, M. Nakabayashi, N. Shibata, C. Pan, T. Takata, and K. Domen, Appl. Catal., A **521**, 26 (2016).
[16] S. S. Kocha, M. W. Peterson, D. J. Arent, J. M. Redwing, M. A. Tischler, and J. A. Turner, J. Electrochem. Soc. **142**, L238 (1995).
[17] Y. Kuang, Q. Jia, H. Nishiyama, T. Yamada, A. Kudo, and K. Domen, Adv. Energy Mater. **6**, 1501645 (2016).
[18] Y. Ohgi, A. Ishihara, K. Matsuzawa, S. Mitsushima, K.-i. Ota, M. Matsumoto, and H. Imai, Electrochim. Acta **68**, 192 (2012).
[19] M. G. Kibria, S. Zhao, F. A. Chowdhury, Q. Wang, H. P. T. Nguyen, M. L. Trudeau, H. Guo, and Z. Mi, Nat. Commun. **5**, 3825 (2014).
[20] B. Xu, J. Haubrich, C. G. Freyschlag, R. J. Madix, and C. M. Friend, Chem. Sci. **1**, 310 (2010).
[21] C. Lun Pang, R. Lindsay, and G. Thornton, Chem. Soc. Rev. **37**, 2328 (2008).
[22] M. A. Henderson, Surf. Sci. Rep. **66**, 185 (2011).
[23] S. Kundu, A. B. Vidal, M. A. Nadeem, S. D. Senanayake, H. Idriss, P. Liu, J. A. Rodriguez, and D. Stacchiola, J. Phys. Chem. C **117**, 11149 (2013).
[24] A. von Weber, E. T. Baxter, S. Proch, M. D. Kane, M. Rosenfelder, H. S. White, and S. L. Anderson, Phys. Chem. Chem. Phys. **17**, 17601 (2015).
[25] H. S. Jung, Y. J. Hong, Y. Li, J. Cho, Y.-J. Kim, and G.-C. Yi, ACS Nano **2**, 637 (2008).

[26]K. Maeda, T. Takata, M. Hara, N. Saito, Y. Inoue, H. Kobayashi, and K. Domen, J. Am. Chem. Soc. **127**, 8286 (2005).
[27]K. Maeda, K. Teramura, T. Takata, M. Hara, N. Saito, K. Toda, Y. Inoue, H. Kobayashi, and K. Domen, J. Phys. Chem. B **109**, 20504 (2005).
[28]T. Ohno, L. Bai, T. Hisatomi, K. Maeda, and K. Domen, J. Am. Chem. Soc. **134**, 8254 (2012).
[29]H. Q. Doan, K. L. Pollock, and T. Cuk, Chem. Phys. Lett. **649**, 1 (2016).
[30]B. AlOtaibi, H. P. T. Nguyen, S. Zhao, M. G. Kibria, S. Fan, and Z. Mi, Nano Lett. **13**, 4356 (2013).
[31]M. Ebaid, D. Priante, G. Liu, C. Zhao, M. S. Alias, U. Buttner, T. K. Ng, T. T. Isimjan, H. Idriss, and B. S. Ooi, Nano Energy **37**, 158 (2017).
[32]V. Bermudez, Surf. Sci. Rep. **72**, 147 (2017).
[33]U. Karrer, O. Ambacher, and M. Stutzmann, Appl. Phys. Lett. **77**, 2012 (2000).
[34]S. L. Kollmannsberger, C. A. Walenta, A. Winnerl, S. Weiszer, R. N. Pereira, M. Tschurl, M. Stutzmann, and U. Heiz, J. Phys. Chem. C **121**, 8473 (2017).
[35]H. Ishikawa, S. Kobayashi, Y. Koide, S. Yamasaki, S. Nagai, J. Umezaki, M. Koike, and M. Murakami, J. Appl. Phys. **81**, 1315 (1997).
[36]R. Hunt, L. Vanzetti, T. Castro, K. Chen, L. Sorba, P. Cohen, W. Gladfelter, J. V. Hove, J. Kuznia, M. Khan *et al.*, Phys. B **185**, 415 (1993).
[37]P. Lorenz, R. Gutt, T. Haensel, M. Himmerlich, J. A. Schaefer, and S. Krischok, Phys. Status Solidi C **7**, 169 (2010).
[38]V. Bermudez and J. Long, Surf. Sci. **450**, 98 (2000).
[39]V. Gottschalch, K. Mergenthaler, G. Wagner, J. Bauer, H. Paetzelt, C. Sturm, and U. Teschner, Phys. Status Solidi A **206**, 243 (2009).
[40]V. S. Smentkowski and J. T. Yates, J. Vac. Sci. Technol., B: Microelectron. Nanometer Struct. **14**, 260 (1996).
[41]E. J. Tarsa, B. Heying, X. H. Wu, P. Fini, S. P. DenBaars, and J. S. Speck, J. Appl. Phys. **82**, 5472 (1997).
[42]A. R. Smith, R. M. Feenstra, D. W. Greve, M. S. Shin, M. Skowronski, J. Neugebauer, and J. E. Northrup, J. Vac. Sci. Technol., B: Microelectron. Nanometer Struct. **16**, 2242 (1998).
[43]A. Winnerl, R. N. Pereira, and M. Stutzmann, J. Appl. Phys. **118**, 155704 (2015).
[44]K. Sasaki, M. Higashiwaki, A. Kuramata, T. Masui, and S. Yamakoshi, Appl. Phys. Express **6**, 086502 (2013).
[45]B. S. Eller, J. Yang, and R. J. Nemanich, J. Electron. Mater. **43**, 4560 (2014).
[46]J. Yang, B. S. Eller, and R. J. Nemanich, J. Appl. Phys. **116**, 123702 (2014).
[47]J. T. Yates, Jr. and T. E. Madey, J. Chem. Phys. **54**, 4969 (1971).
[48]Y. Lilach, I. Danziger, and M. Asscher, Catal. Lett. **76**, 35 (2001).
[49]B. Kim, Z. Li, B. D. Kay, Z. Dohnalek, and Y. K. Kim, Phys. Chem. Chem. Phys. **14**, 15060 (2012).
[50]Y. K. Kim, B. D. Kay, J. M. White, and Z. Dohnálek, J. Phys. Chem. C **111**, 18236 (2007).
[51]H. Idriss and E. Seebauer, J. Mol. Catal. A: Chem. **152**, 201 (2000).
[52]N. J. Watkins, G. W. Wicks, and Y. Gao, Appl. Phys. Lett. **75**, 2602 (1999).
[53]G. Hollinger, R. Skheyta-Kabbani, and M. Gendry, Phys. Rev. B **49**, 11159 (1994).
[54]M. M. Branda, S. E. Collins, N. J. Castellani, M. A. Baltanás, and A. L. Bonivardi, J. Phys. Chem. B **110**, 11847 (2006).
[55]V. M. Bermudez, Langmuir **24**, 12943 (2008).
[56]V. M. Bermudez, J. Appl. Phys. **80**, 1190 (1996).
[57]A. Winnerl, J. A. Garrido, and M. Stutzmann, Appl. Phys. Lett. **110**, 101602 (2017).

Supporting Information: Ethanol Surface Chemistry on MBE-grown GaN(0001), GaO_x/GaN(0001) and $Ga_2O_3(\bar{2}01)$

Sebastian L. Kollmannsberger,[1, a)] Constantin A. Walenta,[1, 2, a)] Andrea Winnerl,[3] Fabian Knoller,[1] Rui N. Pereira,[3] Martin Tschurl,[1] Martin Stutzmann,[2, 3] and Ueli Heiz[1, 2]

[1)] *Chair of Physical Chemistry, Department of Chemistry and Catalysis Research Center, Technische Universität München, Lichtenbergstrasse 4, 85748 Garching, Germany, E-mail: ulrich.heiz@mytum.de; Fax: +49 (0)89 289 13389; Tel: +49 (0)89 289 13391*

[2)] *Nanosystems Initiative Munich (NIM), Schellingstr. 4, 80799 Munich, Germany*

[3)] *Walter Schottky Institute and Physics Department, Technische Universität München, Am Coulombwall 4 85748 Garching*

SUPPORTING INFORMATION

The Supporting Information contains the following content: AFM images from the MBE-grown GaN(0001) surface and the $Ga_2O_3(\bar{2}01)$ single crystal; AES spectra of a MBE-grown GaN(0001) sample, an oxidized sample GaO_x/GaN(0001) and a Ga_2O_3 single crystal; A detailed description of the determination of "native oxide" proportion from AES measurements; XPS of the O 1s, the N 1s, the Ga 3d and the C 1s signals; TPD traces representing the production of CO and ethylene for all three samples.

REFERENCES

[1] E. J. Tarsa, B. Heying, X. H. Wu, P. Fini, S. P. DenBaars, and J. S. Speck, J. Appl. Phys. **82**, 5472 (1997).
[2] A. R. Smith, R. M. Feenstra, D. W. Greve, M. S. Shin, M. Skowronski, J. Neugebauer, and J. E. Northrup, J. Vac. Sci. Technol., B **16**, 2242 (1998).
[3] A. Winnerl, R. N. Pereira, and M. Stutzmann, J. Appl. Phys. **118** (2015).
[4] K. Sasaki, M. Higashiwaki, A. Kuramata, T. Masui, and S. Yamakoshi, Appl. Phys. Express **6**, 086502 (2013).
[5] C. Argile and G. E. Rhead, Surf. Sci. Rep. **10**, 277 (1989).
[6] K. D. Childs, B. A. Carlson, L. A. Vanier, J. F. Moulder, D. F. Paul, W. F. Stickle, and D. G. Watson, *Handbook of Auger Electron Spectroscopy* (Physical Electronics Industries, 1995).
[7] O. Lagerstedt and B. Monemar, Phys. Rev. B **19**, 3064 (1979).
[8] N. J. Watkins, G. W. Wicks, and Y. Gao, Appl. Phys. Lett. **75**, 2602 (1999).
[9] G. Hollinger, R. Skheyta-Kabbani, and M. Gendry, Phys. Rev. B **49**, 11159 (1994).
[10] I. Shalish, Y. Shapira, L. Burstein, and J. Salzman, Journal of Applied Physics **89**, 390 (2001).

[a)] Contributed equally to this work

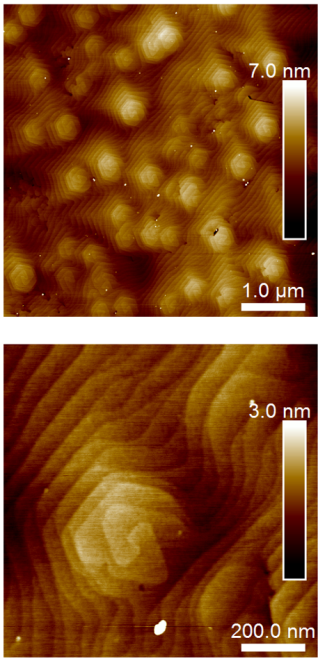

FIG. 1. AFM images of a PIMBE GaN(0001) surface. The morphology is in very good agreement with the general observations of the MBE-grown GaN(0001) epitaxial films in literature.[1–3]

TABLE I. Determined proportion of Ga, N and O of the first and the second layer of the two differently prepared MBE grown GaN samples and the Ga_2O_3 sample. The values of the AES measurements are treated in a similar way as it has been reported for the evaluation of the chemical composition of thin films.[5] In detail, the elemental sensitivities[6] and an exponential decay for the signal intensity with the number of layers are considered. Furthermore, from the universal curve and the GaN lattice parameter[7] it is interpreted that the Auger signal only results from the first four layers. Moreover, it is known that the oxidation of the GaN surface occurs in a layer by layer mode.[8,9] For the Ga_2O_3 sample the assumption of an oxygen rich first layer is chosen from AES measurements. For the GaN samples an oxidation in accordance with the first layer of the Ga_2O_3 sample is applied. Accordingly, the third and the fourth layer are for all three samples stoichiometric.

Material	Layer	Ga	N	O	"Native Oxide" /ML
GaN(0001)	first	0.47	0.33	0.20	0.18
	second	0.50	0.50	0.00	-
GaO_x/GaN(0001)	first	0.30	0.00	0.70	1.00
	second	0.53	0.41	0.06	0.05
$Ga_2O_3(\bar{2}01)$	first	0.30	0.00	0.70	-
	second	0.40	0.00	0.60	-

3

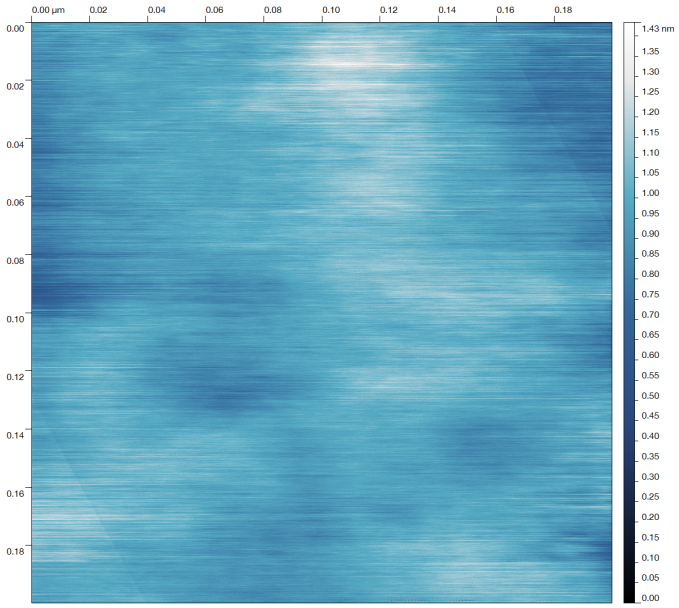

FIG. 2. AFM image of a Ga_2O_3 surface. Neither steps nor kink sites can be seen, which is in good agreement with observations of $Ga_2O_3(\bar{2}01)$ single crystals reported in literature.[4]

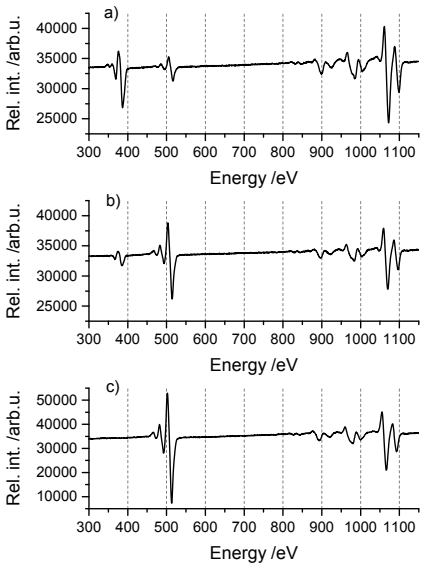

FIG. 3. AES spectra of a MBE-grown GaN(0001) sample (a)), an oxidized sample GaO_x/GaN(0001) (b)) and a Ga_2O_3 single crystal (c)).

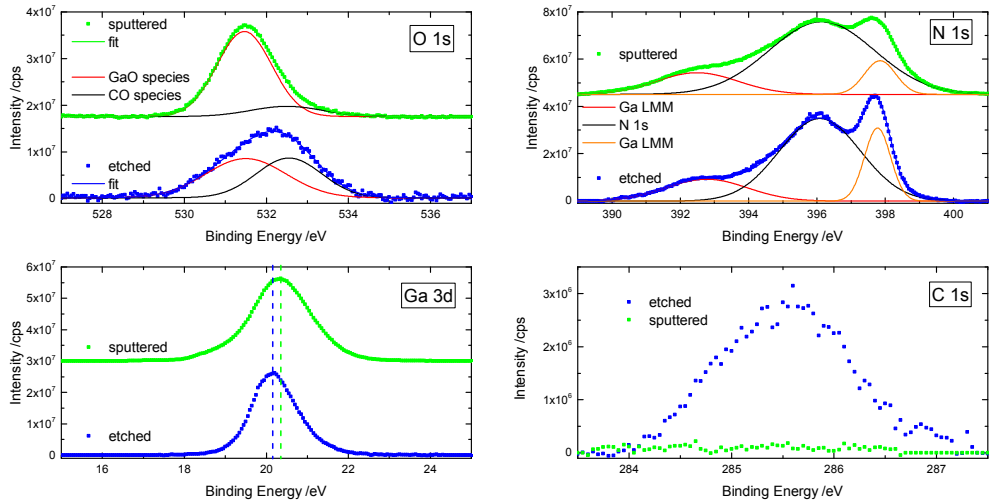

FIG. 4. XPS spectra of the O 1s, N 1s, Ga 3d and C 1s peaks of an etched and a sputtered GaN surface. The signals are intensity normalized to the Ga 3d peak and referenced to the position of the Ga-LMM Auger transitions. The O 1s peak shows that the etched sample exhibits two features, which can be assigned to gallium-oxygen and carbon-oxygen species.[10] While the gallium-oxide peak is growing in intensity, the carbon-oxide feature gets significantly reduced upon sputtering. For the N 1s peak no significant changes upon sputtering are visible. The Ga 3d peak shifts upon sputtering to higher binding energy. This is attributed to surface oxidation, which is in good agreement with the literature.[8] For the C 1s peak it can be seen that a carbon free surface can be obtained after 25 min of Ar sputtering.

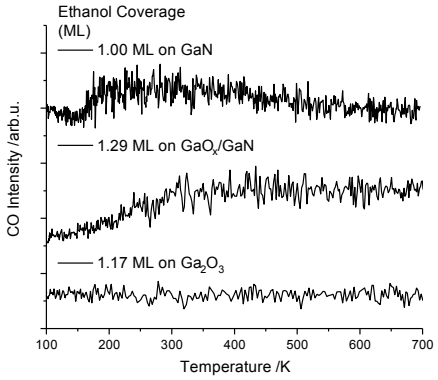

FIG. 5. Fragmentation-corrected CO traces of the TPD spectra for all three samples. It is found that CO and products exhibiting fragments at m/z = 28 are not significantly formed during a TPD run.

5

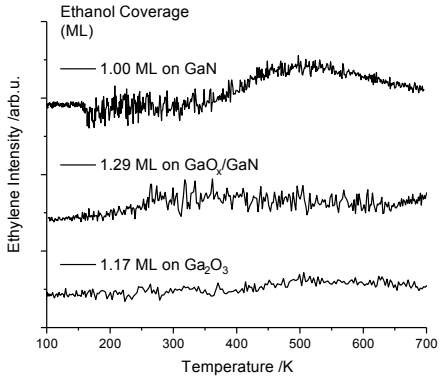

FIG. 6. Fragmentation-corrected ethylene (m/z = 27) traces of the TPD spectra for all three samples. While only a small ethylene yield may be visible on GaN, the sample with a higher degree of surface oxidation does not exhibit any reactivity in this reaction pathway at all. This is again similar to the reaction behavior of the Ga_2O_3 crystal.